UNIVERSIDAD DE EXTREMADURA

TESIS DOCTORAL

Título: Estudio de la optimización de dispositivos microfluídicos y sus aplicaciones

AUTOR/A: Alejandro Rubio González

PROGRAMA DE DOCTORADO: Modelización y Experimentación en Ciencia y Tecnología

Directores: Emilio J. Vega Rodríguez y M. Guadalupe Cabezas Martín

Esta tesis cuenta con la autorización del director/a y codirector/a de la misma y de la Comisión Académica del programa. Dichas autorizaciones constan en el Servicio de la Escuela Internacional de Doctorado de la Universidad de Extremadura.

2024

Study of the optimization of microfluidic devices and their applications

Alejandro Rubio González

Alejandro Rubio González

Study of the optimization of microfluidic devices and their applications

Abstract

This doctoral thesis aims to optimize the manufacturing of microfluidic devices by controlling sizes, shapes, and resolution. The precise control of shape and resolution in the fabrication of theses microfluidic devices will enable the analysis and refinement of production techniques for microjets and micro-nanofibers/microparticles, such as the Flow Focusing technique, as well as in vitro techniques for studying the human microcirculatory system and its components. These techniques have significant applications ranging from Biomedicine to Industrial Engineering. This thesis will also address these potential applications for health and Engineering.

Resumen del trabajo

Esta tesis doctoral tiene como objetivo optimizar la fabricación de dispositivos microfluídicos mediante el control de tamaños, formas y resolución. El control preciso de la forma y la resolución en la fabricación de estos dispositivos microfluídicos permitirá el análisis y la mejora de las técnicas de producción de microchorros y micro-nanofibras/micropartículas, como la técnica de Flow Focusing, así como técnicas in vitro para estudiar el sistema microcirculatorio humano y sus componentes. Estas técnicas tienen importantes aplicaciones que van desde la Biomedicina hasta la Ingeniería Industrial. Esta tesis también aborda estas potenciales aplicaciones para la Salud y la Ingeniería.

A los mios.

Prologue

This thesis presents a compilation of articles authored by the researcher during his doctoral studies in the program "Modeling and Experimentation in Science and Technology" at the University of Extremadura. The collection comprises 7 articles that provide original contributions to the field of Microfluidics and have been published in reputable journals with high impact factors. The research, conducted mainly between 2019 and 2023, took place in the Microfluidics laboratory of the University of Extremadura, with substantial support from the Fluid Mechanics group.

The document is structured into five sections: introduction, objectives, summary and discussion of each article's results, the papers themselves, and the conclusions derived from the thesis.

Contents

x

1
Introduction

Microfluidic technology has emerged as a transformative tool across scientific and industrial domains especially in biotechnology, enabling the manipulation of fluids at the microscale with exceptional precision and control. Numerous applications need techniques to generate droplet, bubbles, jets, emulsions or microcapsules. Therefore, research in microfluidics involves both the development of advanced devices to suit the application requirements and the understanding of the physics of flows at such small scales.

Different procedures have been used to fabricate microfluidic devices. Advances in microelectromechanical systems (MEMS) have led to the development of planar microfluidic devices that enable the fabrication, characterization, and sorting of micro-entities such as drops, bubbles, microcapsules or cells. This two-dimensional systems, often referred to as lab-on-a-chip, have been fabricated using micromachining or soft-lithography and are typically made from polydimethylsiloxane (PDMS). For example, high sensitivity diagnosis devices or organ-on-a-chip systems for drug development [1–3]. These devices, integrated with high-speed imaging, also facilitate real-time deformability cytometry [4], allowing the analysis of over 100 cells per second, and enhancing the diagnostic potential of microfluidic devices for assessing cell deformability. However, the limitations of planar devices, such as their 2D nature, the relatively complex, expensive, slow process and the challenges in integrating complex 3D structures, have led to the development of axisymmetric microfluidic devices for multiple applications [5–9].

Glass is chemically robust and possesses good mechanical and optical properties [10, 11]. This makes it adequate for constructing microfluidic axisymmetric devices. Glass based devices can be a single glass nozzle, as it was the case for a drop on demand system [5], or for deformability essays (Fig 1.1.a) or a complex assembly such as the Gas Dynamic Virtual Nozzle (GDVN) [7] in which an inner needle has to be adequately centered inside a glass nozzle. However, the fabrication of glass devices has some drawbacks, like the nozzle shape reproducibility, and the assembly and proper alignment of the components.

The technological advances in 3D printing techniques have allowed to overcome some of the problems of glass-based devices manufacturing, and to reduce the size of the devices. For example, two-photon polymerization process has been used to fabricate microfluidic devices, due to its high resolution, offering enhanced capabilities for fluid manipulation [12]. GDVNs nozzles have been printed with this technique. Early attemps fabricated devices with the same design as those using ceramic injection molding for the outer nozzle. Later, the geometry of the device was reconsidered, in order to obtain compact, optimized designs with plugging solutions that can be produced within minutes [13].

In this thesis, we have used the two-photon polymerization process to fabricate different
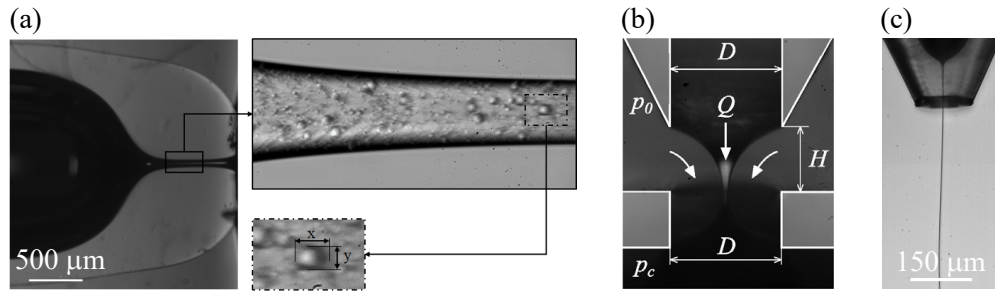
Figure 1.1: Examples of different microfluidic devices developed during this thesis. (a) Glass-nozzle to measure the deformability of flexible microparticles. (b) Flow focusing device with the original plate-orifice configuration built with a 3D printed needle and plate. The orifice is 30 μm in diameter. (c) 3D printed GDVN nozzle with a 75 μm orifice.

microfluidic devices, as a plate-orifice flow focusing system with an orifice as small as 30 μm (Fig. 1.1.b), or a one-piece GDVN nozzle with a 75 μm orifice and adequate connections for the fluid supply (Fig. 1.1.c).

Glass devices and deformability

As I mentioned earlier, microfluidic devices are often built with glass capillaries and nozzles. The latter are typically fabricated from capillaries using two methods: pulling or fire-shaping.

The pulling method has a long history in pipette manufacturing. This well-established technology includes several commercially available pullers, each supplied with a guide detailing the appropriate process parameters for specific pipette applications or geometries. In these pullers, the ends of the capillary are held by two jaws, while its central section is heated using either a electrical resistance or a laser. Then, one or both jaws are moved apart, stretching the capillary in the middle and producing two long, needle-shaped pipettes simultaneously. To separate them, pulling may continue until breakage, or a secondary cutting stage may be necessary. Pulled nozzles are frequently used in emulsion devices [14, 15]. Achieving the desired geometries often requires post-processing [16]. Tipically, the capillaries are pulled to produce a diameter much smaller than needed, and then the tips are sanded using abrasive paper to adjust the diameter and significantly shorten the nozzle length. For instance, the nozzles used in a gold nanoparticle fabrication device had inner diameters ranging from 100 to 240 μm but were created by sanding previously pulled nozzles of 20 μm [14]. Additionally, as the outer diameter of the nozzle tip becomes very small, a chemical coating treatment is usually necessary to prevent wetting along the outer surface of the nozzle, which would otherwise cause the microfluidic device to malfunction [14, 15].

On the contrary, though fire shaped nozzles have frequently been used to build devices, they have been fabricated manually. When heated, the glass flows to minimize its free surface, driven by surface tension forces and overcoming viscous stresses. The material moves inward, reducing both the diameter and the length of the capillary. The result is a convergent-divergent nozzle, much shorter than a pulled one. The divergent region makes fire-shaped interesting to be used as collection tubes for correcting misalignment issues [6, 17]. When used for injection, they do not require chemical treatment, as their shape creates a favorable contact angle to prevent wetting [18].

Recent efforts pretend to automatize the process in order to increase the reproducibility and explore the capabilities of this technique [10, 11]. The nozzles were fabricated with different orientation of the flame (vertical, or horizontal), and also of the capillary. Fire shaping allows the creation of nozzles in different sizes and shapes with adequate reproducibility and excellent symmetry, eliminating the need for post-processing. In this thesis (Paper I), we propose a new fire shaping strategy, in which the capillary is heated at the bottom of a lateral flame, and study the ranges of sizes and shapes that can be produced, and the reproducibility of the process.

The use of fire shaped nozzles has extended since Switzer et al. [19] included one in a drop-on-demand device. They have been combined with pulled nozzles to create devices for generating emulsions [6]. A similar configuration, where two nozzles tips are placed in front of each other, has been used for encapsulation in the food and pharmaceutical industry [9, 20]. Some of these assemblies need to be fixed, and the capillary may be glued using epoxy resin [14]. If disassembly is necessary, standard commercial connectors [18] or dedicated CNC milled blocks with press-fit features [15] can be used to place the capillary.

In addition to the glass properties mentioned earlier, glass nozzles are easy to fabricate and clean. This may make them an interesting alternative to current PDMS devices used for deformability studies. Its use was recently proposed for measuring the evolution of the deformation of red blood cells (RBCs) [5] emulating the strain rate produced in conventional 2D soft-lithography microchannels. In Paper II, we studied the stress peak produced in a fire shaped nozzle to analyze the appropriate flow conditions to perform deformation measurements. In Paper III, we used these nozzles to test the deformability of PDMS particles (Fig. 1.1.a) in an attempt to develop a blood analogue fluid.

Flow Focusing devices

Flow Focusing (FF) [21] is a widely used technique where a liquid is injected at a constant flow rate through a feeding capillary located in front of an orifice or inside a converging nozzle. A coflowing gas stream is forced to cross the orifice/nozzle, creating favorable pressure gradients and viscous stresses that stretch the liquid meniscus that is attached to the capillary tip. Under adequate conditions, a jet much thinner than the nozzle orifice is emitted from the meniscus tip (a phenomenon known as steady jetting via tip-streaming). The jet breaks up into droplets due to capillary instabilities. The stability and size of the produced entities can be finely tuned by adjusting the flow rates and viscosities of the liquids and gases involved. This technique is widely used to produce thin jets [22] or micro-fibers [23] among others.

In the original flow focusing device [24] a capillary is located in front of a plate with an orifice of the same diameter. The stability of steady jetting for this device has been studied [24–27] and the liquid flow rate was found to be the key parameter controlling the meniscus stability [27]. However, the sizes of the devices in these studies are limited by fabrication issues: the use of commercial needles as capillaries and the drilling of the orifice in the plate. The use of 3D printing have allowed us to further reduce the size of the device. In Paper IV, we fabricated smaller tips and orifices of different diameters, up to 30 μm (Fig. 1.1.b). This allowed us to explore a parametric region not previously studied, and to unveil the effect of gas viscosity on the steady jetting stability.

The Gas Dynamic Virtual Nozzle (GDVN) [7] was proposed as an alternative to design the original plate-orifice configuration [21] for axisymmetric Flow Focusing. Initially, the GDVN ejector consisted of a tapered capillary located inside of a fire-shaped glass nozzle. Assembly and alignment of the components of the GDVN was a critical issue. The tube and the capillary were initially aligned using a centering sleeve [7], and were later replaced by other elements, such as a 3D printed part [28]. The alignment problems were also overcome by replacing the outer glass nozzle with an injection-molded opaque ceramic one with alignment features to overcome this problem [29, 30].

The stability of steady jetting in GDVN devices is additionaly hindered by global whipping [31], an undesired phenomenon, not present in the original plate-orifice configuration. When the pressure drop rises, the meniscus may start to oscillate laterally. This may even cause the interruption of the jet if it touches the inner nozzle wall. To prevent this effect, it was suggested to use nozzles with higher convergent rates [31]. In Paper I, we show that this phenomenon can be prevented choosing an adequate nozzle shape. The effect of the shape of the nozzle on the whipping instability was deeper studied in Blanco et al. [22].

The use of 3D printing for GDVN devices fabrication have significantly facilitated their construction what has contributed to make one of the most popular approaches for sample delivery in Serial Femtosecond Crystallography (SFX). SFX is a technique that has revolutionized the molecular determination of complex biochemical species, enabling the study of proteins, viruses, and other biological molecules with unprecedented resolution [32].

The search for extremely thin and fast stable jets, which are essential for applications such as SFX make use of transonic flow focusing, where the outer gas stream is accelerated to transonic speeds and discharged into a low-pressure chamber (Fig. 1.1.c). For example, water jets with diameters of about 1 μm and speeds of up to 100 km/h can be achieved using a transonic helium stream [31, 33]. Transonic flow focusing exhibits distinct differences from its incompressible counterpart. In most practical implementations, the jetting mode instability originates in the tapering meniscus rather than in the emitted jets. Additionally, the whipping instability is suppressed. In Paper V, we study the stability of transonic flow focusing of Newtonian fluids both numerically and experimentally.

In Paper VI, we extend the stability study of transonic flow focusing to slightly viscoelastic solutions, showing that high-velocity gradients in the tapering meniscus can induce a coil-stretch transition in polymer molecules that stabilized the jet and allows to produce smaller diameters (Fig. 1.2). The viscoelastic transition that occurs under very restrictive conditions, produces very long jets. In Paper VII, we study the appearance of the jet instabilities, and we find conditions that allow us to produce thin jets thousands of times longer than their diameter.
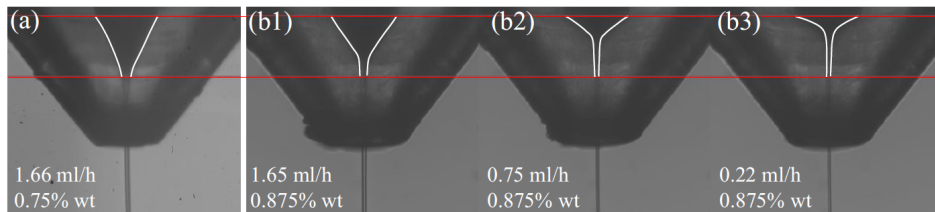

Figure 1.2: Meniscus shape for PEO100K and p_0 = 2.5bar. Images (a) and (b3) correspond to the minimum flow rate for those concentrations. (b1) and (b2) are intermediate steps for the same critical concentration. The white lines mark the meniscus profile and the red lines are a guides to the eye.

Author contributions

The author of this present thesis has made the following contributions to the articles in this compendium:

- **Paper I - Capabilities and limitations of fire-shaping to produce glass nozzles.** Experiments.

- **Paper II - Fire-shaped nozzles to produce a stress peak for deformability studies.** Numerical simulations and experiments.

- **Paper III - A particulate blood analogue based on artificial viscoelastic blood plasma and RBC-like microparticles at a concentration matching the human hematocrit.** Experiments.

- **Paper IV - Influence of the gas viscosity on the stability of flow focusing.** Device design, fabrication and experiments.

- **Paper V - Transonic flow focusing: stability analysis and jet diameter.** Device design, fabrication and experiments.

- **Paper VI - Viscoelastic transition in transonic flow focusing.** Experiments.

- **Paper VII - Unexpected stability micrometer weakly viscoelastic jets.** Experiments.

2
Objectives

The main objective of this thesis is to enhance our understanding of microfluidic devices through the application of various methodologies in their fabrication. The research aims to address outstanding questions regarding the performance of these devices under different conditions and the optimization of their design. Each paper included in this compilation sets specific objectives, detailed on the following page.

Paper I   To analyze the reproducibility and shape capabilities of a new fire-shaping approach for fabricating glass nozzles by heating a vertically rotating capillary at the bottom of a lateral flame. Additionally, the study aims to explore how the nozzle shape affects the performance of microfluidic systems, particularly preventing whipping and extending the pressure range for emitting thin jets.

Paper II   To study numerically the stress produced by a fire-shaped nozzle when used for particle deformability studies, and to evaluate the deformation response to that stress of flexible particles.

Paper III   To find the most adequate compositions of the base fluid and the flexible particles to obtain a complex blood analogue fluid which behave like real blood.

Paper IV   To study the influence of the gas viscosity in the meniscus stability in flow focusing using plate-orifice configuration, by applying dimensional analysis and without actually changing the gas viscosity.

Paper V   To understand the relationship between gas pressure and the minimum flow rate for steady jetting in transonic flow focusing, validate a global stability analysis by experiments, and derive a scaling law for the jet diameter based on liquid flow rate and gas density/pressure.

Paper VI   To understand how very weak viscoelasticity affects in the stability of steady jetting in transonic flow focusing and unveil the mechanism involved.

Paper VII   To analyze the behavior of a micrometer weakly viscoelastic jets, produced with transonic flow focusing, by studying the length of the jets and the instabilities produced by the polymers when the forces are low far away of the birth point of the jet.

3

Summary of results and discussion

On the subsequent pages, you will find concise summaries outlining my contributions to each article. These summaries include key figures from the papers along with the most notable conclusions.

Paper I - Capabilities and limitations of fire-shaping to produce glass nozzles.

Microfluidic devices often include fire-shaped nozzles. Though the size and shape of the nozzles are critical features of the devices, most of them are fabricated manually. Recent works of our group [10, 11] have been the first attempts to automatize the fabrication process. In this work we consider a new strategy of fire shaping, in which the capillary is located below a lateral flame while it is heated.

We studied the effect of the fabrication parameters on both, the nozzle size reproducibility and its shape. The size of the neck depends on the heating time, and position. The complexity of the flame and glass flow phenomena are only one of the causes of the neck size scatter, for the same heating parameters. The variability of the original capillary dimensions, especially the inner diameter, also reduces the reproducibility. The nozzle shape could be varied within a range by modifying the vertical position (distance to the axis of the burner), and the time accordingly, though, for a given diameter reduction, there is a minimum nozzle length due to the overturning of the surface (Fig. 3.1.a).
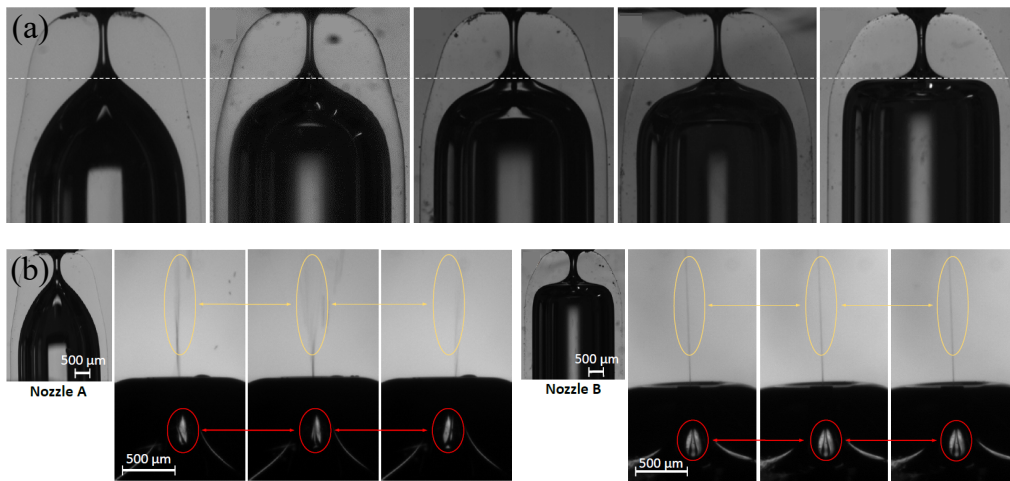

Figure 3.1: (a) Nozzles of $D \approx 135$ μm manufactured at different positions. From left to right: r = 3.5 mm, t = 150 s, ΔL = 1.47 mm; r = 4 mm, t = 250 s, ΔL = 1.40 mm; r = 4.5 mm, t = 325 s, ΔL = 1.26 mm; r = 5 mm, t = 600 s, ΔL = 1.22 mm; r = 5.5 mm, t = 2000 s, ΔL = 1.14 mm, respectively. The line is to guide the eye. (b) Sequences of experimental images of the jet emitted by the two GDVNs devices with Nozzle A and Nozzle B. The distilled water inner flow rate is Q = 6.9 mL/h and the air pressure drop is Δp = 300 mbar.

Different shapes are also obtained changing the original capillary dimensions. The shape reproducibility is excellent for nozzles of the same size produced with the same conditions. We defined the neck aspect ratio (AR) to evaluate the length of the neck channel in terms of its diameter. Large diameter reductions will show higher AR, though the nozzle itself may be

shorter (as the heated material flows inwards and downwards). In general, reducing the capillary inner diameter would reduce the diameter reduction (difference between the original capillary and the nozzle diameters) and the neck channel length. However, this effect may be compensated for by the wall thickness. We showed that, for the same outer diameter, thicker capillaries may produce longer channels, even when they need a smaller diameter reduction. So, the original capillary selection becomes a key aspect determining the nozzle shape and affecting the fabrication reproducibility.

The shape of the nozzle may affect the performance of the devices in some applications. For instance, in the GDVN device used for flow focusing, the whipping instability may prevent steady jet emission. We built two devices using nozzles of the same neck diameter but with different shapes. Whipping was observed in the first device, which included the nozzle, with the smoother diameter transition, but was not present for the second nozzle, with a more abrupt shape (Fig. 3.1.b). There was a range of experimental conditions for which both GDVNs devices emitted a steady jet. However, the jet diameter (and velocity) were also affected by the nozzle shape. A deeper investigation of the effect of the nozzle shape for different liquid-air systems and working conditions can be found in [22].

Paper II - Fire-shaped nozzles to produce a stress peak for deformability.

The mechanical behaviour of deformable particles or capsules is relevant for some applications. For that reason, different microfluidic devices have been developed to measure their deformation when a particular stress is applied. The use of fire-shaped nozzles was recently proposed to study Red Blood Cells deformability [5]. However, to evaluate the results, it is necessary to have further knowledge of the stress associated to the flow in the nozzle.

In this work, we study the flow inside nozzles with the same diameter and different shapes (Fig.3.2.a). These nozzles were manufactured from different original capillaries, different heating times and positions. The nozzle shape was characterized by the convergent length L_c (distance of the convergent region from the original diameter to the neck) and neck length L_n (distance of the final reduction of the neck).
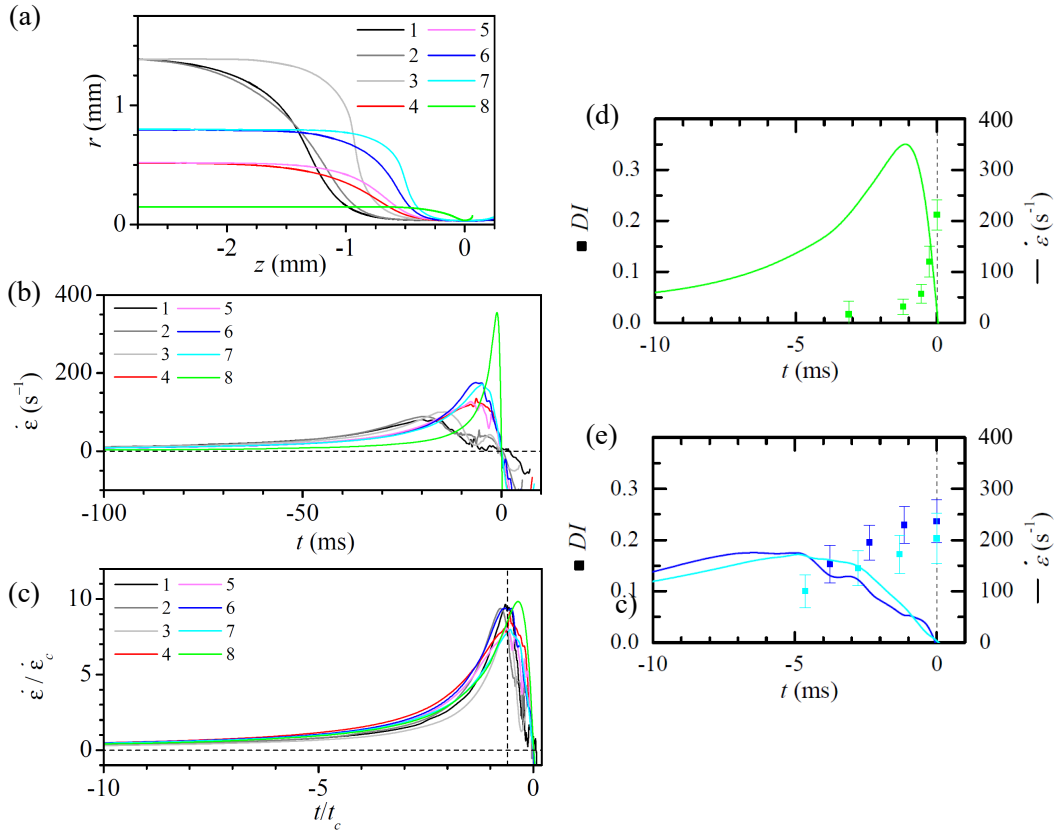

Figure 3.2: (a) Mean profiles of nozzles. (b) Strain rate along the nozzle versus the time. (c) Dimensionless strain rate along the nozzle axis versus dimensionless time to reach the neck. Temporal evolution of the particle deformation (symbols) and numerically calculated strain rate (lines) for (d) nozzle 8 and (e) 6 (blue) and 7 (cyan). $Q = 5$ μL/min in all.

We simulated the flow of the liquid without particles inside the nozzle to obtain the resulting strain rate (Fig. 3.2.b). All nozzles produced a stress peak. Proper adimensionalization

using the mean strain rate in the convergent region $\dot{\varepsilon}_c = v_n/L_c$ and the characteristic time t_c = L_n/v_n, where v_n is the mean velocity in the neck, produced an outstanding overlaping of the curves (Fig. 3.2.c). So, for a fire-shaped nozzle, it is possible to anticipate the stress peak intensity and position from the two parameters L_c and L_n.

We showed that the deformation of viscoelastic particles is not immediate. The timing and location of the stress peak are important factors since they influence the deformation observed in different sections. Nozzles created from smaller and thinner capillaries generate a very sharp peak close to the neck, often resulting in the microcapsule reaching its maximum deformation past the neck (Fig. 3.1.d). On the contrary, nozzles made from larger or thicker capillaries usually have longer necks, causing the stress peak to broaden and shift away from the neck (Fig. 3.1.e). By examining the shape of the microcapsule along the convergent region of the nozzle, one can observe both its deformation and recovery. To ensure the maximum deformation occurs at the neck, the nozzle should create the strain rate peak roughly 5 milliseconds before it reaches that point.

Paper III - A particulate blood analogue based on artifical viscoelastic blood plasma and RBC-like microparticles at a concentration matching the human hematocrit.

In this paper, we describe a protocol to produce a whole human blood analogue to mimic rheological and some physiological characteristics of real human blood at body temperature ($37\,^\circ C$). The blood analogue is composed of a viscoelastic plasma analogue and PDMS flexible spherical microparticles at a concentration matching the human haematocrit (42% by volume). The PDMS microparticles were fabricated using the two-syringe membrane emulsification technique (2SME) [34]. We used glass micronozzles to find the appropriate mixing ratio between base polymer and curing agent of PDMS for the particles to have approximately the same Young's modulus (ε) as that exhibited by real RBCs.

The viscoelasticity of the plasma analogue was adjusted to that of human plasma from Brust et al. [35] and Sousa et al. [36] (Fig. 3.3.a) by adding polyethylene oxide (PEO) with a suitable M_w, among other special conditions.
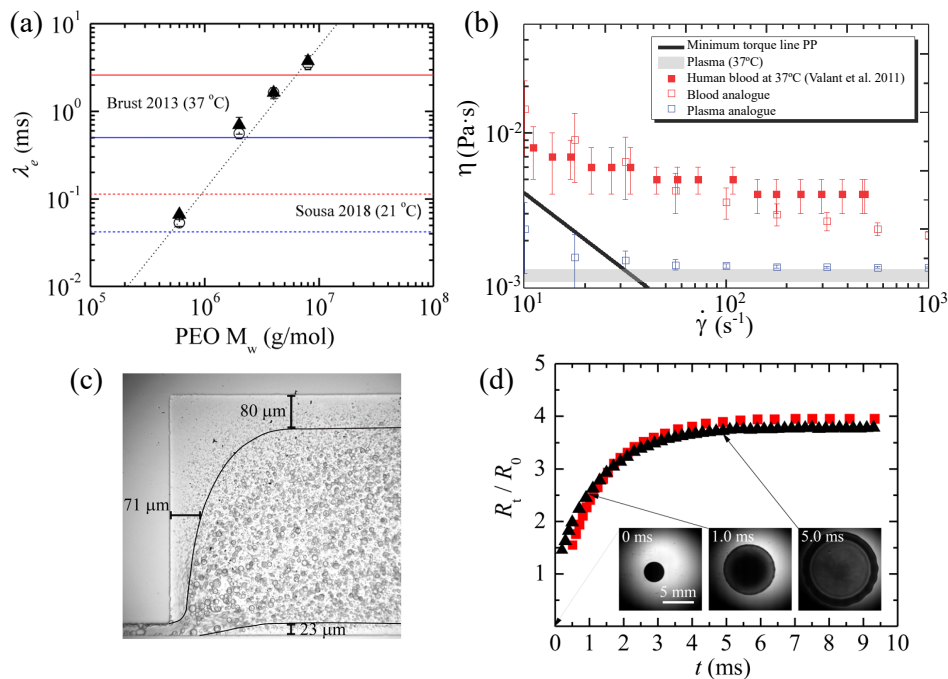

Figure 3.3: (a) Extensional relaxation time λ_e versus M_w of the PEO used in the plasma analogue plasma analogue (white circles) for the blood analogues (around 42% vol. of particles, black triangles). Lines depict the results of the extenional relaxation time for human plasma (blue) and whole blood (red), from Brust et al. (solid line) and Sousa et al. (dash line). The dot line is the fitting. (b) Shear viscosity η upon the shear rate γ of the plasma and the blood analogues at $20\,^\circ C$ in comparison with the real human blood and blood plasma at $37\,^\circ C$. (c) Cell-free layer efect on a microfluidic channel for DMSO/WPEO4M$_{45:1}$. The solid lines are a guide to the eye, marking the free area of particles with $D > 6\mu$m. (d) Time evolution of spreading radius R_t of dog whole blood (red squares) and the DMSO/WPEO4M$_{45:1}$ (black triangles) for the same We. In both cases $t = 0$ ms is the time at which the droplet contacts the solid surface.

The properties used for the comparison were the density, the extensional relaxation times, the linear rheological response and the steady shear viscosities of plasma analogues created with M_w from 600 kDa to 8 MDa.

The shear rheology of the blood analogue only depends significantly on the PDMS particle composition (Fig. 3.3.b). Particles of PDMS 45:1 being in best agreement with the viscous behaviour of human blood [35, 36].

The blood analogue fluid developed in this work success to reproduce some of the multiphase flow effects observed for the blood, such as the cell-free layer effect in a microfluidic channel expansion (Fig. 3.3.c). It also matches the blood behaviour at a microscale level, as the study of the evolution of a droplet impacting on a solid surface (Fig. 3.3.d) used in blood stain pattern analysis.

Paper IV - Influence of the gas viscosity on the stability of flow focusing.

The study of the stability limit of the flow focusing technique is relevant since it determines the minimum size of the jet that can be produced. The parametric range of the previous studies was limited by the size of the devices used, and the gas viscosity was considered to play a secondary role on the minimum flow rate. The use of 3D printing in this work allows to reduce the size of the orifices in a plate-orifice flow focusing device and to explore a different parametric region.

Dimensional analysis was used to study how the gas viscosity affects the stability limit without actually changing the gas viscosity. The relevant dimensional number in the problem were the Ohnesorge number, the capillary number, and the viscosity ratio. The first is determined by properties of the liquid and the size of the device. Liquids or liquids mixtures with different viscosity (and surface tension) were selected accordingly to the orifice size to produce the same Ohnesorge number, and viscosity ratios much smaller than those of previous works. The results show that for low Ohnesorge numbers (Oh = 0.039 ± 0.004) the minimum flow rate for which steady jetting can be produced exhibits a non-monotonous behavior, reaching its lowest value for an optimum viscosity ratio. (Fig. 3.4.a).
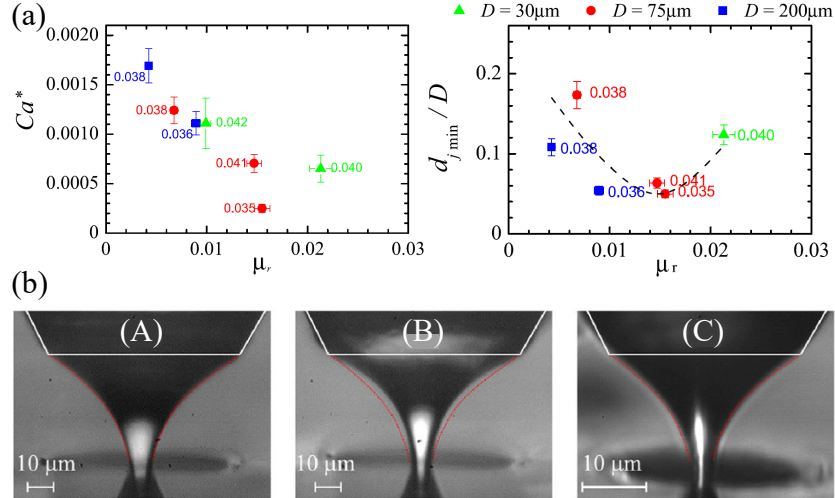

Figure 3.4: (a) Critical capillary number (C^*) and dimensionless jet diameter (d_{jmin}/D), versus the viscosity. Meniscus shape for Oh = 0.038 ± 0.003, C_μ = 0.235, Ca = 1.3 ×10^{-3}, and (A) μ_r = 6.75 ×10^{-3}, (B) μ_r = 1.55 ×10^{-2}, and (C) μ_r = 2.13 ×10^{-2}. The pressure difference Δp was adjusted to produce the same C_μ. The orifice diameter is 75 μm in (A) and (B), and 30 μm in (C). The images have been scaled so that the orifice has approximately the same diameter. The red line indicates the shape of the meniscus (A).

As occurs with the critical capillary number, the meniscus dimensionless shape exhibits a non-monotonous dependence of the viscosity ratio: the shape is practically the same for

the two extreme values of μ_r, while the meniscus thins for the optimum viscosity ratio (Fig. 3.4.b). If we apply these results to a system (with a particular liquid and size), there is an optimum gas viscosity for which the minimum flow rate (and jet size) can be obtained. Our results illustrate the complexity of the flow arising in the tapering meniscus of flow focusing. Increasing the viscous drag exerted by the gas stream does not necessarily stabilizes the meniscus.

Paper V - Transonic flow focusing: stability analysis and jet diameter

Transonic flow focusing is chosen for some applications, such as SFX, because of its capability of producing very thin jets. The reduction of the jet size through the liquid flow rate reduction is limited by the stability of the meniscus. In this work, we use global stability analysis to determine the minimum flow rate for transonic flow focusing using a GDVN device. The same GDVN device used in the simulations was fabricated with the Nanoscribe Photonic Professional GT2. Interestingly, the global stability analysis accurately predicts the minimum flow rate measured in the experiments, Figure 3.5.a. The agreement between the numerical and experimental results is even better than in the incompressible regime [37]. Our results show that the minimum flow rate slightly depends on the stagnation pressure for the range of pressures considered in our analysis. This conclusion is similar to that obtained in the incompressible regime for sufficiently large pressure drops [27]. The steady jetting interruption is caused by the growth of an inertiocapillary perturbation, making the meniscus and jet collapse simultaneously at the stability limit. The simulation satisfactorily reproduces the shape of the experimental tapering meniscus Figure 3.5.b. However, it seems to underestimate the jet diameter.
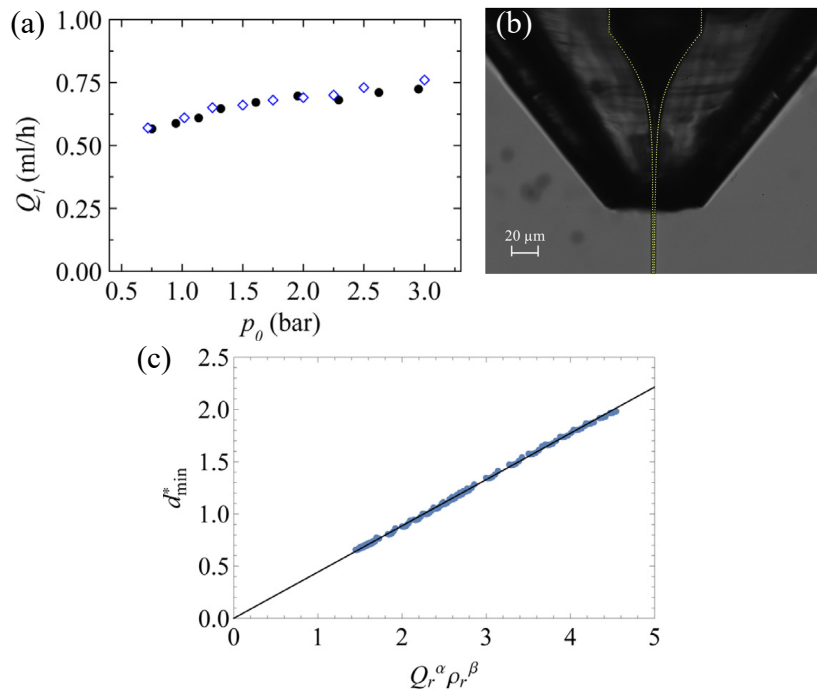

Figure 3.5: (a) Minimum value of the liquid flow rate Q_l as a function of the upstream stagnation pressure p_0 obtained experimentally (open symbols) and numerically (solid symbols). (b) Experimental image and free surface position calculated numerically (dotted line) for $p_0 = 1.75$ bar and $Q_l = 0.68$ ml/h. (c) Scaling law and numerical data (symbols).

We derived a scaling law for the jet diameter that shows that, as expected, the liquid flow rate is the most important control parameter, while the gas pressure (density) plays a secondary role. Equation $d^*_{min} = C\, Q_r^\alpha\, \rho_r^\beta$ with $C = 0.433$ $\alpha = 0.308$ and $\beta = -0.06$ is very accurate within the d_{min} in the range of values between 0.549 and 10.9 μm analyzed in the simulations (Fig. 3.5.c).

Our numerical procedure consumes much less computing time than direct numerical simulations, in which the hydrodynamic equations are integrated over time until the jetting regime is established. For this reason, this procedure can be a helpful tool for determining the optimal parameter conditions in SFX, despite the fact that we cannot calculate the jet breakup length.

Paper VI - Viscoelastic transition in transonic flow focusing.

We studied the stability limit of steady jetting for slightly viscoelastic liquid and discovered that a viscoelastic transition occurred in transonic flow focusing when polymers of low molecular weights are added to water at an adequate concentration. This phenomenon is caused by the coil-stretch transition of polymers in the tapering meniscus, despite the smallness of their relaxation time.

Withing a particular concentration range, the arising elastic stresses collaborate with those exerted by the outer flow in pushing the liquid throughout the meniscus-jet region. The resulting extra acceleration explains the meniscus shrinkage (Fig. 3.6.a). When the flow rate is decreased, the jet speed near the meniscus tip increases, the meniscus length decreases, and, therefore, the strain rate field in the meniscus increases. This effect enhances the building-up of the elastic stress, which explains why the meniscus shrinkage sharply increases as Q decreases reducing the jet diameter in one order of magnitude (Fig. 3.6.b). This phenomenon appears for a wide range of gas stagnation pressures and polymers with different molecular weights.
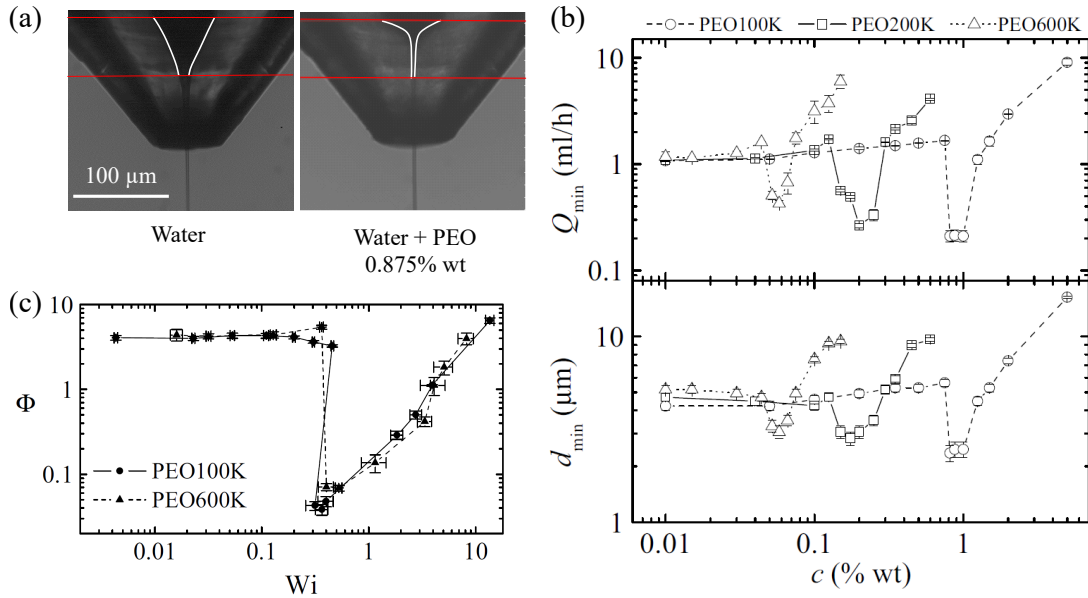

Figure 3.6: (a) Newtonian-type (left) and viscoelastic (right) menisci formed in the experiments with water at $Q = 0.75$ ml/h and PEO100K at $c = 0.875\%$ wt, $Q = 0.22$ ml/h. (b) Minimum flow rates leading to the jetting regime and the corresponding diameters for polymer solutions with different molecular weights. (c) Φ (Wi) for PEO 100K and PEO600K. All the experiments were conducted for $p_0 = 2.5$ bar. Φ is defined as the Reynolds number, and the Capillary number below and above the critical concentration respectively.

Our scaling analysis for the minimum flow rate reveals the role played by the polymer relaxation time and the extensional viscosity in the viscoelastic transition. This transition

takes place at a critical concentration c_1^* that corresponds to a Weissenberg number around 0.5 (Fig. 3.6.c). For subcritical realizations $(C < c_1^*)$, Φ represents the Reynolds number and takes values of order unity , as occurs in the Newtonian low-viscosity case [24, 38]. For supercritical polymer concentrations $(C > c_1^*)$, Φ represents the capillary number, defined in terms of the polymer extensional viscosity, is a function of the Weissenberg number. The smaller values taken by the capillary number are similar to those of the Newtonian high-viscosity case [27].

Paper VII - Unexpected stability micrometer weakly viscoelastic jets.

In the previous work (Paper VI), we identified a viscoelastic transition in transonic gas flow focusing when low molecular weight PEO is dissolved in water at specific concentrations. This transition impacts the stability of the emitted jet making it highly stable. The capillary instability is delayed, and the jet breakup occurs at distances from the ejector of the order of tens of thousands the jet diameter (Fig. 3.7.a). The intense converging extensional flow in the ejection point builds up viscoelastic stress that does not relax in the jet even for times much longer than the polymer relaxation time (Fig. 3.7.b).
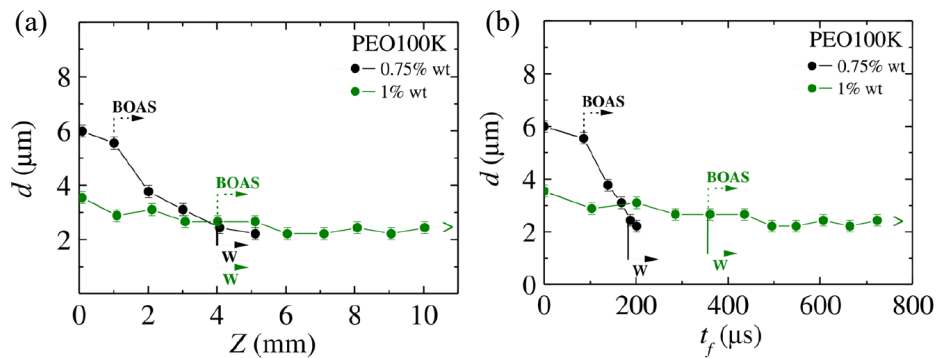

Figure 3.7: Jet diameter d vs the distance from the ejector exit, Z, and the jet flight time, t_f, for the subcritical (c = 0.75 % wt., Q = 1.6 ml/h) and supercritical (c = 1 % wt., Q = 0.4 ml/h) PEO100K jets. The vertical solid and dashed lines indicate the beginning of whipping (W) and beads on a string (BOAS) instability respectively. The chevron-right green arrow indicates that the supercritical jet broke up at distances from the ejector larger than 10 mm.

In the absence of sufficient strain rate beyond the discharge orifice, the polymers are expected to relax to their coiling state, and the extensional viscosity decreases to its equilibrium value. Then, the capillary instability is expected to arise inmediately after polymer relaxation, and produce an incipient beads on a string (BOAS) structure on a timescale given by the inertio-capillary time t_c. This behaviour was observed for subcritical solutions. However, the appearance of the BOAS structure was significantly delayed for supercritical solutions. We found that the maximum jet stabilization in our experiments was achieved by adding PEO100K at a concentration of around 1% wt. In this case, the BOAS instability was considerably delayed, and jets about 2 μm in diameter flow more than 1 cm without breaking up (Fig. 3.7.a). This superstability may be attributed to the axial stress produced by a slightly nonuniform velocity profile in the aerodynamically driven micrometer jet, and long-lived memory effects experienced by the jet. We hypothesize that this last effect is caused by the partial entanglement of the polymers in the tip of the viscoelastic tapering meniscus, even though the polymer molecular weight and concentration are very low.

4

Paper I - Capabilities and limitations of fire-shaping to produce glass nozzles.

Capabilities and Limitations of Fire-Shaping to Produce Glass Nozzles

Alejandro Rubio [1] , **Sergio Rodríguez** [1] **and Maria G. Cabezas** [1,2,*]

[1]   Department of Mechanics, Energetic and Materials Engineering, University of Extremadura,
     E-06006 Badajoz, Spain; arubiorg@unex.es (A.R.); srodriguwk@alumnos.unex.es (S.R.)
[2]   Institute of Advanced Scientific Computation (ICCAEx), University of Extremadura, E-06006 Badajoz, Spain
[*]   Correspondence: mguadama@unex.es

Abstract: Microfluidic devices for drop and emulsion production are often built using fire-shaped (or fire-polished) glass nozzles. These are usually fabricated manually with inexpensive equipment. The shape limitations and poor reproducibility are pointed as the main drawbacks. Here, we evaluate the capabilities of a new fire-shaping approach which fabricates the nozzle by heating a vertical rotating capillary at the Bottom of a Lateral Flame (BLF). We analyze the effect of the heating conditions, and the capillary size and tolerances. The shape reproducibility is excellent for nozzles of the same size produced with the same conditions. However, the size reproducibility is limited and does not seem to be significantly affected by the heating conditions. Specifically, the minimum neck diameter standard deviation is 3%. Different shapes can be obtained by changing the heating position or the capillary dimensions, though, for a given diameter reduction, there is a minimum nozzle length due to the overturning of the surface. The use of thinner (wall or inner diameter) capillaries allows producing much shorter nozzles but hinders the size reproducibility. Finally, we showed an example of how the performance of a microfluidic device is affected by the nozzle shape: a Gas Dynamic Virtual Nozzle (GDVN) built with a higher convergent rate nozzle works over a wider parametric range without whipping.

Keywords: fire-shaping; fire polishing; glass nozzles; Gas Dynamic Virtual Nozzle; flow focusing; microfluidics

1. Introduction

Microfluidics is receiving growing attention in numerous fields, especially in biotechnology where it is becoming a key tool. Research in microfluidics involves both the understanding of the physics of flows at such small scales and the development of the devices for different applications. Two-dimensional systems, usually referred to as lab-on-a-chip, have been fabricated by micromachining or soft-lithography. Low cost-high sensitivity diagnosis devices or organ-on-a-chip systems for drug development and testing are some examples [1]. Three-dimensional devices can be built by the assembly of glass capillaries [2–4]. The advantages of glass are that it is chemically robust, and has good mechanical and optical properties. It allows building very versatile devices, although their fabrication has a few drawbacks. There are limitations to the nozzle shape, and the assembly and proper alignment of the components may be challenging. Different 3D printing techniques have been also proposed for fabricating microfluidic devices, most with millimetric scale features. However, the resolution improvement of some techniques is broadening their applicability for building real microfluidic devices [5].

Capillary devices in which two nozzle tips are placed in front of each other are very common for emulsion production and encapsulation in the food and pharmaceutical industries [3,4,6,7].

A square shape capillary with an inner diameter equal to the outer of circular ones is used for the alignment. The nozzles are shaped at one end of the round capillaries, and then they are inserted in the square one through opposite ends [6–9]. To build a fixed microfluidic device, the square shape capillary may be glued onto a microscope slide using an epoxy resin [9]. If disassembly is necessary, standard commercial connectors [8] or dedicated CNC milled blocks with press-fit features [10] can be used to place the capillary.

The Gas Dynamic Virtual Nozzle (GDVN) [11] is another microfluidic capillary-based device which is very commonly used for liquid sample delivery in Analytical Chemistry. It was proposed as an alternative to the original plate-orifice configuration for axisymmetric Flow Focusing (FF) [12]. The GDVN ejector consists of a tapered capillary located inside of a nozzle. Under adequate working conditions, a meniscus of the inner liquid is attached to the capillary tip, and the coflowing stream stretches it dragging a jet much thinner than the nozzle orifice. Assembly and alignment of the components of the GDVN is also an issue. In the original GDVN device, the tube and the capillary were aligned using a centering sleeve [11], which can be replaced by other elements, such as a 3D printed part [13]. The combination of square and round capillaries has also been considered. The outer nozzle was fire-shaped at a square capillary, and the internal needle had an outer diameter equal to the inner square side [14]. In some newer GDVN designs, the outer glass nozzle has been replaced by an injection-molded opaque ceramic one with alignment features to overcome this problem [15,16]. The use of 3D-printing has also been proposed for the direct fabrication of the whole GDVN device. Among all the numerous methods, the 2-photon-polymerization process is preferred due to its high-resolution. The 3D printed GDVNs designs have evolved from the first attempts, which mimicked the original assembly [17], to compact optimized designs with plugging solutions that can be produced within minutes [18].

In capillary-based microfluidic devices, nozzles are usually fabricated by two procedures: pulling or fire-shaping (also known as fire-polishing). The former has been traditionally used for pipette manufacturing. The technology is mature and several commercial pullers are available, which are supplied with a cookbook indicating the adequate process parameter for a particular pipette application or geometry. In pipette pullers, the capillary ends are held by two jaws, and its central section is heated with an electrical resistance or a laser. Then, one or both jaws are moved apart stretching the capillary in the middle and producing two long and needle-shaped pipettes at the same time. To separate them, pulling may be maintained until breakage or a secondary cutting stage may be necessary. Pulled nozzles are commonly used in emulsion devices [9,10]. To obtain adequate geometries, post-processing is usually necessary [19]. The capillaries are pulled to produce a diameter much smaller than the desired one, and then the tips are grazed against abrasive paper to adjust the diameter and significantly reduce the nozzle length. For example, the nozzles used in a gold nanoparticle fabrication device have inner diameters ranging from 100 to 240 μm and are obtained by grazing previously pulled nozzles of 20 μm (the original capillary is 1.0 mm O.D. and 0.58 mm I.D.) [9]. Additionally, as the outer diameter of the nozzle tip also becomes very small, a chemical coating treatment is usually necessary to prevent wetting along the outer surface of the nozzle that would cause malfunctioning of the microfluidic device [9,10].

Fire-shaping produces the nozzle by heating the capillary tip typically with a flame. It is also known as fire-polishing because it is used to smooth the surface of the pipette's tip after breaking or grazing without significant change in the diameter too. When the capillary tip is heated, the glass flows to reduce its free surface driven by surface tension forces and overcoming the viscous stresses. The material moves inwards reducing the diameter and the length of the capillary. The result is a convergent-divergent nozzle much shorter than a pulled one. The use of these nozzles have extended since Switzer [20] included one in a drop-on-demand device. They have been combined with pulled ones to assemble devices for generating emulsions. The divergent region of fire-shaped nozzles makes them advantageous as collection tubes for correcting misalignment problems [6,21]. When used for injection, they do not need a chemical treatment as their shape creates a favorable contact angle to

prevent wetting [8]. To the best of our knowledge, glass nozzles in GDVNs devices are only fabricated by fire-shaping as in the original design [11]. The latter is widely used to produce the jet that carries the samples for femtosecond X-ray protein nanocrystallography [22]. The nozzle was fire shaped in a square shape capillary for the injector for x-ray scattering studies of biological nanospecies [14]. Liquid-liquid flow-focusing with GDVNs [23] can also be used to produce emulsions. In some devices, as in the assembly to produce nanometric polymeric fiber proposed by Ponce-Torres et al. [24], the divergent region of the fire-shaped nozzle is removed.

Although the use of fire-shaped nozzles is extended, most researchers fabricate them manually. Very few fire-shaping systematic studies have been carried out. First, traditional fire-shaping approaches were analyzed using the flame of a vertical Bunsen burner in a setup designed to reduce the operator intervention [25]. When the vertical capillary is heated at the top of the flame (Figure 1a), highly axisymmetric nozzles are produced. However, it does not seem possible to control the nozzle neck diameter with the heating time. Although the neck reproducibility highly increases when the capillary is heated horizontally on the side of the flame (Figure 1b), the lack of symmetry of the nozzles becomes unacceptable. Those results motivated the development of a new approach in which the capillary is heated at the Top of a Lateral Flame (TLF), i.e., the flame produced by a Bunsen burner with its tube horizontal (Figure 1c) [26]. In this way, highly axisymmetric nozzles were produced with satisfactory neck reproducibility. The shape reproducibility at the same position was excellent, and it was possible to obtain different nozzle shapes working at different heating positions.
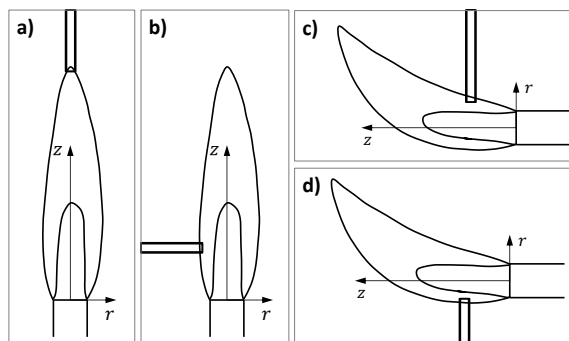

Figure 1. Fire shaping approaches depending on where the capillary is heated: (**a**) Top of a Vertical Flame (TVF), (**b**) Side of a Vertical Flame (SVF), (**c**) Top of a Lateral Flame (TLF) [26], and (**d**) Bottom of a Lateral Flame (BLF). The latter is the approach used in this work.

In this work, we analyze the reproducibility and shape capabilities of a new-fire shaping approach, in which a vertical rotating capillary is heated at the Bottom of a Lateral Flame (BLF) (Figure 1d). The use of this new approach was motivated by the results of preliminary experiments, which showed that the shape variation for different positions was larger than for TLF. We study how the heating position or the dimensions of the original capillary and their variability affect the neck size scattering. The effect of these aspects on the nozzle shape is also explored and the technical limitations are established. BLF is capable of fabricating nozzles with a wide range of shapes. Finally, we show how the nozzle shape may affect the performance of a microfluidic system. In particular, we fabricated two nozzles with significant different shapes and assembled them in a GDVN device for gaseous Flow Focusing. The use of shorter nozzles with a higher convergent rate prevents whipping and extends the pressure range for which it is possible to emit a thin jet.

2. Results

Though the fire-shaping idea is simple, the phenomena involved in the process are not. The glass flow that gives rise to the nozzle occurs as the surface tension forces reduce the glass free surface while the viscous forces oppose the flow. The glass viscosity depends highly upon the temperature.

The glass cannot stand stress and creeps above the strain temperature (515 °C). The viscosity falls to 10^{12} Pa·s at 560 °C (annealing point), and to $10^{6.6}$ Pa·s at 825 °C (softening point). Therefore, the viscous resistance to the flow decreases as the temperature rises, larger velocity gradients are allowed in the glass, and the flow becomes faster. On the other hand, we are heating the tip of the capillary at the flame. Heat is transferred from the flame to the glass. The glass temperature rise depends mostly on the amount of glass (capillary thickness) and on the heating time. Conduction losses along the glass are low (the glass thermal conductivity is below 2 W/m K within the temperature range in the experiments). The temperature is maximum at the capillary tip and then decreases along the capillary, and the heating time increases the temperature. When a section is heated up enough, its viscosity lowers enough and it flows. As heating is maintained, the velocity of the flow increases, and the region of the capillary tip heated enough to flow spreads. The velocity of the flow along the capillary, such as the temperature, is not uniform, creating an additional restriction to the flow. Additionally, as the glass flows inwards and downwards, it moves away to a cooler region of the flame, and so the heat transfer is reduced.

2.1. Effect of the Heating Time

Nozzles manufactured under the same heating conditions have scattered neck diameters. This may be caused either by the heating process or by the geometrical tolerances of the capillaries. The importance of these aspects may also depend on the heating conditions (position and time). In the first run of experiments, we analyzed the effect of increasing the heating time for a fixed heating position ($r = 15$ mm). Table 1 and Figure 2 show the mean geometrical parameter for sets of capillaries type 1 heated at the same position ($r = 3.5$ mm, $z = 15$ mm) for different times. The images of some resulting nozzles are shown in Figure 3. As expected, increasing the heating time involves more material in the flow and allows it to flow further. The glass flows inwards reducing the neck diameter D and downwards shortening the capillary (increasing ΔL). As it accumulates around the nozzle neck, the neck channel becomes longer (as shown by the increasing neck aspect ratio AR). We did not observe neck channel closure and obtained nozzles with neck diameters of a few micrometers. This is the expected behavior for interfaces when the outer fluid (glass in our case) is very viscous, and the inner fluid (air) has low but finite viscosity [27]. As for the TLF approach [26], the shape reproducibility is excellent. The profiles of nozzles of the same diameter produced with identical heating conditions are indistinguishable (Figure 4). Finally, results show that the heating time does not seem to significantly affect the relative variability of the neck diameter ($s_D/\overline{D}$).

Table 1. Mean geometrical parameters for sets of nozzles manufactured at the same position ($r = 3.5$ mm, $z = 15$ mm) from capillaries type 1.

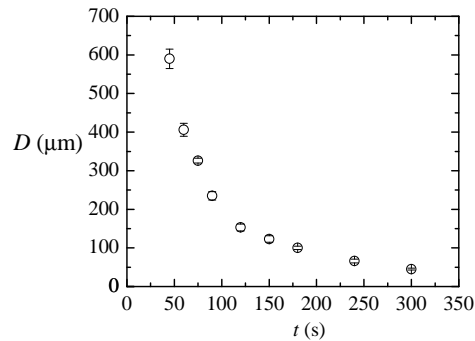| t (s)	$\overline{D}$ (μm)	$s_D/\overline{D}$ (%)	$\overline{\Delta L}$ (mm)	$\overline{AR}$
45	590	4	1.08	0.47
60	406	4	1.21	0.62
75	326	2	1.26	0.78
90	235	4	1.36	1.04
120	153	6	1.48	1.78
150	123	7	1.50	2.55
180	100	4	1.57	3.65
240	66	7	1.65	7.13
300	45	5	1.72	10.1

Figure 2. Mean neck diameter for sets of nozzles manufactured at the same heating position ($r = 3.5$ mm, $z = 15$ mm) from capillaries type 1. The standard deviation is used for the error bars.
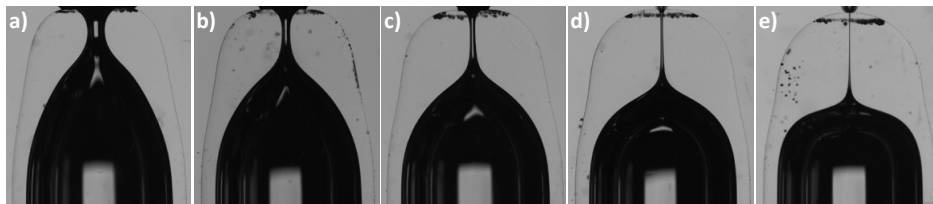

Figure 3. Nozzles manufactured at ($r = 3.5$ mm, $z = 15$ mm) from capillaries type 1: (**a**) $t = 75$ s, $D = 326 \pm 4$ µm; (**b**) $t = 120$ s, $D = 156 \pm 1$ µm; (**c**) $t = 180$ s, $D = 102 \pm 3$ µm; (**d**) $t = 300$ s, $D = 45 \pm 2$ µm; (**e**) $t = 600$ s, $D < 10$ µm (not measurable due to limitations of the characterization setup).
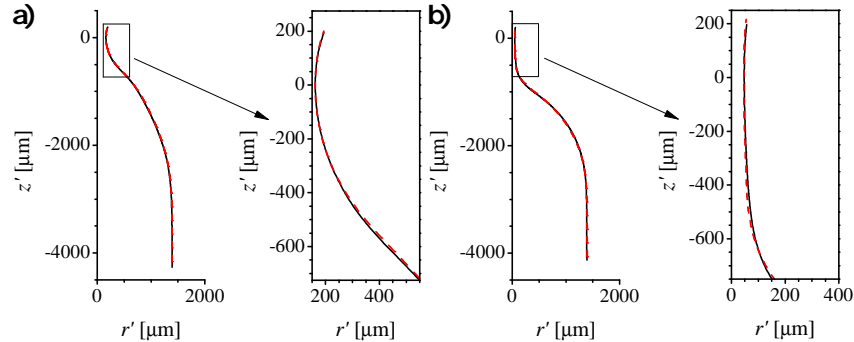

Figure 4. Shape comparison for sets of two nozzles (black and red lines) of the same diameter produced with the same heating conditions from capillaries type 1: (**a**) $r = 3.5$ mm, $t = 75$ s, $D \approx 300$ µm; (**b**) $r = 3.5$ mm, $t = 180$ s, $D \approx 100$ µm.

2.2. Effect of the Geometrical Tolerances of the Capillary

The neck diameter scattering for the same heating conditions may be caused by (i) the particular dimensions of the original capillary, which vary within the tolerances; or (ii) the variability of the shaping process itself. Figure 5 shows the effect of the actual capillary inner diameter and length on the nozzle neck diameter. For each nozzle of the previous experiment, we calculated the relative deviation of its neck diameter from the mean for its set (heating time), and the corresponding absolute deviation of the capillary inner diameter and length. Symbols correspond to different heating times, ranging from 45 to 300 s. The plane is the fit to the experimental data and shows that the variability of the capillary inner diameter affects the neck diameter more than that of the length. Figure 5b shows a view perpendicular to the plane. The scatter of the values around that plane is still significant, showing that the variation of the capillary dimensions is not the only important source of neck size variability. Uncontrollable changes in the flame heating process affect the final neck diameter.
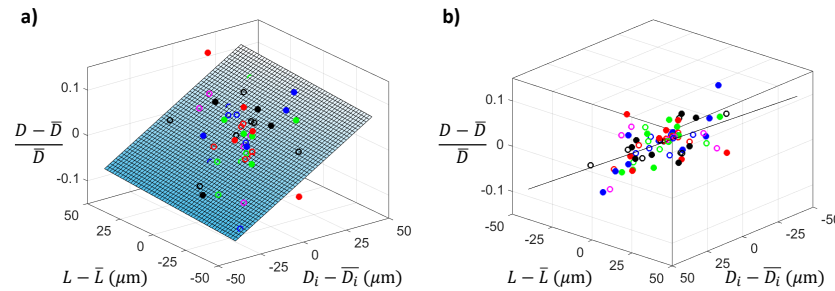
a)
b)

Figure 5. Relative diameter deviation of each nozzle from the mean of the set versus the absolute length and inner diameter deviation of the corresponding original capillary. Symbols correspond to different heating times of the experiments in Table 1 (Capillaries type 1, $r = 3.5$ mm, $z = 15$ mm). The plane is the best fit. Graph (**a**,**b**) represent different view directions.

2.3. Effect of the Heating Position

It is possible to produce nozzles of the same neck diameter with different heating conditions. When the nozzle is produced deeper in the flame, a longer region of the capillary is heated up to a higher temperature. Therefore, a larger length of the capillary participates in the flow, and it moves faster. The diameter reduction is reached sooner because of the faster flow, but also because a longer region of the inner surface moves inwards. This effect produces longer nozzles and neck channels. Additionally, as the glass inwards, it also flows downwards producing a larger shortening of the capillary.

Table 2 shows the mean geometrical parameters for sets of nozzles of $D \simeq 135$ µm produced at different positions using capillaries type 1. The neck diameter variability for the different heating conditions seems to remain within the same range as that for experiments in Table 1. Therefore, the heating position does not seem to affect significantly the neck diameter reproducibility. However, as expected, it has an important effect on the nozzle shape (see Figure 6). As you work outer in the flame, a shorter region of the capillary is heated up and in a cooler region. The necessary heating time t is larger. The glass takes longer to increase the temperature, and the temperature will anyway be lower. The flow will be slower, as shown by the shortening reduction ($\overline{\Delta L}$ decreases about 0.1 mm when you shift the heating position 0.5 mm outer). The capillary length that participates in the flow is smaller. Therefore, less material accumulates around the neck resulting in shorter neck channels (lower $\overline{AR}$). Also, as the diameter reduction happens in a shorter region, the "shoulders" of the nozzle rise. Figure 6e shows what we have called "overturning". At that position, the length of the capillary heated enough to flow is very short. As the diameter reduction happens as the material moves inwards and downwards, when it is heated long enough, it flows below the nozzle shoulders. This overturning of the interface produces a blur in the image (see Figure 7). Such a shape is not usually adequate for applications. Therefore, in fact, it establishes a limitation of the process: there is a minimum nozzle length that can be obtained for a particular diameter reduction with an appropriate nozzle shape. Again, the shape reproducibility was excellent for nozzles of the same diameter produced in the same conditions (Figure 8).

Table 2. Mean geometrical parameters for sets of nozzles of approximately the same diameter produced with different heating conditions. Capillaries type 1, $z = 15$ mm.

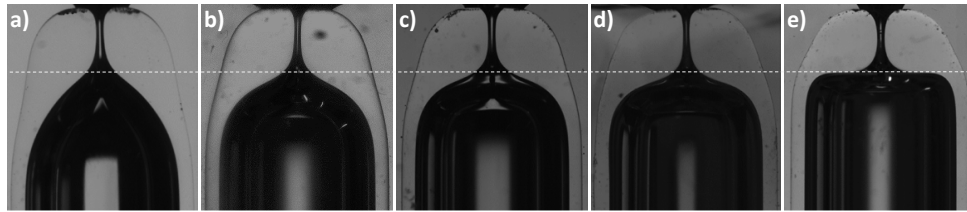| r (mm)	t (s)	$\overline{D}$ (µm)	$s_D/\overline{D}$ (%)	$\overline{\Delta L}$ (mm)	$\overline{AR}$
3.5	150	123	7	1.50	2.55
4.0	250	135	5	1.39	2.46
4.5	325	140	4	1.29	1.81
5.0	600	140	3	1.20	1.73

Figure 6. Nozzles of $D \approx 135$ μm manufactured at different positions: (**a**) $r = 3.5$ mm, $t = 150$ s, $\Delta L = 1.47$ mm; (**b**) $r = 4$ mm, $t = 250$ s, $\Delta L = 1.40$ mm; (**c**) $r = 4.5$ mm, $t = 325$ s, $\Delta L = 1.26$ mm; (**d**) $r = 5$ mm, $t = 600$ s, $\Delta L = 1.22$ mm; (**e**) $r = 5.5$ mm, $t = 2000$ s, $\Delta L = 1.14$ mm. The line is to guide the eye.
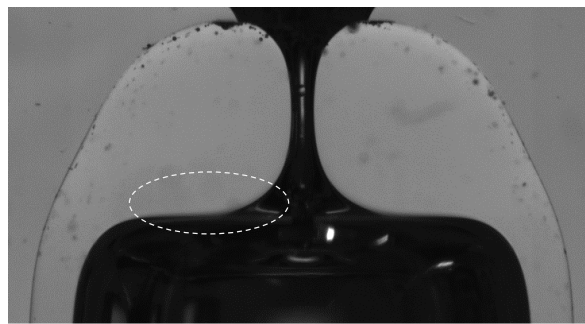

Figure 7. Detail of nozzle presenting overturning (Figure 6e). The slope of the interface shows that the material has flown below the shoulders. The proper inner surface of the nozzle cannot be observed in the image and results in a blur.
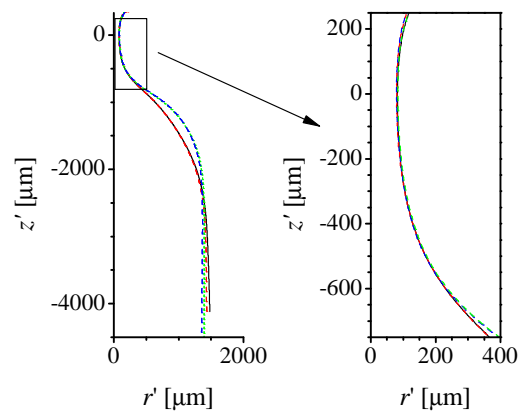

Figure 8. Shape comparison for sets of nozzles with $D \approx 160$ μm produced with different heating conditions from capillaries type 1. The heating conditions were ($r = 3.5$ mm, $t = 120$ s) for the black and the red nozzles, and ($r = 4$ mm, $t = 180$ s) for the blue and the green ones.

2.4. Effect of the Capillary Geometry: Inner Diameter and Thickness

The capillary geometry affects the shaping process in two ways. First, it affects the heat transfer and the glass temperature for a particular heating position. The outer diameter defines the surface in contact with the flame, and an increase would benefit the heat transfer. On the other hand, the glass temperature will depend on the capillary thickness. For thin capillaries, the glass reaches a higher temperature and flows faster. Second, the geometry of the capillary affects the flow. The heating time is determined by the reduction to be obtained which depends on the inner diameter. Additionally, the capillary outer and inner diameters create restrictions to the flow of the glass free surface.

We carried out experiments using different size capillaries to study how the original shape affects the nozzle geometry and the reproducibility of the process. First, we compared capillaries with the same inner diameter and different wall thickness. Table 3 shows the heating conditions and geometrical parameters of sets of nozzles of $D \simeq 120$ μm produced from capillaries type 1 and 2. The thickness of the second almost doubles that of type 1 (see Section 4.2) . The cross-section and therefore the amount of material to be heated are larger. It becomes necessary to work deeper in the flame to heat up the glass enough to flow. Still, the glass temperature is relatively low, and the diameter reduction will need a larger heating time. At the heating conditions analyzed ($z = 15$ mm, $r = 3.5$ mm, $t = 520$ s), we need over three times longer to obtain about the same neck diameter with the thicker capillary. On the other hand, one would expect that the material increase would raise the inertia of the process, and compensate for its variability. However, in our experiments, the neck diameter scatter is larger for the thicker capillaries. Figure 9 shows the relative diameter deviation of each nozzle from the mean value of the set versus the absolute inner diameter deviation of the corresponding original capillary for the thin (circles) and the thick (squares) type. As expected, the slope of the trend line is smaller for the thick capillary (dashed line) than for the thin one (solid line). The larger neck diameter scatter has been probably caused by the larger variability in the original dimensions of the capillaries: the measured inner diameter (wall thickness) standard deviation for type 2 was about twice (three times) that corresponding to type 1.

Table 3. Mean geometrical parameters for sets of nozzles fabricated from capillaries of different thicknesses ($z = 15$ mm).

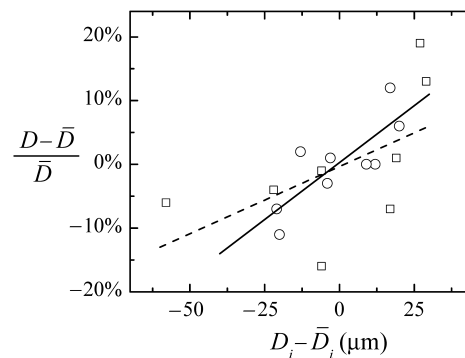| Type	r (mm)	t (s)	$\overline{D}$ (μm)	$s_D/\overline{D}$ (%)	$\overline{\Delta L}$ (mm)	$\overline{AR}$
1	3.5	150	123	7	1.50	2.5
2	3.5	520	115	12	1.28	3.6

Figure 9. Variability of the neck diameter versus the original capillary inner diameter deviation for thin (circles), and thick (squares) wall capillaries. The solid (dashed) line is the linear fit for the thin (thick) capillaries.

The wall thickness also affects the shape of the resulting nozzle. Figure 10 shows two nozzles of the same diameter produced at the same position from a thin (type 1) and a thick (type 2) capillary. As we already mentioned, increasing the thickness slows down the flow and the shortening of the capillary is smaller. However, as the cross-section is greater, the amount of material involved in the flow is still larger, resulting in longer nozzle necks (larger $\overline{AR}$ in Table 3).
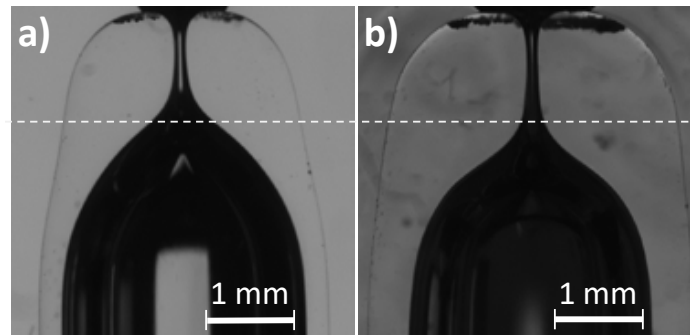
Figure 10. Nozzles of $D \approx 130$ μm manufactured from capillaries of the same inner diameter and different wall thicknesses. (**a**) Capillary type 1, $r = 3.5$ mm, $t = 150$ s, $\Delta L = 1.47$ mm. (**b**) Capillary type 2, $r = 3.5$ mm, $t = 520$ s, $\Delta L = 1.13$ mm. The line is to guide the eye.

Table 4 shows the results of fire shaping smaller capillaries. We used thick (type 3) and thin (type 4) capillaries with a 2 mm outer diameter (see Section 4.2). As their cross-section and/or inner diameter are smaller than for capillaries type 1, the process is very fast, and an outer heating position has to be chosen to be able to control the process (all heating positions in Table 2 are inner than those in Table 4). Type 3 has almost the same cross-section as type 1 but a significantly smaller inner diameter. As the flow has to produce a lower diameter reduction, less material is involved (note that $\overline{\Delta L}$ is much smaller than for all experiments with capillaries type 1). Type 4 has a smaller cross-section than type 3, so with the same heating conditions, the material is heated at a higher temperature. This causes it to flows farther, producing a smaller diameter and a larger shortening, even when the inner capillary diameter is larger. The neck size reproducibility of these two types is quite similar. We checked that the relative variability of the original capillary dimensions stayed within the same range as that for type 1. The causes of the larger neck diameter scattering may be that we work with less material (less inertia), and in a more unstable region of the flame. At the outer heating position studied ($r = 6.6$ mm, $z = 15$ mm) the scatter of the neck diameter becomes unacceptably large.

Table 4. Mean geometrical parameters for sets of nozzles fabricated from different capillary types and with different heating conditions at ($z = 15$ mm).

Type	r (mm)	t (s)	$\overline{D}$ (μm)	$s_D/\overline{D}$ (%)	$\overline{\Delta L}$ (mm)	AR
3	5.5	70	70	19	0.25	4.2
3	6	70	239	12	0.12	1.0
3	6.6	480	221	36	0.08	1.2
4	5.5	70	55	14	0.77	4.6
4	6	70	95	18	0.65	2.6
4	6.6	480	122	29	0.54	1.8

We tested that the shape reproducibility is maintained for these nozzles. Figure 11 shows nozzles of the same diameter produced in capillaries types 1, 3, and 4. The diameter reduction is much smaller for the latter two, and so is the material involved in the flow. The nozzles are significantly shorter for the smaller capillaries. Please note that, again, the thick-wall capillary (b) produces longer neck channels than the thin one (c), even when the diameter reduction is smaller.
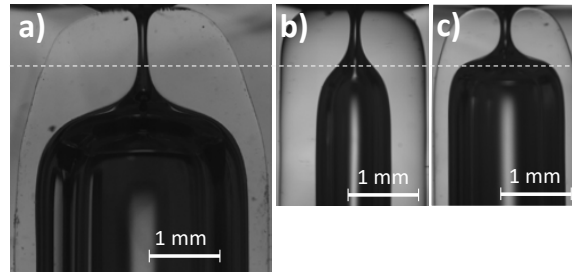
Figure 11. Nozzles of $D \approx 135$ μm manufactured from different size capillaries. (**a**) Capillary type 1, $r = 5$ mm, $t = 600$ s, $\Delta L = 1.22$ mm; (**b**) Capillary type 3, $r = 6.6$ mm, $t = 480$ s, $\Delta L = 0.11$ mm; (**c**) Capillary type 4, $r = 6.6$ mm, $t = 480$ s, $\Delta L = 0.54$ mm. The line is to guide the eye.

3. Discussion

Fire-shaped nozzles are commonly used in microfluidic device assemblies. However, their fabrication is mostly done manually making it difficult to obtain reproducible nozzles or to control its shape. Recently, Muñoz-Sánchez and Cabezas [25] proposed an experimental setup to reduce operator intervention in the process and analyzed the traditional vertical flame fire-shaping approaches. Using a non-traditional approach in which the capillary is heated at the top of a lateral flame allowed to improve the nozzle size reproducibility and its axisymmetry [26]. In particular, it was shown that the shape reproducibility was very good, for nozzles of the same diameter produced under the same conditions. In this work, we propose a new approach that heats the capillary at the bottom of the lateral flame (BLF), which additionally, widens the range of nozzle shapes that can be obtained.

The capabilities and limitations of BLF have been experimentally analyzed. First, we focused on neck size reproducibility. For the same heating conditions, the complexity of the flame and glass flow phenomena are only one of the causes of the neck scattering. The variability of the original capillary dimensions, especially the inner diameter, reduces the reproducibility. On the other hand, the heating position does not seem to play a relevant role within a wide region. Unexpectedly, the use of thick wall capillaries did not benefit the size reproducibility in our experiments, probably because the variability in their original dimensions was significantly larger. Reducing the size of the capillaries makes it more difficult to control the process, and results in a larger neck scattering.

We succeeded in producing nozzles of significantly different shapes. Several aspects affect the geometry of the nozzle. As part of an assembly, some of its dimensions may have some limitations. For example, there may be a minimum limit for its inner diameter if there is another element inside of it. If the nozzle has to fit inside another object, there would be a maximum limit for the outer diameter. The thickness may also be relevant as the nozzle has to resist manipulation, assembly, and functioning. The latter may be significant in some applications, for example, those dealing with high viscosity liquids flowing in narrow channels. The neck size is typically determined by the device application and is related to the jet, drop, particle, or bubble size to be produced. Additionally, with the previous parameters fixed, the shape of the nozzle may affect the performance of the device in some applications, as we will see later.

The design reduction (from the inner capillary diameter to the neck) establishes a limit for the nozzle neck shape. It may be smooth, spreading over the nozzle length, or abrupt, converting the nozzle almost into two tubes in series. We defined the neck aspect ratio (AR) to evaluate the length of the neck channel (with diameter below 110% that of the neck) in terms of its diameter. Nozzles for large diameter reductions will show higher AR, though the nozzle itself may be shorter (as the heated material flows inwards and downwards). Both the nozzle and neck channel lengths can be reduced by heating the capillary outer in the flame for a longer time. However, there is a limit for an acceptable shape and a particular reduction. When the heating time is long enough to allow the glass to flow below the heated length, it produces an undesired overturning of the interface. For the same inner diameter, working with thicker capillaries will result in longer channels. Besides, it may limit the shape

possibilities, as the heating region for a reasonable heating time narrows. In general, reducing the capillary inner diameter would reduce the diameter reduction and the neck channel length. However, this effect may be compensated for by the wall thickness. We have shown that, for the same outer diameter, thicker capillaries may produce longer channels, even when they need a smaller diameter reduction. With this in mind, the original capillary selection becomes a key aspect determining the nozzle shape and affecting the fabrication reproducibility.

Application in Flow Focusing to Prevent Whipping

Flow Focusing is a technique that produces very thin jets by hydrodynamic means. The original plate-orifice design [12] to produce axisymmetric flow focusing, has been replaced for several applications by the GDVN ejector. The latter can be built by inserting an inner tube inside of a fire-shaped glass nozzle. The main geometrical parameters are the nozzle neck diameter D and its distance to the capillary tip H. In gaseous flow focusing, an outer gas stream is used to stretch the meniscus of a liquid formed at the tip of the tube. The air drags the liquid forming a thin jet that travels through the nozzle. That steady jetting is the adequate performance for most applications. Therefore, researchers have studied the parametric region, gas pressure drop Δp and liquid flow rate Q, to obtain stable long jets [4]. The jet diameter can be reduced by decreasing Q or by increasing Δp. The latter mechanism is limited by whipping instability [28–30]. When the energy transferred to the jet is too high, the jet oscillates as a whip. Global whipping is an undesired phenomenon, not present in the original plate-orifice configuration that was observed in GDVN devices and can hinder their applicability. When the pressure drop rises, the meniscus starts oscillating laterally. This may even cause the interruption of the jet if it touches the inner nozzle wall. To prevent this effect, it was suggested to use nozzles with higher convergent rates [28].

We have fabricated two GDVN devices differing only in the nozzle shape and tested their performance. Distilled water was injected through the inner tube at $Q = 6.9$ mL/h, and the outer stream was produced by a pressure drop $\Delta p = 300$ mbar. Figure 12 shows the two nozzles and a sequence of images of the jet emission for the same working conditions. For Nozzle A, global whipping is observed. Both the jet, marked with a yellow circle, and the meniscus, in the red circle, oscillate significantly. On the contrary, Nozzle B, which has a more abrupt shape, produces a steady jet. There is a range of experimental conditions for which both GDVNs devices emit a steady jet. However, its size (and velocity) are also affected by the nozzle shape. Figure 13 shows the water jets emitted by both devices at $Q = 20$ mL/h, and with a pressure drop $\Delta p = 150$ mbar. Nozzle B device produces a 20% thinner jet. A deeper investigation of the effect of the nozzle shape for different liquid-air systems and working conditions can be found in [31].
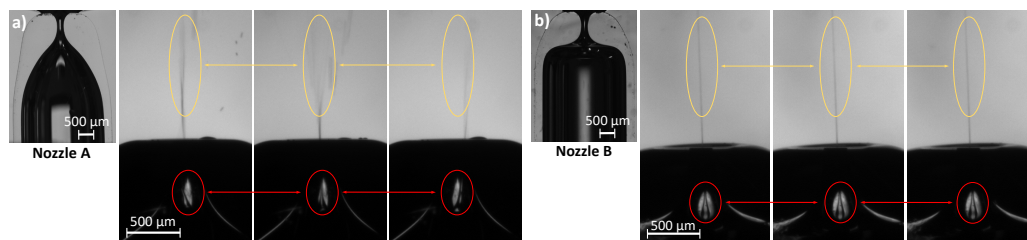

Figure 12. Sequences of experimental images of the jet emitted by the two GDVNs devices with (**a**) Nozzle A and (**b**) Nozzle B. The water inner flow rate is $Q = 6.9$ mL/h and the air pressure drop is $\Delta p = 300$ mbar.
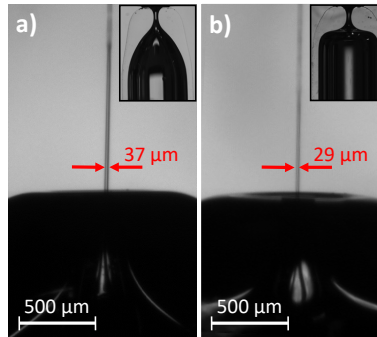
Figure 13. Steady jet emitted by the two GDVNs devices with (**a**) Nozzle A and (**b**) Nozzle B. The water inner flow rate is $Q = 20$ mL/h and the air pressure drop is $\Delta p = 150$ mbar.

4. Materials and Methods

4.1. Fire-Shaping Setup

Figure 14 shows the setup used in the experiments. The flame is produced by a Bunsen burner (JP Selecta, Abrera, Spain, ref. 7000134) (A) with its tube placed horizontally. The burner slots are fully open to produce a hotter flame (with maximum air proportion in the mixture). The flammable gas is butane supplied through a hose that connects the burner to a commercial gas bottle (B). A self-locking gas valve (C) installed in the hose is used to allow or shut off the butane flow. A 0.8 kg/h regulator fitted to the gas bottle ensures a constant gas flow in all the experiments. The capillary is held vertically and attached to a DC motor using a suitable collet and chuck holder set (D). The burner is mounted on a translation stage (E) that moves vertically to control the distance r of the capillary tip to the burner tube axis. A two-axis translation stage (F) allows us to move the capillary horizontally for proper alignment and to control the distance z of the capillary axis to the burner tube exit. The heating time t is controlled by an Arduino board (G) and a servomotor (H) which places a ceramic plate (I) between the burner and the capillary or moves it away.
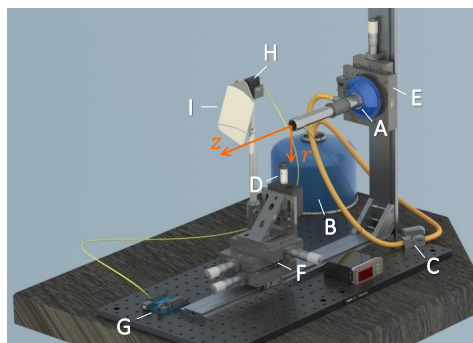

Figure 14. Fire-shaping setup: (A) Bunsen burner, (B) gas bottle, (C) gas valve, (D) collect and chuck holder, (E) vertical translation stage, (F) horizontal two-axis translation stage, (G) Arduino board, (H) servomotor and (I) ceramic plate.

Figure 15 shows an image of the lateral flame and the coordinate system used to define the capillary tip heating position. We used a mineral insulated type K thermocouple (1 mm in diameter) to estimate the temperature at different flame positions. The thermocouple tip was moved to a particular position and, after one minute, 100 hundred measurements were taken at one measurement per second. The measured value is not the flame temperature (it underestimates it), nor the glass temperature during the shaping. However, it can be used to estimate the heat capacity of the flame. Figure 16

shows the temperature profiles at different distances z from the burner exit. The symbols represent the mean value of the measurements, and the standard deviation is used for the error bars. The white symbols correspond to the visible limit of the flame. The presence of the blue cone, which is a cold area, can be appreciated close to the burner ($z < 25$ mm). The temperature rises from room temperature far away from the flame, reaches a maximum at the blue region border, and then decreases as you move towards the burner axis. The maximum temperature is measured around the tip of the blue cone ($r = 0$ mm, $z = 30$ mm). However, to place the capillary tip at that position would mean to heat a very long region of the capillary. Close to the burner, the temperature increment spreads over a shorter distance. Therefore, that position seems to be more adequate to produce short nozzles and to control the nozzle shape. Preliminary experiments confirmed that, for different radial positions, larger variations in the shape were obtained when working closer (lower z) to the burner. Therefore, we chose the closest possible position ($z = 15$ mm) and maintained it for all the experiments.
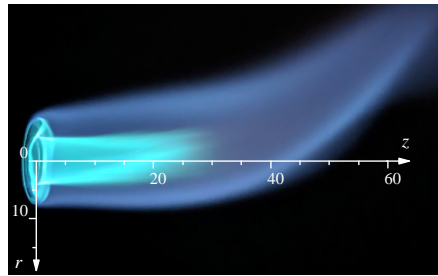

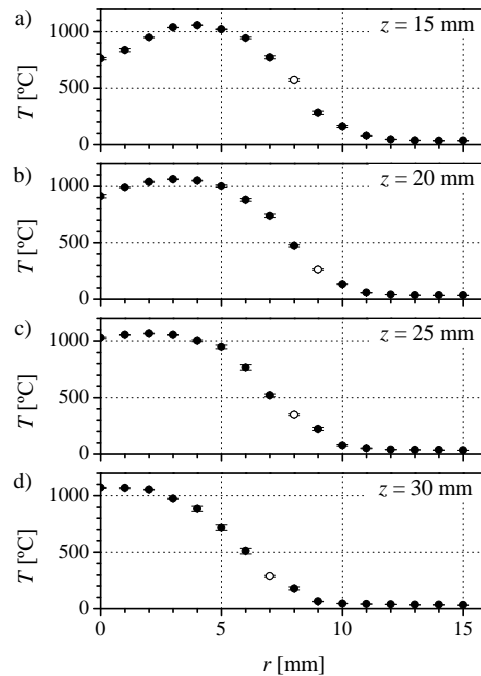**Figure 15.** Image of the flame and coordinate system for the heating position.

Figure 16. Measured temperature profiles at the flame at different distances to the Burner exit: (**a**) $z = 15$ mm, (**b**) $z = 20$ mm, (**c**) $z = 25$ mm, and (**d**) $z = 30$ mm. The white symbol corresponds to the limit of the visible flame.

For each heating conditions (r, t), we manufactured a set of 8 nozzles with the following procedure. First, the heating time is loaded into the Arduino board, and the gas bottle and the burner valves are fully opened. The capillary is placed and tightened with the chuck holder set. Then, the cycle begins when the motor rotation is started and the ceramic plate moves to the isolation position. That allows the operator to open the gas valve and start the flame with a spark lighter before the ceramic plate moves away. The heating starts at that moment and finishes when the ceramic plate is moved back between the capillary and the flame. The operator extinguishes the flame by closing the gas valve. Meanwhile, the capillary remains rotating for the programmed cooling time. Finally, the capillary is released from its holding.

4.2. Capillaries and Nozzles Geometries

To manufacture the nozzles we used cut-end glass capillaries made of borosilicate glass 3.3 (Hilgenberg GmbH). The dimensions and tolerances, according to the supplier, are shown in Table 5.

Table 5. Nominal dimensions and tolerances of the capillaries.

Type	D_o (mm)	D_i (mm)	T (mm)	L (mm)
1	3.3 ± 0.1	2.773 ± 0.1	0.264	100 ± 0.5
2	3.7 ± 0.1	2.775 ± 0.1	0.462	100 ± 0.5
3	2.0 ± 0.1	1.0 ± 0.1	0.5	100 ± 0.5
4	2.0 ± 0.1	1.6 ± 0.1	0.2	100 ± 0.5

We used image analysis to obtain the shape and several geometrical parameters of the nozzles. We take three images of each nozzle with its tip submerged in glycerine and air flowing through it. The air inside the nozzle appears black in the image, making edge detection easier (Figure 3 images of some nozzles). The glycerine bath is used to reduce optical distortion. Then, two (left and right) nozzle contours are obtained for each image by a several-step procedure. The Canny edge detector is used at the pixel level, and a local intensity threshold and interpolation are used to achieve subpixel resolution. Points that are too far from the original pixel are rejected. Finally, the symmetry axis is determined and a single mean profile is calculated. Figure 4 shows the mean profiles corresponding to two different nozzles manufactured with the same conditions. Also, we obtain the nozzle neck diameter D, the outer diameter D_o and inner diameter D_i of the capillary, as well as the neck length L_n, defined as the length of the channel with a diameter below 110% the neck diameter. From those parameters, we calculate the capillary thickness $T = D_o - D_i$, and the neck aspect ratio $AR = L_n/D$. Additionally, we calculate the capillary shortening $\Delta L = L - L_f$ due to fire shaping from the length of the capillary before L and after L_f fire shaping measured with a caliper. For each set of nozzles manufactured in the same conditions, we calculated the mean $\overline{P}$ and the standard deviation s_P for all the geometrical parameters P mentioned above.
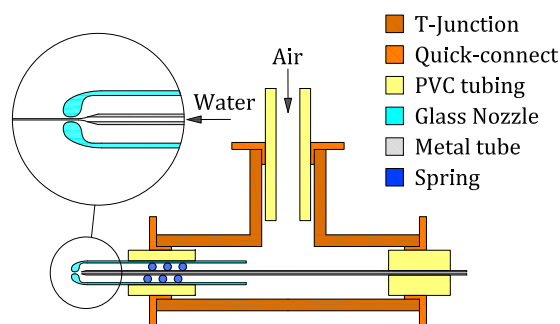
4.3. Gaseous Flow-Focusing

We built two GDVNs ejectors for gaseous flow-focusing differing only in the outer glass nozzle shape. Both nozzles were fabricated from capillaries type 1 following the procedure described in Section 4.1. Nozzle A was fabricated deep in the flame with a short heating time, while Nozzle B was fabricated outer with a much longer time to obtain the same diameter (Table 6). This way, the diameter transition extends over a long region in the former and is more abrupt in the latter (Figure 12).

Table 6. Heating conditions and geometrical parameters of the nozzles assembled in the GDVNs devices (Figure 12).

Noozle	r (mm)	z (mm)	t (s)	D (µm)	AR
A	3.5	15	90	224 ± 2	1.07
B	5	15	700	218 ± 3	0.96

We used a pneumatic tee connector (SMC, KQ2T06-00A) with instant fittings to assemble the device (Figure 17). The glass nozzle was mounted on one side of the T-junction, and the inner tapered metal tube (400 µm OD, 200 µm ID, and 14° angle) was inserted through the opposite side. Fitting and sealing were achieved by using adequate PVC tubing. The tube was aligned using a spring and its exit was located at a distance $H = 450$ µm to the nozzle neck ($D \approx 220$ µm). The lateral port of the T-junction was connected to a compressed air source through a high accuracy pressure regulator valve, which allowed to control the pressure drop Δp of the coflowing air stream through the nozzle. The water was injected through the inner tube at a controlled flow rate Q using a syringe pump (KDS120, kdScientific, Holliston, MA, USA). A CCD camera (AVT Stingray F-125B, Allied Vision, Stadtroda, Germany) and backlighting were used to obtain images of the jet.

Figure 17. Assembly of the GDVN device.

References

1. Sackmann, E.K.; Fulton, A.L.; Beebe, D.J. The present and future role of microfluidics in biomedical research. *Nature* **2014**, *507*, 181–189. [CrossRef]
2. Shang, L.; Cheng, Y.; Zhao, Y. Emerging Droplet Microfluidics. *Chem. Rev.* **2017**, *117*, 7964–8040. [CrossRef]
3. Guerrero, J.; Chang, Y.; Fragkopoulos, A.A.; Fernández-Nieves, A. Capillary-Based Microfluidics-Coflow, Flow-Focusing, Electro-Coflow, Drops, Jets, and Instabilities. *Small* **2020**, *16*, 1904344. [CrossRef]
4. Montanero, J.M.; Gañán-Calvo, A.M. Dripping, jetting and tip streaming. *Rep. Prog. Phys.* **2020**, *83*, 097001. [CrossRef]
5. Nielsen, A.V.; Beauchamp, M.J.; Nordin, G.P.; Woolley, A.T. 3D Printed Microfluidics. *Annu. Rev. Anal. Chem.* **2020**, *13*, 45–65. [CrossRef]

6. Utada, A.S.; Lorenceau, E.; Link, D.R.; Kaplan, P.D.; Stone, H.A.; Weitz, D.A. Monodisperse Double Emulsions Generated from a Microcapillary Device. *Science* **2005**, *308*, 537–541. [CrossRef] [PubMed]

7. Comunian, T.A.; Ravanfar, R.; Alcaine, S.D.; Abbaspourrad, A. Water-in-oil-in-water emulsion obtained by glass microfluidic device for protection and heat-triggered release of natural pigments. *Food Res. Int.* **2018**, *106*, 945–951. [CrossRef] [PubMed]

8. Benson, B.R.; Stone, H.A.; Prud'homme, R.K. An "off-the-shelf" capillary microfluidic device that enables tuning of the droplet breakup regime at constant flow rates. *Lab Chip* **2013**, *13*, 4507. [CrossRef] [PubMed]

9. Bandulasena, M.V.; Vladisavljević, G.T.; Odunmbaku, O.G.; Benyahia, B. Continuous synthesis of PVP stabilized biocompatible gold nanoparticles with a controlled size using a 3D glass capillary microfluidic device. *Chem. Eng. Sci.* **2017**, *171*, 233–243. [CrossRef]

10. Bandulasena, M.V.; Vladisavljevìc, G.T.; Benyahia, B. Versatile reconfigurable glass capillary microfluidic devices with Lego® inspired blocks for drop generation and micromixing. *J. Colloid Interface Sci.* **2019**, *542*, 23–32. [CrossRef]

11. DePonte, D.P.; Weierstall, U.; Schmidt, K.; Warner, J.; Starodub, D.; Spence, J.C.H.; Doak, R.B. Gas dynamic virtual nozzle for generation of microscopic droplet streams. *J. Phys. D Appl. Phys.* **2008**, *41*, 195505. [CrossRef]

12. Gañán-Calvo, A.M. Generation of Steady Liquid Microthreads and Micron-Sized Monodisperse Sprays in Gas Streams. *Phys. Rev. Lett.* **1998**, *80*, 285–288. [CrossRef]

13. Bayram, A.; Serhatlioglu, M.; Ortac, B.; Demic, S.; Elbuken, C.; Sen, M.; Solmaz, M.E. Integration of glass micropipettes with a 3D printed aligner for microfluidic flow cytometer. *Sens. Actuator A Phys.* **2018**, *269*, 382–387. [CrossRef]

14. Weierstall, U.; Spence, J.C.H.; Doak, R.B. Injector for scattering measurements on fully solvated biospecies. *Rev. Sci. Instrum.* **2012**, *83*, 035108. [CrossRef] [PubMed]

15. Beyerlein, K.R.; Adriano, L.; Heymann, M.; Kirian, R.; Knoska, J.; Wilde, F.; Chapman, H.N.; Bajt, S. Ceramic micro-injection molded nozzles for serial femtosecond crystallography sample delivery. *Rev. Sci. Instrum.* **2015**, *86*, 125104. [CrossRef]

16. Piotter, V.; Klein, A.; Plewa, K.; Beyerlein, K.R.; Chapman, H.N.; Bajt, S. Development of a ceramic injection molding process for liquid jet nozzles to be applied for X-ray free-electron lasers. *Microsyst. Technol.* **2018**, *24*, 12471252. [CrossRef]

17. Nelson, G.; Kirian, R.A.; Weierstall, U.; Zatsepin, N.A.; Faragó, T.; Baumbach, T.; Wilde, F.; Niesler, F.B.P.; Zimmer, B.; Ishigami, I.; et al. Three-dimensional-printed gas dynamic virtual nozzles for X-ray laser sample delivery. *Opt. Express* **2016**, *24*, 1515–1530. [CrossRef]

18. Knoška, J.; Adriano, L.; Awel, S.; Beyerlein, K.R.; Yefanov, O.; Oberthuer, D.; Peña Murillo, E.; Roth, N.; Sarrou, I.; Villanueva-Perez, P.; et al. Ultracompact 3D microfluidics for time-resolved structural biology. *Nat. Commun.* **2020**, *11*, 657. [CrossRef]

19. Wei, C.Y.; Yu, C.Z.; Wu, J.J.; Li, J.W.; Li, S.S.; Dai, S.J.; Li, T.J. Easy-to-operate fabrication of tapered glass capillaries for microdroplet generation. *J. Micromech. Microeng.* **2019**, *29*, 037001. [CrossRef]

20. Switzer, G.L. A versatile system for stable generation of uniform droplets. *Rev. Sci. Instrum.* **1991**, *62*, 2765–2771. [CrossRef]

21. Levenstein, M.; Bawazer, L.; Nally, C.M.; Marchant, W.; Gong, X.; Meldrum, F.; Kapur, N. A reproducible approach to the assembly of microcapillaries for double emulsion production. *Microfluid. Nanofluid.* **2016**, *20*, 143. [CrossRef]

22. Chapman, H.N.; Fromme, P.; Barty, A.; White, T.A.; Kirian, R.A.; Aquila, A.; Hunter, M.S.; Schulz, J.; DePonte, D.P.; Weierstall, U.; et al. Femtosecond X-ray protein nanocrystallography. *Nature* **2011**, *470*, 73–79. [CrossRef] [PubMed]

23. Cabezas, M.G.; Rubio, M.; Rebollo-Muñoz, N.; Herrada, M.A.; Montanero, J.M. Global stability analysis of axisymmetric liquid-liquid flow focusing. *J. Fluid Mech.* **2021**, in press.

24. Ponce-Torres, A.; Ortega, E.; Rubio, M.; Rubio, A.; Vega, E.J.; Montanero, J.M. Gaseous flow focusing for spinning micro and nanofibers. *Polymer* **2019**, *178*, 121623. [CrossRef]

25. Muñoz-Sánchez, B.N.; Cabezas, M.G. Borosilicate nozzles manufactured by reproducible fire shaping. *J. Mater. Proces. Tech.* **2018**, *261*, 173–183. [CrossRef]

26. Muñoz-Sánchez, B.N.; Gañán-Calvo, A.M.; Cabezas, M.G. A new fire shaping approach to produce highly axisymmetric and reproducible nozzles. *J. Mater. Process. Tech.* **2019**, *270*, 241–253. [CrossRef]

27. Doshi, P.; Cohen, I.; Zhang, W.W.; Siegel, M.; Howel, P.; Basaran, O.A.; Nagel, S.R. Persistence of memory in drop breakup: The breakdown of universality. *Science* **2003**, *302*, 1185–1188. [CrossRef]

28. Acero, A.J.; Ferrera, C.; Montanero, J.M.; Gañán-Calvo, A.M. Focusing liquid microjets with nozzles. *J. Micromech. Microeng.* **2012**, *22*, 065011. [CrossRef]

29. Wiedorn , M.O.; Awel, S.; Morgan, A.J.; Ayyer, K.; Gevorkov, Y.; Fleckenstein, H.; Roth, N.; Adriano, L.; Bean, R.; et al. Rapid sample delivery for megahertz serial crystallography at X-ray FELs. *IUCRJ* **2018**, *5*, 574–584. [CrossRef]

30. Vakili, M.; Vasireddi, R.; Gwozdz, P.V.; Monteiro, D.C.F.; Heymann, M.; Blick, R.H.; Trebbin, M. Microfluidic polyimide gas dynamic virtual nozzles for serial crystallography. *Rev. Sci. Instrum.* **2020**, *91*, 085108. [CrossRef]

31. Blanco-Trejo, S.; Herrada, M.A.; Gañán-Calvo, A.M.; Rubio, A.; Cabezas, M.G.; Montanero, J.M. Whipping in gaseous flow focusing. *Int. J. Multiphase Flow* **2020**, *130*, 103367. [CrossRef]

4. Paper I - Capabilities and limitations of fire-shaping to produce glass nozzles.

5

Paper II - Fire-shaped nozzles to produce a stress peak for deformability studies.

Fire-Shaped Nozzles to Produce a Stress Peak for Deformability Studies

Alejandro Rubio [ID], Marta López, Emilio J. Vega *[ID] and María G. Cabezas [ID]

Departamento de Ingeniería Mecánica, Energética, y de los Materiales and Instituto de Computación Científica Avanzada (ICCAEx), Universidad de Extremadura, Avda. Elvas s/n, E-06006 Badajoz, Spain; arubiorg@unex.es (A.R.); mlopezfop@alumnos.unex.es (M.L.); mguadama@unex.es (M.G.C.)
* Correspondence: ejvega@unex.es

Abstract: Fire-shaped nozzles can be used to study the deformability of microcapsules, particles, or cells traveling in a flow. Though their geometry depends on the dimensions of the original glass capillary and the heating conditions, they all produce a strain rate peak approximately at the section where the diameter is 1.5 times the minimum. The intensity of this peak and the time from its position to the neck can be easily estimated from the flow rate and three geometrical parameters, without the need for any simulation. In the convergent region of these nozzles, it is possible to observe the evolution of the deformation. It is necessary to use a sufficiently long nozzle to produce the maximum deformation before the neck.

1. Introduction

Capsules consist of an outer membrane or shell that surrounds an inner medium. Their purpose is to contain, protect, transport, and/or deliver an active material. Artificial microcapsules are common in the medical, pharmacy, cosmetic, and food industries. Their composition and structure are usually customized for a particular application. Their flow behavior can be tuned by adjusting the composition and thickness of the shell [1]. Their break-up, or its prevention, is also relevant for some processes [2]. For drug delivery, the agent release at a target can be controlled by using multilayer shells with components that react to physical, chemical, or biological stimuli [3]. Red Blood Cells (RBCs) can be considered natural microcapsules. They are responsible for oxygen transport and its release to the body tissues. The outstanding deformability of their membrane allows them to flow through capillaries smaller than their diameter. RBCs' physical properties are known to play a significant role in blood fluidity both in the bulk flow and microcapillaries [4]. The interest in their study has motivated the development of synthetic microcapsules and microparticles to mimic their behavior [5].

The mechanical properties of micrometric cells, capsules, and particles are crucial for performing their function. For that reason, several methods have been used for their measurement, and are still being developed, which provide complementary information (see Ref. [6] and references therein). Overall properties can be determined from particle suspensions by compression in a rheometer [5] or filterability studies [7], while single-cell measurements can be obtained by micropipette aspiration, atomic force microscopy, or optical tweezers. Additionally, microaspiration, which combines optical observation with ion current signal analysis, was recently proposed to improve the throughput of conventional micropipette aspiration [8]. Advances in microelectromechanical systems (MEMS) have allowed the creation of planar microfluidic devices for the fabrication, characterization, and even sorting and separation of these micro-entities. A single device can be designed to combine several functions, such as polymer microcapsules production and deformability and relaxation measurements [9] or cell elasticity measurement and separation [10].

Microfluidic devices have the potential to become common diagnosis tools for cell deformability (see [11,12] and references therein). The combination of these systems with high-speed imaging has enabled the study of the cell behavior in the flow [13,14]. In real-time deformability cytometry (RT-DC) [15] over 100 cells/s are analyzed. Constrictions, channels with sections smaller than the cell, allow the evaluation of the stiffness from its confined deformation or from the entry or transient times [16]. A decreasing size channel network was used to model the flow of RBCs through capillaries [17], and measure their deformability. The viscoelastic properties of breast cells have been calculated from their deformation under the compression caused by the walls in a confining microchannel [18]. The focus can also be set on the obstruction of the channel, as in the study of the effect of RBCs increasing rigidity at different stages of malaria infection [19]. A new micro-device based on microvascular occlusion were recently proposed to RBCs assessment [20,21], showing its clinical associations in sickle cell disease (SCD) [22]. The loss of RBC deformability during cold storage has been analyzed by using microfluidic capillary networks [23,24], showing more sensitivity than ektactyometry. In devices with sections larger than the cell, the particle deformation is caused contactless by flow stresses which depend on the channel geometry. In straight channels, the velocity gradient is perpendicular to the flow and the particle deforms due to the shear flow. In this case, the measurements are taken far enough from the entrance of the channel [15] so that the particle is not responding to the contraction effect. To reduce the flow resistance, RBCs' shapes change to parachute or slipper-like depending on the flow conditions [13]. Cross-slots microchannels formed by two perpendicular channels with opposite inlet and outlet sections produce a flow with a stagnation point at the center. So, the particle is stretched by the extensional flow associated with the velocity gradient along the flow direction. Alternative cross-Section geometries [25] or the use of a biocompatible viscoelastic medium for the suspension [26] have been proposed to improve the performance of these devices. Channels with contractions also produce an extensional flow due to the velocity gradient along the flow direction. Hyperbolic convergent square-shaped channels are usually chosen to obtain a homogeneous extensional flow. They have been used for observing the evolution of the RBCs deformation along the channel for different flow rates [27], or the RBCs deformability reduction after heating [28], and to state that the cell deformation caused by extensional stress being much larger than the corresponding for a similar magnitude shear stresses [14,29].

The use of glass nozzles and capillaries is common for the construction of three-dimensional microfluidic assemblies, such as those for producing monodisperse droplets, particles or capsules [30,31]. The nozzles are typically fabricated by pulling or fire-shaping, producing the latter significantly shorter nozzles for the same diameter reduction. Fire-shaped nozzles have convergent-divergent shapes. Their geometry depends on the heating conditions, and the dimensions of the original capillary used to produce it [32–34]. The contraction produces an extensional flow, and we recently proposed its use for studying the deformation of RBCs [35]. Our micro-device consists of a simple borosilicate micronozzle whose production is simple, fast, and low-cost by the flame polishing method when compared with other similar microfluidic devices previously mentioned, whose a time-consuming manufacturing process usually involves a soft lithography technique that requires a clean room environment. Moreover, our device allows the deformability assessment of hundreds of particles/cells in a continuous flow, in each experiment, instead of a single particle/cell.

In this work, we analyzed the flow through fire-shaped nozzles to understand the particle deformation measured with this device. We numerically studied the flow through nozzles of approximately the same neck diameter and significantly different shapes. All these nozzles produced a strain rate peak before the neck. So, they can be used to test the response of microparticles to this kind of stress. Our results show that regardless of their shape, the peak is applied at the section of diameter 1.5 times the neck one. Its intensity and time from its position to the neck can be estimated from the flow rate and a few geometrical parameters. We used flexible polydimethylsiloxane (PDMS) particles to

measure the evolution of their deformation and the delay with respect to the stress applied. For deformability studies, nozzles should be sufficiently long to produce the maximum deformation before it crosses the neck.

2. Materials and Methods

2.1. Deformation and Size Measurements

Figure 1 shows the experimental setup used to observe the deformation of the flexible particles while flowing along the nozzle. The glass capillary with the nozzle (Figure 2a) was fastened to the sample holder surface (A). The nozzle end was submerged in a glycerol bath to minimize optical effects in the observation through the glass, while the opposite end was connected to a standard syringe pump using adequate polymer connectors and tubing (from Postnova, IDEX). We used a high-speed CMOS camera (Photron, Fastcam Mini UX50) (B), equipped with the corresponding lenses (C), and an optical fiber light source (D) to observe a 355×130 μm region around the nozzle neck (Figure 2b). The camera could be displaced horizontally and vertically using a triaxial translation stage (E) to focus the micro-entity. Images were acquired at 5000 frames per second, with an 11.11 μs exposure time and a magnification of 0.28 μm/pixel. To evaluate the deformation of the particles, we used the Deformation Index $DI = (X - Y)/(X + Y)$, where X is the length of the particle along the nozzle/capillary axis and Y is the corresponding in the normal direction. In each experiment, 100 particles moving along the nozzle centerline (± 5 μm) were measured when crossing a particular section (± 33 μm). Figure 2c shows the measurement region at the neck section. The particle dimensions were obtained manually at the pixel level, and Chauvenet's criterion was used to identify and reject outliers. The experimental procedure for one DI measurement from a sample of one hundred particles, from sample preparation to data analysis, took typically less than 2 h.
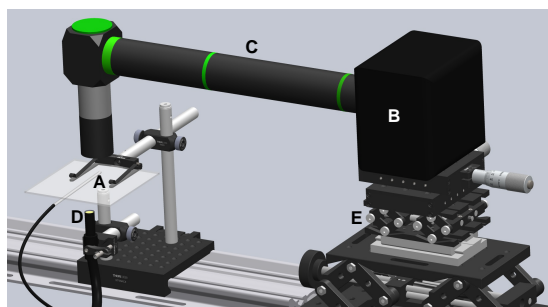
Figure 1. Setup for observing the particle deformation: (A) glass nozzle on the reference surface, (B) CMOS camera, (C) lenses, (D) light source, and (E) translation stage.
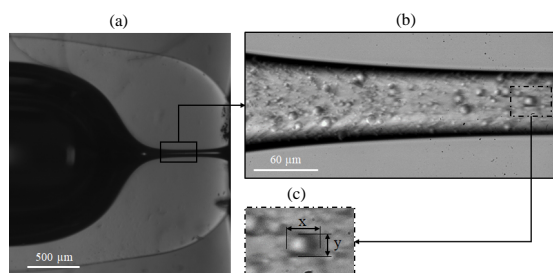

Figure 2. Experimental images used for the characterization of the nozzle shape (**a**), and to evaluate the particles deformation (**b**). Panel (**c**) shows the measurement region for the neck section, and the dimensions of the particle used in the deformation index.

2.2. Fabrication and Characterization of the Nozzles

Glass nozzles were fabricated from commercial capillaries by fire-shaping. The tip of a rotating vertical capillary was introduced at the bottom of a lateral flame, which was produced by a Bunsen burner placed with its tube horizontal. The resulting nozzle geometry depends on the corresponding of the original capillary and on the heating conditions (position and time). When the capillary is heated at an outer position, the diameter reduction takes longer and spreads over a shorter length, therefore resulting in a shorter nozzle. Details on the setup and process can be found in [34].

We fabricated eight nozzles with the same neck diameter ($D \approx 65$ μm) and significantly different shapes using different capillaries (inner diameter ID and outer diameter OD), and/or different heating conditions (radial r_h and axial z_h distance to the burner tube exit center, and heating time t_h) (see Table 1). To characterize their geometry, we took images of three different views of each nozzle (Figure 2a). By an image analysis procedure [33] we obtained the nozzle mean profile and calculated some geometrical parameters as the neck diameter D, the convergent length L_c and the neck length L_n (Figure 3a). The convergent length measures the region where the whole diameter reduction occurs, from $0.98 \times ID$ to D, while the neck length accounts for the final reduction, from $1.5 \times D$ to D.
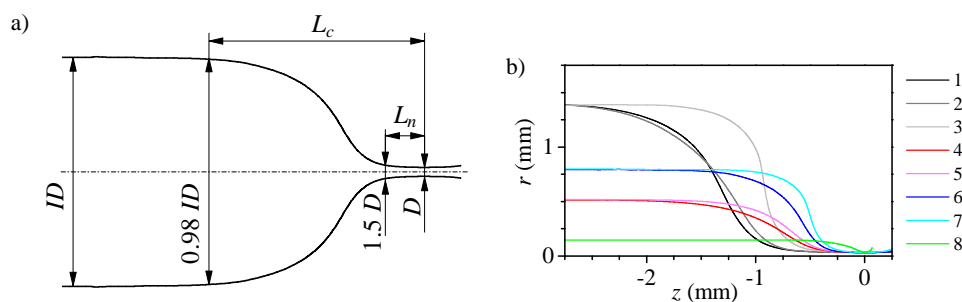

Figure 3. Characteristic geometrical parameters of the nozzle inner shape (**a**), and mean profile of the nozzles (**b**). In the latter, the origin $z = 0$ is located at the nozzle neck, and the line colour indicates the nozzle number in Table 1.

Table 1. Nozzles geometry and fabrication details.

	Nozzle Geometry			Capillary Geometry			Fabrication Parameters		
Nozzle	D [μm]	L_c [mm]	L_n [μm]	OD [mm]	ID [mm]	Wall	r_h [mm]	z_h [mm]	t_h [s]
1	72 ± 2	2.61	672	3.7 ± 0.1	2.8 ± 0.1	Thick	3.5	15	900
2	65 ± 5	2.60	625	3.3 ± 0.1	2.8 ± 0.1	Thin	3.5	15	240
3	73 ± 3	1.61	475	3.3 ± 0.1	2.8 ± 0.1	Thin	4.5	15	600
4	63 ± 3	1.91	327	2.0 ± 0.1	1.0 ± 0.1	Thick	5.5	15	70
5	65 ± 1	1.62	314	2.0 ± 0.1	1.0 ± 0.1	Thick	6	15	120
6	62 ± 1	1.49	271	2.0 ± 0.1	1.6 ± 0.1	Thin	5.5	15	70
7	69 ± 7	1.12	220	2.0 ± 0.1	1.6 ± 0.1	Thin	6.6	15	480
8	72 ± 1	0.57	65	0.4 ± 0.04	0.3 ± 0.03	Thin	7.9	15	9

The difference in the shape of the nozzles is readily appreciated in Figure 3b. When the original capillary is larger (higher ID), so is the desired diameter reduction, and due to the manufacturing process, the nozzle is longer and has a longer neck. The use of thin-wall capillaries significantly reduces the amount of glass involved in the shaping process and consequently the heating time; for example, nozzle 2 only needs about 25% of the corresponding for nozzle 1. However, it does not significantly affect the neck length. Choosing an outer heating position (higher r_h) in the flame allows for reducing the neck and nozzle lengths, especially for thin wall capillaries (see, for instance, nozzles 2 and 3). However, the fabrication time increases sharply which, in practice, establishes a limit to the heating position. Using smaller capillaries (lower ID) reduces the amount of glass involved

in the shaping and the diameter reduction, which accelerates the shaping process. To keep the process under control, it becomes necessary to work outer in the flame. The effect of varying the inner capillary diameter and its wall thickness may compensate, and larger capillaries with thinner walls may result in shorter nozzles (see nozzles 4 and 6). Finally, the use of very thin capillaries (nozzle 8) produces very short nozzles, but the shaping process is very fast and has poor reproducibility [34]. In general, we conducted around seven experiments for each nozzle device.

2.3. PDMS Particle Suspension Preparation

The two-syringe membrane emulsification technique (2SME) [36] was used for fabricating the flexible PDMS particles. First, we prepared the mixture between the siloxane base (Part A) and the curing agent (Part B) (Dow Corning SYLGARD 184 Silicone Elastomer) with a ratio of 30:1 (wt% siloxane base to curing agent) and stirred it manually for ten minutes. Then, we loaded 1 mL of the PDMS precursor mixture in one syringe and 5 mL of distilled water with a surfactant (3 wt% sodium dodecyl sulfate, SDS) on the opposite. The addition of the surfactant prevents sedimentation and flocculation of the particles. The emulsion was produced with five back and forth flow cycles through a 10 µm pore size filter. To cure the PDMS, we placed the emulsion in a standard magnetic stirrer at 70 °C for 3 h, and then we waited for 24 h to reach room temperature. The final particle proportion in the suspension was 1.65 ± 0.24 wt% (calculated by drying different samples). For each experiment, we prepared the particles solution and then modified the liquid phase by adding Dextran 40 (10 wt%). The final suspension density and viscosity are 1048 kg/m^3 and 0.0046 Pa·s. Dextran in the solution decreases sedimentation phenomena in the glass capillary, whereas the dye enhances visualization of the contours of the PDMS microparticles. On the other hand, the surfactant SDS avoids the formation of particle aggregates.

3. Results

3.1. Numerical Study of the Flow

We conducted numerical simulations using Ansys Fluent to analyze the strain rate resulting from the flow through the nozzles. We used the mean profile obtained from the images (Figure 3) to define their geometry and studied the flow of a liquid without particles with the properties shown in Section 2.3. The flow was regarded as axisymmetric. We imposed the non-slip condition on the solid walls and prescribed the inlet mass flow rate and the outlet pressure. We verified that the results were insensitive to the grid size.

The flow accelerates along the convergent region, and the velocity reaches a maximum at the neck, to decrease again downstream in the divergent region (Figure 4 left). As the Reynolds number $Re = 4\rho Q/(\pi \mu D)$ is below 0.5, the velocity profile at the neck section is almost parabolic (Figure 4 right). The difference between the maximum velocity at the neck and the corresponding for the parabolic profile is below 4% for nozzles 1–7, and rises to approximately 8% for nozzle 8.
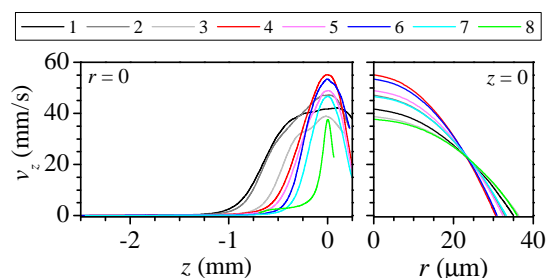

Figure 4. Axial velocity at the axis along the nozzle (**left**), and at the nozzle neck (**right**) for all the nozzles. The line colour indicates the nozzle number in Table 1.

Figure 5 shows the shape and the strain rate $\dot{\epsilon} = \partial v_z / \partial z$ for three of the nozzles. The diameter reduction from the original capillary diameter ID to that of the neck D spreads over a long region. We use two distances to characterize the shape: the convergent length L_c, measured from the section of $0.98 \times ID$ diameter to the neck; and the neck length L_n which measures the region where the final diameter reduction, from $1.5 \times D$ to D. For all the nozzles, the strain rate remains negligible for almost two-thirds of the nozzle length. Then, it shows a peak approximately at the section used to define the neck length. Finally, it falls to zero at the neck and negative on the divergent side. Nozzles produced from larger capillaries (Figure 5a), despite their larger diameter reductions, are longer and have a longer neck which results in a lower strain rate peak located farther from the neck. Figure 6 shows that the distance from the maximum strain rate to the neck is approximately the neck length for all the nozzles. Therefore, in fire-shaped nozzles and regardless of their shape, the peak position can be estimated to be at the section of $1.5 \times D$ diameter (used to evaluate L_n).
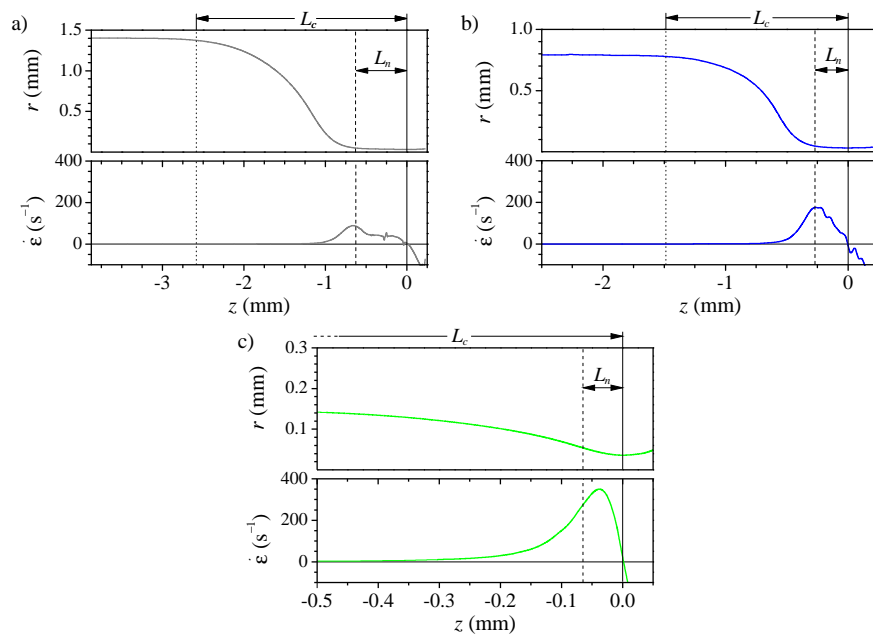

Figure 5. Shape and strain rate along the nozzle axis for nozzles 2 (**a**), 6 (**b**) and 8 (**c**) and $Q = 5$ μL/min. The vertical lines indicate sections of diameter D, i.e., the neck, (solid), $1.5 \times D$ (dashed), $0.98 \times ID$ (dotted). The latter is out of the field in (**c**).
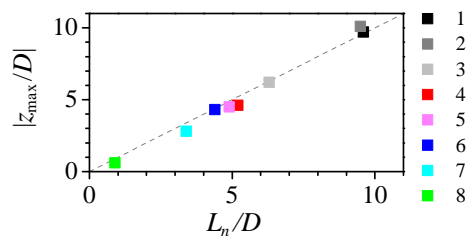
Figure 6. Maximum strain rate position z_{max} versus the neck length L_n for $Q = 5$ μL/min. The colour indicates the nozzle number in Table 1. The dashed line has slope 1.

In deformability studies, the dynamical response of the particle to the stress caused by the fluid is measured. The deformation depends on the magnitude and duration of the stress applied. Figure 7 shows the temporal evolution of the strain rate suffered by a

fluid particle along the axis. The time origin $t = 0$ is set at the instant when the particle crosses the neck, so the (negative) time indicates the remaining time to reach the neck. As the velocity is higher at the neck, the stress peak is very brief (ranging from 20 to 0.1 ms) when compared to the time to travel the whole convergent region (from 0.2 to 25 s). The strain rate peak is more intense for the shorter nozzles, even when the diameter reduction is smaller.
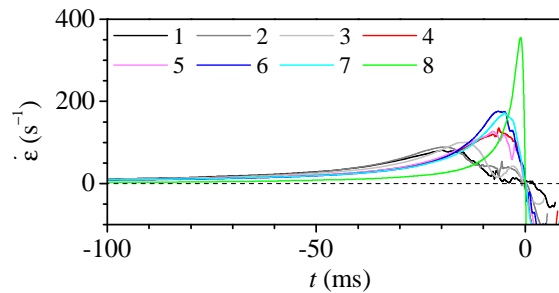

Figure 7. Strain rate along the nozzle axis versus the time to cross the neck for $Q = 5$ μL/min. The colour indicates the nozzle number in Table 1.

We used the mean strain rate in the convergent region $\dot{\epsilon}_c = v_n/L_c$ and the characteristic time $t_c = L_n/v_n$, where $v_n = 4Q/(\pi D^2)$ is the mean velocity at the neck, to calculate the dimensionless strain rate and time in Figure 8. Despite the significant difference in the geometry of the nozzles, the overlapping of the curves is remarkable. This is possible due to the nature of the shaping process, in which the heated glass surface tension force competes against the viscous force. The maximum strain rate ranges from 8 to 10 times the mean value $\dot{\epsilon}_c$ and it occurs approximately 0.6 times t_c before the neck. Therefore, regardless of the nozzle shape, it is possible to estimate the maximum strain rate value and when it occurs just from the main geometrical parameters of the nozzle.
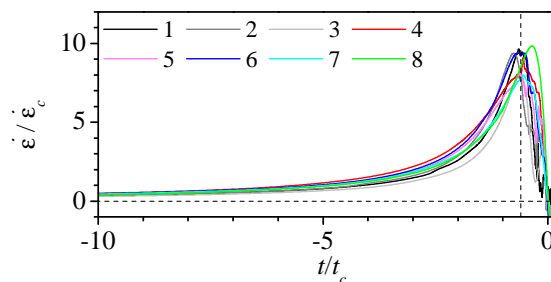
Figure 8. Dimensionless strain rate along the nozzle axis versus the dimensionless time to reach the neck for $Q = 5$ μL/min. The colour indicates the nozzle number in Table 1.

For a given geometry, the strain rate is proportional to the flow rate, and the position of the maximum remains at a fixed position (Figure 9). This linear relation confirms that the flow is practically developed at each nozzle section, which would allow using Poiseuille flow to estimate the velocity and strain rate at the nozzle axis. Figure 10a shows how the strain rate peak increases linearly with the flow rate, but it also becomes briefer and happens closer to the instant when the particle crosses the neck. As expected, the time from the maximum stress section to the neck is inversely proportional to the flow rate (Figure 10b).

Figure 9. Dimensionless strain rate along the axis for nozzle 8 and different flow rates. The lines for all the flow rates overlap.

Figure 10. Strain rate versus time to reach the neck (**a**), and time from the maximum to the neck (**b**) for nozzle 8 at different flow rates. The dashed line in (**b**) correspond to the curve $6.05 \times Q^{-1}$.
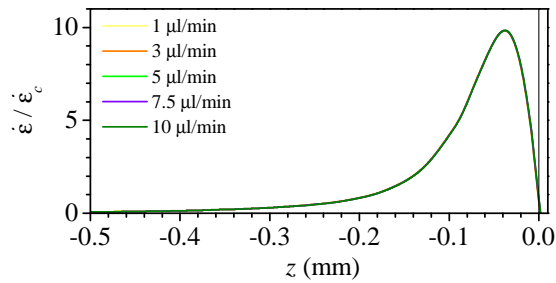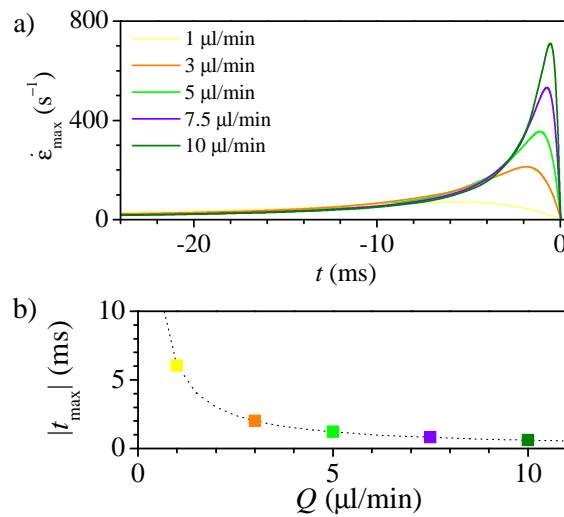
3.2. Experimental Measurement of Particle Deformation

We used a suspension of PDMS particles to study their deformation while traveling in the flow through the nozzles. The particles were fabricated as described in Section 2.3. As the particles move along the nozzle, they are subjected to the variable stress exerted by the surrounding fluid, which causes their deformation. In this kind of flow, the stress source is mainly due to the axial acceleration of the fluid (the strain rate). Though the presence of the particles affects the flow, their volumetric ratio in the fluid is low and their size is small compared to the nozzle diameter. For that reason, the results of the numerical simulations may be adequate to estimate the stress on the particle, and therefore, they will be used to analyze the deformation measurements.

PDMS particles are known to show viscoelastic behavior. So, there is a delay in the particle response to the stress applied. Additionally, the deformation will depend on the stress, its duration, and the measurement position. It is easy to determine the neck section in the image, so the deformation index (DI) is usually measured when the particle crosses the neck. Note that, due to the converging-diverging shape, the strain rate is zero at the neck. So, the measured deformation is the response to the stress on the particle upstream. Figure 11 shows the deformation index at the neck versus the neck aspect ratio $AR = L_n/D$ for the different nozzles. The deformation index is about 0.15 for nozzles with $AR > 4.5$ and rises to approximately 0.23 for $AR < 4.5$. The numerical results showed that the lengths of the convergent region and of the neck are related to the strain rate peak, width and position. The lower deformation index measured for larger AR results from the application

of a lower stress peak farther from the neck. The particle deforms less, and may even be recovering its shape when crossing the neck. The nearly constant deformation measured for $AR < 4.5$ may be caused by different reasons. On the one hand, the AR reduction causes two opposite effects: it increases the stress but reduces its duration and the temporal distance to the neck. The particle deformation may not follow the stress peak because the stress is not maintained long enough or because the measurement is performed too soon (the particle continues deforming in the diverging region). On the other hand, the particle deformability may be limited, i.e., it may not be capable of further deformation even if we maintained a larger strain rate longer.
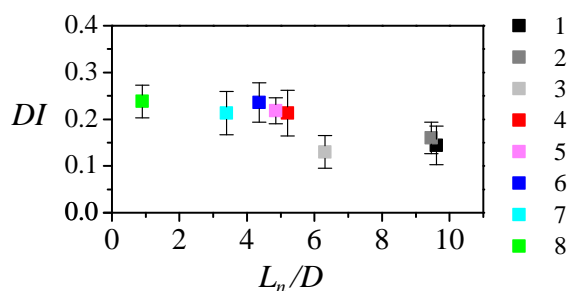

Figure 11. Particle deformation index DI measured at the neck versus the neck aspect ratio AR for the different nozzles. The symbol color indicates the nozzle number in Table 1. The flow rate was $Q = 5\,\mu L/min$.

Particles deform as they travel with the flow, and the deformation at a particular section results from the strain rate upstream and how it is reached. We measured the deformation index at different axial positions within the observation window and used numerical simulations to estimate the time to reach the neck corresponding to that position. Figure 12 shows the particle deformation (symbols) and the numerical strain rate (lines) calculated in the previous section. A significant delay in the particle response is observed, which seems larger when the strain rate peak is more abrupt. For nozzle 8 (Figure 12a), the strain rate starts rising (exceeds $25\,s^{-1}$) 20 ms before the neck. However, the particle reaction seems to initiate 3 ms before the neck. Though it deforms very fast, it does not seem to have finished deforming when it crosses the neck. Nozzles 6 (blue) and 7 (cyan) (Figure 12b) produce similar stress peaks, being that of the latter slightly delayed (approximately 1.6 ms). A similar delay is observed in the deformation trend for both nozzles, while for nozzle 6 the particle deformation seems to have reached its maximum at the neck (approximately 6.4 ms after the stress peak), for nozzle 7, it seems to be still increasing at that section. Nozzle 4 (red) (Figure 12c) has a lower stress peak but at the same position as nozzle 6 (blue). The resulting deformation is slightly smaller and appears to have reached a maximum at the neck.

The flow rate allows controlling the strain rate peak, however, it also moves the peak position. We measured the particles DI at the neck for nozzle 8 at different flow rates (Figure 13). The particle DI increases with the flow rate up to $Q = 5\,\mu L/min$, and then it remains almost constant. As there is a delay in the particle response, and, for this nozzle, the strain rate peak is very close to the neck, the deformation measured at that section is not the maximum. Figure 14a shows the temporal evolution of the deformation for three different flow rates and the strain rate evolution in the nozzle. Approximately the same low deformation is observed up to two milliseconds before reaching the neck. Then, the deformation starts raising earlier for the lower flow rate, for which the peak happens earlier. For the greater flow rate, the deformation occurs later and is sharper. Nevertheless, for all the flow rates, the response to the maximum stress seems to happen in the divergent region. Figure 14b compares the deformation for similar strain rates obtained using two nozzles and flow rates: nozzle 6 and $Q = 5\,\mu L/min$ (cyan) and nozzle 8 with flow rate

$Q = 3$ μL/min (orange). The strain rate peak has to be applied more than 5 ms before the neck, to measure the maximum deformation at that section.
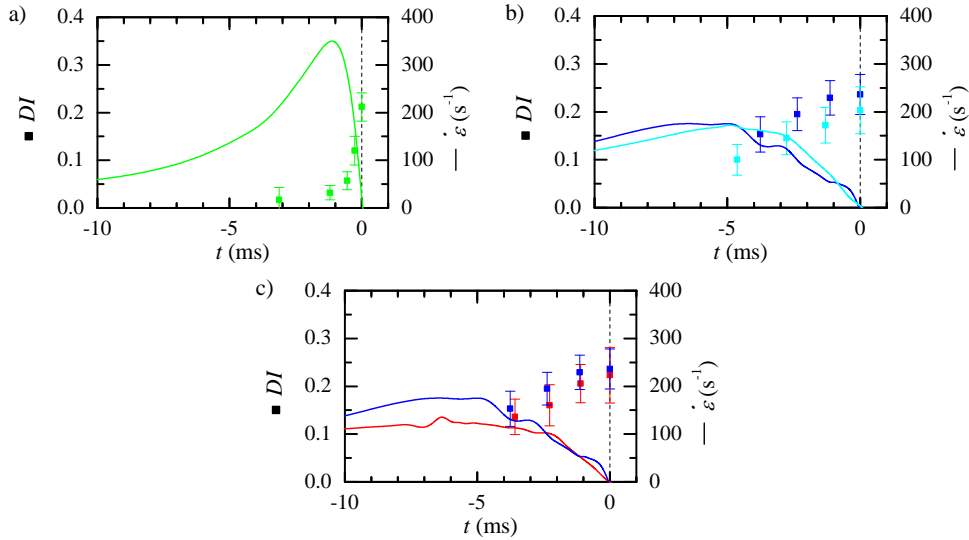
Figure 12. Temporal evolution of the particle deformation (symbols) and numerically calculated strain rate (lines) for nozzle 8 (**a**), 6 (blue) and 7 (cyan) (**b**), and 6 (blue) and 4 (red) (**c**). The flow rate was $Q = 5$ μL/min.
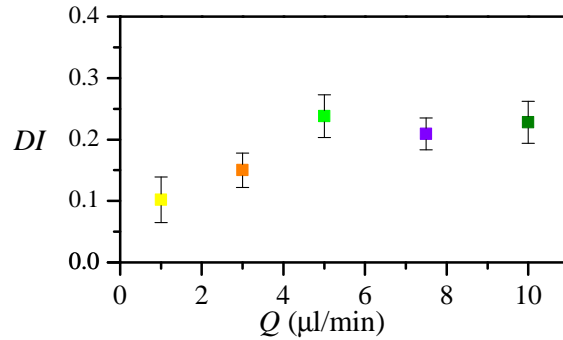
Figure 13. Deformation index DI at the neck versus the flow rate for nozzle number 8.
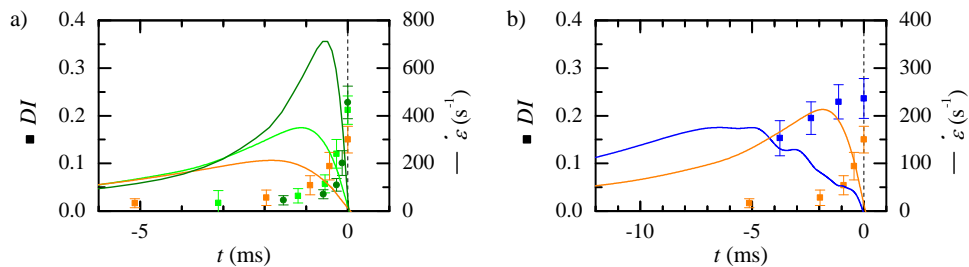
Figure 14. Temporal evolution of the particle deformation (symbols) and numerically calculated strain rate (lines) for: (**a**) nozzle 8, and different $Q = 3$ μL/min (orange), $Q = 5$ μL/min (light green) and $Q = 10$ μL/min (dark green); and (**b**) nozzle 6 and $Q = 5$ μL/min (blue) and nozzle 8 and $Q = 3$ μL/min (orange).

Our DI results for PDMS microparticles agreed with those reported in the literature for similar flow conditions and 2D rectangular microchannels (see, e.g., [5,12,37] and references therein).

4. Conclusions

Microcapsules are commonly used in several industrial applications. In many processes, their deformability is crucial for performing their function. For that reason, numerous methods have been developed to quantify this capability. Among them, the use of microfluidic devices is currently very popular due to the advances in their manufacturing techniques. Glass nozzles produced by fire-shaping are a low-cost alternative for evaluating microcapsules' deformability flowing through constrictions. Mainly, these nozzles produce an extensional flow with a strain rate peak in the convergent region. Our numerical results show that the position and intensity of this peak can be estimated from a few geometrical parameters. Regardless of the nozzle shape, the maximum position occurs approximately at the section of 1.5 times the neck diameter. Its value and the time lag to the neck depend on the flow rate. The maximum ranges from 8 to 10 times the mean strain rate in the convergent region, and it occurs approximately 0.6 times the characteristic time t_c.

When studying the deformation of viscoelastic particles, such as PDMS, the response to the stress is not instantaneous. The duration and position of the peak should be considered as it affects the deformation measured at different sections. Nozzles fabricated on larger (or thicker) capillaries show longer necks, and so, the stress peak widens and moves away from the neck. Analyzing the microcapsule shape along the nozzle convergent region may allow the observation of both its deformation and recovery. On the other hand, nozzles fabricated from small and thin capillaries produce a very sharp peak close to the neck, and the microcapsule maximum deformation may occur beyond the neck. To measure the maximum deformation at the neck, the nozzle must produce the strain rate peak approximately 5 ms before it reaches that section.

Author Contributions: Conceptualization, M.G.C.; methodology, E.J.V.; validation, A.R.; formal analysis, A.R. and M.L.; investigation, A.R., M.L. and E.J.V.; resources, E.J.V.; data curation, A.R., M.L. and E.J.V.; writing—original draft preparation, M.G.C.; writing—review and editing, M.G.C.; visualization, A.R. and M.L.; supervision, E.J.V. and M.G.C. All authors have read and agreed to the published version of the manuscript.

Institutional Review Board Statement: Not applicable.

Informed Consent Statement: Not applicable.

Data Availability Statement: Not applicable.

Conflicts of Interest: The authors declare no conflict of interest.

References

1. do Nascimento, D.F.; Avendaño, J.A.; Mehl, A.; Moura, M.J.; Carvalho, M.S.; Duncanson, W.J. Flow of tunable elastic microcapsules through constrictions. *Sci. Rep.* **2017**, *7*, 11898. [CrossRef] [PubMed]
2. Goff, A.L.; Kaoui, B.; Kurzawa, G.; Haszon, B.; Salsac, A. Squeezing bio-capsules into a constriction: Deformation till break-up. *Soft Matter* **2017**, *13*, 7644. [CrossRef]
3. Delcea, M.; Möhwald, H.; Skirtach, A.G. Stimuli-responsive LbL capsules and nanoshells for drug delivery. *Adv. Drug Deliv. Rev.* **2011**, *63*, 730–747. [CrossRef] [PubMed]
4. Baskurt, O.K.; Meiselman, H.J. Blood Rheology and Hemodynamics. *Semin. Thromb. Hemost.* **2003**, *29*, 435–450.
5. Pinho, D.; Muñoz-Sánchez, B.N.; Anes, C.F.; Vega, E.J.; Lima, R. Flexible PDMS microparticles to mimic RBCs in blood particulate analogue fluids. *Mech. Res. Commun.* **2019**, *100*, 103399. [CrossRef]
6. Neubauer, M.P.; Poehlmann, M.; Fery, A. Microcapsule mechanics: From stability to function. *Adv. Colloid Interface Sci.* **2014**, *207*, 65–80. [CrossRef] [PubMed]
7. Danielczok, J.G.; Terriac, E.; Hertz, L.; Petkova-Kirova, P.; Lautenschläger, F.; Laschke, M.W.; Kaestner, L. Red Blood Cell Passage of Small Capillaries Is Associated with Transient Ca^{2+}-mediated Adaptations. *Front. Physiol.* **2017**, *8*, 979. [CrossRef] [PubMed]

8. Gangotra, A.; Biviano, M.; Dagastine, R.R.; Berry, J.D.; Willmott, G.R. Use of microaspiration to study the mechanical properties of polymer gel microparticles. *Soft Matter* **2017**, *15*, 7286. [CrossRef] [PubMed]

9. Trégouët, C.; Salez, T.; Monteux, C.; Reyssat, M. Microfluidic probing of the complex interfacial rheology of multilayer capsules. *Soft Matter* **2019**, *15*, 2782. [CrossRef] [PubMed]

10. Chen, Z.; Zhu, Y.; Xu, D.; Alam, M.; Shui, L.; Chen, H. Cell elasticity measurement using a microfluidic device with real-time pressure feedback. *Lab. Chip* **2020**, *20*, 2343. [CrossRef]

11. Huisjes, R.; Bogdanova, A.; van Solinge, W.W.; Schiffelers, R.M.; Kaestner, L.; van Wijk, R. Squeezing for Life – Properties of Red Blood Cell Deformability. *Front. Physiol.* **2018**, *9*, 656. [CrossRef]

12. Sadek, S.H.; Rubio, M.; Lima, R.; Vega, E.J. Blood Particulate Analogue Fluids: A Review. *Materials* **2021**, *14*, 2451. [CrossRef]

13. Abkarian, M.; Faivre, M.; Horton, R.; Smistrup, K.; Best-Popescu, C.A.; Stone, H.A. Cellular-scale hydrodynamics. *Biomed. Mater.* **2008**, *3*, 034011. [CrossRef]

14. Piergiovanni, M.; Galli, V.; Holzner, G.; Stavrakis, S.; DeMello, A.; Dubini, G. Deformation of leukaemia cell lines in hyperbolic microchannels: investigating the role of shear and extensional components. *Lab Chip* **2020**, *20*, 2539. [CrossRef]

15. Otto, O.; Rosendahl, P.; Mietke, A.; Golfier, S.; Herold, C.; Klaue, D.; Girardo, S.; Pagliara, S.; Ekpenyong, A.; Jacobi, A.; et al. Real-time deformability cytometry: On-the-fly cell mechanical phenotyping. *Nat. Methods* **2015**, *12*, 199–202. [CrossRef]

16. Guruprasad, P.; Mannino, R.G.; Caruso, C.; Zhang, H.; Josephson, C.D.; Roback, J.D.; Lam, W.A. Integrated automated particle tracking microfluidic enables high-throughput cell deformability cytometry for red cell disorders. *Am. J. Hematol.* **2019**, *94*, 189–199. [CrossRef]

17. Chen, Y.; Chen, G.; Lin, Y.; Wang, G. A lab-on-a-chip capillary network for red blood cell hydrodynamics. *Microfluid Nanofluid* **2010**, *9*, 585–591. [CrossRef]

18. Hu, S.; Lam, R. Characterization of viscoelastic properties of normal and cancerous human breast cells using a confining microchannel. *Microfluid. Nanofluid.* **2017**, *21*, 68. [CrossRef]

19. Shelby, J.P.; White, J.; Ganesan, K.; Rathod, P.K.; Chiu, D.T. A microfluidic model for single-cell capillary obstruction by Plasmodium falciparuminfected erythrocytes. *Proc. Natl. Acad. Sci. USA* **2003**, *100*, 14618–14622. [CrossRef]

20. Man, Y.; Kucukal, E.; An, R.; Watson, Q.D.; Bosch, J.; Zimmerman, P.A.; Little, J.A.; Gurkan, U.A. Microfluidic assessment of red blood cell mediated microvascular occlusion. *Lab. Chip* **2020**, *20*, 2086. [CrossRef] [PubMed]

21. Man, Y.; Maji, D.; An, R.; Ahuja, S.P.; Little, J.A.; Suster, M.A.; Mohseni, P.; Gurkan, U.A. Microfluidic electrical impedance assessment of red blood cell-mediated microvascular occlusion. *Lab. Chip* **2021**, *21*, 1036. [CrossRef] [PubMed]

22. Man, Y.; Kucukal, E.; An, R.; Bode, A.; Little, J.A.; Gurkan, U.A. Standardized microfluidic assessment of red blood cell-mediated microcapillary occlusion: Association with clinical phenotype and hydroxyurea responsiveness in sickle cell disease. *Microcirculation* **2020**, *28*, 12662. [CrossRef] [PubMed]

23. Islamzada, E.; Matthews, K.; Guo, Q.; Santoso, A.T.; Duffy, S.P.; Scott, M.D.; Ma, H. Deformability based sorting of stored red blood cells reveals donor-dependent aging curves. *Lab. Chip* **2019**, *20*, 226. [CrossRef]

24. Piety, N.Z.; Stutz, J.; Yilmaz, N.; Xia, H.; Yoshida, T.; Shevkoplyas, S.S. Microfluidic capillary networks are more sensitive than ektacytometry to the decline of red blood cell deformability induced by storage. *Sci. Rep.* **2021**, *11*, 604. [CrossRef]

25. Galindo-Rosales, F.J.; Oliveira, M.S.N.; Alves, M.A. Optimized cross-slot microdevices for homogeneous extension. *RSC Adv.* **2014**, *4*, 7799–7804. [CrossRef]

26. Cha, S.; Shin, T.; Lee, S.S.; Shim, W.; Lee, G.; Lee, S.J.; Kim, Y.; Kim, J.M. Cell Stretching Measurement Utilizing Viscoelastic Particle Focusing. *Anal. Chem.* **2012**, *84*, 10471–10477. [CrossRef]

27. Yaginuma, T.; Oliveira, M.; Lima, R.; Ishikawa, T.; Yamaguchi, T. Human red blood cell behaviour under homogeneous extensional flow in a hyperbolic-shaped microchannel. *Biomicrofluidics* **2013**, *7*, 054110. [CrossRef] [PubMed]

28. Lee, S.S.; Yim, Y.; Ahn, K.H.; Lee, S.J. Extensional flow-based assessment of red blood cell deformability using hyperbolic converging microchannel. *Biomed. Microdevices* **2009**, *11*, 1021–1027. [CrossRef] [PubMed]

29. Faghih, M.M.; Sharp, M.K. Deformation of human red blood cells in extensional flow through a hyperbolic contraction. *Biomech. Model. Mechanobiol.* **2020**, *19*, 251–261. [CrossRef]

30. Guerrero, J.; Chang, Y.; Fragkopoulos, A.A.; Fernández-Nieves, A. Capillary-Based Microfluidics-Coflow, Flow-Focusing, Electro-Coflow, Drops, Jets, and Instabilities. *Small* **2020**, *16*, 1904344. [CrossRef]

31. Montanero, J.M.; Gañán-Calvo, A.M. Dripping, jetting and tip streaming. *Rep. Prog. Phys.* **2020**, *83*, 097001. [CrossRef] [PubMed]

32. Muñoz-Sánchez, B.N.; Cabezas, M.G. Borosilicate nozzles manufactured by reproducible fire shaping. *J. Mater. Process. Technol.* **2018**, *261*, 173–183. [CrossRef]

33. Muñoz-Sánchez, B.N.; Gañán-Calvo, A.M.; Cabezas, M.G. A new fire shaping approach to produce highly axisymmetric and reproducible nozzles. *J. Mater. Process. Technol.* **2019**, *270*, 241–253. [CrossRef]

34. Rubio, A.; Rodríguez, S.; Cabezas, M.G. Capabilities and limitations of fire-shaping to produce glass nozzles. *Materials* **2020**, *13*, 5477. [CrossRef]

35. Rubio, A.; Faustino, V.; Cabezas, M.G.; Lima, R.; Vega, E.J. Fire-shaped cylindrical glass micronozzles to measure cell deformability. *J. Micromech. Microeng.* **2019**, *29*, 105001. [CrossRef]

36. López, M.; Rubio, M.; Sadek, S.; Vega, E.J. A simple emulsification technique for the production of micro-sized flexible powder of polydimethylsiloxane (PDMS). *Powder Technol.* **2020**, *366*, 610–616. [CrossRef]

37.   Carneiro, J.; Lima, R.; Campos, J.B.L.M.; Miranda, J.M. A microparticle blood analogue suspension matching blood rheology. *Soft Matter* **2021**, *17*, 3963. [CrossRef]

5. Paper II - Fire-shaped nozzles to produce a stress peak for deformability studies.

6

Paper III - A particulate blood analogue based on artificial viscoelastic blood plasma and RBC-like microparticles at a concentration matching the human haematocrit.

Particulate blood analogue based on artiicial viscoelastic blood plasma and RBC-like microparticles at the human haematocrit

A. Rubio[a], M. López[a], T. Rodrigues[b,c], L. Campo-Deaño[b,c], E. J. Vega[a,*]

[a]*Depto. de Ingeniería Mecánica, Energética y de los Materiales and Instituto de Computación Científica Avanzada (ICCAEx), Universidad de Extremadura, E-06006, Badajoz, Spain*
[b]*CEFT, Depto. de Engenharia Mecânica, Faculdade de Engenharia, Universidade do Porto, Rua Dr. Roberto Frias, 4200-465, Porto, Portugal*
[c]*ALiCE, Faculdade de Engenharia, Universidade do Porto, Rua Dr. Roberto Frias, 4200-465, Porto, Portugal*

Abstract

There has been an enormous interest in the production of fluids with rheological properties similar to those of real blood over the last years. Application fields range from Biomicrofluidics (microscale) to Forensic Science (macroscale). The inclusion of flexible microparticles in blood analogue fluids has demonstrated to be essential in order to reproduce the behaviour of blood flow in these fields. Here, we describe a protocol to produce a whole human blood analogue composed of a proposed plasma analogue and flexible spherical microparticles that mimic key structural attributes of RBCs (size and mechanical properties), at a concentration matching the human haematocrit ($\sim 42\%$ by volume). Poly-dimethylsiloxane (PDMS) flexible microparticles were used to mimic RBCs, whose capability to deform is tunable by means of the mixing ratio of PDMS precursor. Their flow through glass micronozzles allowed us to find the proper mixing ratio of PDMS to have approximately the same Young´s modulus (E) as that exhibited by real RBCs. Shear and extensional rheology and microrheology techniques were used to match the properties exhibited by human plasma and whole blood at body temperature (37 °C). Finally, we study the flow of our proposed fluid through a microfluidic channel, showing the *in vitro* reproduction of the multiphase flow effects taking place in the human microcirculatory system, such as the cell-free layer (CFL) and Fåhræus–Lindqvist effect. A macroscale application in the field of Forensic Science is also presented, concerning the impact of our blood analogue droplets onto a solid surface for bloodstain pattern analysis.

Keywords: particulate human blood analogue, shear and extensional rheology,

*Corresponding author
Email address: ejvega@unex.es (E. J. Vega)

passive microrheology, biomicrofluidics, bloodstain pattern analysis, splashing

---

1. Introduction

The use of human blood in fields from Biomicrofluidics to Forensic Science complicates the scientific experimental studies due to diverse problems such as coagulation, sample storage and disposal, ethical and economic issues.

⁵ Enormous interest in the production of fluids with physiological and rheological properties similar to those of real blood has been generated for last years to conduct *in vitro* experiments for biomedical applications at micro and macroscale [see Fig. 1(a)]. The development of blood analogues would allow to perform *in vitro*-studies that would be very helpful in the design and test of ther-
¹⁰ apy strategies and medical devices [1,2]. Several liquid mixtures and solutions have been considered for mimicking blood, and lately, there have also been attempts to create particulate suspensions [1]. The addition of small sized flexible particles to blood analogues to mimic Red Blood Cells (RBC's) has demonstrated to be essential to reproduce multiphase effects taking place in a microcircula-
¹⁵ tory system, such as the cell-free layer (CFL) and Fåhræus–Lindqvist effect or even to drug delivery [3]. Moreover, others capabilities as their ability to reproduce transport-oxygen properties or the necessity to mimic the surface charge of these cells have been also explored [4].

In Forensic Science field, although commercial blood simulants have been
²⁰ created for bloodstain pattern analysis (see Fig. 1.b), the high rigidity of the microparticles used in their formulation avoids the accurate reproducibility of the behaviour of a simple blood droplet impacting onto a solid surface [5]. The capacity to deform (energy dissipation) of the RBC-like microparticles seems to be the key to be able to reproduce more accurately the human blood spreading
²⁵ and splashing behaviour [5].

Therefore, one of the key properties of the particles or capsules used to mimic RBCs is their deformability. The deformation index DI and the elastic modulus E have frequently been used to evaluate it. Several attempts have been done to estimate the RBCs' elastic modulus, mostly using atomic force
³⁰ microscopy [6–11], though it is not uniform over its surface [6]. It has been shown that the measured value depends on several aspects, such as the procedure to prepare the sample [10], the sample storage time [7], and even the particular blood donor [6]. For that reason, reported healthy RBCs mean elastic modulus range from 1 to 30 kPa. Polydimethylsiloxane (PDMS) microparticles are known to
³⁵ show very high deformability [12–14]. For that reason, they are good candidates to mimic RBCs' behavior. PDMS is produced from the mixture of two components: the siloxane base and the curing agent, and the resulting properties depend on the ratio of the precursors in the mixture.

In this paper viscoelastic fluids mimicking the non-Newtonian properties of
⁴⁰ real human plasma (shear viscosity and viscoelastic moduli) were carefully developed. The production and addition of flexible spherical PDMS microparticles that mimic key structural attributes of RBCs (size and mechanical properties),
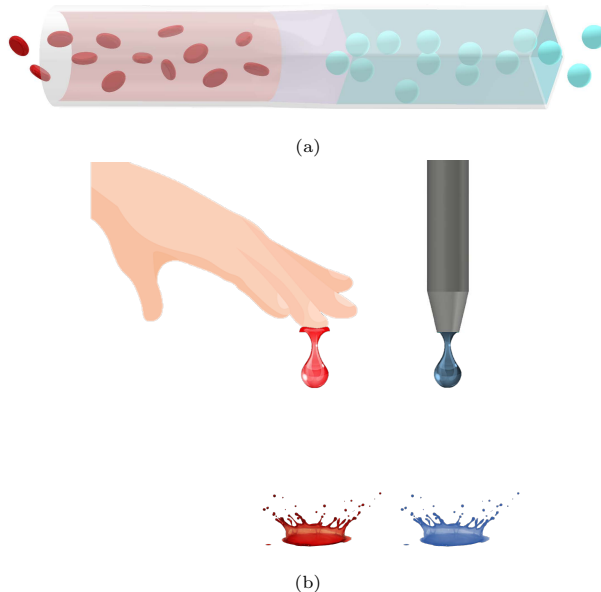
2

Figure 1: Microfluidics as a platform to mimic and study blood flow in the human microcirculatory system (a). Bloodstain pattern analysis in Forensic Science (b).

in 42% by volume (similar to the human haematocrit), provided a new blood particulate analogue fluid. Shear and extensional rheology and microrheology techniques allowed us to match the properties exhibited by human plasma and whole human blood at body temperature. To evaluate the flow and mechanical properties of the particulate blood analogue fluid, the cell (particle) free layer (CFL/PFL) in a microfluidic channel with an important constriction (microstenosis) and the droplet impact for bloodstain pattern analysis were analysed in micro and macroscales, repectively.

2. Materials and methods

2.1. RBC-like PDMS microparticles

The two-syringe membrane emulsification technique (2SME)[13] was used for fabricating the polydimethylsiloxane (PDMS) particles [see Fig. 2(a)]. First, we prepared the mixture between the siloxane base (Part A) and the curing agent (Part B) (Dow Corning SYLGARD 184 Silicone Elastomer) with the desired weight ratio (precursor to curing agent) and stirred it manually for ten minutes. Then, we loaded 1 ml of the PDMS precursor mixture in one syringe and 5 ml of distilled water with a surfactant (3 wt% sodium dodecyl sulfate, SDS) on the opposite. The addition of the surfactant prevents sedimentation and flocculation of the particles. The emulsion was produced with five back and

3

forth flow cycles through a 10 μm pore size filter. To cure the PDMS, we placed the emulsion on the heater of a standard magnetic stirrer at 70 °C for 3 hours, and then we waited for 24 hours to reach room temperature. The final particles proportion in the suspension was 1.65±0.24 wt% (calculated by drying different samples).
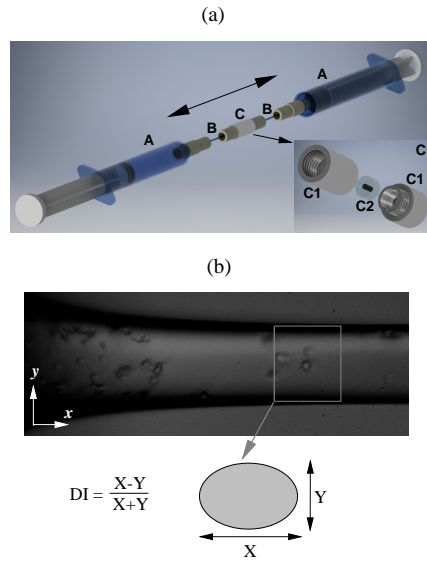

(a)

(b)

$$DI = \frac{X-Y}{X+Y}$$

Figure 2: (a) Elements of the two-syringe membrane emulsification technique (2SME) used to produce PDMS microparticles: two plastic syringes of 5 ml (A), tubing and connectors (B), and an inline filter/membrane (C) composed of a column (C1) and a frit (C2)[13]. (b) Visualization of the microparticles flowing through a glass micronozzle (above) and deformation index (DI) definition (below)[13]. Figures (a) and (b) reproduced from López et al.[13] with permission from Elsevier.

For each deformation assessment, we prepared the particles solution and then modified the liquid phase by adding Dextran 40 (10 wt%) to use the same liquid phase as for the RBC suspension (Dextran is used to preserve the RBC properties) and Rhodamine B to improve particles visualization in the experiments. The solution was injected through a fire-shaped nozzle[15] to evaluate the deformability of RBCs, and to compare it with that of PDMS particles produced from different precursors ratios. We used a micronozzle with 66 ± 3 μm of neck diameter and flow rate $Q = 5\mu$l/min and measured the deformation at the neck. The experimental setup used to observe the deformation of the flexible particles and cells while flowing along the nozzle was the same as that described in[13].

For the RBC suspension preparation, a sample of blood from a healthy donor was collected, adding ethylenediaminetetraacetic acid (2K EDTA) to prevent coagulation. The sample was stored hermetically at 4 °C, and later centrifuged to separate the RBCs from the bulk blood. Then, RBCs were resuspended and

4

washed in Physiological salt solution (PSS) and centrifuged several times again. To maintain the cell homeostasis and avoid sedimentation, 1% by volume of healthy RBCs were redispersed by slow stirring in a 1M solution composed of 5 g of Dextran 40 powders (Sigma-Aldrich), 7.35 ml of $NaCl$, 201 μl of KCl, and 68 μl of $CaCl_2H_2O$ ([16–18]).

The deformation index DI shown in Fig. 2(b) was used, where X is the length of the particle along the nozzle/capillary axis and Y the corresponding in the normal direction. In each experiment, 100 particles/cells moving along the nozzle centerline ($\pm 5\mu$m) were measured when crossing a particular section ($\pm 33\mu$m). Figure 2.b also shows the measurement region at the neck section. The particle/cell dimensions were obtained manually at the pixel level, and Chauvenet's criterion was used to identify and reject outliers.
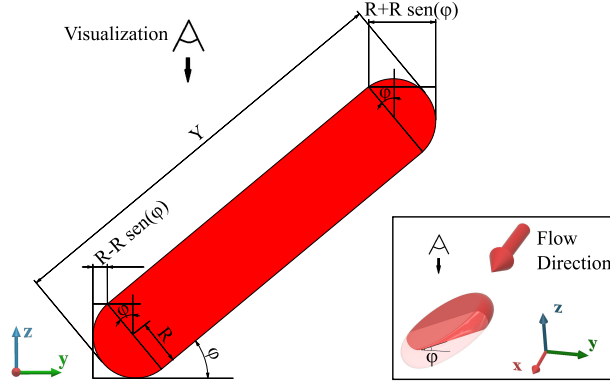
Figure 3: Sketch of the RBC visualization.

The RBCs in our experiments can be assumed to be aligned with the flow direction, i.e., with the nozzle axis x (see Fig. 3). If the flow were perfectly axisymmetric, then the RBC orientation angle φ formed with the y axis would take values in the interval $[0, 2\pi]$ with an equiprobable distribution. In this case, the mean value of the apparent particle length $Y_{\rm app}$ of RBCs randomly chosen is

$$\langle Y_{\rm app}\rangle = \frac{1}{2\pi} \int_0^{2\pi} \left[(Y - 2R)\cos\varphi + 2R\right]\,\mathrm{d}\varphi\,. \tag{1}$$

Eq. (1) allows one to calculate Y from the value of $\langle Y_{app}\rangle$ measured in the experiment. The result differed in about 8% from the value measured with the method described above, which constitutes a consistency test for our measurements.

2.2. Formulation of the working fluids

Figure 4 schematises the formulation of the different working fluids: a base Newtonian solution of 85 wt% of water (W) and 15 wt% of dimethyl sulfoxide

5

(DMSO)[19] with the addition of 50 ppm of polyethylene oxide (PEO) with different molecular weights M_w [600 kDa (PEO600K), 2 MDa (PEO2M), 4 MDa (PEO4M) and 8 MDa (PEO8M)] were prepared in order to confer the required viscoelasticity able to mimic human blood plasma[20,21] (de-ionized water and PEO from Sigma Aldrich, DMSO from Merck); a particulate viscoelastic fluid was prepared with the base solution and with the addition of the aforementioned PDMS microparticles at a concentration of roughly 42 wt%, i.e. matching the human haematocrit (Hct), to reproduce the rheological behavior of whole human blood. It was checked that the blood analogue preserves the properties for about one month when it is properly stored in the fridge.
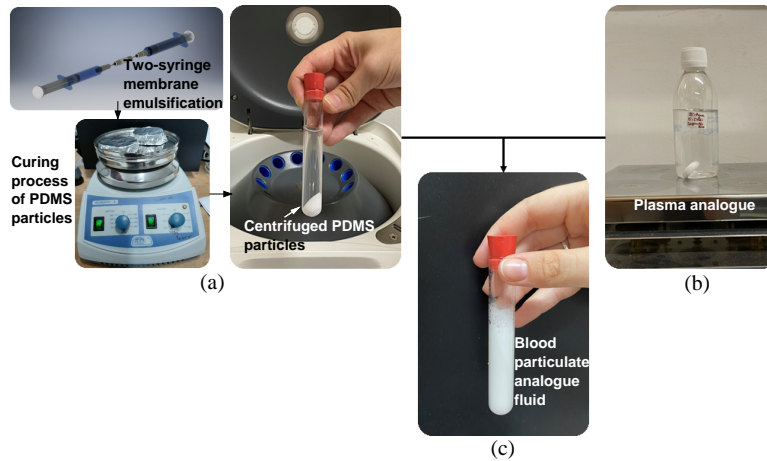
Figure 4: (a) Production, curing and centrifugation of suspension with PDMS microparticles (subsection 2.1). (b) DMSO/water solution (15/85 wt%) with 50ppm of PEO at different molecular weights M_w. (c) Particulate viscoelastic fluid (around 42 vol% of microparticles).

The density ρ of the tested fluids was measured with a pycnometer of 10 ± 1 ml and a precision balance. Table 1 shows the experimental results and the typical values of the density of human plasma[22] at 20℃, and RBCs and whole blood[23] at 37 °C: 1027, 1095 and 1047 kg/m^3, respectively.

Table 1: Densities (ρ) of the working liquids, particles, and whole dispersions at 20 ± 2 °C (RBCs, and whole blood at 37 °C). The PDMS densities ρ for each mixing ratio were estimated from the Hocheng et al.[24]. The rest of the data came from the manufacturer, literature, or were obtained experimentally in the laboratory.

	PEO			PDMS		
	M_w (kDa)	c (wt%)	DMSO (wt%)[a]	Ratio	"Hct" (vol%)[b]	ρ (kg m^{-3})
Blood plasma[22]	—	—	—	—	—	1026.6 ± 0.3
DMSO/W-PEO600K	600	0.005	15	—	—	1012.0
DMSO/W-PEO2M	2000	0.005	15	—	—	1012.8
DMSO/W-PEO4M	4000	0.005	15	—	—	1013.0
DMSO/W-PEO8M	8000	0.005	15	—	—	1013.0
RBCs[23]	—	—	—	—	—	1095 ± 2
PDMS 30:1	—	—	—	$30:1$	—	1050.0
PDMS 45:1	—	—	—	$45:1$	—	1050.0
PDMS 60:1	—	—	—	$60:1$	—	1050.0
Whole blood[23]	—	—	—	—	—	1047 ± 6
DMSO/W-PEO600K$_{45:1}$	600	0.005	15	$45:1$	42	1015.0
DMSO/W-PEO2M$_{45:1}$	2000	0.005	15	$45:1$	42	1015.0
DMSO/W-PEO4M$_{45:1}$	4000	0.005	15	$45:1$	42	1015.1
DMSO/W-PEO8M$_{45:1}$	8000	0.005	15	$45:1$	42	1015.3
DMSO/W-PEO8M$_{30:1}$	8000	0.005	15	$30:1$	42	1015.2
DMSO/W-PEO8M$_{60:1}$	8000	0.005	15	$60:1$	42	1015.3

[a] DMSO-water solution
[b] Microparticle volume fraction or, equivalently, "haematocrit" (Hct)

The surface tension γ, a relevant property for the droplet impact application
presented in subsection 3.6, was also measured with the Theoretical Interface
Fitting Analysis (TIFA) method [25], resulting in a value of 38 mN/m for the
particulate viscoelastic fluid DMSO/W-PEO4M$_{45:1}$, near to the value of human
blood of around 52 mN/m from the literature [26,27]. Steady shear, extensional
rheology and microrheology experiments were used to compare the properties
exhibited by human plasma and whole human blood with that of the working
fluids.

2.3. Steady shear rheology

A stress-controlled rotational rheometer (Anton Paar Physica MCR 301) was
used to obtain the steady shear viscosity, η, as a function of the shear rate, $\dot{\gamma}$ for
all the fluid samples (Fig. 9). A plate-plate geometry (PP50) with a radius of
$R = 25$ mm and a gap of h=100 μm, was used to obtain reliable data in a wide
range of shear rates. The temperature within the fluid volume was set at 20 °C
and controlled by a Peltier cooling system. Steady-state viscosity curves were
obtained from 1 to 10,000 s^{-1}. At least three independent measurements were
performed to ensure the reproducibility of the results, trends were considered
significant when means of compared sets differed at P<0.05 (Student's t-test).
The range of shear rate providing reliable data was set for each sample between
the limit of the rheometer sensitivity (low-shear rate limit) and the onset of
inertial instabilities (high-shear rate limit) [28].

We would like to point out that despite of in previous studies [14,29] serrated
plate-plate geometry was used to conduct steady shear rheology with suspen-
sions, a protrusion flow (at high shear rates) results in non reliable data [30].
Relatively low viscous suspensions should be analysed with geometries having
smooth surfaces, plate-plate geometry [30].

2.4. Extensional rheology

A custom-made capillary breakup extensional rheometer was used to obtain
the extensional relaxation time λ_e, see Fig. 5(a), for all the working fluids. The
experimental setup and procedure used for this purpose is described in detail in
Sousa et al. [21],[31]. Briefly, a liquid bridge about 500 μm in length with the triple
contact lines anchored to the edges of the supporting rods was formed, and the
filament thinning was induced by using the slow retraction method (SRM) [32].
The subsequent filament thinning and breakup was recorded using a high speed
camera (Photron, Fastcam SA5) up to 50,000 frames per second, as illustrated
in Fig. 5(b). The particle sedimentation was insignificant during our extensional
rheology experiments.

The images were processed to determine the filament diameter d with a
sub-pixel resolution technique [33,34]. By plotting the diameter data as function
of time in a semi-log scale, one straightforwardly identifies the time interval
within which the diameter decays exponentially. This interval corresponds to
the elasto-capillary regime, where the balance between tensile stresses and sur-
face tension produces the homogeneous stretching of a quasi-cylindrical thread.
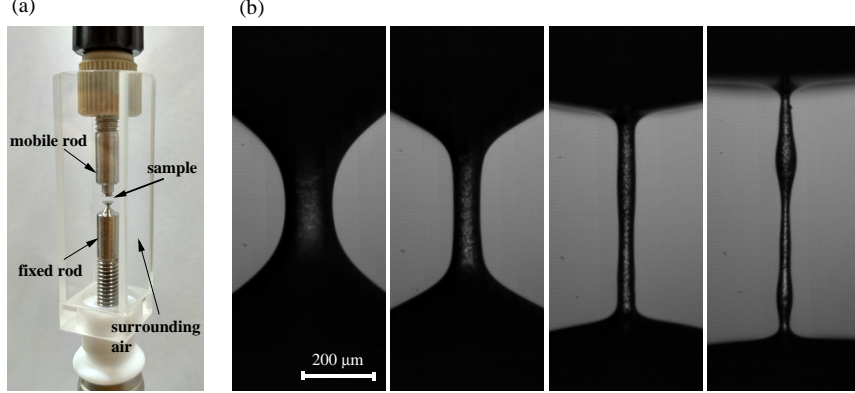
8

Figure 5: (a) Detailed view of the test cell used for the uniaxial extensional rheology measurements, exactly the same configuration used in Sousa et al.[21] for human blood. The sample was placed in between the rods with an initial gap of about 500 μm. To induce the filament thinning, the slow retraction method[32] was used (at a constant velocity of 10 μm/s). (b) Sequence of images of the evolution of a filament of the particulate viscoelastic fluid DMSO/W-PEO4M$_{45:1}$, the time interval between each image is 140 μs.

The time evolution of the filament diameter d in this regime was fitted by the exponential function[35]

$$d(t) = A\ e^{-t/(3\lambda_e)}, \tag{2}$$

in order to calculate of the extensional relaxation time λ_e. Each experiment was conducted five times to assess the reproducibility and to estimate the standard deviation.

2.5. Multiple particle tracking microrheology

Multiple particle tracking (MPT) microrheology was performed as previously described[22]. MPT is a passive microrheological technique in which the Brownian motion of probe particles is measured and related to bulk rheological properties using the generalised Stokes–Einstein relation (GSER) by

$$J(\tau) = \frac{3\pi a}{dkT} \left\langle \Delta r^2(\tau) \right\rangle, \tag{3}$$

where J is the creep compliance, τ is the lag time, kT is the thermal energy, d is the number of spatial dimensions, a is the probe radius and $\left\langle \Delta r^2 \right\rangle$ is the two-dimensional ($d = 2$) ensemble-averaged mean-squared displacement (MSD) of the particles undergoing Brownian motion over time, τ[36,37].

Bulk rheology can be inferred from the passive bead trajectories using the real and imaginary components of the frequency-dependent complex shear modulus $G^* = G' + iG''$ and Euler's formula with

$$G^*(\omega) \sim \frac{dkT \exp\left[i\pi\alpha(1/\omega)/2\right]}{3\pi a \left\langle \Delta r^2(1/\omega) \right\rangle \Gamma\left[1 + \alpha(1/\omega)\right]}, \tag{4}$$

9

where Γ designates the gamma function, $\omega = 1/\tau$ is angular frequency and α is
the logarithmic slope assumed for the MSD[38].

Monodisperse PMMA microspheres with (nominal) radius $a = 3$ μm are
added to the fluids at a concentration of 0.05% (w/w) and used as tracer par-
ticles (Spheromers CA6, Microbeads AS). MPT microrheology measurements
are taken for each equilibrated solution (sample volumes of roughly 260 μl)
pipetted into the sample chamber (137-1-40, Hellma Analytics). The openings
of the chamber are then sealed to prevent the sample from being in contact
with ambient air and, therefore, avoid bulk flow (or drift) and/or evaporation.
Particle motion was observed at room temperature (19.4 ± 0.2℃), resulting in
a reference fluid temperature ($T_{\text{ref}} \sim 20$℃) inside the chamber of 20.8 ± 0.3℃.
Bright-field optical video microscopy with a high-speed CMOS camera (FAST-
CAM UX100, Photron) is used to capture the movement of the probe particles
at $63\times$ magnification using an inverted microscope (DM IL LED, Leica). Data
are collected at $f = 125$ fps and $\phi = 8$ ms exposure time for 3750 frames (30 s).
The probe positions are tracked by an image processing algorithm and two-
dimensional particle trajectories are formed by linking the probes found in con-
secutive video frames[39]. Data were taken at different positions in each sample
to check them for spatial heterogeneity—i.e. ensure that rheological properties
do not vary spatially—and de-drifted (convective drift and vibration can in-
troduce errors)[40]. The MSD values were calculated at various lag times using
unbiased estimates derived elsewhere[41]. The apparent motion of immobilised
tracer particles was measured to determine the noise floor and a resolution of
about 10^{-4} μm^2 in $\langle \Delta r^2 \rangle$ was obtained, which was used to correct the estimated
MSD of the probes for static errors from camera noise[22,42].

3. Results and discussion

3.1. Morphology and mechanical properties of the microparticles

Figure 6 shows the DI at the nozzle neck for PDMS particles fabricated from
different ratios of the precursors and for healthy RBCs. The PDMS precursors
ratio (%wt, siloxane base to curing agent) was varied from the standard 10:1 to
60:1. Above the latest ratio, the material did not crosslink and remained as a
highly viscous liquid. The observed deformability increased with the ratio, and
became close to that of the RBCs for the larger ones.

Figure 7 shows the correlation between the deformation index and the elastic
modulus. The dotted line indicates a possible potential fit line for PDMS parti-
cles to predict the relationship between both parameters for the measurements
in a micronozzle with 66 ± 3 μm of neck diameter and Q=5 μl/min, under the
conditions mentioned in López et al.[13]. The elastic modulus reported for the
largest ratios is also close to that of RBCs. Finally, Figure 8 compares the size
of the RBCs and the PDMS particles sizes for 45:1 and 60:1 ratios. The bars
represent the probability distribution of the RBCs larger dimension D_{RBC} (red)
and the particle diameter D_p (grey). The mean size of the particle for both ra-
tios matches that previously reported for the particle fabrication method lower
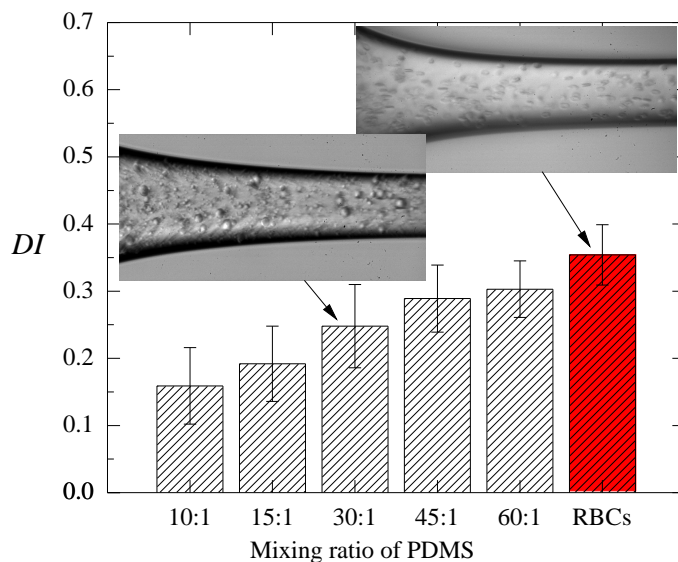
10

Figure 6: Deformation index of PDMS particles produced with different precursor ratio (Part A:Part B) and healthy RBCs. The insets show images of PDMS particles (30:1) and RBCs flowing through our micronozzles.

ratios[13]. However, there is a significant more heterogeneity in size for 60:1 than the 30% reported for this particle fabrication method using lower precursors ratios[13], probably because of the crosslinking disparity due to the low propor-
₂₂₅ tion of the curing agent. Nevertheless, these results show that PDMS particles fabricated from 45:1 or 60:1 may be adequate candidates for mimicking RBC's deformability and hence, to develop viscoelastic particulate blood analogues.

3.2. Shear rheology

The steady shear viscosity of the viscoelastic base solutions for different PEO
₂₃₀ molecular weights M_w is shown in Fig. 9(a). In general, all samples present an almost constant viscosity in agreement with the dilute regime of the PEO solutions prepared[43]. The viscosity value observed at high shear rates (η_∞), varies slightly from 1.33±0.01 mPa.s to 1.42±0.01 mPa.s, corresponding to the solutions with 50ppm of PEO of 600 kDa and 8 MDa, respectively. It is the
₂₃₅ sample prepared with PEO with the lowest molecular weight that is able to match the value of the estimated zero shear viscosity, η_0, obtained for human blood plasma at 37°C by Brust et al.[20] with a value of 1.34mPa.s (shown as grey line in Fig. 9a).

When 42 vol% of the fabricated PDMS particles with different PDMS mixing
₂₄₀ ratios, corresponding to the particles with similar DI of that of RBCs (PDMS 30:1, 45:1 and 60:1), are added to the base viscoelastic solution DMSO/W-PEO8M, the viscosity values increased, and also a shear-thinning behaviour (a

11
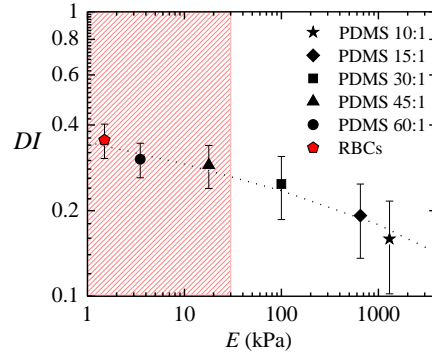
Figure 7: Deformation index DI of PDMS particles produced with different precursor ratios (Part A:Part B) and human healthy RBCs versus the literature elastic modulus E. The red symbol corresponds to the most accepted value for the mean elastic modulus E of RBCs and the red striped region points out the range of E values for human RBCs in the literature. The dotted line shows a possible fitting to the PDMS particle values.

Figure 8: Probability distribution of the resting size of healthy RBCs $\mathcal{P}(D_{RBC})$ (red bars) and PDMS particles $\mathcal{P}(D_p)$ fabricated for precursor ratio, Part A:Part B, 45:1 (a) and 60:1 (b) (striped bars).

12

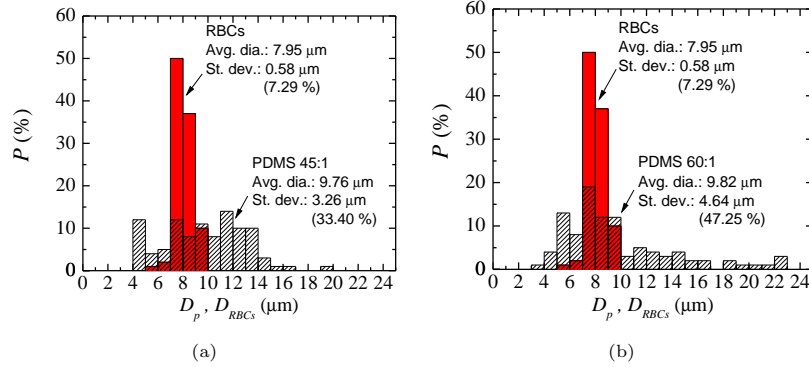decrease of viscosity as a function of shear rate) can be observed for all samples as a result of the initial aggregation and consequent disaggregation of the PDMS particle during flow [Fig. 9(b)]. The mechanism responsible for the shear-thinning behaviour has motivated many studies in the last decades in several systems as Brownian colloidal suspensions and non-Brownian suspensions, and for rigid and less rigid microparticles. The shear-thinning behaviour of our suspensions (in the limit of non-Brownian suspensions) could be mainly caused by the presence of adhesive forces between particles, as it was reported by Gilbert et al. [44] in their study of PDMS suspensions. When these adhesive forces are presented, the shear-thinning behaviour appears because of the formation of agglomerates that break down when the deformation is increased, leading to a reduction of these structures into units and thus decreasing the viscosity with the shear rate[45], as it is the case of blood. Nevertheless, the value of the viscosity and the degree of shear-thinning is different according with the deformation index of the particles. The highest values of the viscosity at low shear rates correspond to the solution with less deformable particles (PDMS precursor mixing ratio of 30:1), maybe related to the fact that these particle are able to resists more to the shear stress leading to a disturbance flow that increase the viscous dissipation rate[46,47].

To further understand these results the ratio between viscous and elastic forces, denoted as the Capillary number Ca, is the most important dimensionless number that takes into account the deformability of the particles. The Capillary number Ca can be written as:

$$Ca = \frac{\sigma}{E} \tag{5}$$

where σ is the shear stress and E the elastic modulus of the particles[48].
Under flow, high values of Ca mean that particles are more sensitive to the variation of the shear rate leading to a change in their shape[49].

The highest Ca corresponds to samples with particles with mixing PDMS ratio of 60:1 ($Ca^{60:1} > Ca^{45:1} > Ca^{30:1}$). The ability to better deform provoke that higher number of particles migrate to the area where the shear rate is low, and as a result the viscosity of the suspension decrease in comparison with the samples with particles of lower mixing ratios.

Moreover, Fig. 9(b) allows one to check the effect of the viscoelastic base solution (potential plasma analogue) on the shear viscosity results, as can be observed the curves for DMSO/W-PEO8M$_{45:1}$ and DMSO/W-PEO4M$_{45:1}$ practically overlap. The present results indicate that the shear rheology depends mostly on the PDMS mixing ratio of the particles, rather than on PEO molecular weight.

The shear viscosity curve for the whole human blood is also represented in Fig. 9(b). For a wide range of shear rates, the base viscoelastic solution with PDMS particles 45:1 seems to match reasonably to that of the real human blood. Nevertheless, even when the viscous behaviour showed in the viscosity curves is close to the viscous behaviour of human blood, the elastic contribution can not be underestimated. In the following sections, uniaxial extensional flow
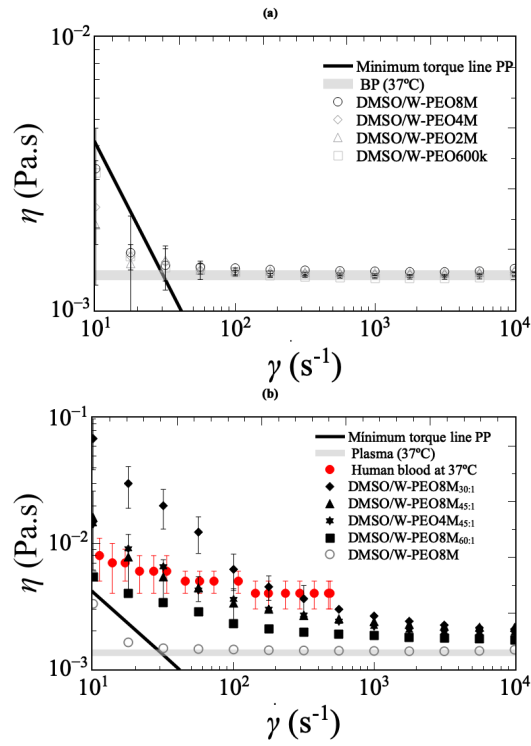
13

Figure 9: Steady shear viscosity curves at 20 °C. (a) Viscoelastic base solutions at different molecular weights of PEO in comparison with the viscosity of human blood plasma at 37°C Brust et al. [20], (b) shear viscosity for the viscoelastic base solution (DMSO/W-PEO8M) and the particulate viscoelastic solution with different PDMS mixing ratios of the added particles.

and microrheology experiments will be carried out to understand the elastic behaviour of the working fluids to be compared to that of the human blood and human blood plasma.

3.3. Extensional relaxation times

Figure 10 depicts the extensional relaxation time λ_e as a function of molecular weight M_w of polymer (PEO) used in our working fluids (see Table 1). The results are compared to those from human plasma and blood from literature, at 37 °C[20] and 21 °C [21]. Note that the very weak viscoelastic character of human plasma/blood obtained in Sousa et al. [21] contrasts with previous observations in Brust et al. [20]. The different experimental conditions, such as the concentration of anticoagulant used in blood collection may explain these significant differences according to Sousa et al. [21]. The results in Fig. 10 exhibit a power law dependence of λ_e upon the molecular weight M_w, in agreement with previous works for other polymeric solutions[50,51]. Moreover, the addition of the PDMS microparticles (around 42 vol%) to the plasma analogues does not modify substantially the results of λ_e without particles, different from what actually happens between plasma and whole blood, where RBCs contributed clearly in the increase of λ_e. Particles with RBC-like morphology may behave differently from their spherical counterparts concerning their physical performances (attachment, adhesion performance, orientation, etc.) giving rise to this different behaviour under an extensional flow.
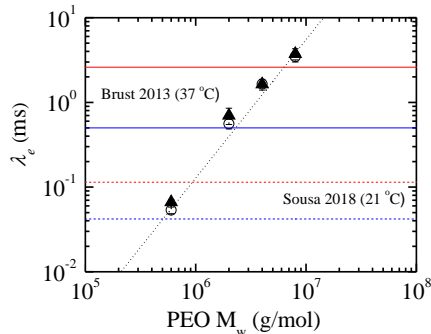

Figure 10: Extensional relaxation time λ_e versus M_w of PEO used. Viscoelastic base solutions (white circles) and particulated viscoelastic solutions (around 42% by volume of particles, black triangles). Lines depict the results of extensional relaxation time for human plasma (blue) and whole blood (red) from Brust et al. [20] (solid line) and Sousa et al. [21] (dash line). The experiments were conducted in air, at 22±2 °C. The dot line is the fitting $\lambda_e = 2 \times 10^{-11} M_w^{1.6342}$ to the experimental results without particles (with λ_e and M_w measured in ms and g/mol, respectively).

As it can be observed, the viscoelastic fluids prepared with PEO of M_w=4 MDa (4×10^6 g/mol) show the best agreement with the results for human plasma and blood presented in Brust et al. [20]. However, the working fluids with PEO of M_w=600 kDa (6×10^5 g/mol) match better the results from Sousa

et al. [21]. In spite of the different time scale and temperature, the breakup of the solution DMSO/W-PEO4M$_{45:1}$, previously showed in Fig. 5(b), is similar to that of human whole blood in Sousa et al. [21]. Therefore, the elasticity of the plasma and blood analogue fluids is tunable by means of the addition of PEO
315 with the suitable M_w, being able to adapt that elasticity for special cases, for example, the variation of the haematocrit by sickness[52].

3.4. Linear viscoelasticity

The diffusive behaviour of the polymer solutions (or plasma analogues) with increasing PEO molecular weight M_w was studied by quantifying the ran-
320 dom walk dynamics of embedded colloidal probe beads, characterised by the ensemble-averaged MSD i.e. a time-dependent quantity related to the diffusion coefficient D by $\langle \Delta r^2 \rangle = 2dD\tau$ in a Newtonian fluid [Fig. 11(a)]. At short timescales, the motion of the particles is sub-diffusive—i.e. the hallmark of viscoelastic behaviour—with power-law exponents lower than unity, consis-
325 tent with the values of longest relaxation time λ_e determined under uniaxial extensional flow: $\alpha_{8M} < \alpha_{4M} < \alpha_{2M} < \alpha_{600K} < 1$. The elastic response is due to the relaxation of the polymers in solution. With increasing PEO molecular weight the MSD decreases and the range of times with a sub-diffusive scaling exponent ($\alpha < 1$) becomes slightly wider, since the polymer coils take
330 longer to relax. The slope of the MSD then exhibits a crossover to diffusive behaviour as it increases to reach a value of unity ($\alpha \rightarrow 1$). At long times, away from the noise floor, the MSDs exhibit a linear trend as a function of lag time ($\alpha = 1$), indicating that the motion of the tracer particles is purely diffusive and the microenvironment surrounding them responds like a viscous (or
335 Newtonian) fluid. At such long timescales, particles are able to diffuse through the molecular network at rates limited by the viscosity η_0 of the complex fluid: $\eta_0^{8M} > \eta_0^{4M} > \eta_0^{2M} > \eta_0^{600K}$. Here, fitting the data to MSD $= 4D\tau$ (for $d = 2$) we obtain a diffusion coefficient, which can then be used to determine the zero-shear viscosity. Ensemble-averaged van Hove correlation functions of the microspheres
340 mixed in the polymer solutions for different values of lag time are well fit to a Gaussian (data not shown), indicating a homogeneous environment[53].

Figure 11(b) shows the viscoelastic moduli G' and G'' as a function of angular frequency ω over roughly two orders of magnitude in frequency. MPT measurements have been performed in the frequency range of 1–125 rad s^{-1}, where the
345 upper limit is given by the acquisition rate f of the camera. For all solutions and times/frequencies investigated it was found that $G'' > G'$ i.e. dissipation dominates storage in the exchange of thermal energy between the probe particles and the medium. It is worth noting that in the case of G', absolute values are in rather good agreement with those determined by Rodrigues and co-workers
350 from MPT measurements on actual plasma at a reference temperature of about 20°C (BP$_{ref}$)[22]. Conversely, they seem to diverge from those obtained at body temperature (BP$_{body}$). This mismatch in G'—i.e. in elasticity—shows that to more accurately model the frequency-dependent linear viscoelastic properties of human blood plasma at 37°C (body temperature) a slightly lower PEO molecu-
355 lar weight and/or concentration should suffice, with little to no solvent tweaking

16

(a)

(b)

(c)

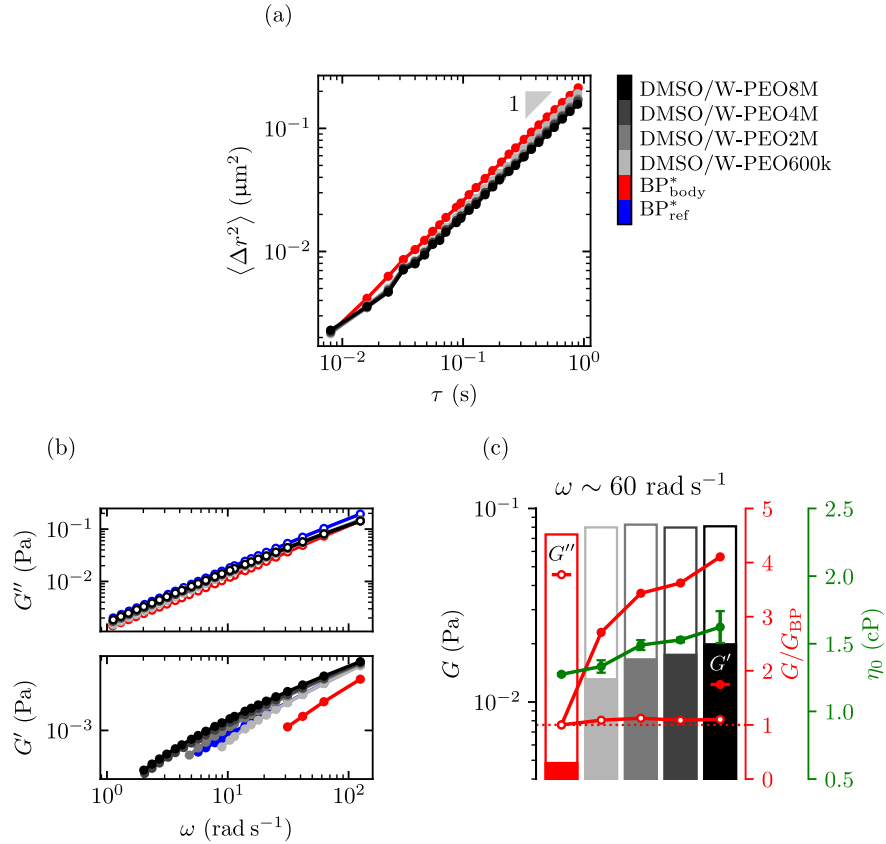$\omega \sim 60\ \mathrm{rad\,s^{-1}}$

Figure 11: Linear rheological response obtained from MPT microrheology for particles moving in artificial and (*) native blood plasma (BP) [22]. (a) Ensemble-averaged MSD as a function of lag time τ. The slope marker indicates the scaling $\left\langle \Delta r^2 \right\rangle \propto \tau$ at the purely viscous long-time limit of the MSDs. Error bars were not shown on MSD plots for clarity. The noise floor is roughly $10^{-4}\ \mu\mathrm{m}^2$ (not shown). Increasing PEO molecular weight results in decreased MSD of particles. (b) Real and imaginary parts of the inferred complex shear moduli G^* (lower and upper plots, respectively) by comparison with human plasma at 37 and 20℃ (red and blue datasets, respectively). (c) Comparison of absolute (black leftmost axis) and scaled (red middle axis) shear moduli at a fixed frequency ($\omega \sim 60\ \mathrm{rad\,s^{-1}}$), and viscosity (green rightmost axis). Increasing PEO molecular weight results in increased viscosity and shear-thinning behaviour.

required (namely of the DMSO-water mixture) in light of the quantitative agreement in G'' already expected from the viscosity curves. Such agreement becomes more apparent by plotting G''/G''_{BP} at a given frequency [Fig. 11(c), red middle axis], with values approaching unity (dotted line) for all PEO molecular weights. The zero-shear viscosity η_0 of the polymer solutions has been determined using a wall-effect corrected form of the classic Stokes–Einstein equation evaluated at the purely viscous long-time slope ($\tau \sim 1$ s) of the MSDs [Fig. 11(c), green rightmost axis][22]. At about 1.5 times that of water, the viscosity values obtained from MPT microrheology are consistent with steady shear rheology using a rotational rheometer. The specific viscosity $\eta_{\mathrm{sp}} = \eta_0/\eta_{\mathrm{s}} - 1$ scales as $\eta_{\mathrm{sp}} \propto M_{\mathrm{w}}^{0.57\pm0.16}$, where $\eta_{\mathrm{s}} \sim 1.30$ cP is the solvent viscosity (at 20℃) and the exponent is obtained from a power-law fit to the data (not shown). All in all, a general qualitative agreement is found between the frequency behaviour of the four PEO solutions formulated and that reported in the literature for native blood plasma[22]. As far as matching the linear viscoelastic response of the biofluid at body temperature goes, the moduli of the $M_{\mathrm{w}} = 600$ kDa PEO solution makes it the best candidate for a rheological analogue; this is in line with the shear viscosity measurements [Fig. 9(a)]. Bear in mind, though, that different relaxation times have been reported for blood plasma, possibly a consequence of the ratio and type of anticoagulant used in the blood collection[20,21] (see also Fig. 10).

3.5. Cell-free layer (CFL) in a microfluidic channel

As previously mentioned, the use of microparticles in blood analogue fluids has demonstrated to be essential to reproduce multiphase effects taking place in the human microcirculatory system, such as the cell-free layer (CFL) phenomena. The flow of the plasma analogue fluid (DMSO/W-PEO4M) with a 20% by volume of PDMS microparticles (45:1) was analyzed through a microfluidic channel with a important constriction, to simulate a microstenosis, and the results were compared with those of human blood[54], also with a concentration of 20% by volume of RBCs. Figure 12-a shows the design of the microfluidic device used in this study, the same as that used in Rodríguez-Villarreal et al.[54] to study the effect of temperature and the flow rate on the cell-free area. For the flow rates (Q) used in the *in vitro* experiments, this geometry gave rise to a high shear rates of around 10^4 s^{-1}, and allowed one to get a wide free layer of particles due to the flow inertia. RBCs are subjected to similar shear rates in physiological conditions in the smallest and atherosclerotic arteries[55]. Images of the flow i n t he i nterest a rea (red r ectangle) w ere t aken b y u sing a high-speed camera (Photron, Fastcam Mini UX50) equipped with the corresponding lenses, and an optical fibre light source. During the flow experiments through our PDMS microchannel (microstenosis), sedimentation was not observed, but the contraction was partially blocked after around ten minutes in most of the experimental runs. Please, note that the concentration of particles is relatively high for this type of CFL studies (see[1] and references therein).

Figure 12 shows the results for RBCs suspended in plasma [Figure 12(b)][54] and PDMS (ratio 45:1) particles in the plasma analogue (DMSO/W-PEO4M)

18

(a)

Flow direction

400 μm

35 μm

30 μm

600 μm

4 cm

800 μm

4 cm

(b)

46 μm

46 μm

150 μm

27 μm

(c)

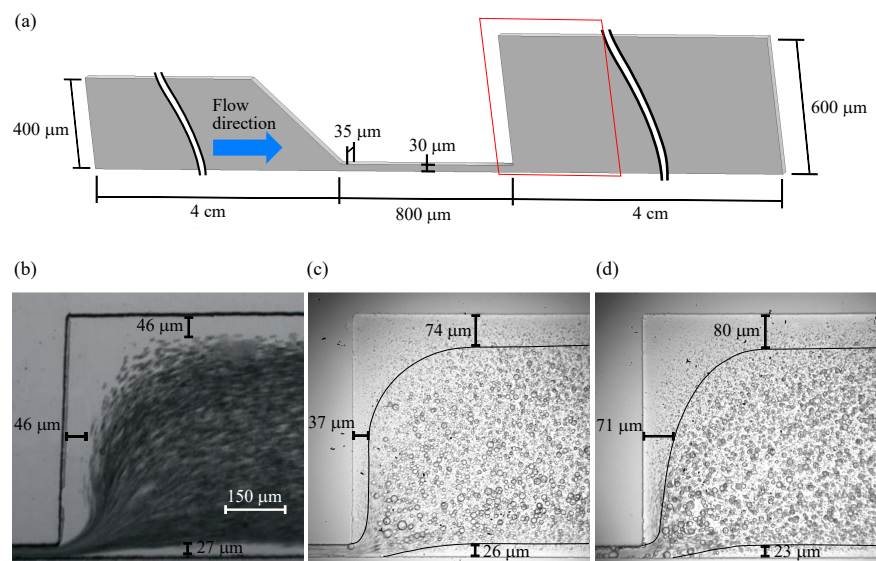74 μm

37 μm

26 μm

(d)

80 μm

71 μm

23 μm

Figure 12: Cell(particle) free layer (CFL/PFL) effect in a microfluidic channel designed from Rodríguez-Villarreal et al.[54]. (a) Schematic representation of the microfluidic channel. The red rectangle marks the window used in the experiments (b), (c), and (d). (b) Image of RBCs suspended in plasma at a concentration of 20% by volume, at 27 °C, and at Q=6 ml/h of flow rate[54] (in Rodríguez-Villarreal et al.[54], results for 27 and 37 °C were similar). (c) and (d) images of PDMS 45:1 particles in the plasma analogue DMSO/W-PEO4M at a concentration of around 20% by volume, at room temperature, and at Q=6 and 12 ml/h, respectively. The solid lines in (c) and (d) are guides to the eye, marking the free area of particles with diameters higher than 6 μm (sizes similar to RBCs). Figure (b) reproduced from Rodríguez-Villarreal et al.[54] with permission from MDPI.

19

[Figure 12(c) and (d)]. The solid lines in (c) point out the free area of particles with diameters higher than 6 μm (sizes similar to RBCs). It should be noted that the size distribution $\mathcal{P}$ of our PDMS particles is much wider than that of RBCs, see Fig. 8 (left). It was more difficult to move the smallest particles (sizes similar to platelets) to the center of the stream, but most of the particles were in the area marked with the solid lines. For that reason, the attention was focused on the particles with sizes similar to RBCs. The particulate blood analogue (plasma analogue + 20% of PDMS particles) exhibits a clear area or layer free of PDMS particles, showing a good agreement with the results for RBCs in plasma. For a higher flow rate Q=12 ml/h, as expected, the particle free area increased [see Fig. 12(d)], and, in this case, a layer completely free of particles can be seen, of around 10 μm from the walls.

3.6. Droplet impact behaviour onto a solid surface

A macroscale application in the field of Forensic Science is also presented in this manuscript, concerning the impact of the blood analogue droplets onto a solid surface for bloodstain pattern analysis. Recently, an experimental study concluded that the use of deformable particles rather than rigid particles in blood simulants was highly recommended to better reproducibility of human blood spreading and splashing behaviour in droplet impact for bloodstain pattern analysis[5].

Following the experimental procedure described in Yokoyama et al.[5], experiments of droplet impact of the proposed blood analogue DMSO/W-PEO4M$_{45:1}$ were conducted. The results were compared to those of dog blood (similar to human blood)[5]. It should be noted that the blood analogue fluid has been developed to match the blood properties at 37 °C (body temperature) while it is used at room temperature, whereas, in the literature of this field, the impact of blood droplets is studied at 20 °C. Thus, the physical blood properties vary considerably, specially viscosity, and therefore Reynolds number (Re). In fact, the cooling of blood drops in flight and during impact has never been addressed in the context of bloodstain patterns analysis[56]. Drop in-flight atomization, impact spreading and splashing should be affected by the temperature of the fluid, and probably, in most of the cases, the temperature might be near to 37 rather than 20 °C, because the spatter originates from blood at body temperature, but this issue is out of the scope of this work.

Briefly, the proposed blood analogue fluid was injected slowly through a steel capillary (1.27 mm in outer diameter) forming a pendant drop that eventually detached under its own weight. The capillary could be displaced along a vertical support to control the height over the target substrate, and consequently the normal impact velocity V (between 2 and 4 m/s). The target substrate consists of a clean glass slide with a typical root-mean-square roughness of a few nanometres. Bottom-view and side-view images of the drop impact were taken by using a high-speed camera (Photron, Fastcam SA5) at 10,000 and 150,000 frames per second, respectively. More details of the experimental procedure can be found in Yokoyama et al.[5]. Figure 13 shows the good agreement for the

20

evolution of spreading radius R_t of dog's whole blood[5] and the blood particulate analogue fluid DMSO/W-PEO4M$_{45:1}$ for Weber number, We, around 200, $We = \rho R_0 V^2/\gamma$, where ρ is the density, R_0 the initial radius of the impacting drop, V the normal velocity of impact of the drop, and γ the surface tension. A crucial parameter for reconstructing a crime scene through bloodstain pattern analysis is the spreading factor R_{max}/R_0, and the result of our blood analogue is similar to that of whole blood.
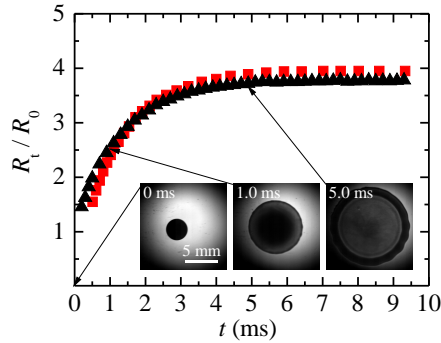

Figure 13: Time evolution of spreading radius R_t of dog's whole blood (red squares,[5]) and the blood particulate analogue fluid DMSO/W-PEO4M$_{45:1}$ (black triangles), with We around 200 in both cases. $t = 0$ is the time at which the droplet contacts the solid surface. The insets are bottom-view images of the impacting droplet at different times.

Figure 14 compares the splashing of dog's whole blood (a) from Yokoyama et al.[5] to our blood particulate analogue fluid DMSO/W-PEO4M$_{45:1}$ (b) for a higher We of around 600. In the case of real blood, a clear and typical Corona splash is observed in the images, which normally takes places for a Ohnesorge number Oh, $Oh = \mu/\sqrt{\rho R_0 \gamma}$, above 0.0062 (relatively viscous liquids)[5]. The splashing of our blood analogue could be also considered as Corona splash, although without a clear lift-off of the lamella. As aforementioned, our fluid was developed to match the blood properties at 37 °C, and its Oh is around 0.008, near to the transition from Corona to prompt splash, what may explain the different behaviour between both droplet impacts. Furthermore, the transfer of momentum between particles is suppressed by the high capacity to deform of our PDMS particles (similar to RBCs) and no particle ejection was expected/obtained (tiny-splashing) different from blood simulant containing rigid particles[5].

Our results show the potential of our developed fluid to be used as blood simulant in Forensic Science, taking into account the fluid body temperature in the droplet impact for bloodstain pattern analysis, Fig. 14(b) illustrates this application.
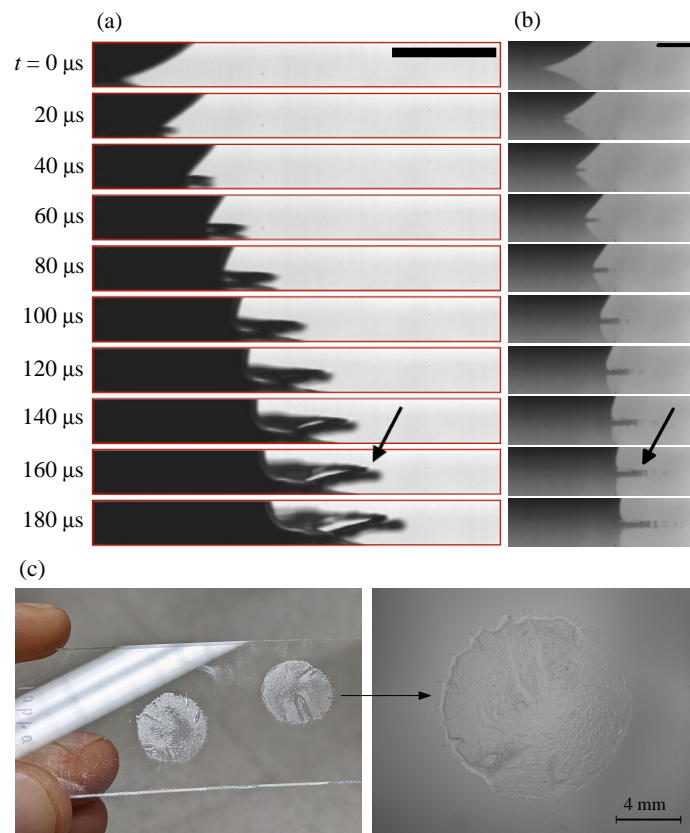
21

Figure 14: Side-view images of impacting droplets of dog's whole blood (a), from Yokoyama et al. [5], and our blood particulate analogue fluid DMSO/W-PEO4M$_{45:1}$ (b), at We around 600. The arrows point out the splashing. The scale bar in (a) and (b) correspond to 1 mm. (c) Images of the dry stain, after the evaporation of the analogue plasma, for bloodstain pattern analysis. Figure (a) reproduced from Yokoyama et al. [5] with permission from Elsevier.

4. Conclusions

A novel particulate blood analogue fluid able to reproduce rheological and some physiological characteristics of real human blood at body temperature was developed. The blood analogue is based on a viscoelastic solution, able to reproduce the rheological behavior of blood plasma, with deformable PDMS particles at a concentration similar to the human haematocrit. The general mechanical deformability of RBCs were captured by an intelligent fabrication of simple spherical PDMS particles, used in this work as RBC templates. The improvement of the monodispersity of those PDMS particles, while keeping the high production rate, is desirable to match the size distribution of RBCs, and continues to be a grand challenge (see[1] and references therein).

The shear rheology of the blood analogue only depends significantly on the PDMS particle composition, being the solution with particles of PDMS 45:1 the best agree with human blood viscous behaviour. The elastic behaviour under uniaxial extensional flow of the blood analogues DMSO/W-PEO4M$_{45:1}$ and DMSO/W-PEO600K$_{45:1}$ agree with the results of Brust et al.[20] and Sousa et al.[21], respectively. The elasticity of the developed plasma analogue can be adjusted to the results of human plasma from Brust et al.[20] or Sousa et al.[21] by means of the addition of PEO with the suitable M_w, among others special conditions (sickness). The viscoelastic moduli of the plasma analogues obtained by means of passive microrheology are in good agreement with the results of the steady shear experiments, indicating that the DMSO/W-PEO600k solution is a fairly good candidate for mimicking the non-Newtonian behaviour of blood plasma at body temperature.

The flow of the particulate blood analogue fluid DMSO/W-PEO4M$_{45:1}$ through a narrow microchannel reproduced the CFL phenomena, showing its potential for the *in vitro* study of multiphase flow effects in the microcirculatory system. On the other hand, its application in bloodstain pattern analysis is promising and it would allow to consider the fluid body temperature in the droplet impact, while working at room temperature.

It is worthy to point out that the developed blood analogues just present similar rheological behavior with blood flow under certain flow conditions. The purpose of this study is to look for a replacement solution able to reproduce specific flow characteristics with the aim to understand the features found in the human circulatory system due to the viscoelastic properties of blood (microscale and confinement characteristics) and/or for other technical purposes as the analysis of some patterns due to a blood drop impact (macroscale without confinement). The physiological functions of these blood analogues are out of the scopes of this work. Moreover, the rheological differences in terms of viscosity and elasticity can be adjusted varying the amount of polymer and mixing ratios of the solvent, as well as the concentration of the PDMS particles to adjust them to any specific situation (temperature, level of hematocrit, . . .). Nevertheless, any comparison with real blood flow has to be made with criticism as many rheological characteristics of blood as thixotropy of yield stress are even not reproduced in these analogues.

23

Author contributions

E.J.V. and L.C.D. conceptualization, formal analysis, writing, reviewing and editing, funding acquisition and supervision; A.R. experimental data, writing; M.L. experimental data; T.R. multiple particle tracking data, writing.

Conflicts of interest

There are no conflicts to declare.

Acknowledgements

References

[1] S. H. Sadek, M. Rubio, R. Lima, E. J. Vega, Blood particulate analogue fluids: A review, Materials 14 (2021) 2451.

[2] M. Belenkovich, J. Sznitman, N. Korin, Micro-particle entrapment dynamics in microfluidic pulmonary capillary networks, J. Biomech. 137 (2022) 111082.

[3] N. Doshi, A. S. Zahr, S. Bhaskar, J. Lahann, S. Mitragotri, Red blood cell-mimicking synthetic biomaterial particles, PNAS 106 (2009) 21495–21499.

[4] C. L. Modery-Pawlowski, L. L. Tian, V. Pan, A. Sen Gupta, Synthetic approaches to rbc mimicry and oxygen carrier systems, Biomacromolecules 14 (2013) 939–948. PMID: 23452431.

[5] Y. Yokoyama, A. Tanaka, Y. Tagawa, Droplet impact of blood and blood simulants on a solid surface: Effect of the deformability of red blood cells and the elasticity of plasma, Forensic Sci. Int. 331 (2021) 111138.

[6] G. Ciasca, M. Papi, S. Di Claudio, M. Chiarpotto, V. Palmieri, G. Maulucci, G. Nocca, C. Rossi, M. De Spirito, Mapping viscoelastic properties of healthy and pathological red blood cells at the nanoscale level, Nanoscale 7 (2015) 17030–17037.

[7] J. Liu, Y. Han, W. Hua, Y. Wang, G. You, P. Li, F. Liao, L. Zhao, Y. Ding, Improved flowing behaviour and gas exchange of stored red blood cells by a compound porous structure, Artif. Cell. Nanomed. B. 47 (2019) 1888–1897.

[8] S. Barns, M. A. Balanant, E. Sauret, R. Flower, S. Saha, Y. Gu, Investigation of red blood cell mechanical properties using afm indentation and coarse-grained particle method, BioMed. Eng. OnLine 16 (2017) 140.

[9] I. M. Lamzin, R. Khayrullin, The quality assessment of stored red blood cells probed using atomic-force microscopy, Anat. Res. Int. 2014 (2014) 869683.

[10] K. E. Bremmell, A. Evans, C. A. Prestidge, Deformation and nano-rheology of red blood cells: An afm investigation, Colloid Surf. B-Biointerfaces 50 (2006) 43–48.

[11] I. Dulińska, M. Targosz, W. Strojny, M. Lekka, P. Czuba, W. Balwierz, M. Szymoński, Stiffness of normal and pathological erythrocytes studied by means of atomic force microscopy, J. Biochem. Biophys. Methods 66 (2006) 1–11.

[12] D. Pinho, B. N. Muñoz-Sánchez, C. F. Anes, E. J. Vega, R. Lima, Flexible pdms microparticles to mimic rbcs in blood particulate analogue fluids, Mech. Res. Commun. 100 (2019) 103399.

[13] M. López, M. Rubio, S. H. Sadek, E. J. Vega, A simple emulsification technique for the production of micro-sized flexible powder of polydimethylsiloxane (pdms), Powder Technol. 366 (2020) 610–616.

[14] J. Carneiro, R. Lima, J. B. L. M. Campos, J. M. Miranda, A microparticle blood analogue suspension matching blood rheology, Soft Matter 17 (2021) 3963–3974.

[15] A. Rubio, S. Rodríguez, M. G. Cabezas, Capabilities and limitations of fire-shaping to produce glass nozzles, Materials 13 (2020) 5477.

[16] L. Vilas-Boas, V. Faustino, R. Lima, J. M. Miranda, G. Minas, C. S. Veiga-Fernandes, S. Oliveira-Catarino, Assessment of the deformability and velocity of healthy and artificially impaired red blood cells in narrow polydimethylsiloxane (pdms) microchannels, Micromachines 9 (2018) 384.

[17] V. Faustino, S. O. Catarino, D. Pinho, R. Lima, G. Minas, A passive microfluidic device based on crossflow filtration for cell separation measurements: a spectrophotometric characterization, Biosensors 8 (2018) 125.

[18] A. Rubio, V. Faustino, M. G. Cabezas, R. Lima, E. J. Vega, Fire-shaped cylindrical glass micronozzles to measure cell deformability, J. Micromech. Microeng. 29 (2019) 105001.

25

[19] R. G. Lebel, D. A. I. Goring, Density, viscosity, refractive index, and hygroscopicity of mixtures of water and dimethyl sulfoxide, J. Chem. Eng. 7 (1962) 100–101.

[20] M. Brust, C. Schaefer, R. Doerr, L. Pan, M. Garcia, P. E. Arratia, C. Wagner, Rheology of Human Blood Plasma: Viscoelastic Versus Newtonian Behavior, Phys. Rev. Lett. 110 (2013) 078305.

[21] P. C. Sousa, R. Vaz, A. Cerejo, M. S. N. Oliveira, M. A. Alves, F. T. Pinho, Rheological behavior of human blood in uniaxial extensional flow, J. Rheol. 62 (2018) 447–456.

[22] T. Rodrigues, R. Mota, L. Gales, L. Campo-Deaño, Understanding the complex rheology of human blood plasma, J. Rheol. 66 (2022) 761–774.

[23] T. Kenner, The measurement of blood density and its meaning, Basic Res. Cardiol. 84 (1989) 111–124.

[24] H. Hocheng, C. M. Chen, Y. C. Chou, C. H. Lin, Study of novel electrical routing and integrated packaging on bio-compatible flexible substrates, Microsyst. Technol. 16 (2010) 423–430.

[25] C. Ferrera, J. M. Montanero, M. G. Cabezas, An analysis of the sensitivity of pendant drops and liquid bridges to measure the interfacial tension, Meas. Sci. Technol. 18 (2007) 3713–3723.

[26] J. Rosina, E. Kvašňák, D. Šuta, H. Kolářová, J. Málek, L. Krajči, Temperature dependence of blood surface tension, Physiol. Res. 56 (Suppl. 1) (2007) S93–S98.

[27] S. S. Yadav, B. S. Sikarwar, P. Ranjan, R. Janardhanan, A. Goyal, Surface tension measurement of normal human blood samples by pendant drop method, J. Med. Eng. Technol. 44 (2020) 227–236.

[28] T. Rodrigues, F. J. Galindo-Rosales, L. Campo-Deaño, Haemodynamics around confined microscopic cylinders, J. Non-Newton. Fluid Mech. 286 (2020) 104406.

[29] P. C. Sousa, J. Carneiro, R. Vaz, A. Cerejo, F. T. Pinho, M. A. Alves, M. S. N. Oliveira, Shear viscosity and nonlinear behavior of whole blood under large amplitude oscillatory shear, Biorheology 50 (2013) 269–282.

[30] E. D. Coninck, F. H. Marchesini, V. Vanhoorne, T. D. Beer, C. Vervaet, Viscosity of api/fatty acid suspensions: Pitfalls during analysis, Int. J. Pharm. 584 (2020) 119447.

[31] P. C. Sousa, E. J. Vega, R. G. Sousa, J. M. Montanero, M. A. Alves, Measurement of relaxation times in extensional flow of weakly viscoelastic polymer solutions, Rheol. Acta 56 (2017) 11–20.

[32] L. Campo-Deaño, C. Clasen, The slow retraction method (SRM) for the determination of ultra-short relaxation times in capillary breakup extensional rheometry experiments, J. Non-Newtonian Fluid Mech. 165 (2010) 1688–1699.

[33] C. Ferrera, M. G. Cabezas, J. M. Montanero, An experimental analysis of the linear vibration of axisymmetric liquid bridges, Phys. Fluids 18 (2006) 082105.

[34] E. J. Vega, J. M. Montanero, J. Fernández, On the precision of optical imaging to study free surface dynamics at high frame rates, Exp. Fluids 47 (2009) 251–261.

[35] A. V. Bazilevsky, V. M. Entov, A. N. Rozhkov, Liquid filament microrheometer and some of its applications, volume 1 of *Proocedings of Third European Rheology Conference and Golden Jubilee Meeting of the British Society of Rheology*, Oliver DR (ed), pp. 41–43.

[36] T. A. Waigh, Microrheology of complex fluids, Rep. Prog. Phys. 68 (2005) 685–742.

[37] T. G. Mason, D. A. Weitz, Optical Measurements of Frequency-Dependent Linear Viscoelastic Moduli of Complex Fluids, Phys. Rev. Lett. 74 (1995) 1250–1253.

[38] T. G. Mason, Estimating the viscoelastic moduli of complex fluids using the generalized Stokes–Einstein equation, Rheol. Acta 39 (2000) 371–378.

[39] J. C. Crocker, D. G. Grier, Methods of Digital Video Microscopy for Colloidal Studies, J. Colloid Interface Sci. 179 (1996) 298–310.

[40] E. M. Furst, T. M. Squires, Microrheology, Oxford Univ. Press, New York, US, 2017.

[41] T. Savin, P. S. Doyle, Statistical and sampling issues when using multiple particle tracking, Phys. Rev. E 76 (2007) 021501.

[42] T. Savin, P. S. Doyle, Static and Dynamic Errors in Particle Tracking Microrheology, Biophys. J. 88 (2005) 623–638.

[43] Rheological characterization of poly(ethylene oxide) solutions of different molecular weights, J. Colloid Interface Sci. 336 (2009) 360–367.

[44] D. Gilbert, R. Valette, E. Lemaire, Impact of particle stiffness on shear-thinning of non-brownian suspensions, J. Rheol. 66 (2022) 161–176.

[45] A. Papadopoulou, J. J. Gillissen, H. J. Wilson, M. K. Tiwari, S. Balabani, On the shear thinning of non-brownian suspensions: Friction or adhesion?, J. Non-Newton. Fluid Mech. 281 (2020) 104298.

[46] Rheology and migration of deformable particles in dense suspensions, Classical Physics [physics.class-ph] Université Grenoble Alpes (2021).

[47] M. M. Villone, P. L. Maffettone, Dynamics, rheology, and applications of elastic deformable particle suspensions: a review, Rheol. Acta 58 (2019) 109–130.

[48] D. Gilbert, R. Valette, E. Lemaire, Impact of particle stiffness on shear-thinning of non-brownian suspensions, J. Rheol. 66 (2022) 161–176.

[49] L. F. Chiara, M. E. Rosti, F. Picano, L. Brandt, Suspensions of deformable particles in poiseuille flows at finite inertia, Fluid Dyn. Res. 52 (2020) 065507.

[50] F. Berzin, B. Vergnes, L. Delamare, Rheological behavior of controlled-rheology polypropylenes obtained by peroxide-promoted degradation during extrusion: Comparison between homopolymer and copolymer, J. Appl. Polym. Sci. 80 (2001) 1243–1252.

[51] J. F. Vega, S. Rastogi, G. W. M. Peters, H. E. H. Meijer, Rheology and reptation of linear polymers. ultrahigh molecular weight chain dynamics in the melt, J. Rheol. 48 (2004) 663–678.

[52] D. Pinho, L. Campo-Deaño, R. Lima, F. T. Pinho, In vitro particulate analogue fluids for experimental studies of rheological and hemorheological behavior of glucose-rich rbc suspensions, Biomicrofluidics 11 (2017) 054105.

[53] M. T. Valentine, P. D. Kaplan, D. Thota, J. C. Crocker, T. Gisler, R. K. Prud'homme, M. Beck, D. A. Weitz, Investigating the microenvironments of inhomogeneous soft materials with multiple particle tracking, Phys. Rev. E 64 (2001) 061506.

[54] A. I. Rodríguez-Villarreal, M. Carmona-Flores, J. Colomer-Farrarons, Effect of temperature and flow rate on the cell-free area in the microfluidic channel, Membranes 11 (2021) 109.

[55] K. S. Sakariassen, L. L. Orning, V. T. Turitto, The impact of blood shear rate on arterial thrombus formation, Future Sci. OA 1 (2015) FSO30.

[56] P. M. Comiskey, A. L. Yarin, S. Kim, D. Attinger, Prediction of blood back spatter from a gunshot in bloodstain pattern analysis, Phys. Rev. Fluid 1 (2016) 043201.

28

6. Paper III - A particulate blood analogue based on artificial viscoelastic blood plasma and RBC-like microparticles at a concentration matching the human haematocrit.

7

Paper IV - Influence of the gas viscosity on the stability of flow focusing.

Influence of the gas viscosity on the stability of flow focusing

A. Rubio,[1] B. N. Muñoz-Sánchez,[1] M. G. Cabezas,[1] and J. M. Montanero[1]

[1]*Depto. de Ingeniería Mecánica, Energética y de los Materiales and*
Instituto de Computación Científica Avanzada (ICCAEx),
Universidad de Extremadura, E-06006 Badajoz, Spain

We measure the minimum liquid flow rate $Q_{\min}$ to produce steady jetting in gaseous flow focusing with orifices of diameters down to 30 μm. We compare the results obtained for different diameters and liquids. Using dimensional analysis, we determine the influence of the gas viscosity on this stability limit. For low and moderately low-viscosity liquids, there is an optimum value of the gas viscosity for which $Q_{\min}$ reaches its lowest value. This optimum value leads to the minimum jet diameter in front of the discharge orifice.

The controlled production of tiny fluid entities such as drops, bubbles, emulsions, and capsules has been extensively investigated over the last decades because of its enormous relevance for a great variety of applications. Tip streaming is an adequate candidate for this purpose because it allows reducing the size of those entities to the micrometer scale with much larger orifices. Extensional coflows produce tip streaming through the pressure and viscous forces exerted by an outer stream, which stretches the interface until a small jet is emitted from its tip [1–4]. The jet breaks up due to the capillary Rayleigh instability, giving rise to quasi-monodisperse collections of droplets.

In gaseous flow focusing [5], a liquid is injected at a constant flow rate through a feeding capillary located in front of an orifice. A coflowing gas stream produces favorable pressure gradients and viscous stresses that sharpen the liquid meniscus attached to the feeding capillary and pull a thin jet from the meniscus tip. The original plate-orifice configuration [5–8] was adapted to focus the liquid current inside a converging nozzle [9]. This technique has proved to be useful for producing very thin and ultrafast liquid jets in a gaseous ambient. In fact, it has become the most successful way to introduce samples in Serial Femtosecond Crystallography (SFX) [10, 11], which has revolutionized the molecular determination of complex biochemical species from proteins to viruses. Different configurations have been explored for that purpose [12]. Mechanical disturbances can be applied to the jet to modulate the formation of droplets [13, 14], which extends the practical applications of gaseous flow focusing.

Experimental results have repeatedly shown that the energy per unit volume transferred to the liquid in the tapering meniscus of flow focusing is essentially determined by the pressure drop Δp applied to the gas stream and is practically independent of the injected flow rate Q [15]. The gas viscosity is supposed to play a secondary role. This means Δp essentially determines the jet velocity v_j at the discharge orifice ($v_j \sim \Delta p^{1/2}$) and, therefore, the jet diameter d_j scales as $Q^{1/2}$ ($Q \sim d_j^2 v_j \sim d_j^2 \Delta p^{1/2}$). We conclude that reducing the jet diameter, which is essential in most applications, requires reducing the liquid flow rate. However, there is a minimum value of this parameter for each experimental configuration below which the meniscus becomes unstable. This stability limit has been the subject of several works because of its importance at the technological level. The role played by the geometrical parameters, liquid properties, and applied pressure drop have been analyzed in detail (see, e.g., Refs. [6, 7]).

The effect of the gas viscosity on the meniscus stability has not been examined yet. This study is relevant because it allows one to gain insight into mechanisms responsible for the flow instability. In principle, one can analyze the influence of the gas viscosity by changing its value while keeping the rest of the parameters constant. However, this is not practical because the range of gas viscosities is small, even for very different temperatures. In fact, increasing the air viscosity in one order of magnitude requires increasing the temperature in two orders of magnitude, which is practically impossible. In this work, we miniaturize the plate-orifice flow focusing configuration and study the meniscus stability for different liquid viscosities. The dimensional analysis allows us to determine the effect of the gas viscosity as if this parameter were increased in one order of magnitude.

In our experiments, a feeding capillary was co-axially located at a distance H above a circular orifice of practically the same diameter D (Fig. 1a). The orifice is located at the upper face of a chamber. A liquid of density ρ_l and viscosity μ_l was injected at a constant flow rate Q through the capillary. The air stream of density ρ_g and viscosity μ_g crossed the orifice driven by the difference between the ambient pressure p_0 and the chamber pressure p_c. Due to the action of the air stream, a conical liquid meniscus formed with its triple contact line anchored to the feeding capillary edge. The meniscus was held by the surface tension σ. If the rest of the parameters are fixed, the liquid meniscus becomes unstable when the flow rate Q decreases below a minimum value $Q_{\min}$.

We fabricated plates with an orifice and feeding capillaries using Nanoscribe Photonic Professional GT2 with the Dip-in Laser Lithography (DiLL) configuration. The diameters were $D = 30$, 75, and 200 μm. The plate was mounted onto the cap of a discharge glass cell (Fig. 1b). The capillary was positioned above the plate orifice using a high-precision orientation-translation system. We established the pressure p_c inside the cell using a suction pump. The liquid was injected through the capillary
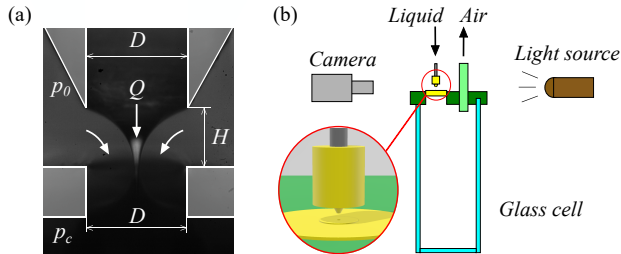
FIG. 1. (a) Sketch of the fluid configuration. The image corresponds to a silicone oil jet emitted with $\{D = 75\ \mu\text{m},\ Q = 0.17$ ml/h, $p_c = 850$ mbar$\}$, and (b) experimental setup.

with a syringe pump (LEGATO210, KD-SCIENTIFIC). A high enough flow rate Q was injected to produce steady jetting. Then, it was decreased in steps ΔQ until the meniscus became unstable. The minimum flow rate $Q_{\min}$ is calculated as the average of those of the last stable realization and the first unstable one. Images of the liquid meniscus were acquired using a high-speed video camera and white back-lighting. The jet diameter in front of the discharge orifice was measured with pixel resolution. We used n-hexane and several mixtures of water, glycerol, and silicone oils to adjust the viscosity and surface tension values. More details of the experimental method can be found in the Supplemental Material.

The main geometrical parameters affecting the meniscus stability are D and H. In all our experiments, $H = 0.6D$, which approximately corresponds to the optimum capillary-to-orifice distance [16]. Once the geometry has been fixed, the problem can be formulated in terms of the dimensional variables $\{D;\ Q,\ p_c;\ \rho_l,\ \mu_l,\ p_0,\ \rho_0,\ \mu_g,\ \sigma\}$. Using the liquid properties, D, and $U = Q/D^2$ as the characteristic quantities, we define dimensionless parameters

$$Ca = \frac{\mu_l U}{\sigma} = \frac{\mu_l Q}{D^2 \sigma}, \quad \text{Re} = \frac{\rho_l U D}{\mu_l} = \frac{\rho_l Q}{D\mu_l}, \quad \mu_r = \frac{\mu_g}{\mu_l}. \tag{1}$$

The compressibility and gas density effects are quantified by the dimensionless numbers

$$\frac{p_c}{p_0} \quad \text{and} \quad \frac{\rho_0}{\rho_l}, \tag{2}$$

respectively. The last dimensionless number is

$$C_\mu = \frac{\mu_l \Delta p^{1/2}}{\sigma \rho_l^{1/2}}, \tag{3}$$

which can be regarded as the capillary number defined in terms of the jet velocity $v_j \sim (\Delta p/\rho_l)^{1/2}$, where $\Delta p = p_0 - p_c$. The effect of gravity is negligible due to the smallness of fluid the configuration (the Bond number $B = (\rho_l - \rho_0)gD^2/\sigma < 0.01$ in practically all cases).

In our experiments, $\rho_0/\rho_l \simeq$ const. Therefore, this parameter does not play a significant role. We conducted our experiments in the incompressible regime

$(p_c/p_0 \simeq 1)$, which implies that the pressures p_0 and p_c only intervene in the problem through the pressure drop Δp. Typically, a few tens of mbars are required to produce steady jetting. The jet becomes convectively unstable [15] for sufficiently large values of Δp (within the incompressible regime). In this case, this parameter hardly affects the minimum flow rate $Q_{\min}$ [6, 7, 16] (Fig. 2). The jet capillary number C_μ is the only dimensionless parameter involving Δp. Therefore, C_μ does not affect the meniscus stability under the conditions mentioned above. Hereafter, we considered $\Delta p = 150$ mbar unless otherwise is stated.
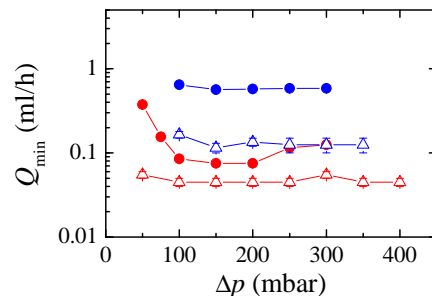

FIG. 2. $Q_{\min}$ as a function of Δp for a water-glycerol mixture (66-34% wt) and an orifice diameter $D = 75\ \mu$m (blue circles), a mixture of silicone oils of 1cSt and 5cSt (90-10% wt) and $D = 75\ \mu$m (red circles), a water-glycerol mixture (80-20% wt) and $D = 30\ \mu$m (blue triangles), a silicone oil of 1cSt and an orifice diameter $D = 30\ \mu$m (red triangles).

Taking into account the above considerations, the stability limit in the incompressible regime can be written as

$$f(Ca^*, \text{Re}^*, \mu_r) = 0 \tag{4}$$

where $Ca^* = \mu_l Q_{\min}/(D^2\sigma)$ and $\text{Re}^* = Q_{\min}\rho_l/(D\mu_l)$ are the capillary and Reynolds numbers defined in terms of $Q_{\min}$, respectively. The stability curve (4) was determined experimentally using a discharge orifice of diameter $D = 200\ \mu$m [7] (Fig. 3). Liquid viscosities in the interval $1 \lesssim \mu_l \lesssim 500$ mPa were considered to sweep several orders of magnitude the capillary and Reynolds numbers. Consequently, the viscosity ratio μ_r varied two orders of magnitude in those experiments. If we assume that the viscosity ratio μ_r does not significantly influence the meniscus stability, then that stability curve must be universal.

In this work, we reduced considerably the orifice diameter D with respect to that used in previous experiments (see, e.g., Refs. [6, 7]). Using this microflow focusing configuration and adjusting the flow rate, we obtained the same capillary and Reynolds numbers but with much less viscous liquids (much higher viscosity ratio). Specifically, the values of Ca and Re for $D = 30$ and $75\ \mu$m are similar to those obtained in Ref. [7] for liquids with viscosities up to one order magnitude higher than in the present work. Therefore, the comparison between the flow focusing and microflow focusing experiments for the same
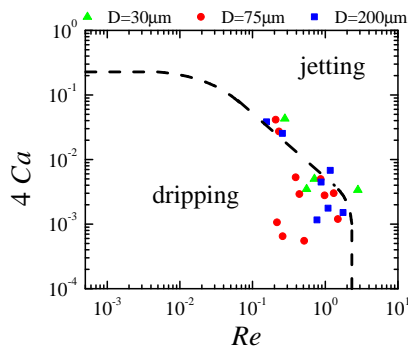
FIG. 3. Stable steady jetting realizations obtained in this work. The line represents the stability limit shown in Fig. 9 of Ref. [7].

capillary and Reynolds numbers allows us to observe the effect of the viscosity ratio. Figure 3 shows stable steady jetting realizations obtained for $D = 30$, 75, and 200 μm. For sufficiently small Ca, steady jetting was produced within the unstable region delimited in Ref. [7], which reveals the significant role played by the viscosity ratio μ_r.

The meniscus stability can also be formulated in terms of the capillary number Ca, the viscosity ratio μ_r, and the Ohnesorge number

$$\text{Oh} = \left(\frac{Ca}{\text{Re}}\right)^{1/2} = \frac{\mu_l}{(\rho_l \sigma D)^{1/2}}. \tag{5}$$

In this way, Ca is the only parameter involving the flow rate, which allows one to write the stability limit as

$$Ca^* = g(\text{Oh}, \mu_r). \tag{6}$$

If we reduce the characteristic length D with respect to that of previous experiments, we can obtain the same Ohnesorge numbers but with less viscous liquids (larger viscosity ratios). The comparison between the corresponding stability limits allows us to examine the effect of μ_r.

Figure 4 shows the critical capillary number as a function of the viscosity ratio for three values of the Ohnesorge number. Pure liquids and mixtures with approximately the same Oh value were used for different orifice diameters (see Supplemental Material). There are small variations of Oh in each case due to the difficulty in adjusting the surface tensions and liquid viscosities. Variations of up to one order of magnitude in the viscosity ratio were obtained by reducing the orifice diameter. For Oh = 0.017 and 0.039, the viscosity ratio affects the stability limit in the entire the range of μ_r explored in our experiments. The critical capillary number reaches a minimum value around $\mu_r = 0.035$ and 0.015 for Oh = 0.017 and 0.039, respectively.

The critical capillary number does not considerably depend on μ_r for the viscous case Oh = 0.19. These results can also be observed in Fig. 3: the value of Ca^* can be significantly decreased below the previous stability limit for sufficiently small values of Ca, while this does not occur for larger values of this parameter. It must be noted that the range of the viscosity ratio explored for Oh = 0.19 is much smaller than in the other two cases, which may explain why the variations of Ca^* are much smaller as well. Considering larger viscosity ratios for Oh = 0.19 requires considerably reducing the orifice diameter below 30 μm, which constitutes a formidable task.

The critical capillary number Ca^* and viscosity ratio μ_r are the only parameters involving the minimum flow rate $Q_{\min}$ and the gas viscosity μ_g, respectively. This allows us to interpret Fig. 4 in dimensional terms as follows. Consider a flow focusing realization with a given ejector and focused liquid. The orifice diameter D and liquid properties μ_l and σ are fixed. We change only the viscosity μ_g of the focusing gas. In this case, Oh is fixed, Ca^* equals $Q_{\min}$ multiplied by a constant factor $\mu_l/(D^2\sigma)$, and μ_r equals μ_g divided by the constant value μ_l. As applied to this example, Fig. 4 shows the dependence of $Q_{\min}$ on μ_g except for constant scale factors in the axes Ca^* and μ_r. This interpretation of Fig. 4 allows us to conclude that, for low and moderate liquid viscosities (Ohnesorge numbers up to 10^{-2}), there is an optimum value of μ_g for which $Q_{\min}$ reaches its lowest value. For instance, if water is focused with an orifice of 75 μm in diameter, the optimum gas viscosity is around 0.035 mPa·s, almost twice the air viscosity. The optimum gas viscosity would lead to a reduction of around 100% of the minimum flow rate.

Figure 5 compares the "dimensionless shape" (the shape in terms of D) of the liquid meniscus when all the dimensionless parameters take the same values except for the viscosity ratio μ_r. As occurs with the critical capillary number, the meniscus shape exhibits a non-monotonous dependence on the viscosity ratio: the shape is practically the same for the two extreme values of μ_r, while the meniscus thins for the optimum viscosity ratio. This means that the dimensionless strain rate $v_j/H (U/D)^{-1} \sim (D/d_j)^2$ is larger for the optimum viscosity ratio. This result confirms the existence of an optimum gas viscosity leading to the most efficient transfer of momentum to the liquid.

Finally, we compare the meniscus shapes at the corresponding critical capillary numbers (minimum flow rates) in Fig. 6. The optimum viscosity ratio allows the maximum reduction of the capillary number and, therefore, it leads to the maximum liquid dimensionless acceleration, i.e., the minimum value of d_j/D. This effect can also be observed in Fig. 7, which shows $d_{j\min}/D$ (i.e., d_j/D for $Q = Q_{\min}$) for Oh = 0.017 and 0.039 as a function of the viscosity ratio μ_r. The scatter of the data is partially caused by C_μ variations, which do not significantly alter the meniscus stability but affect the jet diameter.

We have verified that the jet diameter approximately follows the classical scaling law $d_j \sim Q^{1/2}$ independently of the viscosity ratio. This result allows us to conclude
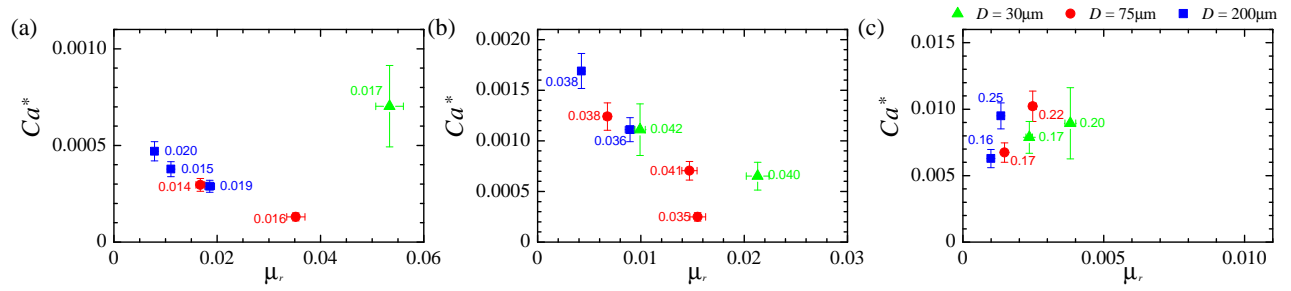
FIG. 4. Ca^* as a function of the viscosity ratio μ_r for (a) Oh $= 0.017 \pm 0.003$, (b) Oh $= 0.039 \pm 0.004$ and (c) Oh $= 0.19 \pm 0.05$. The labels indicate the Ohnesorge number.
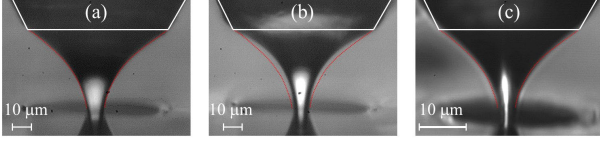
FIG. 5. Meniscus shape for {Oh = 0.038 ± 0.003, $C_\mu = 0.235$, $Ca = 1.3 \times 10^{-3}$}, and (a) $\mu_r = 6.75 \times 10^{-3}$, (b) $\mu_r = 1.55 \times 10^{-2}$, and (c) $\mu_r = 2.13 \times 10^{-2}$. The pressure difference Δp was adjusted to produce the same C_μ. The orifice diameter is 75 μm in (a) and (b), and 30 μm in (c). The images have been scaled so that the orifice has approximately the same diameter. The red line indicates the shape of the meniscus (a).
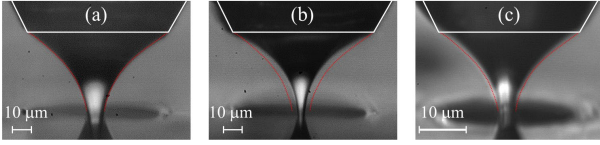
FIG. 6. Meniscus shape of the last stable realization for {Oh = 0.038 ± 0.003, $C_\mu = 0.235$}, and (a) {$\mu_r = 6.75 \times 10^{-3}$, $Ca = 1.3 \times 10^{-3}$} (b) {$\mu_r = 1.55 \times 10^{-2}$, $Ca = 3 \times 10^{-4}$}, and (c) {$\mu_r = 2.13 \times 10^{-2}$, $Ca = 7 \times 10^{-4}$}. The pressure difference Δp was adjusted to produce the same C_μ. The orifice diameter is 75 μm in (a) and (b), and 30 μm in (c). The images have been scaled so that the orifice has approximately the same diameter. The red line indicates the shape of the meniscus (a).

that for $D = 75$ μm and water (experimental conditions typically considered in SFX), the minimum jet diameter $d_{j\min}$ for $\mu_g = 0.035$ mPas is around half of the corresponding value for air. Viscous gases such as neon ($\mu_g = 0.032$ mPa·s) approximately satisfy this condition. Therefore, the use of these gases in incompressible flow focusing may result in much thinner jets maintaining the same orifice diameter.

If the liquid flow rate Q_D^* dragged across the boundary layer next to the interface is of the order of the injected flow rate Q, then two recirculation cells appear in the liquid meniscus. It has been hypothesized that the growth of such recirculation cells causes the flow focusing instability for low-viscosity liquids. In other words, the liquid meniscus becomes unstable as Q_D^*/Q exceeds a critical value [7, 17].

Based on the above hypothesis, we rationalize our experimental results from the following scaling analysis. The liquid flow rate dragged across the boundary layer next to the interface is $Q_D^* \sim v_s[R_s^2 - (R_s - \delta_l)^2]$, where v_s, R_s, and $\delta_l \sim (D\mu_l/\rho_l v_s)^{1/2}$ are characteristic values of the velocity on the free surface, the free surface radius, and the liquid boundary layer thickness, respectively (Fig. 8). It can readily be seen that $Q_D^* \sim Q_D(2R_s/\delta_l - 1)$, where $Q_D \equiv D\mu_l/\rho_l$ is the characteristic flow rate used in previous studies [7, 17]. If the boundary layer expands over practically all the meniscus tip
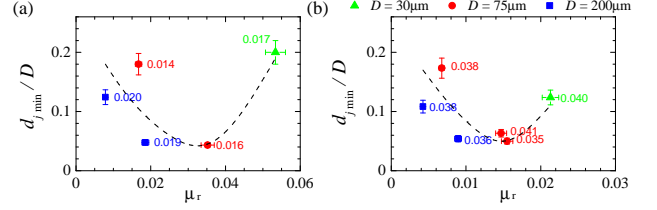

FIG. 7. Dimensionless jet diameter $d_{j\min}/D$ (measured at the orifice entrance) for $Q = Q_{\min}$ versus the viscosity ratio μ_r for (a) Oh = 0.017 ± 0.003 and (b) Oh = 0.039 ± 0.004. The labels indicate the Ohnesorge number. The dashed line is a guide to the eye.

($\delta_l \simeq R_s$), then $Q_D^* \sim Q_D$. The condition $\delta_l \simeq R_s$ at the meniscus tip was assumed in Refs. [7, 17] to simplify the analysis. Here, we relax that condition and calculate the dragged flow rate Q_D^*.
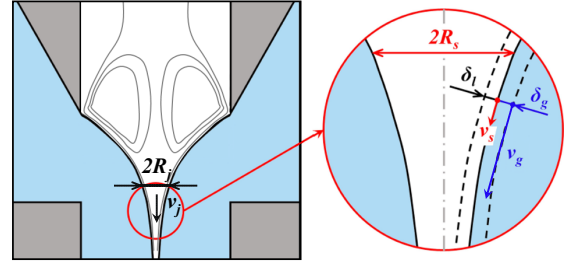

FIG. 8. Sketch of the liquid and gas boundary layers before the orifice entrance.

The free surface radius at the meniscus tip can be estimated from the energy balance equation

$$\frac{1}{2}\rho_l v_j^2 \simeq \Delta p(1 - \Phi_v) + \mathcal{C}\frac{\mu_g v_g}{\delta_g}, \quad (7)$$

where v_j is the liquid jet mean velocity in front of the discharge orifice, $\mathcal{C}$ is a dimensionless positive constant which accounts for the free surface shape, $v_g \sim (\Delta p/\rho_g)^{1/2}$ is the gas outer stream velocity, and $\delta_g \sim (D\mu_g/\rho_g v_g)^{1/2}$ is the thickness of the gas viscous boundary layer (Fig. 8). The term $\Phi_v > 0$ represents the loss of pressure in the discharge orifice due to the gas viscosity. In other words, $\Delta p(1 - \Phi_v)$ is the pressure drop in the liquid meniscus. As can be observed, Eq. (7) includes the small effects of the gaseous viscous dissipation and shear stress, both neglected in the classical formula of flow focusing [5].

The Taylor series around $\mu_r = 0$ of the solution to the energy equation (7) is

$$d_j \simeq d_{\mathrm{FF}}\left(1 - \alpha\,\mu_r^{1/2} + \frac{5}{2}\alpha^2\mu_r + \frac{1}{4}\mathcal{B}\,\mu_r + \cdots\right), \quad (8)$$

where $d_j = (4Q/\pi v_j)^{1/2}$ is the jet diameter, $d_{\mathrm{FF}} = [8\rho_l Q^2/(\pi^2\Delta p)]^{1/4}$ is the classical approximation for that

quantity [5], and $\alpha = \mathcal{C}\mu_l^{1/2}/(4D^{1/2}\Delta p^{1/4}\rho_g^{1/4})$. To derive Eq. (8), we have assumed that the dissipation in the orifice scales as μ_g, i.e., $\Phi_v \sim \mathcal{B}\mu_r$, where $\mathcal{B}$ is a dimensionless function of the governing parameters. Equation (8) reproduces the non-monotonous behavior of the jet diameter with respect to μ_r shown in Fig. 5.

Assuming that $R_s \simeq d_j/2$, Eq. (8) can be written as

$$\frac{Q_D^*}{Q_D} \simeq \frac{d_{\mathrm{FF}}}{\delta_l}\left(1 - \alpha\,\mu_r^{1/2} + \frac{5}{2}\alpha^2\mu_r + \frac{1}{4}\mathcal{B}\mu_r\right) - 1. \quad (9)$$

For $\delta_l \simeq d_{\mathrm{FF}}/2$ ($\delta_l \simeq R_s$) and $\mu_r \simeq 0$, the previous result $Q_D^* \simeq Q_D$ is recovered [7]. As can be observed, the liquid flow rate Q_D^* dragged within the boundary layer first decreases and then increases as the gas viscosity increases. This result explains why $Q_{\min}$ exhibits that non-monotonous dependence on μ_g as well.

To summarize, we have analyzed the non-trivial role played by the gas viscosity in the stability of the tapering meniscus formed in flow focusing. The minimum flow rate for which steady jetting can be produced exhibits a non-monotonous behavior, reaching its lowest value for an optimum gas viscosity that depends on the liquid viscosity. The dependence of the meniscus shape on the gas viscosity reflects this non-monotonous behavior: the maximum liquid (dimensionless) acceleration is achieved for the optimum gas viscosity. Our results illustrate the complexity of the flow arising in the tapering meniscus of flow focusing. Increasing the viscous drag exerted by the gas stream does not necessarily stabilizes the meniscus. The global stability analysis of the base flow may allow a deeper study of the gas viscosity effect on the meniscus stability and the flow pattern. This will be the object of a future work

Our results show the existence of a new optimum parameter region for which the minimum flow rate can be reduced below the limit found in previous works [7]. This reduction entails a significant decrease in the diameter of the emitted jet, which may enhance the applicability of gaseous flow focusing to revolutionary techniques such as SFX.

[1] I. Cohen, H. Li, J. L Hougland, M. Mrksich, and S. R. Nagel, "Using selective withdrawal to coat microparticles," Science **292**, 265–267 (2001).

[2] A. S. Utada, E. Lorenceau, D. R. Link, P. D. Kaplan, H. A. Stone, and D. A. Weitz, "Monodisperse double emulsions generated from a microcapillary device," Science **308**, 537–541 (2005).

[3] S. Takeuchi, P. Garstecki, D. B. Weibel, and G. M. Whitesides, "An axisymmetric flow-focusing microfluidic device," Adv. Mater. **17**, 1067–1072 (2005).

[4] F. Blanchette and W. W. Zhang, "Force balance at the transition from selective withdrawal to viscous entrainment," Phys. Rev. Lett. **102**, 144501 (2009).

[5] A. M. Gañán-Calvo, "Generation of steady liquid microthreads and micron-sized monodisperse sprays in gas streams," Phys. Rev. Lett. **80**, 285–288 (1998).

[6] T. Si, F. Li, X.-Y. Yin, and X.-Z. Yin, "Modes in flow focusing and instability of coaxial liquid-gas jets," J. Fluid Mech. **629**, 1–23 (2009).

[7] J. M. Montanero, N. Rebollo-Muñoz, M. A. Herrada, and A. M. Gañán-Calvo, "Global stability of the focusing effect of fluid jet flows," Phys. Rev. E **83**, 036309 (2011).

[8] J. Zhao, Z. Ning, M. Lv, and C. Sun, "Experimental study on gas liquid interaction outside flow focusing/blurring nozzle," J. Taiwan Inst. Chem. Eng. **134**, 104304 (2022).

[9] D. P. DePonte, U. Weierstall, K. Schmidt, J. Warner, D. Starodub, J. C. H. Spence, and R. B. Doak, "Gas dynamic virtual nozzle for generation of microscopic droplet streams," J. Phys. D: Appl. Phys. **41**, 195505 (2008).

[10] H. N. Chapman *et al.*, "Femtosecond X-ray protein nanocrystallography," Nature **470**, 73–79 (2011).

[11] S. Boutet *et al.*, "High-resolution protein structure determination by serial femtosecond crystallography," Science **337**, 362–364 (2012).

[12] M. Vakili *et al.*, "3D printed devices and infrastructure for liquid sample delivery at the european XFEL," J. Synchrotron Rad. **29**, 1–16 (2022).

[13] C. Yang, R. Qiao, K. Mu, Z. Zhu, R. X. Xu, and T. Si, "Manipulation of jet breakup length and droplet size in axisymmetric flow focusing upon actuation," Phys. Fluids **31**, 091702 (2019).

[14] X. Xu, Z. Zhu, K. Mu, F. Huang, and T Si, "Parametric study on breakup of liquid jet in a gas-driven flow focusing process upon external excitation," Phys. Fluids **34**, 042001 (2022).

[15] J. M. Montanero and A. M. Gañán-Calvo, "Dripping, jetting and tip streaming," Rep. Prog. Phys. **83**, 097001 (2020).

[16] E. J. Vega, J. M. Montanero, M. A. Herrada, and A. M. Gañán-Calvo, "Global and local instability of flow focusing: The influence of the geometry," Phys. Fluids **22**, 064105 (2010).

[17] M. A. Herrada, A. M. Gañán-Calvo, A. Ojeda-Monge, B. Bluth, and P. Riesco-Chueca, "Liquid flow focused by a gas: Jetting, dripping, and recirculation," Phys. Rev. E **78**, 036323 (2008).

Influence of the gas viscosity on the stability of flow focusing.
Suplemental Material

A. Rubio,[1] B. N. Muñoz-Sánchez,[1] M. G. Cabezas,[1] and J. M. Montanero[1]

[1]*Depto. de Ingeniería Mecánica, Energética y de los Materiales and*
Instituto de Computación Científica Avanzada (ICCAEx),
Universidad de Extremadura, E-06006 Badajoz, Spain

I. LIQUIDS

Table I shows the properties of the liquids used in the experiments. The liquids or liquid mixtures were selected to produce a desired Ohnesorge number Oh = $\mu_l(\rho_l\sigma D)^{-1/2}$ with a given orifice diameter D and different liquid viscosity. We conducted experiments with nHexane (PanReac AppliChem 362063.1611), distilled water and 0.65, 1 and 5 cSt silicone oils (Xiameter PMX-200, Dow Corning). We will use SOXX to refer to the silicone oil of viscosity XX cSt. The properties of these liquids were taken from the manufactures data sheets. We also prepared two mixtures to adjust the Ohnesorge number Oh for a given orifice diameter D. Water/glycerol solutions were produced by mixing deionized water and glycerol (PanReac AppliChem 151339.1211). We will refer to these solutions as W/G X/Y, where "X" and "Y" indicate the relative concentration in weight of water and glycerol, respectively. We also prepared mixtures of two viscosity silicone oils (Xiameter PMX-200, Dow Corning). We will refer as SOXX/SOYY X/Y to the mixture with "X" and "Y" relative concentration in weight of the XX and YY cSt viscosity silicone oils, respectively. The liquids were mixed in a magnetic stirrer for one day. Then, we measured the density ρ_l with a Gay-Lussac pycnometer (Glassco), the viscosity μ_l with an adequate Cannon-Fenske viscometer (Fungilab), and the surface tension σ with the TIFA (Theoretical Image Fitting Analysis) method [1].

II. EXPERIMENTAL PROCEDURE

To calculate the minimum flow rate for steady jetting we set the pressure difference Δp and injected a liquid flow rate Q high enough to produce this mode. Then, we decreased the flow rate in steps ΔQ until the steady jetting becomes unstable. The minimum flow rate $Q_{\min}$ is calculated as the average of the flow rates of the last stable realization and the first unstable one. The corresponding value for each liquid is shown in Table I. A video of an unstable meniscus of W/G 66/34 with a 75 μm diameter orifice at a flow rate below the minimum (Q=0.3 ml/h) is available as Supplemental Material.

We used the standard method to obtain the minimum flow rate. One can also increase Q and determine the minimum value for steady jetting to appear. It is well known that this procedure overestimates the value of $Q_{\min}$ due to hysteresis effects.

III. ERRORS

The error propagation rule is used to estimate the error in the dimensionless numbers. We consider that errors in the orifice diameter and density are negligible, and estimated a 5% relative error of the viscosity ($\delta\mu_l/\mu_l$) and the surface tension ($\delta\sigma/\sigma$) due to limitations of the measurement procedure. $\Delta Q/2$ is used as an estimate of the error of the minimum flow rate. For example, the error of the minimum capillary number $Ca^* = \mu_l Q_{\min}/(D^2\sigma)$, is calculated as

$$\frac{\delta Ca^*}{Ca^*} = \left(\frac{\delta\mu_l}{\mu_l}\right) + \left(\frac{\delta\sigma}{\sigma}\right) + \left(\frac{\Delta Q/2}{Q_{\min}}\right). \qquad (1)$$

[1] M. G. Cabezas, A. Bateni, J. M. Montanero, and A. W. Neumann, "A new drop-shape methodology for surface tension measurement," Appl. Surf. Sci. **238**, 480–484 (2004).

Liquid	ρ_l (kg/m^3)	μ_l (mPa·s)	σ (mN/m)	D (μm)	Oh	$Q_{\min}$ (ml/h)	Ca^*
n-Hexane	661	0.33	17.9	30	0.017	0.125	7.03 10^{-4}
SO0.65	760	0.49	15.9	75	0.016	0.085	1.30 10^{-4}
Water	998	1.04	72.0	75	0.014	0.415	2.96 10^{-4}
SO1/SO5 95.3/4.7	815	0.94	14.3	200	0.019	0.635	2.89 10^{-4}
W/G 91/9	1031	1.58	56.1	200	0.015	1.93	3.78 10^{-4}
W/G 69.5/30.5	1060	2.21	57.5	200	0.020	1.76	4.70 10^{-4}
SO1	816	0.82	17.4	30	0.040	0.045	0.65 10^{-3}
W/G 80/20	1034	1.76	56.3	30	0.042	0.115	1.11 10^{-3}
SO1/SO5 90/10	822	1.12	16.7	75	0.035	0.075	0.25 10^{-3}
SO1/SO5 78.9/21.1	829	1.18	13.7	75	0.041	0.165	0.71 10^{-3}
W/G 66/34	1056	2.58	58.2	75	0.038	0.565	1.24 10^{-3}
SO1/SO5 51/49	858	1.95	17.4	200	0.036	1.43	1.11 10^{-3}
W/G 56/44	1097	4.09	52.7	200	0.038	3.15	1.69 10^{-3}
SO5	913	4.57	19.7	30	0.197	0.125	0.89 10^{-2}
W/G 44/56	1129	7.39	55.0	30	0.171	0.190	0.79 10^{-2}
SO5/SO10 34.6/65.4	920	7.01	14.4	75	0.223	0.425	1.02 10^{-2}
W/G 37.2/62.8	1148	11.8	54.8	75	0.171	0.635	0.67 10^{-2}
SO10/SO20 63/27	933	12.9	14.7	200	0.247	1.56	0.95 10^{-2}
W/G 31.9/68.1	1158	17.5	53.6	200	0.157	2.78	0.63 10^{-2}

TABLE I. Properties of the liquids and mixtures used in the experiments and Oh, $Q_{\min}$ and Ca* for the corresponding orifice diameter.

7. Paper IV - Influence of the gas viscosity on the stability of flow focusing.

8

Paper V - Transonic flow focusing: stability analysis and jet diameter.

Transonic flow focusing: stability analysis and jet diameter

M. Rubio[a], A. Rubio[a], M. G. Cabezas[a], M. A. Herrada[b], A. M. Gañán-Calvo[b], J. M. Montanero[a,*]

[a]*Departamento de Ingeniería Mecánica, Energética y de los Materiales and*
Instituto de Computación Científica Avanzada (ICCAEx),
Universidad de Extremadura, E-06006 Badajoz, Spain
[b]*Departamento de Ingeniería Aerospacial y Mecánica de Fluidos, Universidad de Sevilla,*
Camino de los Descubrimientos s/n 41092, Spain.

Abstract

We study numerically and experimentally the stability of the transonic flow focusing used in serial femtosecond crystallography (SFX) to place complex biochemical species into the beam focus. Both the numerical and experimental results indicate that the minimum flow rate for steady jetting increases slightly with the gas stagnation pressure. There is a remarkable agreement between the stability limit predicted by the global stability analysis and that obtained experimentally. Our simulations show that the steady jetting interruption at the critical flow rate is caused by the growth of a perturbation with a constant phase shift. This result is consistent with the experimental observations, which indicate that both the meniscus tip and the emitted jet collapse almost simultaneously at the stability limit. We derive a scaling law for the jet diameter as a function of the liquid flow rate and gas density/pressure from more than one hundred simulations. The scaling law provides accurate predictions for the jet diameter within the range of values $[0.549, 10.9]$ μm analyzed in this work.

1. Introduction

In the original gaseous flow focusing configuration (Gañán-Calvo, 1998), the liquid is injected at a constant flow rate Q_l across a feeding capillary placed in front of a discharge orifice whose diameter is commensurate with that of the capillary. A high-speed gaseous stream coflows with the liquid across the discharge orifice. The pressure drop Δp and viscous shear stress caused by the gaseous current drives the liquid flow, while the energy transferred to the system by injecting the liquid at the flow rate Q_l is negligible. A very thin jet tapers from the tip of the meniscus attached to the edge of the feeding capillary. DePonte et al. (2008) modified the original plate-orifice flow focusing configuration (Gañán-Calvo, 1998) by introducing the feeding capillary in a fire-shaped nozzle to produce the focusing effect. They coined the expression "Gas

¹Corresponding author: J. M. Montanero (jmm@unex.es)

Dynamic Virtual Nozzle" (GDVN) to refer to this ejector. Gaseous flow focusing is a paradigmatic example of tip streaming (Montanero and Gañán-Calvo, 2020) used in multiple applications.

In the incompressible regime, and neglecting the role of both surface tension and viscosity in the liquid and gas phases, the jet diameter d_j in the two configurations can be calculated as (Gañán-Calvo, 1998)

$$d_j = \left(\frac{8\rho_l Q_l^2}{\pi^2 \Delta p}\right)^{1/4},$$ (1)

where ρ_l is the liquid density. The viscous shear stress exerted by the gaseous stream on the liquid surface transfers axial momentum to the jet and can significantly reduce its diameter below the inviscid approximation (1). This approximation can be improved by considering the viscous drag force both in the discharge orifice and beyond it (Gañán-Calvo et al., 2011). To the best of our knowledge, a scaling law for the jet diameter (speed) has not yet been derived for the compressible (transonic) regime.

The serial femtosecond crystallography (SFX) is probably the most important gaseous flow focusing application. In SFX, complex biochemical species are analyzed by recording single flash diffraction patterns of many individual protein crystals (Chapman *et al.*, 2011). X-ray free-electron lasers (XFELs) produce flashes sufficiently bright to generate resolvable diffraction patterns from sub-micron crystals. These flashes destroy the crystals, which implies that the data are to be collected from a row of crystals streaming across the X-ray beam. Most SFX experiments make use of a thin liquid jet to place the sample into the beam focus. SFX demands stringent conditions for jet emission. The jet must be at most very few microns in diameter to reduce the background diffraction signal. The jet must be long enough because the jet portion interacting with the X-ray pulse must be located sufficiently far away from the nozzle exit to avoid a rapid collection of sputtered material from the explosion. The jet must be perfectly steady to ensure a consistent interaction with the X-ray beam. Finally, the jet must be fast enough to allow the exposed sample to exit the interaction region before the next flash strikes the jet Stan *et al.* (2016); Wiedorn *et al.* (2018). To summarize, liquid jets as thin, long, steady, and fast as possible are required for the proper functioning of the SFX technique.

Gaseous flow focusing (aerodynamic focusing) (Gañán-Calvo, 1998; DePonte et al., 2008; Gañán-Calvo et al., 2010) with converging nozzles has been the preferred method to produce jets fulfilling the above severe constraints. The search for the best ejection conditions has led to the use of transonic and supersonic streams of helium to focus the liquid jet on one side and the optimization of the nozzle geometry (Beyerlein et al., 2015; Piotter et al., 2018; Wiedorn *et al.*, 2018) on the other side. Different geometrical configurations have been considered to minimize/maximize the jet's diameter/speed. For instance, and following the idea proposed by Acero et al. (2013), Nazari et al. (2020) have recently used liquid feeding capillaries with syringe shape to produce jets with diameters down to 325 nm and speeds up to 170 m/s. Despite the advances mentioned above,

the optimization of the liquid ejection remains an open problem due to the continuously increasing frequency of SFX repetition rates.

The gas compressibility significantly affects the outcome of flow focusing for gas velocities similar to the sound speed. Obtaining an accurate but simple scaling law to predict the jet diameter (speed) in the transonic regime is of great importance for applications such as SFX. As occurs in the incompressible regime [Eq. (1)], the liquid flow rate is the major factor determining the jet diameter. As the flow rate decreases, the specific energy transferred to the liquid increases, and the jet diameter/speed decreases/increases. However, the flow rate cannot be reduced without limit because the jetting regime produced by flow focusing becomes unstable for flow rates below a certain minimum value, which depends on the rest of governing parameters. Therefore, the search for the optimum liquid ejection conditions necessarily involves two aspects of the problem: (i) the maximization of the energy transmitted by the gas stream to the liquid jet, and (ii) the stabilization of the flow producing the liquid ejection. Understanding the physical mechanism responsible for the transonic flow focusing instability at the minimum flow rate has considerable implications at both the fundamental and practical levels.

Direct numerical simulations of transonic flow focusing (Zahoor et al., 2018c) have been conducted from the time integration of the Navier-Stokes equations in the laminar regime with the Volume of Fluid (VoF) method (Hirt and Nichols, 1981). These simulations have proved to constitute a useful tool for analyzing different aspects of the problem. Among the geometrical parameters analyzed in the simulations, the nozzle outlet diameter has the biggest influence on the jet diameter. In contrast, the feeding capillary angle and the capillary-to-orifice distance have a very small effect on the liquid flow (Zahoor et al., 2018a). The influence of this distance on the minimum liquid flow rate approximately follows the scaling law empirically derived by Vega et al. (2010) in the incompressible regime. Sarler et al. (2021) have recently shown that a change in angle of the nozzle outlet orifice has a significant effect on the jet emission. The influence of the gas (Zahoor et al., 2018b) and liquid (Zahoor et al., 2020) properties on the jet's characteristics has been examined from direct numerical simulations as well. Zahoor et al. (2018c) found a qualitative agreement between the scaling law (1) for the incompressible regime and their numerical results.

The calculation of the flow under steady conditions (the so-called base flow) is probably the most efficient way of determining the jet diameter. Once a numerical solution of the hydrodynamic equations has been found, the values of the governing parameters can be swept to produce systematically new numerical flow focusing realizations with relatively short computing time. In this way, one can determine the optimal conditions that maximize the energy transfer from the gas to the liquid. However, this study must be accompanied by the stability analysis of the steady solutions to verify whether those numerical realizations are physically meaningful. The global linear stability analysis (Theofilis, 2003; Chomaz, 2005; Theofilis, 2011) is probably the best procedure to fulfill that purpose. In this procedure, we calculate the eigenmodes describing the response of the base flow to small-amplitude perturbations (Theofilis, 2003; Chomaz, 2005;

Theofilis, 2011). One assumes that a base flow corresponds to a true jetting realization if and only if all the eigenmodes decay on time. Cruz-Mazo et al. (2017) showed that the global stability analysis predicts reasonably well the stability of gaseous flow focusing for large applied pressure drops in the incompressible regime. This analysis has recently been extended to liquid-liquid systems (Cabezas et al., 2021) with similar conclusions. It must be noted that the calculation of the base flow and its eigenmodes does not allow one to predict the jet breakup length, which is an important parameter in applications such as SFX. That prediction requires the time integration of the hydrodynamic equations to determine where the growth of unstable perturbations gives rise to the droplet formation.

The global stability analysis of freely moving jets must be conducted carefully. The physical domain is unbounded downstream, making it necessary to impose an arbitrary cut-off in the numerical domain far away from the discharge orifice. "Soft" boundary conditions are frequently prescribed on that outlet surface. The cut-off may significantly affect eigenmodes corresponding to instabilities that originated in the emitted jet. However, and as will be shown in Sec. 5, these instabilities are subdominant in our problem, and both the cut-off length and the outlet boundary condition have a small effect on the growth rate of the dominant global mode (Tammisola et al., 2012; Gordillo et al., 2014; Augello et al., 2018). For this reason, the stability analysis is expected to be accurate for the present fluid configuration. It is worth mentioning that this may also occur in viscous capillary systems, which explains why perturbations can be forced to vanish at the outlet of those systems (Sauter and Buggisch, 2005; Tammisola et al., 2012; Rubio-Rubio et al., 2013; Augello et al., 2018).

In this paper, we study numerically and experimentally the transonic flow focusing used in SFX. In the numerical analysis, the steady base flow is obtained as a function of the liquid flow rate and gas stagnation pressure. The stability of the base flow is determined from the calculation of the linear eigenmodes. This analysis allows us to determine the parameter conditions leading to the steady jetting instability. The results are compared with the experimental measurements, and the physical mechanisms responsible for the instability are elucidated. Finally, potential applications of our numerical approach are discussed. Specifically, we derive a scaling law to estimate the jet diameter for the geometrical configuration and physical properties considered in our analysis.

2. Formulation of the problem

Consider a flow focusing realization in which a gas stream is injected from a chamber pressurized at a pressure p_0 and temperature T_0. The gas enters into a converging nozzle with an exit orifice of diameter D (Fig. 1) and discharges into a chamber connected to that orifice. The parameters governing the gas flow are the shear viscosity μ_g, the heat coefficients c_v and c_p, the thermal conductivity κ_g, the upstream stagnation temperature T_0 and pressure p_0, as well as the pressure of the gas stream at the discharge chamber exit p_e. The dilatational coefficient of viscosity λ_g is taken as $\lambda_g = -2/3\,\mu_g$. To simplify the analysis, we
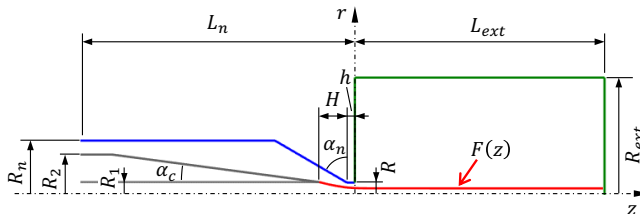
4

Figure 1: Flow focusing ejector analyzed in our numerical simulations. The values of the geometrical parameters are: $R = D/2 = 35$ μm, $R_1 = D_1/2 = 37.5$ μm, $R_2 = 175$ μm, $\alpha_c = 7.5°$, $R_n = 245$ μm, $h = 40$ μm, $\alpha_n = 60°$, $L_n = 1260$ μm, $L_{\text{ext}} = 1260$ μm, $R_{\text{ext}} = 560$ μm. We conducted simulations for $H = 140$ μm. The function $F(z)$ represents the distance of the free surface to the symmetry axis z.

neglect the influence of both the pressure and temperature on the gas properties $\{\mu_g, c_v, c_p, \kappa_g\}$. This approximation is acceptable for our purposes because (i) helium viscosity and thermal conductivity are hardly affected by the pressure (Flynn et al., 1963), and (ii) the temperature of the gas layer in contact with the liquid is practically the liquid temperature T_0, except at the nozzle exit where variations of around 10% are found (Zahoor et al., 2018a).

The gas flow drives the liquid ejection inside the nozzle. The liquid response to the aerodynamic force is determined by its density ρ_l and viscosity μ_l, the free surface tension σ, and the injected flow rate Q_l. In addition, the temperature distribution in the liquid phase depends on the thermal conductivity κ_l as well. We also neglect the influence of the temperature on the liquid properties $\{\rho_l, \mu_l, \sigma, \kappa_l\}$ because it remains practically constant in the liquid phase.

Taking into account the above considerations, and for a fixed geometry, the flow is a function of the set of dimensional parameters

$$\{D; \mu_g, c_v, c_p, \kappa_g; T_0, p_0, p_e; \rho_l, \mu_l, \sigma, \kappa_l; Q_l\}. \tag{2}$$

As can be observed, they correspond to the scale of the ejector, the physical properties of the gas, the gas control parameters, the physical properties of the liquid, and the only liquid control parameter. Both the simulations and experiments are conducted for distilled water ($\rho_l = 998$ kg/m^3, $\mu_l = 1$ mPa·s, $\kappa_l = 0.58$ W/(m·K)) and helium ($\mu_g = 0.018$ mPa·s, $c_p = 5190$ m^2/(s^{2}K), $c_v = 3120$ m^2/(s^{2}K), $\kappa_g = 0.142$ W/(m·K)). The surface tension value is $\sigma = 72$ mN/m. To reproduce the experimental conditions, we set $T_0 = 300$ K and $p_e = 75$ mbar in the simulations. The ranges of values of p_0 and Q_l in this work are similar to those typically used in SFX.

When the ratio p_0/p^* between the stagnation pressure p_0 and the hydrostatic pressure p^* at the nozzle orifice exceeds the critical value $p_0/p^* = [(\gamma + 1)/2]^{\gamma/(\gamma-1)}$, the 1D isentropic gas flow becomes chocked (Shapiro, 1953). In this case, the gaseous flow in the nozzle cannot be accelerated by increasing p_0 (and keeping T_0 constant). The increase of the stagnation pressure increases the mass flow rate by raising the gas density, but it does not affect the velocity

field inside the nozzle. In addition, the temperature field and, therefore, the gas viscosity do not change when the stagnation pressure is increased. This implies that the viscous stress exerted by the outer stream on the liquid current inside the nozzle remains practically constant when p_0 is increased under choking flow conditions. On the contrary, the gas density, mass flow rate, and pressure drop in the nozzle do increase with p_0. In our simulations and experiments, the 2D gaseous flow becomes chocked at the nozzle exit even for the smallest value of the upstream stagnation pressure. Therefore, the increase of that pressure hardly affects the viscous stress exerted on the free surface.

As mentioned above, one can assume as a first approximation that the gas flow is essentially governed by the control parameters $\{T_0, p_0, p_e\}$. In fact, these parameters essentially determine the force driving the liquid ejection, while the flow rate Q_l controls the response of the liquid to that force. In a second approximation, one must also consider the influence of Q_l on the gaseous flow. The liquid current moves much slower than the gas stream and acts as a still solid boundary for the gaseous flow. The liquid flow rate Q_l determines the free surface contour, and, therefore, it somehow controls the shape of the nozzle crossed by the gas stream, thus affecting all the properties of that stream. In other words, there is feedback from the liquid flow to the gas stream.

3. Governing equations and numerical method

In the simulations, we integrate the conservation equations for mass, momentum, and energy for the two phases. The general form of those equations is:

$$\frac{\partial \rho}{\partial t} + \nabla \cdot (\rho \mathbf{v}) = 0, \tag{3}$$

$$\rho \frac{D\mathbf{v}}{Dt} = -\nabla p + \nabla \cdot \boldsymbol{\tau}, \tag{4}$$

$$\rho \frac{D(c_v T)}{Dt} = -p \nabla \cdot \mathbf{v} + \boldsymbol{\tau} : \nabla \mathbf{v} - \nabla \cdot \mathbf{q}, \tag{5}$$

where $\rho(\mathbf{r}, t)$, $\mathbf{v}(\mathbf{r}, t) = v_r(\mathbf{r}, t)\mathbf{e}_r + w(\mathbf{r}, t)\mathbf{e}_z$, $p(\mathbf{r}, t)$, and $T(\mathbf{r}, t)$ are the density, velocity, pressure, and temperature fields in each phase, respectively, and D/Dt is the material derivative. These equations are completed with the constitutive relationships for the viscous stress tensor $\boldsymbol{\tau}$ and the heat flux vector $\mathbf{q}$:

$$\boldsymbol{\tau} = \mu \left(\nabla \mathbf{v} + (\nabla \mathbf{v})^{\mathrm{T}} \right) + \lambda (\nabla \cdot \mathbf{v}) \mathbf{I}, \quad \mathbf{q} = -\kappa \nabla T, \tag{6}$$

where μ, λ, and κ represent the shear viscosity, dilatational coefficient of viscosity, and thermal conductivity of each phase, respectively, and $\mathbf{I}$ is the identity matrix. In addition, the equation of state $p = \rho R_g T$ is considered in the gas phase, where $R_g = c_p - c_v$ is the gas constant. We assume that the liquid is incompressible, i.e. $\nabla \cdot \mathbf{v} = 0$ in the liquid phase.

6

The continuity of velocity, temperature, stress and heat flux at the interface yields

$$||\mathbf{v}|| = 0, \quad ||T|| = 0, \quad \mathbf{n} \cdot ||\boldsymbol{\tau}|| - ||p||\mathbf{n} = \sigma(\nabla \cdot \mathbf{n})\mathbf{n}, \quad ||\kappa \, \partial T/\partial n|| = 0, \quad (7)$$

where $||A||$ denotes the difference between the values taken by the quantity A on the two sides of the interface, and $\mathbf{n}$ is the unit outward normal vector. The kinematic compatibility condition reads

$$\frac{\partial F}{\partial t} - v_r + w\frac{\partial F}{\partial z} = 0 \,, \tag{8}$$

where $F(z,t)$ is the distance of an interface element from the axis of symmetry z.

Parabolic and uniform axial velocity profiles are imposed at the liquid and gas inlets, respectively. The mass flow rate m'_0 and stagnation temperature T_0 are prescribed at the gas inlet, while the flow rate Q_l and temperature T_0 are set at the inlet of the liquid feeding capillary. The values m'_0 and T_0 prescribed in the simulations can be readily translated into the governing parameters p_0 and T_0 introduced in Sec. 2. The zero-gradient (outflow) boundary condition is imposed at the gas and liquid outlets for all the variables except for the pressure whose value p_e is fixed at that section. The no-slip $\mathbf{v} = \mathbf{0}$ and no-temperature jump $T = T_0$ boundary conditions are imposed on the solid surfaces. We verified that the results are practically the same if the condition $T = T_0$ is replaced by the adiabatic wall boundary condition $\partial T/\partial n = 0$ on the solid surfaces. We did not consider the latter because it hinders the solution convergence. To complete the set of boundary conditions, we assume $\partial p/\partial n = 0$ on both the solid surfaces and the free surface.

The linear global axisymmetric modes are calculated by assuming the temporal dependence

$$\Phi(r,z;t) = \Phi_0(r,z) + \varepsilon\, \phi(r,z)\, e^{-i\omega t} \quad (\varepsilon \ll 1), \tag{9}$$

where Φ, Φ_0, and ϕ represent any hydrodynamic quantity, the base (steady) solution, and the spatial dependence of the eigenmode, respectively, while $\omega = \omega_r + i\omega_i$ is the eigenfrequency. Both the eigenmodes and corresponding eigenfrequencies are obtained as a function of the governing parameters. The dominant eigenmode is that with the largest growth factor ω_i. If that growth factor is positive, the base flow is asymptotically unstable (Theofilis, 2011). Non-axisymmetric (lateral) modes are not contemplated in our analysis because the rarefied conditions in the discharge chamber suppress the whipping instability.

The base flow and the corresponding eigenmodes are calculated with a variation of the boundary fitted method described by Herrada and Montanero (2016). A quasi-elliptic transformation (Dimakopoulos and Tsamopoulos, 2003) is applied to generate the grid (Fig. 2), which allows us to deal with the sharp reduction of the free surface radius in the meniscus tip. The equations are discretized in the transformed radial direction η using $n_\eta^\ell = n_\eta^{g1} = 45$ and $n_\eta^{g2} = 69$ Chebyshev collocation points (Khorrami, 1989) in the liquid and gas domains,
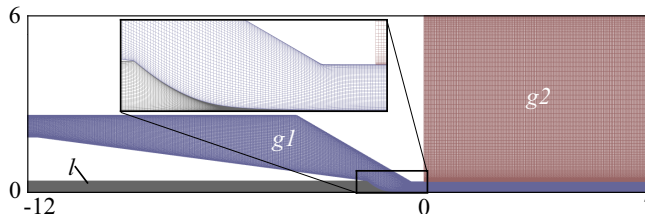
7

Figure 2: Detail of the mesh used in the numerical simulations. The colors indicate the three blocks (l, $g1$ and $g2$).

respectively. The transformed axial direction ξ is discretized using fourth-order finite differences with $n_\xi^\ell = n_\xi^{g1} = 859$ and $n_\xi^{g2} = 313$ equally spaced points. The grid points accumulate near the free surface, allowing one to integrate the gaseous viscous boundary layer accurately. The simulations were run on one core of the processor Intel$^©$ Xeon$^©$ Cascade lake Platinum 8260 2.4 GHz. The base flow is calculated in around 15 min, while it takes about 50 min to obtain the eigenvalues.

Figure 3 shows the eigenvalues around the dominant one for a quasi-marginally stable base flow. The results were calculated with the grid described above and with $n_\eta^\ell = n_\eta^{g1} = 45$, $n_\eta^{g2} = 69$, $n_\xi^\ell = n_\xi^{g1} = 859$ and $n_\xi^{g2} = 313$. As can be observed, the eigenfrequency of the critical mode is practically insensitive to the grid size. The loss of stability occurs through a Hopf bifurcation ($\omega_r \neq 0$), owing to the growth of an oscillatory (periodic) perturbation. The oscillation frequency is commensurate with the inverse of the inertio-capillary time $t_c = [\rho_l D_1^3/(8\sigma)]^{1/2}$ defined in terms of the feeding capillary diameter D_1. This result suggests that the perturbation responsible for the instability affects the emitted jet and the liquid meniscus.

4. Experimental method

We fabricated the flow focusing ejector used in our experiments. The design was inspired by the devices developed by Knoska *et al.* (2020), modifying the nozzle tip and porting region to suit our requirements (Fig. 4). The nozzle was printed using Nanoscribe Photonic Professional GT2 with the Dip-in Laser Lithography (DiLL) configuration, dipping the $25\times$ objective into the IP-S resin droplet on an ITO coated glass substrate. We chose the shell and scaffolds writing strategy and produced a 20 μm thickness shell delimiting the structure and an internal scaffold to stabilize the structure. The writing time was 35 h. The part was developed in ∼25 ml of PGMEA for one hour and then cleaned in ethanol for 10 min. Then, unexposed resin inside the shell was cured for 60 min inside the UV Curing Chamber (XYZprinting).

The main elements of the experimental setup are shown in Fig. 4. A glass cell was closed by a specially designed sealing cap. The nozzle was mounted
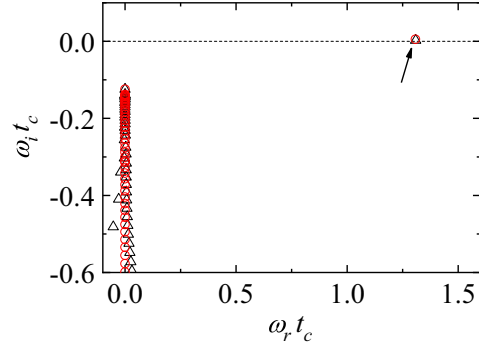
8

Figure 3: Spectrum of eigenvalues for $p_0 = 1.6$ bar and $Q_l = 0.65$ ml/h calculated with $-0.1 \leq \omega_r \leq 1.6$ and $\omega_i > -0.7$. The circles and triangles correspond to $(n_\eta^\ell = n_\eta^{g1} = 45, n_\eta^{g2} = 69, n_\xi^\ell = n_\xi^{g1} = 859, n_\xi^{g2} = 313)$ and $(n_\eta^\ell = n_\eta^{g1} = 51, n_\eta^{g2} = 79, n_\xi^\ell = n_\xi^{g1} = 969, n_\xi^{g2} = 353)$, respectively. The arrow indicates the eigenvalue corresponding to the dominant mode.
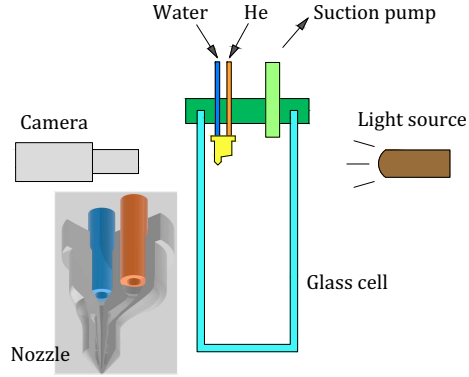

Figure 4: Main elements of the experimental setup.

onto that cap. We established a negative gauge pressure inside the cell using a suction pump. Distilled water was injected with a syringe pump (KDS100, KD-Scientific). We controlled the helium flow with the pressure regulator of the bottle and verified that the loss of stagnation pressure in the gas circuit was less than 3%. We installed a mass flow meter (FLOW SELECT F-201 CV) to determine the linear relationship $m' = 20\,p_0 - 2.0$ between the applied stagnation pressure p_0 (mbar) and the resulting mass flow rate m' (mg/min) for $0.3 \leq p_0 \leq 1.6$ bar. The upstream stagnation temperature and the temperature in the cell were measured with thermocouples. The pressure in the cell was measured with a gauge indicator.

Digital images of the liquid meniscus and jet were acquired at 10^5 fps using a high-speed video camera (KIRANA-5M) equipped with optical lenses (NAVITAR 12X) and a microscope objective (10X MITUTOYO). The images consisted of 924×768 pixels. The magnification was 53×, which resulted in 0.56 μm/pixel. The camera could be displaced both horizontally and vertically using a triaxial translation stage with one of its horizontal axes motorized (THORLABS Z825B) and controlled by the computer. The camera was illuminated with white backlighting and was triggered by an optical trigger (SI-OT3, SPECIALISED IMAGING). The optical trigger was equipped with optical lenses and illuminated with white backlighting. All the elements of the experimental setup were mounted on an optical table with a pneumatic anti-vibration isolation system to damp the vibrations coming from the building.

To determine the minimum flow rate, we first set the upstream stagnation pressure. Then, a relatively large liquid flow rate was injected through the feeding capillary. After a short transient regime, a steady liquid meniscus was formed attached to the feeding capillary edge. Finally, the liquid flow rate was reduced in steps of 0.01 ml/h until the jetting regime became unstable. Unfortunately, we could not obtain reliable measurements of the jet diameter for the extremely thin jets produced in our experiments. According to our estimations, the errors associated with the diffraction limit are of the order of 30%-50% for flow rates close to the critical value.

5. Results

Figure 5 shows the good agreement between the free surface shape in the experiment and that calculated with our numerical simulation for a quasi-marginally stable realization. This comparison should be taken with caution because the unknown optical distortion caused by the nozzle was not considered. The jet diameter in the simulation seems to be smaller than that obtained experimentally. However, it is difficult to determine the difference quantitatively due to the experimental uncertainty associated with the image's spatial resolution and the diffraction limit (the jet diameter is of the order of 1 μm). The minimum values of liquid flow rate Q_l obtained in the experiments are practically the same as those calculated from the global stability analysis (Fig. 6). As can be observed, the critical flow rate hardly depends on the upstream stagnation pressure for the range of values analyzed in this work, as occurs in
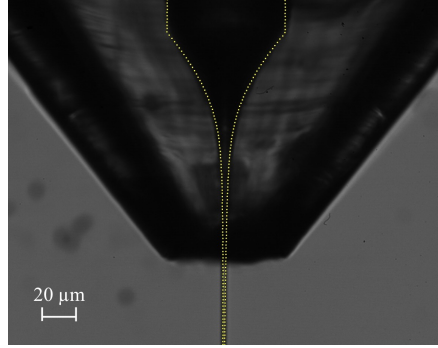
10

Figure 5: Experimental image and free surface position calculated numerically (dotted line) for $p_0 = 1.75$ bar and $Q_l = 0.68$ ml/h.
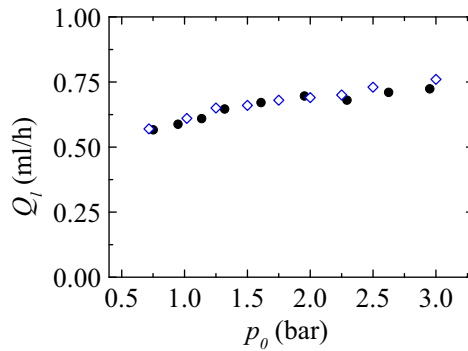

Figure 6: Minimum value of the liquid flow rate Q_l as a function of the upstream stagnation pressure p_0 obtained experimentally (open symbols) and numerically (solid symbols).

the incompressible regime (Si et al., 2009; Montanero et al., 2011). This result may be expected because, as mentioned in Sec. 2, the increase of the stagnation pressure above the critical value leading to sonic choking hardly affects the viscosity force exerted by the gas stream on the free surface. The minimum flow rate can be significantly reduced only by appropriately changing the ejector geometry (for a fixed couple of fluids). It must be pointed out that unstable steady solutions are obtained as the liquid flow rate is decreased below the critical value. For this reason, the global linear stability analysis is required to determine the physically meaningful numerical realizations.

For the sake of illustration, Fig. 7 shows the streamlines for the quasi-marginally stable flow obtained for $p_0 = 1.67$ bar and $Q_l = 0.75$ ml/h. Similar results were obtained for other marginally stable cases. The major characteristic of the liquid flow pattern is the two counter-rotating recirculation cells in
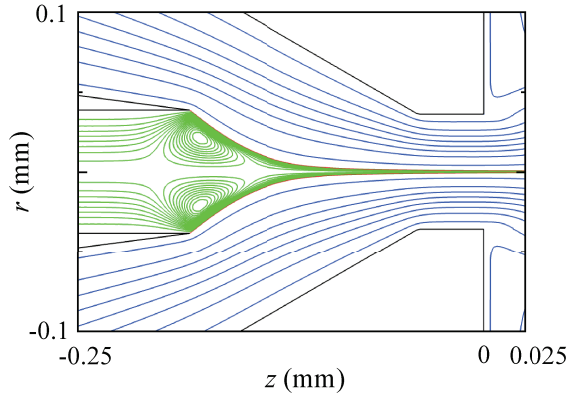
11

Figure 7: Streamlines for $p_0 = 1.67$ bar and $Q_l = 0.75$ ml/h.

the liquid meniscus. As occurs in the incompressible case (Montanero et al., 2011; Cruz-Mazo et al., 2017; Mu et al., 2021), these cells arise for sufficiently low viscosity and liquid flow rate. Under these conditions, it has been speculated that the loss of stability of steady jetting is caused by the destabilization of those vortices (Montanero et al., 2011).

As can be observed in Fig. 8, both the gas and liquid temperature take homogeneous values in most of the fluid domain. However, the gas stream expands into the low-vacuum chamber at the nozzle exit, which causes a sharp drop in its temperature there. Despite the slenderness of the liquid jet, its temperature hardly decreases. This can be explained in terms of the low density of the surrounding gas and the small residence time of the liquid particle (Zahoor et al., 2018c). As can be observed in Fig. 8-b, there is a significant increase of the hydrostatic pressure in the tip of the liquid meniscus due to the accumulation of momentum in that region. This pressure increase makes the liquid flow back along the central part of the meniscus (Fig. 7). We plot in Fig. 8c the Mach number $M = v/a$, where v is the fluid velocity magnitude and a the sound speed. As expected, the flow is subsonic everywhere except in the nozzle exit, where transonic and supersonic conditions are reached.

In flow focusing, the outer gas stream stretches the liquid meniscus and sets in motion a certain volume of liquid. This volume must be continuously replaced by the liquid injection across the feeding capillary to reach steady conditions. The liquid meniscus tip inevitably thins and stops ejecting the liquid for injected flow rates lower than that dragged by the gaseous current. This instability mechanism is consistent with the images acquired in our experiments. Figure 9a shows a sequence of images acquired when the liquid flow rate is decreased below its minimum value. During the time interval $0 \leq t \leq 30$ μs, steady jetting is observed. For $30 \leq t \leq 50$ μs, both the meniscus tip and the emitted jet seem to collapse almost simultaneously, leaving a mark in the image corresponding
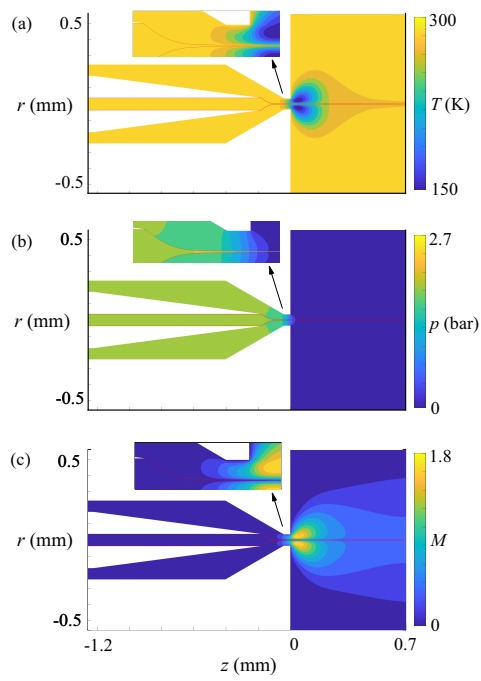
12

Figure 8: Temperature (a), pressure (b) and Mach number (c) for $p_0 = 1.67$ bar and $Q_l = 0.75$ ml/h. The red line indicates the free surface position.
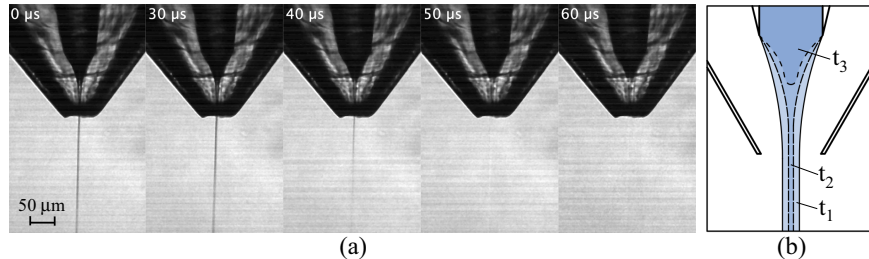
13

Figure 9: (a) Sequence of images acquired when the liquid flow rate is decreased below its minimum value $Q_l = 0.69$ ml/h for $p_0 = 2$ bar. (b) Sketch to illustrate the free surface evolution during breakup.

to $t = 40$ μs. For $t \geq 50$ μs, the ejection does not take place, and the meniscus slightly retracts towards the feeding capillary. The dynamics of the system leading to the ejection interruption are sketched in Fig. 9b.

The free surface evolution is probably the best indicator of the mechanism responsible for the instability of flow focusing. In the global stability analysis, we assume the temporal dependence

$$F(z,t) = F_0(z) + \varepsilon f(z)e^{-i\omega t} \; (\varepsilon \ll 1) \qquad (10)$$

for the free surface position $F(z,t)$, where $F_0(z)$ stands for the steady free surface shape (see, e.g., the dotted line in Fig. 5). Figure 10 shows the magnitude of $f(z)$ for a marginally stable numerical solution. The real and imaginary parts of f are practically the same, which means that $F(z) - F_0(z) \simeq |f(z)| \sin(\omega_r t)$. This result implies that the perturbation corresponds to an oscillation with a constant phase shift of the entire free surface. This behavior may be explained in terms of the strong convective character of the system, which "synchronizes" the free surface deformation throughout the tapering meniscus and the emitted jet. The above result is consistent with the breakup dynamics observed in the experiments (Fig. 9), where both the meniscus tip and emitted jet seem to collapse simultaneously. We have verified that the above conclusions apply to the range of stagnation pressures analyzed in this work.

Due to the difficulties inherent to the fabrication of the flow focusing ejectors in SFX, numerical simulations have come up as a valuable alternative to search for the optimum ejector geometry (Sarler et al., 2021). The numerical method proposed in the present work is very useful for that purpose because it consumes much less computing time than any direct numerical simulation method. In this work, we calculated the minimum diameter $d_{\min}$ of the jet in the numerical domain as a function of the upstream stagnation pressure and liquid flow rate. We only considered stable realizations. It must be noted that $d_{\min}$ is expected to be smaller than the jet diameter at the nozzle exit due to the extra liquid acceleration caused by the gas stream in the discharge chamber.

Gañán-Calvo et al. (2011) examined the deviation of the jet diameter from
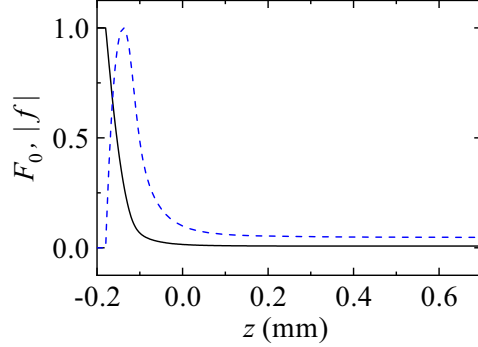
14

Figure 10: Steady free surface position $F_0(z)$ (black solid line) and magnitude of the free surface perturbation, $|f(z)|$ (dashed blue line), for $p_0 = 1.6$ bar and $Q_l = 0.65$ ml/h. The curves have been normalized dividing by the corresponding maximum value.

the scaling law (1) due to the liquid viscosity and the action of the tangential viscous stresses of the focusing gas in the incompressible regime. Following the same procedure, we here calculate the dimensionaless diameter $d^*_{\min} \equiv d_{\min}/d_j$ to analyze the deviation of the jet diameter $d_{\min}$ from the value d_j given by the scaling law (1) (with $\Delta p = p_0 - p_e$). This deviation can be attributed to the gas compressibility and viscosity. For the purposes of dimensional analysis, it is convenient to formulate the problem in terms of the density $\rho_0 = p_0/(R_g T_0)$ instead of the temperature T_0. Then, the dimensionless diameter $d^*_{\min}$ can be expressed as

$$d^*_{\min} \equiv d_{\min}/d_j = f(\gamma, \mu_r, \kappa_r, \mathrm{Oh}_l; p_r, \rho_r, Q_r), \qquad (11)$$

where $\gamma = c_p/c_v$, $\mu_r = \mu_g/\mu_l$, $\kappa_r = \kappa_g/\kappa_l$, $\mathrm{Oh}_l = \mu_l(\rho_l D\sigma)^{-1/2}$, $p_r = p_0/p_e$, $\rho_r = \rho_0/\rho_l$, $Q_r = Q_l/Q_D$, and $Q_D = D\mu_l/\rho_l$. In our numerical simulations, we fixed the values of the adiabatic constant γ, the viscosity and thermal conductivity ratios, μ_r and κ_r, and the Ohnesorge number Oh_l, while the values of p_r, ρ_r, and Q_r were changed.

In the incompressible regime (Gañán-Calvo et al., 2011), the main contribution to the deviation f from unity must be assigned to Q_r, which controls the area where the gas exerts the viscous tangential stresses. We expect Q_r to affect significantly the value of f in the compressible regime as well. In addition, the influence of p_r on $d_{\min}$ is approximately taken into account in (11) through the diameter d_j given by (1). For this reason, we select ρ_r as the remaining (subdominant) control parameter. Thus, we search for a scaling law of the form (Barenblatt, 2003)

$$d^*_{\min} = \mathcal{C} \, Q_r^\alpha \rho_r^\beta. \qquad (12)$$

Using the optimization method described by Montanero and Gañán-Calvo (2020), the best collapse of the numerical data around (12) is obtained for $\mathcal{C} = 0.433$, $\alpha = 0.308$ and $\beta = -0.06$ (Fig. 11). As expected, $\alpha \gg |\beta|$, which shows the
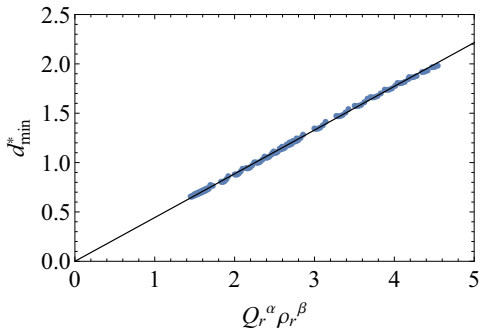
Figure 11: $d^*_{\min} = d_{\min}/d_j$ versus $Q_r^\alpha \rho_r^\beta$ for $\alpha = 0.308$ and $\beta = -0.06$. The solid line is the function $y = 0.443x$.

385 dominant role of Q_r. The scaling law remarkably fits the numerical data in the
386 range of values $0.549 \lesssim d_{\min} \lesssim 10.9$ μm calculated in our simulations.

The scaling law (12) implies that the jet's minimum diameter $d_{\min}$ and maximum velocity $v_{\max} = 4Q_l/(\pi d^2_{\min})$ scale as

$$d_{\min} \sim Q_l^{0.808} p_0^{-0.31}, \quad v_{\max} \sim Q_l^{-0.616} p_0^{0.19}, \tag{13}$$

387 respectively, when the ejector geometry, properties of the fluids, and stagnation
388 temperature are fixed. The minimum liquid flow rate decreases with the stag-
389 nation pressure (Fig. 6) approximately as $Q_l \sim p_0^{0.18}$. Taking into account the
390 scaling law (13), $d_{\min} \sim p_0^{-0.17}$ at the stability limit. This implies that thinner
391 jets can be produced as p_0 increases even though the minimum flow rate slightly
392 increases with p_0. As mentioned in Sec. 2, the variation of p_0 hardly affects the
393 viscous stress exerted on the free surface under chocking flow conditions. There-
394 fore, the term $p_0^{0.19}$ in Eq. (13) indicates that the drop of hydrostatic pressure
395 contributes to the liquid acceleration as well.

396 6. Concluding remarks

397 We studied numerically and experimentally the transonic flow focusing used
398 in SFX to place the sample into the beam focus. In the numerical analysis, the
399 steady base flow was calculated as a function of the injected liquid flow rate
400 and upstream gas stagnation pressure. Then, we solved the eigenvalue problem
401 to obtain the linear global mode responsible for the steady jetting instability.
402 In this way, we determined the minimum flow rate below which steady jetting
403 cannot be reached.

404 Our results show that the minimum flow rate slightly depends on the stag-
405 nation pressure for the range of pressures considered in our analysis. This con-
406 clusion is similar to that obtained in the incompressible regime for sufficiently

16

large pressure drops (Montanero et al., 2011). The simulation satisfactorily reproduces the shape of the experimental tapering meniscus. However, it seems to underestimate the jet diameter obtained experimentally.

Interestingly, the global stability analysis accurately predicts the minimum flow rate measured in the experiments. The agreement between the numerical and experimental results is even better than in the incompressible regime (Cruz-Mazo et al., 2017). The steady jetting interruption is caused by the growth of an inertio-capillary perturbation, making the meniscus and jet collapse simultaneously at the stability limit.

The scaling law for the jet diameter shows that the liquid flow rate is the most important control parameter, while the gas pressure (density) plays a secondary role. Equation (12) with $\alpha = 0.308$ and $\beta = -0.06$ is very accurate within the range of values $0.549 \lesssim d^*_{\min} \lesssim 10.9$ μm analyzed in the simulations. Significant deviations may be expected for other ejector geometries and higher liquid viscosities. These are probably the two major factors affecting the exponents in Eq. (12). The analysis of the influence of these factors will be the subject of future work.

Our numerical procedure consumes much less computing time than direct numerical simulations, in which the hydrodynamic equations are integrated over time until the jetting regime is established. For this reason, this procedure can be a helpful tool for determining the optimal parameter conditions in SFX. The major disadvantage of the present approach is that we cannot calculate the jet breakup length, which is an essential parameter in SFX. In fact, we cannot ascertain whether the minimum diameter $d_{\min}$ is attained before the jet breaks up. If that were the case, the scaling law (12) could not be used to calculate the diameter of the droplets resulting from the jet breakup.

To the best of our knowledge, transonic and supersonic flow focusing has been used only in SFX. The large liquid speed and the low pressure of the discharge chamber are not demanded in other existing applications and can constitute an obstacle for techniques such as fiber extruding or bioplotting. However, new applications will likely come up in the future to take advantage of the large kinetic energy of the emitted jet.

Acknowledgements

References

Acero, A.J., Rebollo-Muñoz, N., Montanero, J.M., Gañán-Calvo, A.M., Vega, E.J., 2013. A new flow focusing technique to produce very thin jets. J. Micromech. Microeng. 23, 065009.

Augello, L., Fani, A., Gallaire, F., 2018. The influence of the entry region on the instability of a coflowing injector device. J. Phys.: Condens. Matter 30, 284003.

Barenblatt, G.I., 2003. Scaling. Cambridge University Press, Cambridge, UK.

Beyerlein, K.R., Adriano, L., Heymann, M., Kirian, R., Knoska, J., Wilde, F., Chapman, H.N., Bajt, S., 2015. Ceramic micro-injection molded nozzles for serial femtosecond crystallography sample delivery. Rev. Sci. Instrum. 86, 125104.

Cabezas, M.G., Rubio, M., Rebollo-Muñoz, N., Herrada, M.A., Montanero, J.M., 2021. Global stability analysis of axisymmetric liquid-liquid flow focusing. J. Fluid Mech. 909, A10.

Chapman *et al.*, H.N., 2011. Femtosecond X-ray protein nanocrystallography. Nature 470, 73–79.

Chomaz, J., 2005. Global instabilities in spatially developing flows. Annu. Rev. Fluid Mech. 37, 357–392.

Cruz-Mazo, F., Herrada, M.A., Gañán-Calvo, A.M., Montanero, J.M., 2017. Global stability of axisymmetric flow focusing. J. Fluid Mech. 832, 329–344.

DePonte, D.P., Weierstall, U., Schmidt, K., Warner, J., Starodub, D., Spence, J.C.H., Doak, R.B., 2008. Gas dynamic virtual nozzle for generation of microscopic droplet streams. J. Phys. D: Appl. Phys. 41, 195505.

Dimakopoulos, Y., Tsamopoulos, J., 2003. A quasi-elliptic transformation for moving boundary problems with large anisotropic deformations. J. Comput. Phys. 192, 494–522.

Flynn, G.P., Hanks, R.V., Lemaire, N.A., Ross, J., 1963. Viscosity of nitrogen, helium, neon, and argon from $-78.5°$ to $100°C$ below 200 atmospheres. J. Chem. Phys. 38, 154–162.

Gañán-Calvo, A.M., 1998. Generation of steady liquid microthreads and micronsized monodisperse sprays in gas streams. Phys. Rev. Lett. 80, 285–288.

Gañán-Calvo, A.M., DePonte, D.P., Herrada, M.A., Spence, J.C.H., Weierstall, U., Doak, R.B., 2010. Liquid capillary micro/nanojets in free-jet expansion. Small 6, 822–824.

Gañán-Calvo, A.M., Ferrera, C., Montanero, J.M., 2011. Universal size and shape of viscous capillary jets: application to gas-focused microjets. J. Fluid Mech. 670, 427–438.

Gordillo, J.M., Sevilla, A., Campo-Cortés, F., 2014. Global stability of stretched jets: conditions for the generation of monodisperse micro-emulsions using coflows. J. Fluid Mech. 738, 335–357.

Herrada, M.A., Montanero, J.M., 2016. A numerical method to study the dynamics of capillary fluid systems. J. Comput. Phys. 306, 137–147.

Hirt, C.W., Nichols, B.D., 1981. Volume of Fluid (VOF) method for the dynamics of free boundaries. J. Comput. Phys. 39, 201–225.

Khorrami, M.R., 1989. Application of spectral collocation techniques to the stability of swirling flows. J. Comput. Phys. 81, 206–229.

Knoska *et al.*, J., 2020. Ultracompact 3D microfluidics for time-resolved structural biology. Nat. Commun. 11, 657.

Montanero, J.M., Gañán-Calvo, A.M., 2020. Dripping, jetting and tip streaming. Rep. Prog. Phys. 83, 097001.

Montanero, J.M., Rebollo-Muñoz, N., Herrada, M.A., Gañán-Calvo, A.M., 2011. Global stability of the focusing effect of fluid jet flows. Phys. Rev. E 83, 036309.

Mu, K., Qiao, R., Guo, J., Yang, C., Wu, Y., Si, T., 2021. Parametric study on stability and morphology of liquid cone in flow focusing. Int. J. Multiphase Flow 135, 103507.

Nazari, R., Zaare, S., Alvarez, R.C., Karpos, K., Engelman, T., Madsen, C., Nelson, G., Spence, J.C.H., Weierstall, U., Adrian, R.J., Kirian, R.A., 2020. 3D printing of gas-dynamic virtual nozzles and optical characterization of high-speed microjets. Opt. Express 28, 21749–21765.

Piotter, V., Klein, A., Plewa, K., Beyerlein, K.R., Chapman, H.N., Bajt, S., 2018. Development of a ceramic injection molding process for liquid jet nozzles to be applied for X-ray free-electron lasers. Microsyst. Technol. 24, 1247–1252.

Rubio-Rubio, M., Sevilla, A., Gordillo, J.M., 2013. On the thinnest steady threads obtained by gravitational stretching of capillary jets. J. Fluid Mech. 729, 471–483.

Sarler, B., Zahoor, R., Bajt, S., 2021. Alternative geometric arrangements of the nozzle outlet orifice for liquid micro-jet focusing in gas dynamic virtual nozzles. Materials 14, 1572.

Sauter, U.S., Buggisch, H.W., 2005. Stability of initially slow viscous jets driven by gravity. J. Fluid Mech. 533, 237–257.

Shapiro, A.H., 1953. Compressible fluid flow. John Wiley and Sons Inc., New York, USA.

Si, T., Li, F., Yin, X.Y., Yin, X.Z., 2009. Modes in flow focusing and instability of coaxial liquid-gas jets. J. Fluid Mech. 629, 1–23.

Stan *et al.*, C.A., 2016. Liquid explosions induced by X-ray laser pulses. Nat. Phys. 12, 966–971.

19

Tammisola, O., Lundell, F., Soderberg, L.D., 2012. Surface tension-induced global instability of planar jets and wakes. J. Fluid Mech. 713, 632–658.

Theofilis, V., 2003. Advances in global linear instability of nonparallel and three-dimensional flows. Prog. Aerosp. Sci. 39, 249–315.

Theofilis, V., 2011. Global linear instability. Annu. Rev. Fluid Mech. 43, 319–352.

Vega, E.J., Montanero, J.M., Herrada, M.A., Gañán-Calvo, A.M., 2010. Global and local instability of flow focusing: The influence of the geometry. Phys. Fluids 22, 064105.

Wiedorn *et al.*, M.O., 2018. Megahertz serial crystallography. Nat. Commun. 9, 4025.

Zahoor, R., Bajt, S., Sarler, B., 2018a. Influence of gas dynamic virtual nozzle geometry on micro-jet characteristics. Int. J. Multiphase Flow 104, 152–165.

Zahoor, R., Bajt, S., Sarler, B., 2018b. Numerical investigation on influence of focusing gas type on liquid micro-jet characteristics. Int. J. Hydromechatronics 1, 222–237.

Zahoor, R., Belsak, G., Bajt, S., Sarler, B., 2018c. Simulation of liquid micro-jet in free expanding high-speed co-flowing gas streams. Microfluidics and Nanofluidics 22, 87.

Zahoor, R., Regvar, R., Bajt, S., Sarler, B., 2020. Simulation of liquid micro-jet in free expanding high-speed co-flowing gas streams. Microfluidics and Nanofluidics 20, 71–83.

8. Paper V - Transonic flow focusing: stability analysis and jet diameter.

9

Paper VI - Viscoelastic transition in transonic flow focusing.

Viscoelastic transition in transonic flow focusing

A. Rubio [1], F. J. Galindo-Rosales [2], E. J. Vega [1], J. M. Montanero [1], and M. G. Cabezas [1,*]

[1]*Depto. de Ingeniería Mecánica, Energética y de los Materiales and Instituto de Computación Científica Avanzada (ICCAEx), Universidad de Extremadura, E-06006 Badajoz, Spain*
[2]*CEFT, Departamento de Engenharia Química, Faculdade de Engenharia da Universidade do Porto, Rua Dr. Roberto Frias, 4200-465 Porto, Portugal*

We find and study the viscoelastic transition in transonic flow focusing when polymers of low molecular weights are dissolved in water at the appropriate concentration. This phenomenon is explained in terms of the coil-stretch transition of the polymers crossing the tapering meniscus, where the airstream produces very large strain rates. The resulting elastic stress stabilizes the flow, reducing the minimum liquid flow rate leading to jetting. As a consequence, we produce jets much thinner and longer than their Newtonian counterparts, which has important consequences at the technological level. We present a scaling analysis to show the role played by the polymer relaxation time and extensional viscosity in the viscoelastic transition.

I. INTRODUCTION

In gaseous flow focusing [1], a liquid is injected at a constant flow rate through a feeding capillary located in front of an orifice [1] or inside a converging nozzle [2,3]. A coflowing gas stream is forced to cross the orifice/nozzle, which originates favorable pressure gradients and viscous stresses. The resulting forces sharpen the liquid meniscus attached to the feeding capillary and pull a thin jet from the meniscus tip. Straight and very thin jets can be produced when the outer gas stream is accelerated up to the sound speed and discharged into a low-pressure chamber (Fig. 1). For instance, water jets ~ 1 μm in diameter and ~ 100 km/h in speed can be produced with this technique when they are powered by a transonic current of Helium [4,5].

Transonic flow focusing exhibits significant differences with respect to the original incompressible version of this technique [1]. In almost all the practical realizations, the jetting mode instability is originated in the tapering meniscus, while the convective-to-absolute instability transition [6] is not observed in the emitted jets [7]. The whipping (bending) instability [3] is suppressed because the jet is discharged into a low-pressure chamber. Besides, the scaling law for the jet diameter significantly differs from its counterpart in the incompressible mode [7].

Gaseous flow focusing has many important applications. Tiny droplets/capsules are formed with an acceptable degree of monodispersity from the breakup of the emitted simple/compound jets owing to the capillary instability. Microbubbles can also be ejected at the tip of a gaseous tapering meniscus when the outer (focusing, continuous) and inner (focused, dispersed) phases are exchanged. In all these cases, the size of the produced microfluidic entity is much smaller than that of any passage of the ejector owing to the action of the focusing current. Gaseous flow focusing has been used to produce, for instance, microparticles of complex structures [8,9] or to form stimuli-responsive microbubbles [10] for a wide range of applications in pharmacy and

---

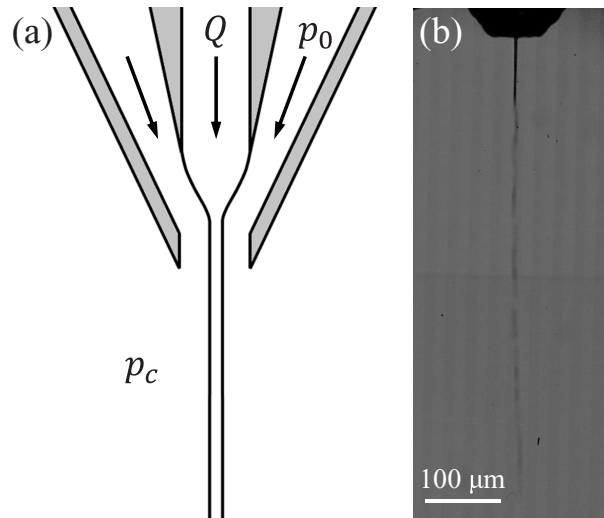*Corresponding author: mguadama@unex.es

FIG. 1. (a) Sketch of the fluid configuration. (b) Water jet emitted at the flow rate $Q = 0.75$ ml/h driven by an air current with a stagnation pressure $p_0 = 2.5$ bar and discharged into a pressure chamber $p_c = 75$ mbar.

biomedicine. Transonic flow focusing has become one of the most successful ways to introduce samples in serial femtosecond crystallography (SFX) [4,5], which has revolutionized the molecular determination of complex biochemical species from proteins to viruses. The jet speed/diameter must be sufficiently large/low to fulfill the requirements of the high pulse rates used in SFX.

The flow focusing principle has also been applied to produce viscoelastic threads by replacing the Newtonian dispersed phase with a polymer solution [11,12]. In this case, the straining flow driven by the gaseous current increases the solution extensional viscosity, stabilizing the ejected thread until the solvent evaporation occurs. The focusing of viscoelastic solutions with gaseous currents [13,14] has been proposed for smooth printing and bioplotting [15], and to fabricate fibers with diameters ranging from a few microns down to hundreds of nanometers [16,17]. The flow focusing of weakly viscoelastic liquids in the transonic regime has not been analyzed yet.

Many dilute polymer solutions exhibit a practically constant viscosity (shear thinning behavior can be neglected) over a wide range of shear rates [18] so that the major polymer effects are the increase of the solution shear viscosity and elasticity. In ideal dilute solutions, neutral chains adopt a random coil configuration at equilibrium. The relaxation from the stretched to coil conformations consists of multiple processes. If the polymer relaxation time λ_p characterizing the slowest process is much larger than the rest of the spectrum, then the polymer solution elasticity can approximately be quantified by this parameter.

The response of the viscoelastic solution to a straining flow is generally characterized by the so-called extensional relaxation time λ_r, measured in filament thinning rheometers such as CaBER [19] and FiSER [20]. This parameter is usually linked to the polymer relaxation time λ_p, and increases with the polymer concentration of a dilute solution due to the hydrodynamic (flow-mediated) interaction among polymers.

It has been recognized for a long time that high-velocity gradients can cause the transition from a coil to a nearly completely stretched conformation of polymer chains [21]. For instance, and according to the Oldroyd-B and FENE-P models [22], the coil-stretch transition takes place in a uniaxial extensional flow if the stretching rate exceeds the threshold $\dot{\varepsilon} = 1/(2\lambda_r)$ [23].

In some applications of gaseous flow focusing, such as SFX [4,5], the outer gas stream causes extremely high-velocity gradients in the tapering meniscus, which can induce the coil-stretch transition of polymer molecules even with low molecular weights (low relaxation times). In that case, the elastic stresses built up in the meniscus may substantially alter the flow stability and, therefore, the performance of the flow focusing technique. The major experimental finding of this work is
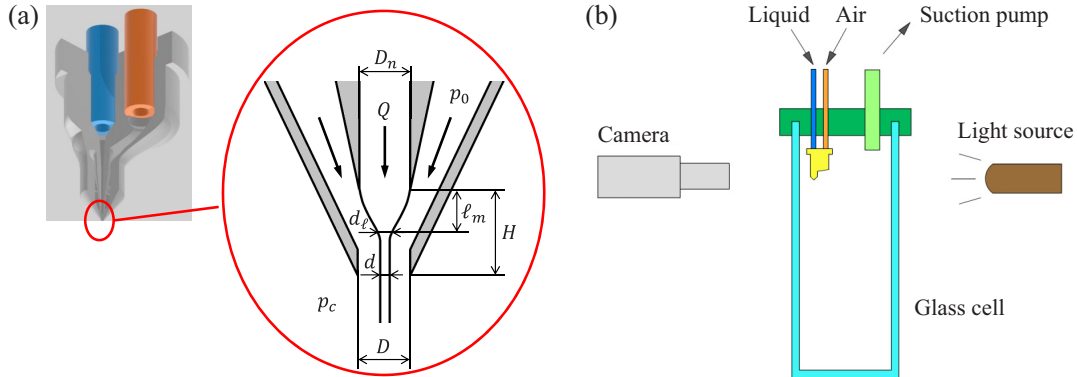
FIG. 2. Ejector (a) and elements of the experimental setup (b).

the existence of a viscoelastic transition in transonic flow focusing for small polymer molecular weights and appropriate concentrations. This transition leads to a substantial stabilization of the jetting regime, which reduces the minimum diameter of the emitted jet in one order of magnitude. This effect entails important advantages at the practical level.

II. MATERIALS AND METHODS

A. Experimental setup and procedure

The main elements of the experimental setup are shown in Fig. 2. A converging submillimeter nozzle was mounted onto the cap of a discharge glass cell. The nozzle tip consisted of a sharp inner needle of diameter $D_n = 75$ μm, located at a distance $H = 180$ μm from the nozzle orifice exit of diameter $D = 75$ μm. We established a pressure $p_c = 75$ mbar inside the cell using a suction pump. The working liquid was injected at a constant flow rate Q through the inner needle with a syringe pump (Legato210, KD-Scientific). The focusing air stream was controlled by setting the stagnation pressure p_0 upstream with the pressure regulator of the compressed air line for positive gauge pressures and throttling the flow from the atmosphere with a valve for the negative. We verified that the loss of stagnation pressure in the gas circuit was less than 3%.

Digital images of the liquid meniscus and jet were acquired at 2000 fps using a high-speed video camera (Fastcam Mini UX50) equipped with optical lenses (Optem Zoom 70XL) and a microscope objective (20X Optem) and white back-lighting. The images consisted of 1280×1024 pixels. The magnification was $3\times$, which resulted in 0.236 μm/pixel. The camera could be displaced both horizontally and vertically using a triaxial translation stage. All the elements of the experimental setup were mounted on an optical table with a pneumatic antivibration isolation system to damp the vibrations coming from the building.

In steady jetting, a jet is emitted from the tip of the meniscus anchored to the inner needle [Fig. 2(a)]. We measure the jet diameter d at the nozzle exit with pixel resolution. The meniscus length ℓ_m is measured from the needle to the section at which the diameter has reached 80% of the total reduction $(D_n - d)$. In other words, the meniscus length is the distance between the needle exit and the meniscus section with diameter $d_\ell = 0.2(D_n - d) + d$. To determine the minimum flow rate for steady jetting, we first set the upstream stagnation pressure and a sufficiently large liquid flow rate. Then, the latter was decreased in steps of 0.01 ml/h until the jetting regime became unstable. We repeated each experimental run three times to calculate the average value and the uncertainty, defined as the difference between the minimum and maximum values. We also determined the critical flow rate by increasing the flow rate until the jet became stable. We verified that the critical values obtained in this way differed in less than the experimental uncertainty. Therefore, hysteresis effects are negligible.

B. Nozzle fabrication

The nozzle [Fig. 2(a)] was printed using Nanoscribe Photonic Professional GT2 with the dip-in laser lithography (DiLL) configuration, dipping the $25\times$ objective into the IP-S resin droplet on an ITO coated glass substrate. We chose the shell and scaffolds writing strategy and produced a 20 μm thickness shell delimiting the structure and an internal scaffold to stabilize the structure. The writing time was 35 h. The part was developed in $\sim$25 ml of propylene glycol monomethyl ether acetate (PG-MEA) for 1 h and then cleaned in ethanol for 10 min. Then, unexposed resin inside the shell was cured for 60 min inside the UV Curing Chamber (XYZprinting).

C. Liquids

Aqueous polymeric solutions with different molecular weights and concentrations c were used as working liquids. The polymer was polyethylene oxide (Sigma Aldrich) with molecular weights $M_w = 100 \times 10^3$, 200×10^3, 600×10^3, 1000×10^3, and 2000×10^3 g/mol. Hereafter, the acronym PEOX stands for a PEO aqueous solution with molecular weight of X (g/mol). Stock polymeric solutions were prepared by dissolving the polymers in deionized water with a magnetic stirrer for five days at low angular speeds to minimize mechanical degradation of the long polymer chains. These solutions are Boger fluids [18], i.e., they exhibit negligible shear thinning over a large range of shear rates, which allows analyzing the effects of elasticity separately. Using polymers with several molecular weights at different concentrations enabled us to vary the characteristic time λ_r systematically.

For the sake of comparison, we also conducted experiments with water-glycerol mixtures with the same Ohnesorge number $\mathrm{Oh} = \eta(\rho\gamma D_n/2)^{-1/2}$ as some polymeric solutions. We will refer to these solutions as WX GY, where "X" and "Y" indicate the relative concentration in weight of water and glycerol, respectively.

D. Liquids characterization

The surface tension γ was measured with a Sigma 700 force tensiometer (Biolin Scientific, Espoo, Finland) equipped with a Du Noüy ring of 0.185 mm in thickness and 9.58 mm in diameter. This device was equipped with a spherical glass probe of 0.8836 cm^3 to measure the density ρ.

A stress-controlled rotational rheometer (Anton Paar MCR301) was used to obtain the steady shear viscosity η as a function of the shear rate $\dot{\gamma}$ of the polymeric solutions and the viscosity of the water-glycerol mixtures. We used a plate-plate geometry of 25 mm in radius, with a gap of 400 μm. The temperature within the fluid volume was set at 20 °C and controlled by a Peltier element. Steady-state viscosity curves were obtained from 1 to 10^4 s^{-1}. At least three independent measurements were performed to ensure the reproducibility of the results. The range of shear rates providing reliable data was set for each sample between the limit of the rheometer sensitivity (low-shear rate limit) and the onset of elastic instabilities (high-shear rate limit). Figure 3 show the dependence of the solution shear viscosity η upon the shear rate $\dot{\gamma}$ for PEO100K [Fig. 3(a)] and PEO600K [Fig. 3(b)]. The shear thinning is negligible for all the cases but for the largest PEO100K concentration. We calculated the viscosity η as the mean value within the reliable measurement range. The results are shown in Fig. 3(c).

This work compares the behavior of flow focusing viscoelastic realizations and their corresponding Newtonian counterparts, i.e., those with the same value of the Ohnesorge number. Table I shows the measured properties and Ohnesorge number for the water/glycerol mixtures and the corresponding polymeric solutions. The values for the water/glycerol mixtures agree with those reported in the literature [24].

Rubio *et al.* [25] used a modified version of the capillary breakup extensional rheometer to measure the relaxation time λ_r of PEO100K dissolved in water at different concentrations. The results are shown in Fig. 4. This figure also shows the values for PEO600K measured in the present work with essentially the same procedure. The experimental data were fitted by power laws [26] to estimate the values of λ_r corresponding to the critical concentrations c_1^* defined in Sec. III. Those values are 20.3 and 14 μs for PEO100K and PEO600K, respectively.
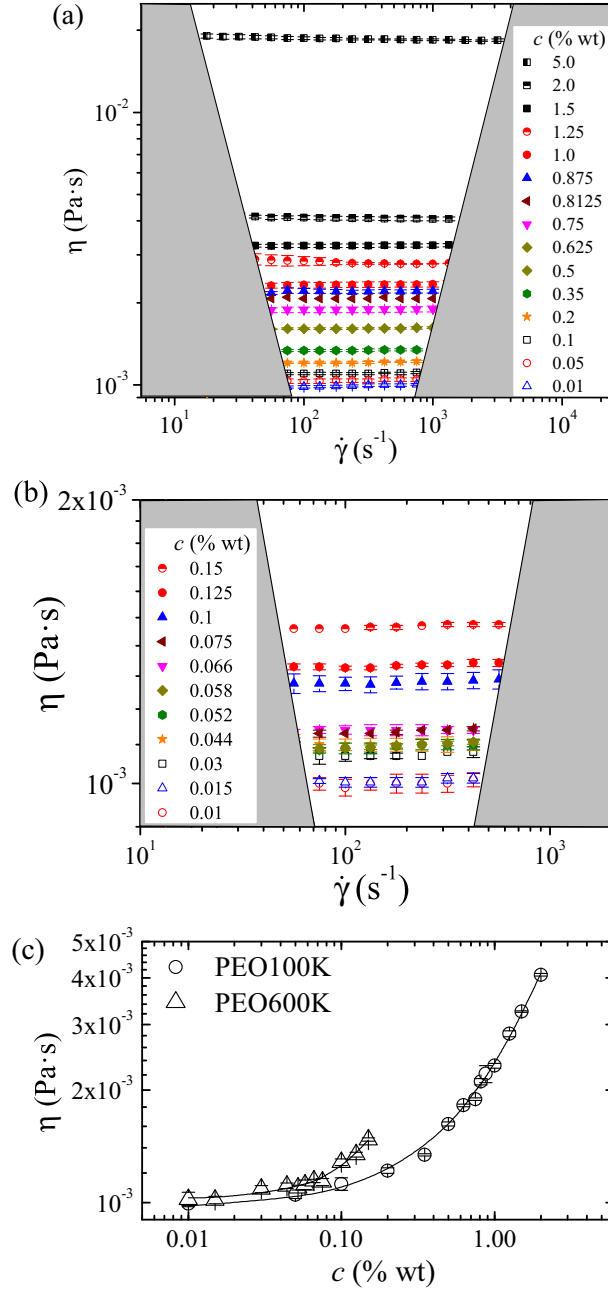
FIG. 3. Dependence of the solution shear viscosity η upon the shear rate $\dot{\gamma}$ at 20 °C for (a) PEO100K and (b) PEO600k solutions. (c) Mean shear viscosity dependence on the concentration. The solid lines are the fittings $\eta = (0.17c^2 + 1.23c + 0.97) \times 10^{-3}$ and $\eta = (12.94c^2 + 1.12c + 1.01) \times 10^{-3}$ for PEO100K and PEO600K respectively (with η and c measured in Pa s and %wt, respectively).

III. RESULTS AND DISCUSSION

Three types of menisci were found for the polymer solutions with the lowest molecular weights, PEO100K, PEO200K and PEO600K (Fig. 5). For small c and/or large Q, a "Newtonian-type meniscus" [Fig. 5(a1)] was observed. The shape of this meniscus was similar to that of

TABLE I. Density ρ, shear viscosity η, surface tension γ, and Ohnesorge number Oh for PEO solutions and the corresponding water/glycerol mixtures.

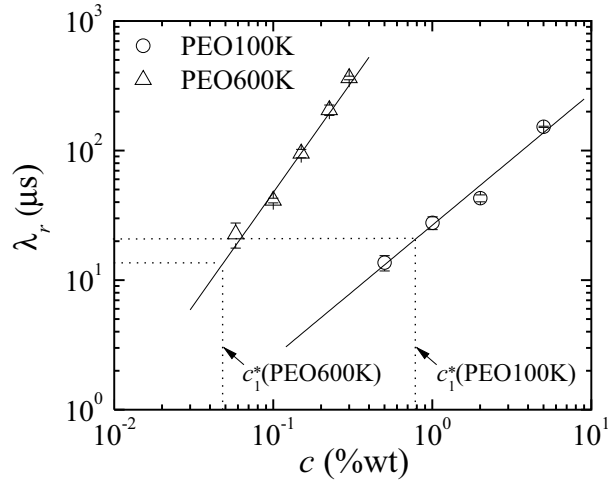| Liquid	ρ (kg/m^3)	η (mPa s)	γ (mN/m)	Oh
PEO100K 0.5%	1000	1.60	60.4	0.034
W80 G20	1043	1.77	66.5	0.035
PEO100K 0.875%	1000	2.21	60.5	0.046
W72 G28	1063	2.36	59.8	0.048
PEO100K 1.5%	1001	3.25	59.3	0.069
W60 G40	1090	3.28	69.0	0.062
PEO100K 2.0%	1002	4.41	59.6	0.093
W50 G50	1114	6.15	65.3	0.118

FIG. 4. Relaxation time λ_r of PEO100K and PEO600K dissolved in water at different concentrations. The solid lines are the fittings $\lambda_r = 26.18\, c^{1.020}$ and $\lambda_r = 2707\, c^{1.733}$ to the experimental results for PEO100K and PEO600K, respectively (with λ_r and c measured in μs and %wt, respectively). The dashed lines indicate the values of λ_r at the corresponding critical concentration c_1^* as defined in Sec. III.
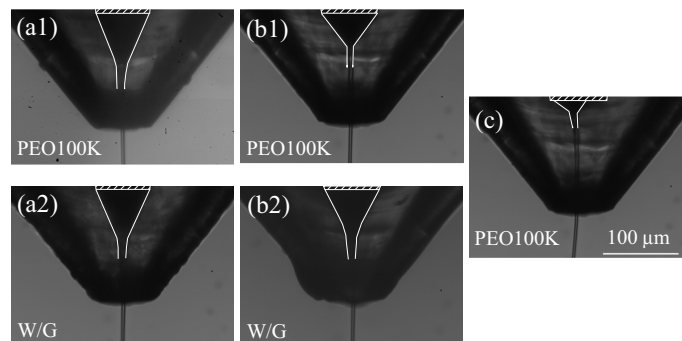
FIG. 5. Newtonian-type (a1) and viscoelastic (b1) menisci formed in the experiments with PEO100K for $\{c = 0.5\%$ wt, $Q = 1.57$ ml/h$\}$ and $\{c = 0.875\%$ wt, $Q = 1.38$ ml/h$\}$, respectively. Images (a2) and (b2) show the menisci of the water-glycerol mixture for the same Ohnesorge number and flow rate as those of the corresponding polymer solution. Image (c) shows the ejection mode following the pull-out instability for PEO100K, $c = 1.25\%$ wt, and $Q = 1$ ml/h. All the experiments were conducted for $p_0 = 2.5$ bar. The striped rectangle marks the needle tip, and the white lines the meniscus shape.

FIG. 6. Meniscus shape for PEO100K and $p_0 = 2.5$ bar. Images (a) and (b3) correspond to the minimum flow rate for those concentrations. The white lines mark the meniscus profile and the red lines are a guides to the eye.

water-glycerol with the same Ohnesorge number [Fig. 5(a2)]. For adequate values of c and Q, the meniscus significantly shrunk (the meniscus length decrea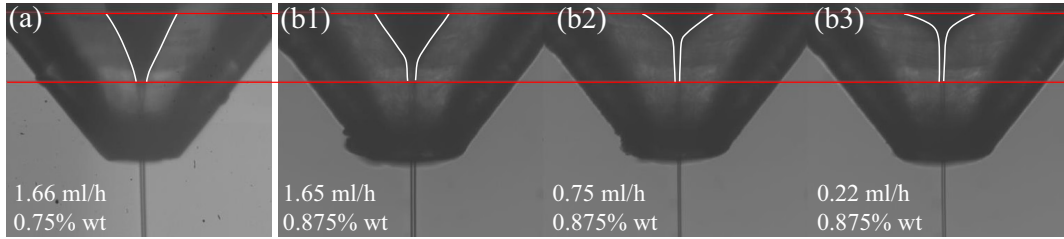sed) [Fig. 5(b1)], while the triple contact line remained anchored to the needle edge. The shape of this "viscoelastic meniscus" noticeably differed from its water-glycerol counterpart [Fig. 5(b2)].

The viscoelastic effect was appreciable when the polymer concentration was slightly increased above the critical concentration c_1^* [Figs. 6(a) and 6(b1)]. For $c \gtrsim c_1^*$, the meniscus shrinkage considerably increased as Q decreased. In fact, the meniscus shape shown in Fig. 6(b3) has not been observed in any Newtonian flow focusing realization [7,27], regardless of the liquid viscosity and gas speed. Finally, the so-called pull-out effect was observed for large values of c and small values of Q. The contact line depinned from the capillary edge and moved upwards over the inner wall of the feeding capillary [Fig. 5(c)]. In this case, the jet was prone to whipping instability at the nozzle exit.

The Ohnesorge number of the viscoelastic meniscus in Fig. 5(b1) practically equals that of its water-glycerol counterpart [Fig. 5(b2)]. Figure 7 shows the meniscus length ℓ_m and the jet diameter d as a function of the flow rate Q for those two liquids. Steady jetting can be maintained for significant lower flow rates in the viscoelastic case. Although the jet diameter is similar for both fluids, the meniscus is significantly shorter in the viscoelastic case. The meniscus shrinkage must be attributed to elasticity because the Ohnesorge number is almost the same for the two liquids. Fluid particles undergo an intense extensional flow next to the meniscus interface dragged by the outer gas stream. In fact, the liquid velocity increases from values ~ 1 mm/s at the capillary exit up to the jet speed $v_j \sim 10$ m/s near the meniscus tip. This sharp increase takes place along distances $s \sim 100$ μm. The resulting strain rate, $\dot{\varepsilon} \simeq v_j/s \sim 10^5$ s^{-1}, is commensurate with the inverse of the extensional relaxation time λ_r^{-1} (see Fig. 4) for PEO100K, and the coil-stretch transition of the dissolved polymers occurs. The elastic stresses arising from that transition collaborate with those exerted by the outer flow in pushing the liquid throughout the meniscus-jet region. The resulting extra acceleration explains the meniscus shrinkage. When the flow rate is decreased, the jet speed near the meniscus tip increases [7], the meniscus length decreases (Fig. 7), and, therefore, the strain rate field in the meniscus increases. This effect enhances the building-up of the elastic stress, which explains why the meniscus shrinkage sharply increases as Q decreases.

Finally, if the polymer concentration is further increased, then the large tensile stress arising in the meniscus makes it detach from the needle edge and climb over the inner needle wall (the pull-out effect [28–30]). In this case, the final position of the triple contact line is essentially determined by the balance between the tensile force originating from the Poiseuille-like flow in the needle, and that exerted by the emitted jet. This pull-out phenomenon has frequently been observed in fiber spinning [28–30].

The transition from a quasi-Newtonian to viscoelastic behavior described above considerably alters the stability map of transonic flow focusing. Figure 8(a) shows the ejection modes adopted by our configuration for different concentrations of PEO100K. The smallness of the error bars shows the high degree of experimental reproducibility. For $c < c_1^*$ ($c_1^* \simeq 0.78\%$ wt), the minimum flow
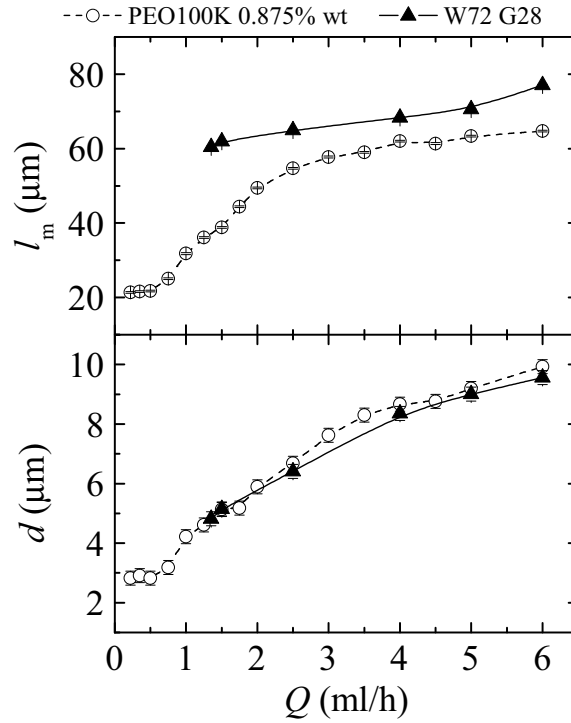
FIG. 7. Meniscus length ℓ_m and jet diameter d as a function of the flow rate Q for PEO100K at $c = 0.875\%$ wt (circles) and the water-glycerol mixture with the same Oh (triangles). The lowest flow rate in each case shows the corresponding stability limit. The experiments were conducted for $p_0 = 2.5$ bar.

rate $Q_{\min}$ leading to the jetting regime slightly increases with c. The same trend is observed for the water/glycerine (Newtonian) mixtures with the same Onhesorge numbers. Therefore, this effect can be attributed to the increase of the solution viscosity. At the critical concentration $c = c_1^*$, $Q_{\min}$ plunges. The critical flow rate remains almost constant in the interval $c_1^* < c < c_2^*$ ($c_2^* \simeq 1.13\%$ wt), and is around six times smaller than the value $Q_{\min} = 1.4$ ml/h measured for water-glycerol with a similar Ohnesorge number. The sharp decrease of $Q_{\min}$ at $c = c_1^*$ is caused by the coil-stretch transition also responsible for the meniscus shrinkage. As mentioned above, this transition triggers the polymeric force, which collaborates with the outer stream force in pushing the liquid throughout the critical meniscus-jet region. This effect helps the fluid to overcome the resistant viscous and surface tension forces emerging in that region. Finally, $Q_{\min}$ sharply increases at $c = c_2^*$. This effect is associated with the pull-out instability described above.

The results shown above indicate that, when PEO polymers of low molecular weights are dissolved in water at the appropriate concentration, the flow rate can be reduced in around one order of magnitude while keeping the steady jetting regime running. This reduction has important practical consequences because it allows one to produce much thinner jets than their Newtonian counterparts [see Figs. 7 and 8(b)]. For instance, the minimum jet diameter $d_{\min}$ (d at $Q = Q_{\min}$) of water becomes 2–3 times smaller when PEO100K molecules are dissolved at the concentration $c = 0.8125\%$ wt (Fig. 9). This minimum jet diameter is smaller than that expected from the Newtonian scaling law $d_{\min} \sim Q_{\min}^{0.808}$ [7], probably due to the increase of the extensional viscosity associated with the polymer stretching.

Interestingly, the jet's length drastically increased at $c = 0.75\%$ wt, i.e., the concentration just below the critical one c_1^*. In fact, we could not observe the breakage of viscoelastic jets for concentrations larger than that value (Fig. 9). This result indicates that the viscoelastic transition in the tapering meniscus and in the emitted jet occurs at practically the same concentrations.
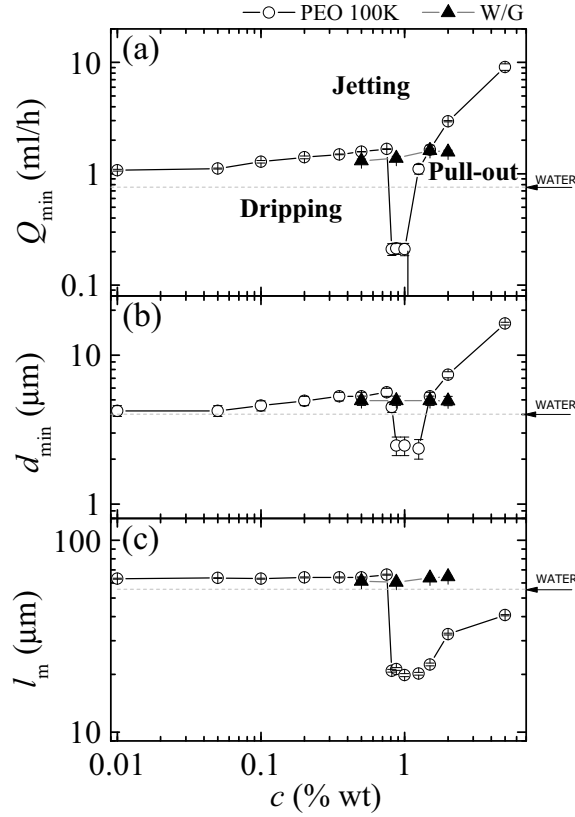
FIG. 8. (a) Ejection modes adopted by flow focusing. The symbols indicate the minimum flow rates leading to the jetting regime. (b) Jet diameter d_{min} at the minimum flow rate. The circles correspond to the viscoelastic solutions and the triangles to the water-glycerol mixtures with the same Ohnesorge number as the polymer solution of concentration c. The solid lines are guides to the eye. The horizontal dashed line indicates the minimum flow rate and diameter for water. The experiments were conducted for $p_0 = 2.5$ bar.

We analyze the effect of the outer stream stagnation pressure p_0 on the viscoelastic transition in Fig. 10. The critical concentration c_1^* hardly depends on p_0. This can be explained as follows. The transonic gas flow is chocked for all the stagnation pressures applied in the experiments, which implies that the viscous driving force exerted by the outer stream on the liquid meniscus remains practically constant when p_0 is varied [7]. Therefore, the strain rate field induced by the outer stream in the liquid meniscus slightly depends on p_0, which means that the coil-stretch transition comes into play practically at the same polymer concentration c_1^*. As explained above, the pull-out instability results from the imbalance between the normal stresses at the inlet and outlet sections of the meniscus. The variation of p_0 does affect the hydrostatic pressure distribution along the meniscus axis. This explains why the critical concentration c_2^* increases for small stagnation pressures, which implies that the optimum interval of c leading to the flow stabilization increases as p_0 decreases.

Results similar to those of PE0100K have also been obtained for other low-molecular-weight polymers, such as PEO200K and PEO600K (Fig. 11). The curves $Q_{min}(c)$ and $d_{min}(c)$ shift towards lower concentrations when the molecular weight is increased. This occurs because the extensional relaxation time λ_r increases with the molecular weight, and, therefore, it exceeds the threshold leading to the coil-stretch transition for lower concentrations. In fact, the values of λ_r for PEO100K and PEO600K at their respective critical concentrations c_1^* are commensurate with each other (see Fig. 4). The decrease in Q_{min} at the critical concentration c_1^* becomes smaller as the molecular
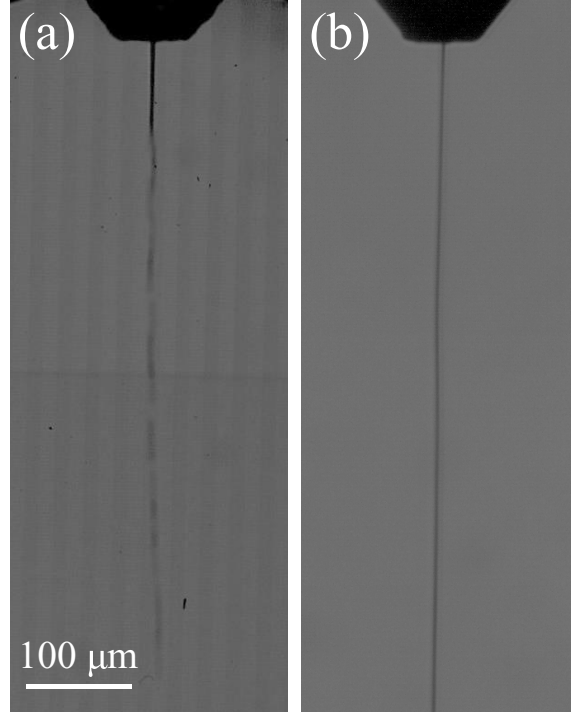
FIG. 9. Comparison of the jets emitted at the corresponding minimum flow rate: (a) water at $Q = 0.75$ ml/h and (b) PEO100K at $c = 0.8125\%$ and $Q = 0.2$ ml/h. The experiments were conducted for $p_0 = 2.5$ bar.

weight increases. Our experiments for molecular weights greater than 600K (i.e., for PEO1M and PEO2M) showed the pull-out effect at all the polymer concentrations.

As mentioned above, the viscoelastic transition takes place when the strain rate in the tapering meniscus exceeds the critical value leading to the coil-stretch transition. For this reason, we define the Weissenberg number $\mathrm{Wi} = \lambda_r \langle \dot{\varepsilon} \rangle$, where $\langle \dot{\varepsilon} \rangle = v_\ell / \ell_m$ is the mean strain rate along the meniscus axis. Here, v_ℓ is the liquid velocity at the end of the meniscus and ℓ_m the meniscus length, as mentioned above.
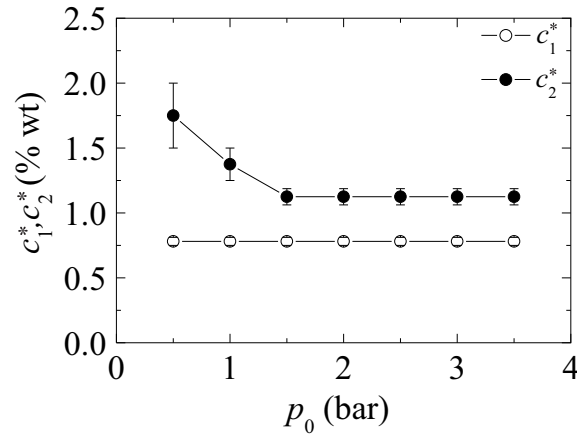

FIG. 10. Critical concentrations c_1^* and c_2^* as a function of the outer stream stagnation pressure p_0 for PEO100K.
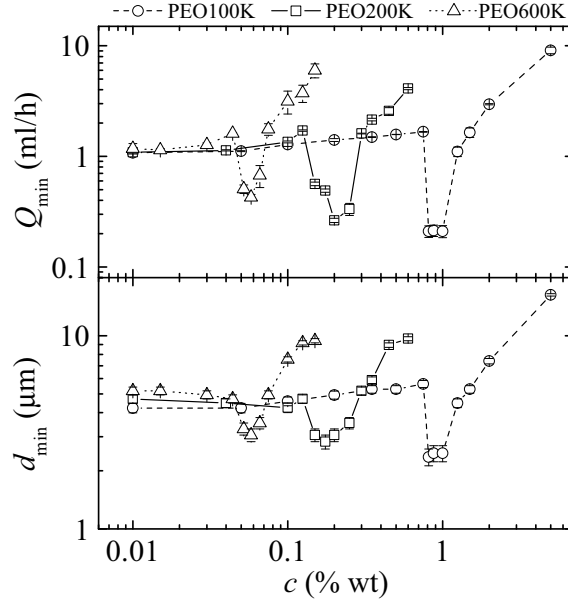
FIG. 11. Minimum flow rates leading to the jetting regime and the corresponding diameters for polymer solutions with different molecular weights.

In the low-viscosity Newtonian case, the flow instability is believed to be caused by the growth of recirculation cells in the tapering meniscus for small flow rates [27,31]. This mechanism is controlled by the liquid shear viscosity. For this reason, the minimum flow rate Q_{min} scales as the characteristic flow rate $Q_D = D_n \eta / \rho$ [27,31,32], defined in terms of the shear viscosity η. In the high-viscosity Newtonian case, viscous stresses "arrange" the streamlines and "direct" the flow in the meniscus tip. The recirculation cells disappear, and the instability is determined by the balance between the pressure drop and surface tension [27]. Then, the minimum flow rate scales as $Q_v = D_n^2 \gamma / \eta_e$. The inclusion of the Newtonian extensional viscosity $\eta_e = 3\eta$ (instead of η) in the definition of Q_v does not significantly change the scaling of Montanero *et al.* [27] because it only introduces a constant factor. The viscosity of the water-glycerol mixtures ranges from 1.8 to 6.2 mPa s, which corresponds to a moderately low viscosity regime. As expected, Q_{min} is of the order of Q_D for these liquids.

In this work, we propose the natural extension of the above scaling for Newtonian liquids to the weakly viscoelastic case. For $c < c_1^*$, the tapering meniscus can be regarded as a Newtonian low-viscosity meniscus. Therefore, the minimum flow rate is expected to scale as Q_D [31,32]. For $c > c_1^*$, the stretching of the polymer chains drastically increases the solution extensional viscosity η_e, and the minimum flow rate is expected to scale as Q_v. When the coil-stretch transition takes place, the scale of the extensional viscosity can be calculated as $\eta_e = 3\lambda_r \gamma / d_\ell$ [23], where d_ℓ is the diameter at the meniscus end. The above scaling leads to the following definition of the dimensionless minimum flow rate:

$$\Phi = \begin{cases} \mathrm{Re} = Q_{min}/Q_D & \text{for } c < c_1^* \\ \mathrm{Ca} = Q_{min}/Q_v & \text{for } c > c_1^*. \end{cases} \tag{1}$$

The dimensionless number Φ reduces to the Reynolds number based on the shear viscosity η for $c < c_1^*$ and the capillary number based on the extensional viscosity η_e beyond the viscoelastic transition.

Figure 12 shows $\Phi(\mathrm{Wi})$ for the two polymers with considerably different molecular weights, PEO100K and PEO600K. The two curves practically overlap, which shows the validity of our scaling. The viscoelastic transition takes place around $\mathrm{Wi} = 1/2$, the critical value for the coil-stretch
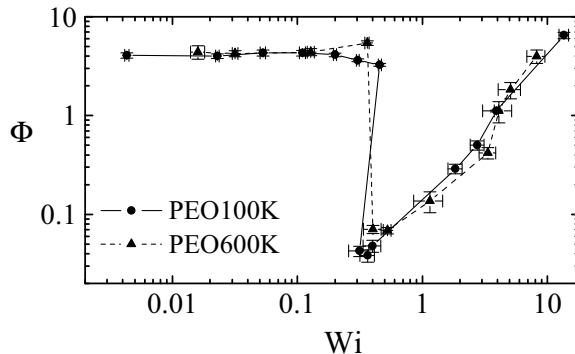
FIG. 12. $\Phi(Wi)$ for PEO100K and PEO600K. Experiments were conducted for $p_0 = 2.5$ bar.

transition in a simple extensional flow [23,33]. This result confirms that the sharp decrease of the minimum flow rate and, consequently, the minimum jet diameter is caused by the coil-stretch transition triggered by the large strain rate arising in the flow focusing meniscus. The Reynolds number (Φ for $c < c_1^*$) takes an approximately constant value, which indicates that the minimum flow rate scales as the viscosity. The values of the Reynolds number are similar to those of Newtonian low-viscosity menisci [27]. The capillary number (Φ for $c > c_1^*$) takes values of the same order of magnitude as that of the Newtonian high-viscosity case [27]. The experimental realizations for large Wi are affected by the pull-out instability. In this case, the triple contact line detaches from the capillary edge, and the balance between the spinning force and the normal stress in the feeding capillary determines the new position of the meniscus inside the capillary [30] (see Fig. 4 in Ref. [13]). We do not have a definitive explanation of the power law followed by $\Phi(Wi)$ when the triple contact line is detached.

IV. CONCLUSIONS

We have analyzed the viscoelastic transition occurring in transonic flow focusing when polymers of low molecular weights are added to water at an adequate concentration. This phenomenon is caused by the coil-stretch transition of polymers in the tapering meniscus. Despite the smallness of their relaxation time, the large strain rate produced by the transonic outer stream manages to stretch the polymers. The elastic stresses built up in the meniscus shrink it and stabilize the flow, which reduces the minimum flow rate for which the jetting regime is obtained. The phenomenon described above is reproducible and robust. It appears for a wide range of gas stagnation pressures and polymers with different molecular weights. When working in the appropriate parameter window, the flow rate and the jet diameter in transonic flow focusing can be reduced in one order of magnitude.

Our scaling analysis for the minimum flow rate reveals the role played by the polymer relaxation time and extensional viscosity in the viscoelastic transition. This transition takes place for Weissenberg numbers around 0.5. The Reynolds number takes values of order unity for subcritical realizations ($c < c_1^*$), as occurs in the Newtonian low-viscosity case [31,32]. For supercritical polymer concentrations ($c > c_1^*$), the capillary number, defined in terms of the polymer extensional viscosity, is a function of the Weissenberg number. The smaller values taken by the capillary number are similar to those of the Newtonian high-viscosity case [27].

The discontinuity seen in Fig. 12 is inherent to the viscoelastic transition taking place at $c = c_1^*$ and cannot be smoothed by an alternative scaling. In fact, the coil-stretch transition alters the microscopic structure of the focused liquid, and, therefore, the fluid behavior is expected to be fundamentally different beyond the critical concentration.

A natural question is whether polymers may suffer some kind of degradation or entanglement during the liquid ejection for the critical conditions. In principle, this possibility could be tested

by conducting extensional rheometry after the liquid ejection. However, measuring extensional relaxation times below 50 μs is very challenging [25]. The problem becomes even more complicated when one has to collect the sample after the ejection because contamination and/or evaporation would make the measurement unreliable.

The results presented in this paper may be of interest for researchers working in several fields, such as microfluidics, pharmacy, biotechnology, and crystallography. In essence, we have found a small parameter window within which much thinner jets can be produced with flow focusing. In our experiments, the water jet diameter was reduced in one order of magnitude without substantially changing its chemical composition (the polymer molecular weight and concentration were very small), which enhances the applications of flow focusing, particularly in highly demanding and important applications such as SFX.

[1] A. M. Gañán-Calvo, Generation of Steady Liquid Microthreads and Micron-Sized Monodisperse Sprays in Gas Streams, Phys. Rev. Lett. **80**, 285 (1998).

[2] D. P. DePonte, U. Weierstall, K. Schmidt, J. Warner, D. Starodub, J. C. H. Spence, and R. B. Doak, Gas dynamic virtual nozzle for generation of microscopic droplet streams, J. Phys. D: Appl. Phys. **41**, 195505 (2008).

[3] A. J. Acero, C. Ferrera, J. M. Montanero, and A. M. Gaán-Calvo, Focusing liquid microjets with nozzles, J. Micromech. Microeng. **22**, 065011 (2012).

[4] H. N. Chapman *et al.*, Femtosecond X-ray protein nanocrystallography, Nature (London) **470**, 73 (2011).

[5] S. Boutet *et al.*, High-resolution protein structure determination by serial femtosecond crystallography, Science **337**, 362 (2012).

[6] P. Huerre and P. A. Monkewitz, Local and global instabilites in spatially developing flows, Annu. Rev. Fluid Mech. **22**, 473 (1990).

[7] M. Rubio, A. Rubio, M. G. Cabezas, M. A. Herrada, A. M. Gañán-Calvo, and J. M. Montanero, Transonic flow focusing: Stability analysis and jet diameter, Int. J. Multiphase Flow **142**, 103720 (2021).

[8] A. M. Gañán-Calvo, R. González-Prieto, P. Riesco-Chueca, M. A. Herrada, and M. Flores-Mosquera, Focusing capillary jets close to the continuum limit, Nat. Phys. **3**, 737 (2007).

[9] A. M. Gañán-Calvo, J. M. Montanero, L. Martín-Banderas, and M. Flores-Mosquera, Building functional materials for health care and pharmacy from microfluidic principles and Flow Focusing, Adv. Drug Deliv. Rev. **65**, 1447 (2013).

[10] T. Si, G. B. Li, Q. Wu an Z. Q. Zhu, X. S. Luo, and R. X. Xu, Optical droplet vaporization of nanoparticle-loaded stimuli-responsive microbubbles, Appl. Phys. Lett. **108**, 111109 (2016).

[11] K. V. Edmond, A. B. Schofield, M. Marquez, J. P. Rothstein, and A. D. Dinsmore, Stable jets of viscoelastic fluids and self-assembled cylindrical capsules by hydrodynamic focusing, Langmuir **22**, 9052 (2006).

[12] L. Derzsi, M. Kasprzyk, J. P. Plog, and P. Garstecki, Flow focusing with viscoelastic liquids, Phys. Fluids **25**, 092001 (2013).

[13] A. Ponce-Torres, J. M. Montanero, E. J. Vega, and A. M. Gañán-Calvo, The production of viscoelastic capillary jets with gaseous flow focusing, J. Non-Newtonian Fluid Mech. **229**, 8 (2016).

[14] E. Hofmann, K. Krüger, C. Haynl, T. Scheibel, M. Trebbin, and S. Förster, Microfluidic nozzle device for ultrafine fiber solution blow spinning with precise diameter control, Lab Chip **18**, 2225 (2018).

[15] A. Ponce-Torres, E. J. Vega, A. A. Castrejón-Pita, and J. M. Montanero, Smooth printing of viscoelastic microfilms with a flow focusing ejector, J. Non-Newtonian Fluid Mech. **249**, 1 (2017).

[16] A. Ponce-Torres, E. Ortega, M. Rubio, A. Rubio, E. J. Vega, and J. M. Montanero, Gaseous flow focusing for spinning micro and nanofibers, Polymer **178**, 121623 (2019).

[17] R. Vasireddi, J. Kruse, M. Vakili, S. Kulkarni, T. F. Keller, D. C . F. Monteiro, and M. Trebbi, Solution blow spinning of polymer/nanocomposite micro-/nanofibers with tunable diameters and morphologies using a gas dynamic virtual nozzle, Sci. Rep. **9**, 14297 (2019).

[18] D. F. James, Boger fluids, Annu. Rev. Fluid Mech. **41**, 129 (2009).

[19] G. H. McKinley and A. Tripathi, How to extract the Newtonian viscosity from capillary breakup measurements in a filament rheometer, J. Rheol. **44**, 653 (2000).

[20] S. L. Anna and G. H. McKinley, Elasto-capillary thinning and breakup of model elastic liquids, J. Rheol. **45**, 115 (2001).

[21] A. Peterlin, Hydrodynamics of linear macromolecules, Pure Appl. Chem. **12**, 563 (1966).

[22] R. B. Bird, R. C. Armstrong, and O. Hassager, *Dynamics of Polymeric Liquids Volume I: Fluid Mechanics; Volume II: Kinetic Theory* (Wiley, New York, 1987).

[23] J. Eggers and E. Villermaux, Physics of liquid jets, Rep. Prog. Phys. **71**, 036601 (2008).

[24] K. Takamura, H. Fischer, and N. R. Morrow, Physical properties of aqueous glycerol solutions, J. Pet. Sci. Eng. **98–99**, 50 (2012).

[25] M. Rubio, A. Ponce-Torres, E. J. Vega, and J. M. Montanero, Experimental analysis of the extensional flow of very weakly viscoelastic polymer solutions, Materials **13**, 192 (2020).

[26] P. E. Rouse, A theory of the linear viscoelastic properties of dilute solutions of coiling polymers, J. Chem. Phys. **21**, 1272 (1953).

[27] J. M. Montanero, N. Rebollo-Muñoz, M. A. Herrada, and A. M. Gañán-Calvo, Global stability of the focusing effect of fluid jet flows, Phys. Rev. E **83**, 036309 (2011).

[28] T. Sridhar and R. K. Gupta, Fluid detachment and slip in extensional flows, J. Non-Newtonian Fluid Mech. **30**, 285 (1988).

[29] M. J .H. Bulters and H. E. H. Meijer, Analogy between the modelling of pullout in solution spinning and the prediction of the vortex size in contraction flows, J. Non-Newtonian Fluid Mech. **38**, 43 (1990).

[30] C. van der Walt, M. A. Hulsen, A. C. B. Bogaerds, H. E. H. Meijer, and M. J. H. Bulters, Stability of fiber spinning under filament pull-out conditions, J. Non-Newtonian Fluid Mech. **175-176**, 25 (2012).

[31] M. A. Herrada, A. M. Gañán-Calvo, A. Ojeda-Monge, B. Bluth, and P. Riesco-Chueca, Liquid flow focused by a gas: Jetting, dripping, and recirculation, Phys. Rev. E **78**, 036323 (2008).

[32] T. Si, F. Li, X.-Y. Yin, and X.-Z. Yin, Modes in flow focusing and instability of coaxial liquid-gas jets, J. Fluid Mech. **629**, 1 (2009).

[33] V. M. Entov and E. J. Hinch, Effect of a spectrum of relaxation times on the capillary thinning of a filament of elastic liquid, J. Non-Newtonian Fluid Mech. **72**, 31 (1997).

9. Paper VI - Viscoelastic transition in transonic flow focusing.

10

Paper VII - Unexpected stability of micrometer weakly viscoelastic jets.

A. Rubio, E. J. Vega, A. M. Gañán-Calvo, et al.

View Online   Export Citation   CrossMark

ARTICLES YOU MAY BE INTERESTED IN

On Oreology, the fracture and flow of "milk's favorite cookie®"
Physics of Fluids **34**, 043107 (2022); https://doi.org/10.1063/5.0085362

Interface evolution characteristics of dual droplet successive oblique impact on liquid film
Physics of Fluids **34**, 062115 (2022); https://doi.org/10.1063/5.0096585

Lagrangian filtered density function modelling of a turbulent stratified flame combined with flamelet approach
Physics of Fluids (2022); https://doi.org/10.1063/5.0093942

Physics of Fluids

AIP Publishing

Unexpected stability of micrometer weakly viscoelastic jets

A. Rubio,[1] (ID) E. J. Vega,[1] (ID) A. M. Gañán-Calvo,[2] (ID) and J. M. Montanero[1,a)] (ID)

AFFILIATIONS

[1]Depto. de Ingeniería Mecánica, Energética y de los Materiales and Instituto de Computación Científica Avanzada (ICCAEx),
 Universidad de Extremadura, E-06006 Badajoz, Spain
[2]Departamento de Mecánica de Fluidos e Ingeniería Aeroespacial, Universidad de Sevilla, E-41092 Sevilla, Spain

[a)]Author to whom correspondence should be addressed: jmm@unex.es

ABSTRACT

We study experimentally the stability of micrometer weakly viscoelastic jets produced with transonic flow focusing. Highly stable jets are formed when a low molecular weight polymer is added to water at a given low concentration, and the injected flow rate is reduced to its minimum value. In this case, the capillary instability is delayed, and the jet breakup occurs at distances from the ejector of the order of tens of thousands the jet diameter. The results indicate that the intense converging extensional flow in the ejection point builds up viscoelastic stress that does not relax in the jet even for times much longer than the polymer relaxation time. We hypothesize that the drag (shear) force exerted by the outer gas stream prevents the stress relaxation. It is also possible that partial polymer entanglement at the jet emission point contributes to this effect. We measure the jet length and the diameter at the ejector orifice and breakup point. The diameter takes values just above 2 μm at the breakup point regardless of the liquid flow rate and gas pressure.

Published under an exclusive license by AIP Publishing. https://doi.org/10.1063/5.0091095

I. INTRODUCTION

Many dilute polymer solutions exhibit a practically constant viscosity (shear thinning behavior can be neglected) over a wide range of shear rates[1] so that the major polymer effects are the increase in the solution viscosity and elasticity. The elastic response of the polymer solution to a straining flow is quantified by the so-called extensional relaxation time λ_r, measured in filament thinning rheometers, such as CaBER[2] and FiSER.[3]

Flows with sufficiently high strain rates compared to λ_r^{-1} can cause the so-called coil-stretch transition of the dissolved polymer molecules, producing a sharp increase in the viscoelastic stress.[4] For instance, the coil-stretch transition takes place in a simple extensional flow described by the Oldroyd-B[5] or FENE-P[4] model when the strain rate $\dot{\varepsilon}$ exceeds the threshold $\dot{\varepsilon} = 1/(2\lambda_r)$.[6,7] The polymer chains recoil back to their equilibrium conformation if the strain rate decreases below the critical value. This relaxation process occurs at times of the order of λ_r.

In the framework of the Oldroyd-B model,[5] the local temporal linear stability of viscoelastic jets is determined by the Ohnesorge and Deborah numbers, and the viscosity ratio,[8]

$$\text{Oh} = \eta(\rho\sigma d)^{-1/2}, \quad \text{De} = \frac{\lambda_r}{t_c}, \quad \eta_r = \frac{\eta_s}{\eta}, \qquad (1)$$

where ρ, η, and σ are the solution density, viscosity, and surface tension, respectively, d is the jet diameter, $t_c = (\rho d^3/\sigma)^{1/2}$ is the inertio-capillary time, and η_s is the solvent viscosity. The elasticity number

$$El = \text{Oh}\,\text{De} = \lambda_r\eta/(\rho d^2) \qquad (2)$$

is frequently used to quantify the elastic effects as well. The solution of the Oldroyd-B model[5] shows that a relaxed (i.e., in the absence of polymeric axial stress) viscoelastic jet is more unstable than its Newtonian counterpart (i.e., that with the same Ohnesorge number) due to the apparent shear thinning caused by viscoelasticity.[9,10] Specifically, the growth rate of the dominant mode increases with the Deborah number. In addition, the critical Weber number We $= \rho v_j^2 d/(2\sigma)$ (v_j is the jet velocity) leading to the convective-to-absolute instability transition[11] decreases as De increases.[12] This means that a relaxed viscoelastic jet breaks up faster than the corresponding Newtonian one.[13]

Axial elastic stresses are almost always built up during the ejection of viscoelastic threads.[14,15] The presence of unrelaxed elastic tension in the jet drastically increases the extensional viscosity, which reduces the growth rate of both axisymmetric[16–18] and lateral (bending)[7] modes. The unrelaxed stress also affects the Weber number at the convective-to-absolute instability transition in a non-trivial way.[19]

The axial polymer stress explains the high stability exhibited by viscoelastic jets in many experiments.

The upper-convected Maxwell model[4] is an appropriate constitutive equation for viscoelastic liquids experiencing strong uniaxial stretching.[7] The combination of the upper-convected Maxwell model and the 1D approximation[20] leads to the following equation for the axial deviatoric stress τ_{zz} in an aerodynamically driven viscoelastic jet[7]

$$v_j \frac{d\tau_{zz}}{dz} = 2 \frac{dv_j}{dz} \tau_{zz} + \frac{2\eta}{\lambda_r} \frac{dv_j}{dz} - \frac{\tau_{zz}}{\lambda_r}. \tag{3}$$

The drag force exerted by the outer gaseous medium does not explicitly appear in Eq. (3), but implicitly through the (mean) velocity profile $v_j(z)$ adopted by the jet along the axial coordinate z. If one assumes that $dv_j/dz \simeq$ const., the integration of (3) approximately gives[7]

$$\tau_{zz} = \tau_{zz}^0 \exp\left[-\left(1/\lambda_r - 2\,dv_j/dz\right)(t - t_0)\right], \tag{4}$$

where τ_{zz}^0 is the axial deviatoric stress at $t = t_0$. If the jet acceleration dv_j/dz can be neglected (quasi-cylindrical jets), then τ_{zz} decreases exponentially both along the distance from the ejector and in time. The relaxation length and time are $v_j\lambda_r$ and λ_r, respectively. This behavior has been observed in, for instance, viscoelastic electrospun jets.[15] In this case, experiments show that the axial deviatoric stress τ_{zz} of a jet material element decays exponentially over a time approximately given by λ_r (slightly corrected by the jet acceleration). In other words, the electrospun jet acceleration is sufficiently weak (according to the polymer rheology terminology) for the stress relaxation to follow the expression $\tau_{zz} \propto \exp(-t/\lambda_r)$.[7]

A high-speed coflowing gas stream can not only accelerate the jet but also produce a velocity gradient in the radial direction. In fact, the liquid resistance to shear stress can be much smaller than to the extensional one owing to the strong anisotropy of the stretched liquid thread. The shear rate at the free surface of an aerodynamically driven Oldroyd-B jet produces an axial stress given by the expression[18]

$$\tau_{zz} = 2\,\rho\,v_j^2\,(1 - \eta_r)\,El\,\dot{\gamma}^2, \tag{5}$$

where $\dot{\gamma} = w'\,d/v_j$ is the dimensionless shear rate evaluated at the free surface and $w'(r)$ the derivative of the axial velocity w with respect to the radial coordinate r. The elasticity number El takes values much greater than unity in micrometer jets even for polymer relaxation times of the order of tens of microseconds and solution viscosities of the order of that of water. For this reason, significant axial stress τ_{zz} can be generated even if $\dot{\gamma}$ is smaller than unity. As will be shown, this may be the case in our experiments.

The capillary instability in a viscoelastic jet is followed by a non-linear phase in which a thin cylindrical thread connects two consecutive drops (beads), giving rise to the so-called Beads-on-a-String (BOAS) morphology.[9,21–23] The surface tension drives the thread thinning against the growing axial stress caused by the elasticity of the dissolved polymer molecules. In this elasto-capillary regime, the thread diameter decreases following an exponential function, which delays the jet breakup a few extensional relaxation times.[3,24]

As mentioned above, the viscoelastic axial stress has a strong stabilizing effect. For this reason, the capillary instability leading to the BOAS structure is expected to arise once the viscoelastic stress has relaxed. In quasi-cylindrical jets ($dv_j/dz \simeq 0$), this occurs at flight times of the order of λ_r or at distances from the ejector of the order of $v_j\lambda_r$. As will be shown in Sec. IV A, jets flow-focused under certain particular conditions challenge this expectation. These jets exhibit some "elastic hysteresis:" the extensional viscosity does not fall back to its zero strain rate value downstream. For this reason, the BOAS instability is delayed, and, more importantly, the jet flows without breaking up in the region considered in our experiments.

This paper will analyze experimentally the stability of weakly viscoelastic jets produced by transonic flow focusing. We will examine the jet shape to determine the jet acceleration and the distance from the orifice at which the BOAS and whipping instabilities arise. Special attention will be paid to the diameter at the ejector orifice, as well as the breakup length and diameter.

II. VISCOELASTIC FLOW FOCUSING

The viscoelastic version[25] of gaseous flow focusing (GFF)[26] is probably the ideal candidate to produce straight weakly viscoelastic jets very few micrometers in diameter. In this technique (see Fig. 1), the polymer solution is injected at a constant flow rate Q through a capillary around $100\,\mu m$ in diameter. A transonic gas stream coflows with the liquid through a nozzle driven by a stagnation pressure p_0. The liquid is accelerated in front of the discharge orifice by the gaseous current to form a liquid meniscus, which emits a very thin jet from its tip.[25,26] The viscous shear stress exerted by the gas stream accelerates the jet beyond the discharge orifice reducing the jet diameter down to values close to $1\,\mu m$. The liquid and gaseous streams discharge into a partial vacuum, which suppresses the aerodynamic whipping (bending) instability. In this way, thin and straight jets of weakly viscoelastic polymeric solutions can be produced with velocities up to around $30\,m/s$.[27]

GFF offers several advantages over other tip streaming techniques such as electrospinning,[28] solution blowing (SB),[7,29] and solution

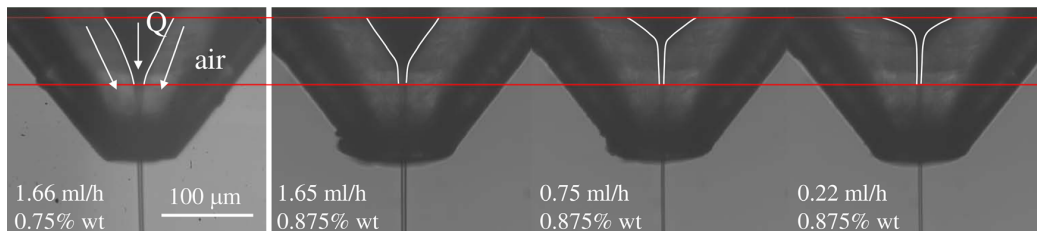**FIG. 1.** Viscoelastic gaseous flow focusing. Meniscus shape for an aqueous solution of polyethylene oxide polymers of molecular weight $M_w = 100 \times 10^3$ g/mol.[27] The labels indicate the liquid flow rate and the polymer concentration. In all the experiments, the air stagnation pressure was $p_0 = 2.5$ bar. The white lines mark the meniscus profile, and the red lines are a guide to the eye.

blow spinning (SBS).[30] In the electrospinning of leaky-dielectric[31] liquids, the required electrical properties limit the range of applicability of the technique. In addition, the electric field complicates the analysis and promotes the jet whipping instability.[32] There are noticeable differences between viscoelastic GFF and the SB/SBS technique commonly employed to produce micro- and nanometer fibers by aerodynamic means. While GFF takes advantage of the focusing effect caused by the high-speed gas stream in front of the discharge orifice, the gaseous current in SB/SBS interacts with the polymer jet only beyond the orifice. For this reason, the axial polymer stress is built up in the tapering meniscus of GFF, while in SB/SBS, this process occurs inside the solid nozzle. One can state that GFF ejects the viscoelastic thread through a "fluid nozzle" whose shape changes with the injected liquid flow rate.

GFF and SB/SBS operate differently beyond the discharge orifice as well. The velocity of the coflowing gas stream is commensurate with the sound speed in both GFF and SB/SBS. However, the gas density is much lower in GFF,[27] which reduces the dynamical pressure and, therefore, inhibits the whipping instability.[7] The reduction of the gas density does not essentially affect the driving viscosity force. This allows GFF to produce almost straight, fast polymer jets over long distances. Finally, the liquid jet in GFF moves much faster than that formed in SB/SBS. This suppresses the solvent evaporation in GFF, at least in the region analyzed in our experiments. Viscoelastic GFF has been applied only to a limited range of polymer solutions. The conditions for its extension to other liquids are yet to be determined.

Rubio et al.[27] have recently analyzed the viscoelastic transition occurring in transonic GFF when polyethylene oxide (PEO) polymers of low molecular weights M_w are added to water at an adequate concentration. For the sake of completeness, here we summarize the major results of that work.

When working in the appropriate parameter window, the liquid flow rate and the jet diameter can be reduced in one order of magnitude with respect to the corresponding values in the Newtonian case. Figure 2 shows the minimum liquid flow rate, Q_{min}, for which steady jetting can be produced with PEO solutions with $M_w = 100 \times 10^3$ g/mol (PEO100K) and 600×10^3 g/mol (PEO600K). For $c < c_1^*$ ($c_1^* \simeq 0.78$

and 0.048 wt. % for PEO100K and PEO600K, respectively), Q_{min} slightly increases with c due to the increase in the solution viscosity. At the critical concentration $c = c_1^*$, Q_{min} plunges. The minimum flow rate remains almost constant in the small interval $c_1^* < c < c_2^*$ ($c_2^* \simeq 1.13$ and 0.071 wt. % for PEO100k and PEO600K, respectively). Finally, Q_{min} sharply increases at $c = c_2^*$ owing to the pull-out instability,[33] which prevents the pinning of the triple contact line to the capillary edge.[27]

The viscoelastic transition described above can be explained by the coil-stretch transition undergone by the polymers in the tip of the tapering meniscus. Despite the smallness of the polymer relaxation time, the large strain rate produced by the transonic gas stream manages to stretch the polymers if $c_1^* < c < c_2^*$ and $Q \simeq Q_{min}$. The elastic stress shrinks the meniscus (Fig. 1) and stabilizes the flow, which reduces the minimum flow rate for which the jetting regime can be obtained.

Rubio et al.[27] did not study the behavior of the jets produced with GFF. The present work analyzes experimentally the stability, diameter, and length of the viscoelastic jets emitted with GFF. Special attention is paid to those produced under the critical conditions $c_1^* < c < c_2^*$ and $Q \simeq Q_{min}$, which exhibit an unexpected stability.

The present study also examines the viscoelastic transition when polyvinylpyrrolidone (PVP) with $M_w = 360 \times 10^3$ g/mol (PVP360K) is dissolved in water, which shows that this transition is not exclusive to PEO solutions. As can be observed in Fig. 3, Q_{min} gradually decreases as c increases until it reaches its minimum value $Q_{min} \simeq 0.34$ ml/h for $c^* \simeq 1.5$ (wt. %). For $c > c^*$, the pull-out instability arises, and Q_{min} sharply increases. As occurs with PEO100K, the viscoelastic stress stabilizes the flow when PVP360K is dissolved at the appropriate concentration. However, the viscoelastic transition for PVP360K exhibits two distinct features: (i) for $c < c^*$, Q_{min} decreases gradually as c increases instead of plunging at the critical concentration c_1^*; and (ii) the minimum value of $Q_{min}(c)$ is reached at the concentration $c^* \simeq 1.5$ (wt. %) instead of in the interval $c_1^* < c < c_2^*$.

The absence of the optimum interval $c_1^* < c < c_2^*$ for PVP360K is caused by the earlier irruption of the pull-out instability in this case.
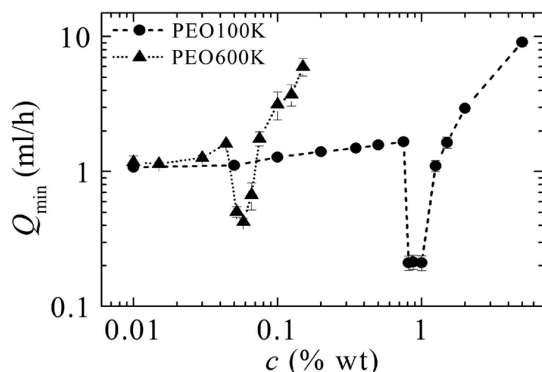

FIG. 2. Minimum flow rates leading to the jetting regime for aqueous solutions of PEO100K and PEO600K Reproduced with permission from Rubio et al., "Viscoelastic transition in transonic flow focusing," Phys. Rev. Fluid ■, ■ (2022). Copyright 2022 ■.[27] The air stagnation pressure was $p_0 = 2.5$ bar.
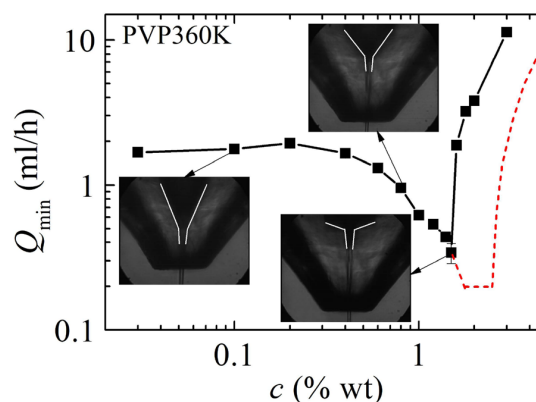

FIG. 3. Minimum flow rates leading to the jetting regime for aqueous solutions of PVP360K. The air stagnation pressure was $p_0 = 1.1$ bar. The dashed line represents the hypothetical (not measured in the experiments) values of $Q_{min}(c)$ if the polymer relaxation time were sufficiently small for the pull-out instability to be shifted toward larger concentrations.

TABLE I. Density ρ, shear viscosity η, surface tension σ, relaxation time λ_r, and overlap concentration c_{ov} for the PEO and PVP solutions.

Liquid	ρ (kg/m^3)	η (mPa · s)	σ (mN/m)	λ_r (μs)	c_{ov} (% wt)
PEO100K 0.75%	1000	1.89	60.5	19.5	0.72
PEO100K 1%	1000	2.33	60	26.2	0.72
PEO600K 0.044%	999	1.11	60	12.1	0.19
PEO600K 0.058%	999	1.12	59.3	19.5	0.19
PVP360K 1.5%	999	4.07	62	53.6	0.57

This instability is enhanced by the larger polymer relaxation time (extensional viscosity) of the PVP360K solution for $c^* \simeq 1.5$ (wt. %) (see Table I in Sec. III). To illustrate this comment, the dashed line in Fig. 3 represents the hypothetical (not measured in the experiments) values of $Q_{min}(c)$ if the polymer relaxation time was sufficiently small for the pull-out instability to be shifted toward larger concentrations. It is worth noting that polymer solutions with moderate and high molecular weights are characterized by polymer relaxation times greater than 100 μs even for very small concentrations. In this case, the pull-out instability is expected to arise for concentrations smaller than those leading to the flow stabilization. This explains why the viscoelastic transition described in this section has been observed only for low-molecular-weight polymers.

III. EXPERIMENTAL METHOD

Figure 4 depicts the main elements of the experimental setup. The flow focusing ejector was printed using Nanoscribe Photonic Professional GT2 with the Dip-in Laser Lithography (DiLL) configuration, as described by Rubio et al.[27] The ejector consists of a sharp inner capillary 75 μm in diameter coaxially placed inside a converging nozzle. The capillary edge is located at a distance of 180 μm from the nozzle orifice, whose diameter is 75 μm. The viscoelastic liquid was injected across the inner capillary at a constant flow rate with a syringe pump (LEGATO210, KD-SCIENTIFIC). The focusing airstream was
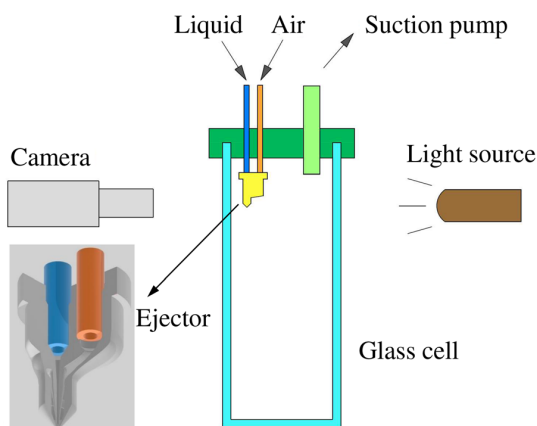
FIG. 4. Ejector and rest of elements of the experimental setup.

established by setting an upstream stagnation pressure $p_0 = 1.1$ bar unless the contrary is expressly stated. We mounted the ejector onto the cap of a discharge glass cell and established a pressure of 15 mbar inside the cell using a suction pump.

We used a high-speed video camera (KIRANA) to take digital images of the jet at 5×10^6 fps. The camera was equipped with optical lenses (NAVITAR 12×) and a microscope objective (OPTEM 20×) and was illuminated with white back-lighting. The images consisted of 974 × 768 pixels. The magnification was 7×, which resulted in 0.222 μm/pixel. We illuminated the jet with a laser (SI-LUX 640, SPECIALIZED IMAGING) synchronized with the camera, which reduced the effective exposure time down to 150 ns. The camera could be displaced vertically using a triaxial translation stage with its vertical axis motorized (THORLABS Z825B) and controlled by the computer. To examine the jet behavior at different jet stations, this displacement was conducted in steps of 0.5 or 1 mm depending on the jet length. The images were analyzed to measure the jet diameter with pixel resolution at those stations. For some representative cases, we repeated the experiment several times. We concluded that the experimental uncertainty in the jet diameter measurement was around one-pixel size.

We observed the jet at each camera position over several seconds to determine the station at which the BOAS and whipping instabilities appeared. We considered that the BOAS instability was present if the diameter increased more than 10% of its average value in that jet station. Analogously, we considered that the whipping instability was present if there were bending oscillations with amplitudes greater than twice the jet diameter.

We used aqueous solutions of PEO100K, PEO600K, and PVP360K (Sigma Aldrich) at different concentrations c. We prepared stock polymeric solutions by dissolving the polymers in de-ionized water with a magnetic stirrer for five days at low angular speeds to minimize mechanical degradation of the polymer chains. The density ρ was measured with a pycnometer of 10 ± 1 ml and a precision balance, while the surface tension σ was determined with the TIFA method.[34] The shear viscosity η of these fluids has recently been measured as a function of the shear rate using a stress-controlled rotational rheometer.[27] These solutions can be regarded as low-viscosity Boger (shear-thinning free) fluids.[27]

The dependence of the relaxation time λ_r on the polymer concentration has been determined from a variant of CaBER-DoS rheometry[35] in which tiny droplets were broken before they were deposited on the substrate.[36] Figure 5 shows a sequence of the last images of the filament formed before the droplet breakup. The filament adopted a quasi-cylindrical shape for $162 \gtrsim t \gtrsim 42$ μs (t is the time to the filament breakup). The relaxation time was determined from the exponential thinning of the filament in this time interval. For $t \lesssim 42$ μs, the filament radius decreased next to the lower drop, which resembles what occurs during the pinch-off of a viscous Newtonian thread. We assume that this change in the filament shape occurs when the polymers have reached their maximum extensibility. The axial stress at that stage is of the order of σ/r^*, where r^* is the filament radius.[37]

Table I shows the physical properties of the liquids analyzed in this work. Due to the low polymer molecular weight and concentration, the jets produced in our experiments remained in their liquid phase. (Fibers were not formed.)
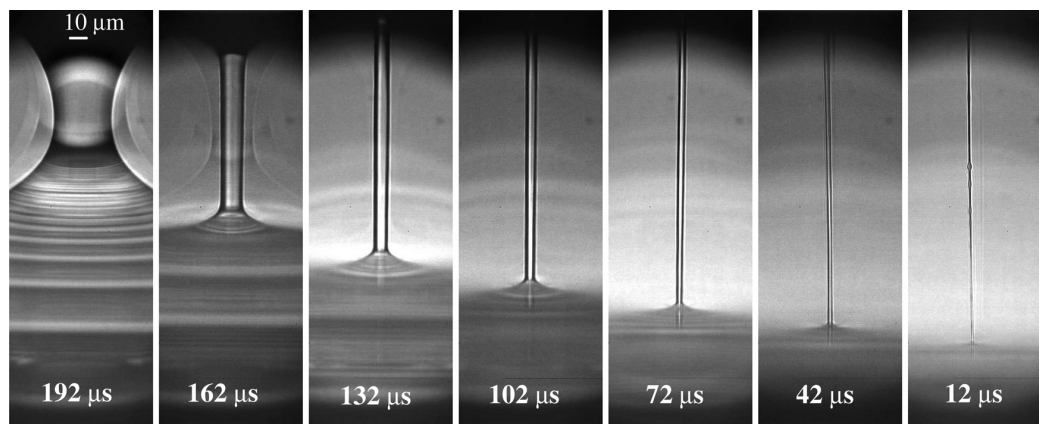
FIG. 5. Images of aqueous solutions of PEO100K for $c = 1\%$ wt in a CaBER-DoS rheometry experiment.[36] The labels indicate the time to the filament breakup.

IV. RESULTS

A. Stability

As mentioned in Sec. II, Rubio *et al.*[27] have recently found a viscoelastic transition in transonic GFF when PEO of low molecular weight is dissolved in water at the appropriate concentration. This transition is expected to affect the stability of the emitted jet. The open symbols in Fig. 6 indicate the experimental conditions at which the jets analyzed in Figs. 7 and 9–11 were produced. As can be observed, they were ejected with a flow rate just above the minimum value Q_{min} for the corresponding concentration. We will call supercritical jets those produced for $c_1^* < c < c_2^*$ (and $Q \simeq Q_{min}$) (red symbols) and subcritical jets otherwise (black symbols).

Figure 7-left compares the diameter of subcritical ($c = 0.75$ wt. %) and supercritical ($c = 1$ wt) PEO100K jets as function of the distance Z from the discharge orifice. The subcritical jet is progressively
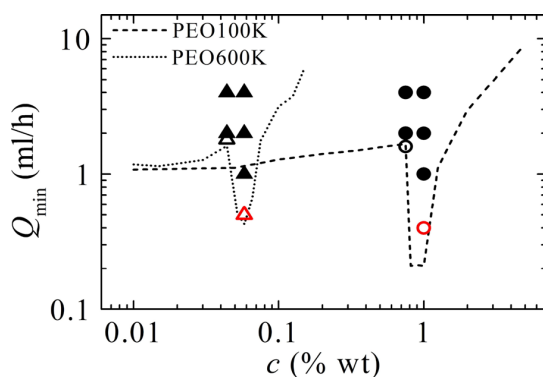

FIG. 6. Minimum flow rate leading to the jetting regime for aqueous solutions of PEO100K and PEO600K and $p_0 = 2.5$ bar (lines). The open symbols indicate the concentrations and flow rates at which the jets analyzed in Figs. 7 and 9–11 were produced. The red symbols correspond to the supercritical jets. Both the open and solid symbols indicate the concentrations and flow rates at which the jets analyzed in Figs. 12 and 13 were produced.

accelerated (the diameter decreases) beyond the discharge orifice. The BOAS instability occurs for $Z \gtrsim 1$ mm, while the jet breakup occurs at $Z \simeq 4$ mm. In the supercritical case, the liquid in the tapering meniscus undergoes a larger acceleration than in the subcritical case. In fact, the supercritical jet diameter next to the emission point is approximately the same as in the rest of the region analyzed. The BOAS instability arises at $Z \simeq 4$ mm ($\sim 2000\ d$), a much larger distance than in the subcritical case. Interestingly, we could not observe the breakup of the supercritical jet because it flowed without breaking up within the region analyzed $Z \leq 10$ mm ($\sim 5000\ d$) (as indicated by the arrow). The beads formed by the BOAS instability (Fig. 8) are separated by distances much larger than the jet diameter. For this reason, they do not significantly alter the diameter of the perturbed jet. For instance, the distance between two consecutive beads for ($c = 0.75$ wt. %, $Q = 1.6$ ml/h) was around 300 μm, which corresponds to a decrease in the jet diameter of around 10%.

The low pressure of the discharge chamber practically suppresses the whipping (bending) instability caused by the difference between the speeds of the liquid and air streams. In fact, the aerodynamic Weber number $We_g = \rho_g (v_g - v_j)^2 d/(2\sigma)$ (v_g is the gas velocity) takes values much smaller than unity in all the experimental realizations. However, small-amplitude lateral oscillations were observed sufficiently far from the discharge orifice. It must be emphasized that the whipping amplitude remained small over the entire jet, much smaller than those observed in jets discharged in atmospheric pressure.[7] The whipping oscillations neither reduced the jet diameter nor prevented us from determining the free surface contour, despite our microscope's very small depth of field. In the subcritical case, the whipping instability arises after the formation of beads (Fig. 7), while both effects are practically simultaneous in the supercritical jet. The whipping instability arises at $Z \simeq 4$ mm in both the subcritical and supercritical jets. The jet diameter and gas velocity take similar values in the two cases at that jet station and so does the aerodynamic Weber number We_g.

The jets analyzed in Fig. 7 were ejected at different flow rates, and therefore, they flow at considerably different speeds even if their diameters take similar values. For this reason, it is instructive to examine the results in terms of the "flight" time t_f. We define $t_f(Z)$ as the time
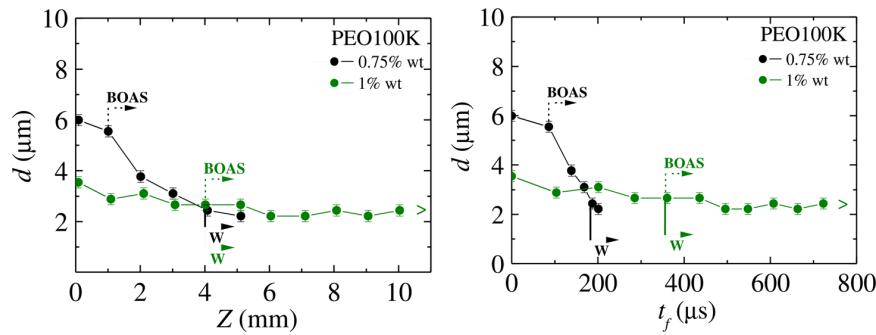
FIG. 7. Jet diameter d vs the distance from the ejector exit, Z, and the jet flight time, t_f, for the subcritical ($c = 0.75$ wt. %, $Q = 1.6$ ml/h) and supercritical ($c \gtrsim 1$ wt. %, $Q = 0.4$ ml/h) PEO100K jets. The vertical solid and dashed lines indicate the beginning of whipping (W) and BOAS instability, respectively. The chevron-right green arrow indicates that the supercritical jet broke up at distances from the ejector larger than 10 mm.

elapsed between the instant at which the jet's material element was ejected and the instant at which that element reaches the axial position Z. This flight time is given by the expression

$$t_f(Z) = \int_0^Z \frac{dz}{v_j(z)}. \qquad (6)$$

Using the trapezoidal rule, this integral can be approximately calculated from the jet velocity $v_j = 4Q/(\pi d^2)$ at several jet stations. Figure 7 shows the noticeable difference between the stability of the supercritical and subcritical jets.

It is well known that, when a viscoelastic jet is emitted through a feeding capillary/nozzle at a sufficiently high speed, the polymers stretch in the capillary/nozzle, increasing the extensional viscosity.[14,15] In the absence of sufficient strain rate beyond the discharge orifice, the polymers relax to their coiling state, and the extensional viscosity decreases to its equilibrium value. As mentioned in the introduction, a

relaxed viscoelastic jet is more prone to the capillary linear instability than its Newtonian counterpart, i.e., that with the same Ohnesorge number.[9,10] Therefore, one expects the capillary instability to arise right after the polymer relaxation takes place, i.e., for $t_f \gtrsim \lambda_r$. The small-amplitude capillary instability produces an incipient BOAS structure on a timescale given by the inertio-capillary time t_c. This characteristic time takes values of the order of 100 ns for our micrometer jet. Therefore, one can state that the capillary instability and the incipient BOAS structure appear almost simultaneously on the timescale of hundreds of microseconds of the jet flight. This allows us to conclude that, in the absence of sufficient strain rate beyond the discharge orifice, beads should be detected for $t_f \gtrsim \lambda_r$. In fact, this approximately occurs for the subcritical jet analyzed in Fig. 7-right: beads were formed for times smaller than 100 μs, while the polymer relaxation time is about 26 μs. On the contrary, our observations for the supercritical jet contradict that conclusion. As can be observed in Fig. 7-right, the BOAS instability was detected at $t_f \simeq 350$ μs.

The jet produced with GFF is subject to the viscous force exerted by the coflowing gas stream beyond the discharge orifice. A natural question is whether the supercritical jet experiences a sufficiently large acceleration that prevents the polymer relaxation. To answer this question, we calculated the Weissenberg number $\text{Wi} = \dot{\varepsilon}\lambda_r$ as a function of the dimensionless flight time t_f/λ_r, where $\dot{\varepsilon} = dv_j/dz$ is the strain rate. As can be observed in Fig. 9, the Weissenberg number takes values much smaller than the threshold leading to the coil-stretch transition in a simple extensional flow ($\text{Wi} = 0.5$), which suggests that the polymer should have been relaxed after a few relaxation times.

We examined in more detail the intriguing behavior of the supercritical PEO100K jet for $Z \lesssim 3$ mm. For this purpose, we took images of the jet with a larger magnification (0.109 μm/pixel), moving the camera downstream in steps of 62.5 μm. In this way, we determined more accurately the free surface position and the velocity profile $v_j(Z)$ (Fig. 10). The jet velocity increases sharply next to the discharge orifice and linearly for $Z \gtrsim 0.15$ mm. In this last interval, $\dot{\varepsilon} = dv_j/dz \simeq 3200$ s^{-1}. This value is much smaller than the inverse of the polymer relaxation time ($\lambda_r^{-1} \simeq 38\,000$ s^{-1}). Therefore, the polymer stress should exponentially relax over a flight time of the order of $\lambda_r \simeq 26$ μs [Eq. (4)], or along a distance of the order of $\lambda_r v_j \simeq 0.5$ mm. In rheology terms, the outer gaseous flow is weak for $Z \gtrsim 0.15$ mm. This implies that the axial stress is expected to relax exponentially on a distance much smaller than that at which the BOAS instability arises in the experiment.

The most noticeable result of the present analysis is that the supercritical jet of PEO100K broke up at distances from the ejector
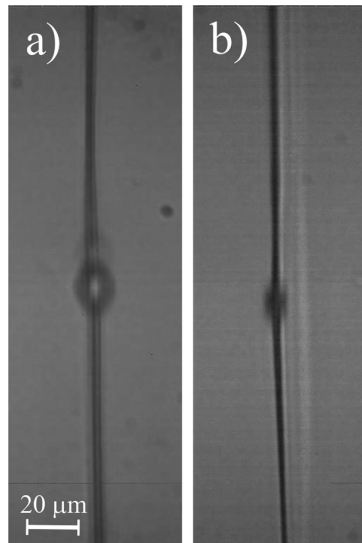

FIG. 8. Images of beads following the BOAS instability in a (a) subcritical ($c = 0.75$ wt. %, $Q = 1.6$ ml/h) and (b) supercritical ($c = 1$ wt. %, $Q = 0.4$ ml/h) jet of PEO100K at $Z \simeq 3$ and 5 mm, respectively.
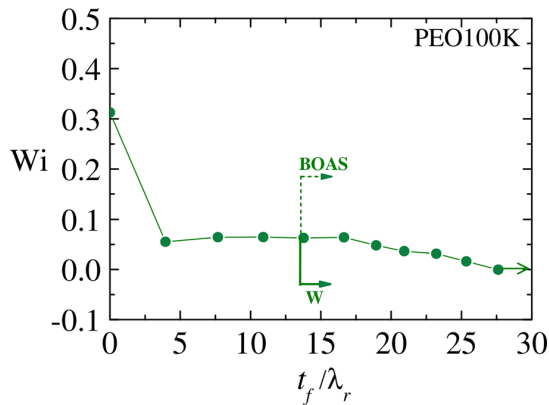
FIG. 9. Weissenberg number Wi vs the dimensionless jet flight time t_f/λ_r for the supercritical jet ($c = 1$ wt. %, $Q = 0.4$ ml/h). The vertical solid and dashed lines indicate the beginning of whipping (W) and BOAS instabilities, respectively. The chevron-right green arrow indicates that the supercritical jet of PEO100K broke up at dimensionless times larger than 30.
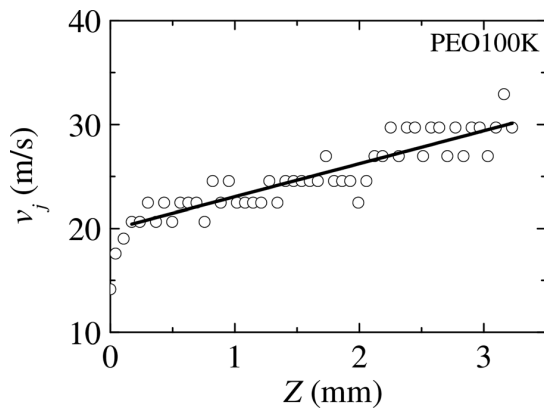

FIG. 10. Jet velocity $v_j(Z)$ for the supercritical jet ($c = 1$ wt. %, $Q = 0.4$ ml/h) of PEO100K. The solid line is the linear fit for $Z > 0.15$ mm.
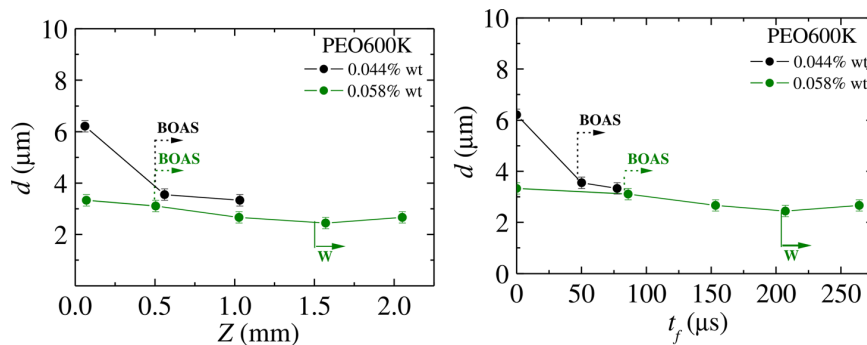

larger than 10 mm. As will be shown in Sec. IV B, the jet length L was at least two orders of magnitude larger than that of its Newtonian counterpart (a microjet with the same Ohnersorge number). The prolonged survival of the supercritical jet cannot be attributed to solvent evaporation. The Hertz–Knudsen–Langmuir evaporation speed in a vacuum[38,39] is given by

$$v_{\mathrm{ev}} = \frac{\alpha_c P_s(T)}{\sqrt{2\pi}\rho(R_{gv}T)^{1/2}},\qquad(7)$$

where α_c is the evaporation coefficient ($\alpha_c \simeq 0.2$ in our case), $P_s(T)$ is the vapor pressure at the temperature T, and R_{gv} is the gas constant of the vapor. The non-dimensional number $G = v_{\mathrm{ev}}\pi d_j L/(v_j \pi d_j^2/4)$ measures the relative rate of evaporation along a jet of diameter d_j and length L. The velocity of a low-viscosity jet flow-focused by gas can be estimated as $v_j \simeq (2p_0/\rho)^{1/2}$, which leads to

$$G \simeq \frac{\alpha_c P_s(T)}{2\sqrt{\pi}(\rho p_0 R_{gv}T)^{1/2}}\frac{4L}{d_j}.\qquad(8)$$

For the supercritical jet of PEO100K, G is of the order of 10^{-4}. Therefore, evaporation does not significantly increase the polymer concentration.

The unexpected huge stability of the supercritical jet cannot be explained in terms of the elasto-capillary regime arising in the nonlinear phase of the jet breakup. In the BOAS structure, the liquid filament connecting two consecutive beads undergoes an exponential thinning characterized by the polymer relaxation time. However, and as can be observed in Fig. 7, the supercritical jet survives at least tens of times the relaxation time after the BOAS structure has arisen.

The results for PEO600K (Fig. 11) are less conclusive than those described above for PEO100K. The breakup point of the supercritical jet considerably moves away from the ejector. However, the jet is much less stable than its PEO100K counterpart. In addition, the BOAS instability occurs at practically the same dimensionless time t_f/λ_r in the subcritical and supercritical cases. We do not have a definitive explanation for the differences between the behavior of the supercritical jets of PEO100K and PEO600K. The solution viscosity η and relaxation time λ_r of PEO100K are commensurate with the corresponding values of PEO600K (see Table I). However, the polymer viscosity $\eta_p = \eta - \eta_s$ of PEO600K is one order of magnitude smaller than that of PEO100K. This difference may explain why the reduction

FIG. 11. Jet diameter d vs the distance from the ejector exit, Z, and the jet flight time, t_f, for the subcritical ($c = 0.044$ wt. %, $Q = 1.8$ ml/h) and supercritical ($c = 0.058$ wt. %, $Q = 0.5$ ml/h) PEO600K jets. The vertical solid and dashed lines indicate the beginning of whipping (W) and BOAS instability, respectively.
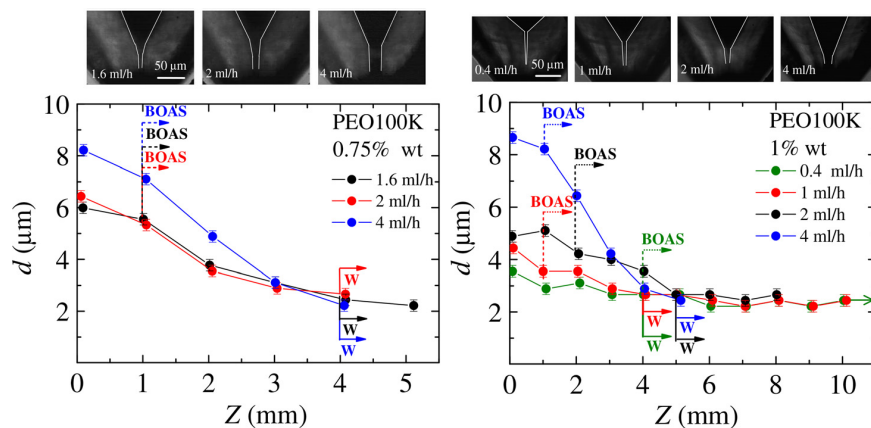
FIG. 12. Jet diameter d vs the distance from the ejector exit, Z, for PEO100K. The vertical solid and dashed lines indicate the beginning of whipping (W) and BOAS instabilities, respectively. The chevron-right green arrow indicates that the supercritical jet broke up at distances from the ejector larger than 10 mm. The upper images show the meniscus shape in each case.

in the minimum flow rate at the viscoelastic transition $c = c_1^*$ is smaller for PEO600K (Fig. 2), and the supercritical PEO600K jet is less stable.

Figure 12 compares the results obtained for several flow rates at subcritical ($c < c_1^*$) and supercritical ($c_1^* < c < c_2^*$) concentrations for PEO100K. The flow rates correspond to the symbols in Fig. 6. The upper images show the meniscus shape in each case. As can be observed, the flow rate has a small influence on the jet behavior for the subcritical concentration $c = 0.75\%$ wt because the tapering meniscus does not considerably shrink as Q decreases in this case. Neither the distance at which the BOAS instability arises nor the jet breakup length is considerably affected by the flow rate. On the contrary, the BOAS instability is generally delayed as the flow rate decreases for the supercritical concentration $c = 1\%$ wt. This occurs because the jet extensional viscosity and its relaxation distance increase as Q decreases. The most important effect is the increase in the breakup length as Q approaches its minimum value. This effect is not observed for PEO600K (Fig. 13). In fact, the length of the supercritical PEO600K jet ($c = 0.058\%$ wt, $Q = 0.5$ ml/h) is considerably shorter than that for $Q = 1$ ml/h. In addition, the BOAS instability arises at $Z \simeq 0.5$ mm in all the cases.

As explained in Sec. II, this work extends the study of Rubio et al.[27] by examining the viscoelastic transition for aqueous solutions of PVP360K (Fig. 3). The supercritical PVP360K jet also exhibits huge stability, similar to that of its PEO100K counterpart. Figure 14 shows a comparison between the diameters measured in those two cases. The BOAS and whipping instabilities arose at approximately the same distance from the ejector. Neither of the two jets broke up in the region analyzed in the experiments, as indicated by the arrows. The two jets reached an approximately constant diameter $d \simeq 2$ μm sufficiently far from the ejector. The diameter of the PVP360K jet significantly decreased behind the ejector orifice because the flow rate $Q = 0.5$ ml/h is significantly greater than the minimum value (see Fig. 3).

This section closes with a discussion about the possible origin of the unexpected stability exhibited by the supercritical jets. This stability is attributed to the existence of an unrelaxed stress, which survives during the jet flight. We have shown that the viscoelastic axial stress cannot be maintained by the negligible strain rate dv_j/dz experienced by the supercritical PEO100K jet far from the discharge orifice. However, and as explained in the Introduction, the coflowing gas current can produce shear rates at the free surface leading to significant axial stresses [Eq. (5)]. If one assumes that the polymers are fully

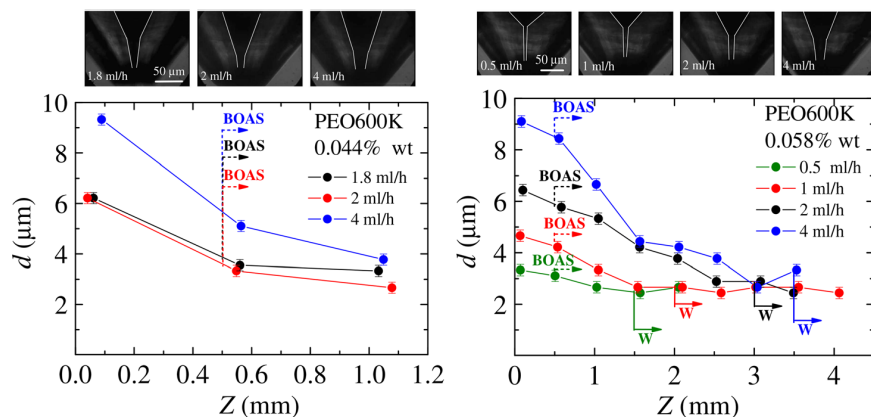**FIG. 13.** Jet diameter d vs the distance from the ejector exit, Z, for PEO600K. The vertical solid and dashed lines indicate the beginning of whipping (W) and BOAS instabilities, respectively. The upper images show the meniscus shape in each case.
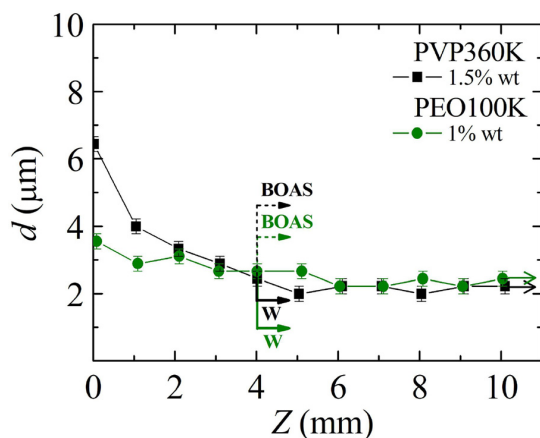
FIG. 14. Jet diameter d vs the distance from the ejector exit, Z, for the supercritical (PEO100K, $c = 1$ wt. %, $Q = 0.4$ ml/h) and (PVP360K, $c = 1.5$ wt. %, $Q = 0.5$ ml/h) jets. The vertical solid and dashed lines indicate the beginning of whipping (W) and BOAS instability, respectively. The arrows indicate that the supercritical jets broke up at distances from the ejector larger than 10 mm.

stretched in the tip of the supercritical meniscus, then the axial stress there is $\tau_{zz} \sim \sigma/r^*$, where r^* is the minimum radius reached by the exponential thinning in CaBER-DoS rheometry (see Sec. III). According to Eq. (5), the dimensionless shear rate $\dot{\gamma}$ leading to $\tau_{zz} \sim \sigma/r^*$ is

$$\dot{\gamma} \sim [2\text{We}(1 - \eta_r)\, El]^{-1/2}, \qquad (9)$$

where we have taken into account that $r^* \sim d/2 \sim 1\,\mu$m for the supercritical PEO100K jet. The above expression leads to dimensionless shear rates of the order 10^{-1}. This means that small shear rates produced by the coflowing air stream may be responsible for the persistence of the axial viscoelastic jet far from the orifice. The key element is the jet thinness ($d \simeq 2\,\mu$m), which leads to high values of the elasticity number even for small values of the polymer relaxation time and viscosity.

The above explanation is not fully satisfactory. First, the gas flow has practically decayed before the appearance of BOAS instability in the supercritical PEO100K jet. Even if we assume that the gas streams affects the jet dynamics far from the orifice, the noticeable difference between the stability of (PE0100K, $c = 1$ wt. %, $Q = 0.4$ ml/h) and (PE0100K, $c = 1$ wt. %, $Q = 4$ ml/h) contradicts the above explanation as well. In the framework of the Oldroyd-B model, the jets dynamics are characterized by the set of parameters $\{d, \rho, \mu, \mu_s, \sigma,\ \lambda_r\}$. For $Z \gtrsim 4$ mm, the jet diameter (and the rest of parameters) of (PE0100K, $c = 1$% wt, $Q = 4$ ml/h) and (PE0100K, $c = 1$% wt, $Q = 0.4$ ml/h) take similar values (Fig. 12). In addition, the outer stream exerts the same viscous drag (whether negligible or significant) in those two cases. Therefore, one expects a similar jet behavior in the two experiments. However, the supercritical jet (PE0100K, $c = 1$%, $Q = 0.4$ ml/h) survives for distances $Z > 10$ mm, while the subcritical jet (PE0100K, 1%, $Q = 4$ ml/h) breaks up at $Z \simeq 5$ mm. This occurs even though the supercritical jet moves much slower than the subcritical one for $Z \gtrsim 4$ mm. The difference between the jet length in these two cases suggests that the tapering meniscus leaves an imprint in the

supercritical jet. These memory effects persist for $Z > 4$ mm and times much larger than the polymer relaxation time.

Another possible explanation for the enormous stability exhibited by the supercritical PEO100K jet is the following. The large acceleration (intense extensional flow) suffered by the liquid in the supercritical meniscus triggers the coil-stretch polymer transition. This transition drastically increases the extensional viscosity at the emission point. The strong converging flow in the meniscus tip causes some entanglement or self-assembly of the stretched polymers. This effect hinders the viscosity relaxation and delays the capillary BOAS instability. The viscoelastic stress does not relax in the filament formed between the beads, making the jet breakup at distances larger than 10 mm. This molecular phenomenon could explain the noticeable difference between the supercritical jets of PEO100K/PVP360K and PEO600K despite their similar hydrodynamic properties. Interestingly, the polymer concentration of the supercritical PEO100K and PVP360K jets exceeds the corresponding overlap concentration, while this does not occur for PEO600K (see Table I).

B. Jet diameter and length

We measured the jet diameter at the ejector orifice exit, d_e, as a function of the liquid flow rate Q and air stagnation pressure p_0 for (PE0100K, $c = 1$ wt. %) and (PE0600K, $c = 0.058$ wt. %). We applied an optimization method[40] to search for the optimum values of the exponents α and β in the scaling law $d_e \propto A^{\alpha}B^{\beta}$, where A and B are two governing parameters. For $p_0 = 1.1$ bar, this optimization method leads to $d_e \propto \lambda_r^{-0.06}Q^{0.505}$, which indicates that the polymer relaxation time plays a secondary role. A similar result, $d_e \propto \eta^{-0.025}Q^{0.515}$, is obtained when the shear viscosity is used to characterize the polymer solution. These results indicate that d_e essentially depends on Q and p_0.

The optimization method as applied to all the measurements leads to $d_e \propto p_0^{-0.19}Q^{0.495}$, which approximately coincides with the classical scaling law,[26] $d_e/d_0 = (8/\pi^2)^{1/4}(Q/Q_0)^{1/2}$ ($d_0 \equiv \sigma/p_0$ and $Q_0 \equiv \sigma^2/(\rho p_0^3)^{1/2}$) (Fig. 15), for the Newtonian and incompressible regime.[26,41] We conclude that the viscoelastic jet velocity at the ejector orifice $v_j = 4Q/(\pi d_e^2)$ is essentially independent of Q and scales approximately as $p_0^{1/2}$. The major difference between Newtonian and
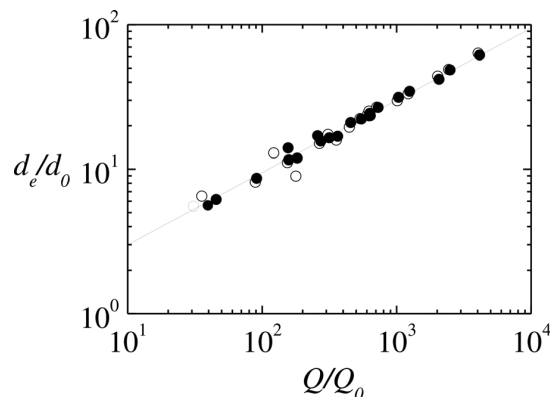

FIG. 15. d_e/d_0 vs Q/Q_0. The open and solid symbols correspond to PEO100K and PEO600K, respectively. The solid line is the function $d_e/d_0 = (8/\pi^2)^{1/4}(Q/Q_0)^{1/2}$.

viscoelastic flow focusing is the enhanced stability of the viscoelastic jet, which results in the increase in the jet length and the decrease in the diameter at the breakup point.

Figure 16 shows the jet diameter at the breakup point, d_b, measured for different flow rates and stagnation pressures. As can be observed, d_b is slightly greater than $2\,\mu m$ in most experiments (only some values for PEO600K and $Q \geq 4\,ml/h$ clearly exceed that diameter). A qualitative explanation of this result is the following. The jet surface exposed to the outer stream is sufficiently large for the gas to transfer its momentum to the jet. The gaseous flow is chocked in all our experiments. For this reason, the gas velocity field and, therefore, the viscous drag is essentially independent of p_0. This explains why p_0 has little influence on d_b. On the other hand, the flow rate only affects the distance from the orifice at which the lower bound of the jet diameter, $d \simeq 2\,\mu m$, is reached. The jet diameter at the orifice, d_e, increases with Q (Fig. 15) and, therefore, so does the distance from the orifice at which the jet reaches the minimum diameter (see Figs. 12 and 13). We do not have an explanation of why the minimum value $d_b \simeq 2\,\mu m$ cannot be beaten in our experiments.

Gañán-Calvo et al.[40] have recently derived a scaling law for the length of Newtonian jets. For low viscosity liquids, the jet length L is given by

$$\frac{L}{d_0} = \alpha_\rho \left(\frac{8^{1/2}}{\pi}\right)^{3/4} \left(\frac{Q}{Q_0}\right)^{3/4}, \tag{10}$$

where $\alpha_\rho = 15.0$ is the prefactor obtained by fitting experimental data.[40] As can be observed in Fig. 17, the weakly viscoelastic jets produced in our experiments are much longer than their Newtonian counterparts, especially for small flow rates. In this case, the PEO100K jet length becomes two orders of magnitude larger than that of the corresponding Newtonian jet. As mentioned above, the supercritical PEO100K jet did not break up in the region analyzed in our experiments, as indicated by the arrow.
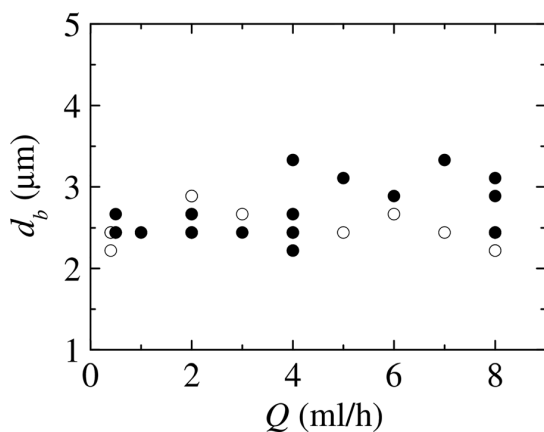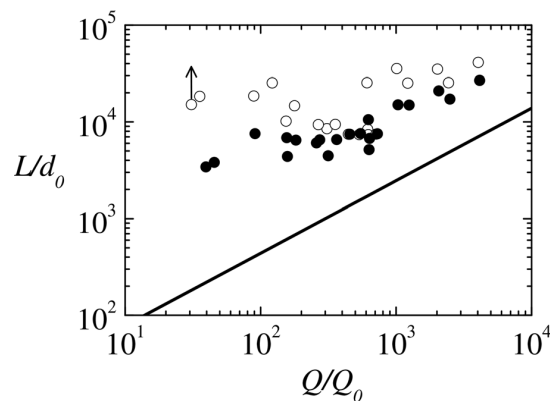

FIG. 17. L/d_0 vs Q/Q_0. The open and solid symbols correspond to PEO100K and PEO600K, respectively. The line is the scaling law (10). The arrow correspond to the supercritical PEO100K jets, which do not break up in the region analyzed in our experiments.

V. CONCLUDING REMARKS

We produced jets of nearly Newtonian (weakly viscoelastic) liquids that flow without breaking over distances much larger than in the Newtonian case. The jet diameter at the orifice exit approximately follows the classical law for the Newtonian incompressible regime. The jet thins while flying in the discharge chamber until it reaches a practically constant diameter, which is essentially independent of the applied pressure and injected flow rate.

We have found that the maximum jet stabilization is achieved by adding PEO100K at a concentration of around 1 wt. %. In this case, the BOAS instability is considerably delayed, and jets about $2\,\mu m$ in diameter flow more than 1 cm without breaking up. This superstability may be attributed to: (i) the axial stress produced by a slightly non-uniform velocity profile in the aerodynamically driven micrometer jet, and (ii) long-lived memory effects experienced by the jet. We hypothesize that this last effect is caused by the partial entanglement of the polymers in the tip of the viscoelastic tapering meniscus, even though the polymer molecular weight and concentration are very low.

Polymer entanglement in viscoelastic liquids is typically produced by increased polymer concentration due to evaporation. As mentioned in Sec. IV, evaporation does not play a significant role due to the very small residence time of a fluid particle in our experiments. Polymer entanglement was also observed during the capillary thinning of elastic polymer solutions. In this case, flow-induced phase separation makes the polymer concentration increase so that polymers become entangled while solvent drains from the filament.[37] We do not have any indication of phase separation in our experiments. Complex phenomena also take place in the electrospinning of polymer liquids. For instance, birefringent electrospun jets always have an outer layer brighter than the core, which indicates the existence of a shell structure with higher polymer concentration and relaxation time.[42] Mittal et al.[43] have reported the flow-assisted organization of cellulose nanofibrils into macroscale fibers with nearly perfect unidirectional alignment. This phenomenon (on a greater scale) is similar to the polymer self-assembly, which might explain the unexpected stability of the supercritical jets analyzed in the present work.

FIG. 16. Diameter at the breakup point, d_b, as a function of the flow rate Q. The open and solid symbols correspond to PEO100K and PEO600K, respectively.

If we assume that the polymers are fully stretched in the jet, then the polymer stress can be estimated as $\tau_{zz} = \sigma/r^*$, where r^* is the filament radius at the end of the cylindrical thinning in the CaBER-DoS rheometry (Fig. 5).[6] This estimation leads to $\tau_{zz} \simeq 20–40$ kPa for the supercritical jet, which lies in the range of values measured by Han *et al.*[15] for electrospun jets with much higher elasticity. This axial stress yields the elastic velocity[44] $v_e = \sqrt{\tau_{xx}/\rho} \simeq 5$ m/s. Interestingly, the capillary velocity $v_c = d/t_c$ takes values around 5 m/s as well. Both the elastic and capillary velocities are much smaller than the jet speed (of the order of 30 m/s), which shows the strong convective character of the flow-focused jet. This character prevents the jet from suffering both the jetting-to-dripping transition[11] and the die swell instability[45] at the discharge orifice.

The whipping instability arises at $Z \simeq 4$ mm in both the subcritical (relaxed) and supercritical (unrelaxed) PEO100K jets. Since the aerodynamic Weber number We_g is practically the same in the two cases, the unrelaxed axial stress does not seem to stabilize the supercritical jet under lateral perturbations.

There are noticeable differences between the supercritical jets of PEO100K and PEO600K even though they have similar viscosities and polymer relaxation times. These differences reveal the complexity of the phenomenon, which probably involves physical properties not accounted for in the present analysis.

ACKNOWLEDGMENTS

AUTHOR DECLARATIONS
Conflict of Interest

The authors have no conflicts to disclose.

Author Contributions

A. Rubio: Data curation (equal); Investigation (equal); Methodology (equal); Visualization (equal). **E. J. Vega:** Data curation (equal); Investigation (equal); Supervision (equal). **A. M. Gañán-Calvo:** Conceptualization (equal); Supervision (equal). **J. M. Montanero:** Conceptualization (equal); Formal analysis (equal); Supervision (equal); Writing – original draft (equal); Writing – review and editing (equal).

DATA AVAILABILITY

The data that support the findings of this study are available from the corresponding author upon reasonable request.

REFERENCES

[1]D. F. James, "Boger fluids," Annu. Rev. Fluid Mech. **41**, 129–142 (2009).
[2]G. H. McKinley and A. Tripathi, "How to extract the Newtonian viscosity from capillary breakup measurements in a filament rheometer," J. Rheol. **44**, 653–670 (2000).
[3]S. L. Anna and G. H. McKinley, "Elasto-capillary thinning and breakup of model elastic liquids," J. Rheol. **45**, 115–138 (2001).
[4]R. B. Bird, R. C. Armstrong, and O. Hassager, *Dynamics of Polymeric Liquids Volume I: Fluid Mechanics; Volume II: Kinetic Theory* (Wiley, New York, 1987).
[5]J. G. Oldroyd, "On the formulation of rheological equations of state," Proc. R. Soc. London, Ser. A **200**, 523–541 (1950).
[6]J. Eggers and E. Villermaux, "Physics of liquid jets," Rep. Prog. Phys. **71**, 036601 (2008).
[7]A. L. Yarin, B. Pourdeyhimi, and S. Ramakrishna, *Fundamentals and Applications of Micro- and Nanofibers* (Cambridge University Press, Cambridge, Great Britain, 2014).
[8]T. Funada and D. D. Joseph, "Viscoelastic potential flow analysis of capillary instability," J. Non-Newtonian Fluid Mech. **111**, 87–105 (2003).
[9]M. Goldin, J. Yerushalmi, R. Pfeffer, and R. Shinnar, "Breakup of a laminar capillary jet of a viscoelastic fluid," J. Fluid Mech. **38**, 689–711 (1969).
[10]Z. Liu and Z. Liu, "Linear analysis of three-dimensional instability of non-Newtonian liquid jets," J. Fluid Mech. **559**, 451–459 (2006).
[11]P. Huerre and P. A. Monkewitz, "Local and global instabilites in spatially developing flows," Annu. Rev. Fluid Mech. **22**, 473–537 (1990).
[12]J. M. Montanero and A. M. Gañán-Calvo, "Viscoelastic effects on the jetting-dripping transition in co-flowing capillary jets," J. Fluid Mech. **610**, 249–260 (2008).
[13]S. Middleman, "Stability of a viscoelastic jet," Chem. Eng. Sci. **20**, 1037–1040 (1965).
[14]S. L. Goren and J. Gavis, "Transverse wave motion on a thin capillary jet of a viscoelastic liquid," Phys. Fluids **4**, 575–579 (1961).
[15]T. Han, A. L. Yarin, and D. H. Reneker, "Viscoelastic electrospun jets: Initial stresses and elongational rheometry," Polymer **49**, 1651–1658 (2008).
[16]S. Goren and M. Gottlieb, "Surface-tension-driven breakup of viscoelastic liquid threads," J. Fluid Mech. **120**, 245–266 (1982).
[17]A.-C. Ruo, F. Chen, C.-A. Chung, and M.-H. Chang, "Three-dimensional response of unrelaxed tension to instability of viscoelastic jets," J. Fluid Mech. **682**, 558–576 (2011).
[18]Z. Ding, K. Mu, T. Si, and Y. Jian, "Linear instability analysis of a viscoelastic jet in a co-flowing gas stream," J. Fluid Mech. **936**, A6 (2022).
[19]A. S. Mohamed, M. A. Herrada, A. M. Gañán-Calvo, and J. M. Montanero, "Convective-to-absolute instability transition in a viscoelastic capillary jet subject to unrelaxed axial elastic tension," Phys. Rev. E **92**, 023006 (2015).
[20]J. Eggers, "Nonlinear dynamics and breakup of free-surface flows," Rev. Mod. Phys. **69**, 865–929 (1997).
[21]H.-C. Chang, E. A. Demekhin, and E. Kalaidin, "Iterated stretching of viscoelastic jets," Phys. Fluids **11**, 1717–1737 (1999).
[22]M. S. N. Oliveira and G. H. McKinley, "Iterated stretching and multiple beads-on-a-string phenomena in dilute solutions of highly-extensible flexible polymers," Phys. Fluids **17**, 071704 (2005).
[23]C. Clasen, J. Eggers, M. A. Fontelos, J. Li, and G. H. McKinley, "The beads-on-string structure of viscoelastic threads," J. Fluid Mech. **556**, 283–308 (2006).
[24]A. V. Bazilevsky, S. I. Voronkov, V. M. Entov, and A. N. Rozhkov, "Orientational effects in capillary breakup of jets and threads of dilute polymer solutions (English version in vol. 26)," Dokl. Akad. Nauk SSSR **257**, 336–339 (1981).
[25]A. Ponce-Torres, J. M. Montanero, E. J. Vega, and A. M. Gañán-Calvo, "The production of viscoelastic capillary jets with gaseous flow focusing," J. Non-Newtonian Fluid Mech. **229**, 8–15 (2016).
[26]A. M. Gañán-Calvo, "Generation of steady liquid microthreads and micron-sized monodisperse sprays in gas streams," Phys. Rev. Lett. **80**, 285–288 (1998).
[27]A. Rubio, F. Galindo, E. J. Vega, J. M. Montanero, and M. G. Cabezas, "Viscoelastic transition in transonic flow focusing," (to be published).
[28]J. Doshi and D. R. Reneker, "Electrospinning process and applications of electrospun fibers," J. Electrost. **35**, 151–160 (1995).
[29]M. Lauricella, S. Succi, E. Zussman, D. Pisignano, and A. L. Yarin, "Models of polymer solutions in electrified jets and solution blowing," Rev. Mod. Phys. **92**, 035004 (2020).
[30]J. L. Daristotle, A. M. Behrens, A. D. Sandler, and P. Kofinas, "A review of the fundamental principles and applications of solution blow spinning," ACS Appl. Mater. Interfaces **8**, 34951–34963 (2016).

[31]D. A. Saville, "Electrohydrodynamics: The Taylor-Melcher leaky dielectric model," Annu. Rev. Fluid Mech. **29**, 27–64 (1997).

[32]D. H. Reneker, A. Yarin, H. Fong, and S. Koombhongse, "Bending instability of electrically charged liquid jets of polymer solutions in electrospinning," J. Appl. Phys. **87**, 4531–4547 (2000).

[33]C. van der Walt, M. A. Hulsen, A. C. B. Bogaerds, H. E. H. Meijer, and M. J. H. Bulters, "Stability of fiber spinning under filament pull-out conditions," J. Non-Newtonian Fluid Mech. **175–176**, 25–37 (2012).

[34]M. G. Cabezas, A. Bateni, J. M. Montanero, and A. W. Neumann, "A new drop-shape methodology for surface tension measurement," Appl. Surf. Sci. **238**, 480–484 (2004).

[35]S. Sur and J. Rothstein, "Drop breakup dynamics of dilute polymer solutions: Effect of molecular weight, concentration, and viscosity," J. Rheol. **62**, 1245–1259 (2018).

[36]M. Rubio, A. Ponce-Torres, E. J. Vega, and J. M. Montanero, "Experimental analysis of the extensional flow of very weakly viscoelastic polymer solutions," Materials **13**, 192 (2020).

[37]R. Sattler, C. Wagner, and J. Eggers, "Blistering pattern and formation of nanofibers in capillary thinning of polymer solutions," Phys. Rev. Lett. **100**, 164502 (2008).

[38]T. Alty, "The maximum rate of evaporation of water," London, Edinburgh, Dublin Philos. Mag. J. Sci. **15**, 82–103 (1933).

[39]A. H. Persad and C. A. Ward, "Expressions for the evaporation and condensation coefficients in the Hertz-Knudsen relation," Chem. Rev. **116**, 7727–7767 (2016).

[40]A. M. Gañán-Calvo, H. N. Chapman, M. Heymann, M. O. Wiedorn, J. Knoska, B. Gañán-Riesco, J. M. López-Herrera, F. Cruz-Mazo, M. A. Herrada, J. M. Montanero, and S. Bajt, "The natural breakup length of a steady capillary jet: Application to serial femtosecond crystallography," Crystals **11**, 990 (2021).

[41]T. Si, F. Li, X.-Y. Yin, and X.-Z. Yin, "Modes in flow focusing and instability of coaxial liquid-gas jets," J. Fluid Mech. **629**, 1–23 (2009).

[42]D. H. Reneker, A. L. Yarin, E. Zussman, and H. Xu, "Electrospinning of nanofibers from polymer solutions and melts," Adv. Appl. Mech. **41**, 345–346 (2007).

[43]N. Mittal, F. Ansari, K. Gowda, C. Brouzet, P. Chen, P. T. Larsson, S. V. Roth, F. Lundell, L. Wagberg, N. A. Kotov, and L. D. Soderberg, "Multiscale control of nanocellulose assembly: Transferring remarkable nanoscale fibril mechanics to macroscale fibers," ACS Nano **12**, 6378–6388 (2018).

[44]D. D. Joseph, *Fluid Dynamics of Viscoelastic Liquids* (Springer-Verlag, 1990).

[45]P. C. Hiemenz and T. Lodge, *Polymer Chemistry* (CRC, New York, 2007).

11
Conclusions

This thesis is a compendium of seven papers on the optimization of different microfluidic devices and their uses. These papers contain both experimental and numerical results. My major contribution is of experimental character, although I also conducted numerical simulations with a commercial software. The discusses are about various advanced techniques and findings related to microcapsule deformability, jet stability, and flow focusing in microfluidics. It highlights the use of fire-shaped borosilicate nozzles for evaluating microentity deformability, introduces a novel blood analogue fluid mimicking human blood properties, and explores the impact of gas viscosity and viscoelastic transitions in flow focusing. The research offers insights into optimizing jetting conditions and has applications in diagnosing diseases, drug testing, and fields like microfluidics, pharmacy, biotechnology, and crystallography. The specific conclusions of each paper are summarized on the following pages.

Paper I This work evaluates the capabilities and limitations of using fire-shaping techniques to produce glass nozzles. A new approach was experimentally assessed, heating the capillary at the base of the lateral flame to obtain a wider variety of nozzle shapes. Overall, significantly different nozzle shapes were produced, potentially affecting device performance in specific applications.

Paper II Microcapsules' deformability is essential in various industrial applications, and microfluidic devices, including fire-shaped glass nozzles, are popular for evaluating this. These nozzles create an extensional flow with a strain rate peak in the convergent region. The peak's position and intensity, which depend on flow rate, occur around 1.5 times the neck diameter and range from 8 to 10 times the mean strain rate. For viscoelastic particles like PDMS, peak duration and position impact deformation measurement. Larger capillaries create wider peaks, while smaller ones create sharper peaks near the neck. Optimal measurement occurs with a peak 5 ms before the neck.

Paper III A novel blood analogue fluid mimics the rheological and physiological properties of human blood at body temperature. It uses a viscoelastic solution with deformable PDMS particles matching human haematocrit. While improvements in particle monodispersity are needed, PDMS 45:1 particles best replicate human blood's viscosity. The analogue's flow in microchannels mimics the cell-free layer (CFL) phenomenon, useful for in vitro studies and bloodstain analysis. However, it only simulates certain flow conditions, not the full physiological functions of blood. Adjustments in polymer and PDMS concentration can fine-tune its properties.

Paper IV We analyzed the impact of gas viscosity on the stability of the tapering meniscus in flow focusing. The minimum flow rate for steady jetting shows non-monotonous behavior, reaching its lowest value at an optimal gas viscosity dependent on liquid viscosity. The meniscus shape and liquid acceleration also reflect this behavior. Our findings highlight the complexity of flow in the meniscus, where increased gas viscosity does not always stabilize it.

Paper V Our study provides a comprehensive analysis of transonic flow focusing in SFX, demonstrating the effectiveness of our numerical stability analysis and the accuracy of the derived scaling laws. The results offer practical insights for optimizing jetting conditions, with potential applications extending beyond SFX to other fields requiring precise control of liquid jets. This research contributes to a deeper understanding of the dynamics involved in transonic flow focusing, paving the way for future investigations into more complex configurations and higher viscosity liquids.

Paper VI We studied the viscoelastic transition in transonic flow focusing with low molecular weight polymers in water. The coil-stretch transition in the tapering meniscus stabilizes the flow and lowers the minimum flow rate for jetting. This effect, robust across various conditions, reduces flow rate and jet diameter by an order of magnitude. The transition occurs at Weissenberg numbers around 0.5, altering fluid behavior significantly at critical polymer concentrations. These findings are valuable for applications in microfluidics, pharmacy, biotechnology, and crystallography.

Paper VII We produced nearly Newtonian jets that flow without breaking for extended distances, stabilized by adding 1% wt. PEO100K. This delays the BOAS instability, allowing jets about 2 μm in diameter to flow over 1 cm. The stability is attributed to axial stress from a non-uniform velocity profile and long-lived memory effects due to polymer entanglement. Despite low molecular weight and concentration, these effects prevent the jetting-to-dripping transition and die swell instability, highlighting the complexity of the phenomena involved.

Conclusiones en castellano

Esta tesis es un compendio de siete trabajos sobre la optimización de diferentes dispositivos microfluídicos y sus usos. Estos trabajos contienen tanto resultados experimentales como numéricos. Mi principal contribución es de carácter experimental, aunque también realicé simulaciones numéricas con un software comercial. Los temas discutidos incluyen varias técnicas avanzadas y hallazgos relacionados con la deformabilidad de microcápsulas, la estabilidad de chorros y el enfoque de flujo en microfluídica. Se destaca el uso de toberas de borosilicato en conformadas con fuego, para evaluar la deformabilidad de microentidades, se introduce un nuevo fluido análogo a la sangre que imita las propiedades de la sangre humana y se explora el impacto de la viscosidad del gas y las transiciones viscoelásticas en el enfoque de flujo. La investigación ofrece información sobre la optimización de las condiciones de chorro y tiene aplicaciones en el diagnóstico de enfermedades, pruebas de medicamentos y campos como la microfluídica, la farmacia, la biotecnología y la cristalografía.

Artículo I Este trabajo evalúa las capacidades y limitaciones del uso de técnicas de modelado por fuego para producir toberas de vidrio. Se evaluó experimentalmente un nuevo enfoque, calentando el capilar en la base de la llama lateral para obtener una mayor variedad de formas de toberas. En general, se produjeron formas de toberas significativamente diferentes, lo que podría afectar el rendimiento del dispositivo en aplicaciones específicas.

Artículo II La deformabilidad de las microcápsulas es esencial en diversas aplicaciones industriales, y los dispositivos microfluídicos, incluidas las toberas de vidrio moldeadas por fuego, son populares para evaluarla. Estos dispositivos crean un flujo extensional con un pico de velocidad de deformación en la región convergente. La posición e intensidad del pico, que dependen del caudal, ocurren aproximadamente a 1.5 veces el diámetro del cuello y varían entre 8 y 10 veces la velocidad de deformación media. Para partículas viscoelásticas como el PDMS, la duración y posición del pico afectan la medición de la deformación. Los capilares más grandes crean picos más amplios, mientras que los más pequeñas crean picos más agudos cerca del cuello. La medición óptima ocurre con un pico 5 ms antes del cuello.

Artículo III Un nuevo fluido análogo de sangre imita las propiedades reológicas y fisiológicas de la sangre humana a la temperatura corporal. Utiliza una solución viscoelástica con partículas deformables de PDMS que coinciden con el hematocrito humano. Aunque se necesitan mejoras en la monodispersidad de las partículas, las partículas PDMS 45:1 replican mejor la viscosidad de la sangre humana. El flujo del análogo en microcanales imita el fenómeno de la capa libre de células (CFL), útil para estudios in vitro y análisis de manchas de sangre. Sin embargo, solo simula ciertas condiciones de flujo, no todas las funciones fisiológicas de la sangre. Los ajustes en la concentración de polímeros y PDMS pueden afinar sus propiedades.

Artículo IV Analizamos el impacto de la viscosidad del gas en la estabilidad del menisco estrechante en el enfoque de flujo. La tasa de flujo mínima para producir un chorro estable muestra un comportamiento no monótono, alcanzando su valor más bajo a una viscosidad óptima del gas que depende de la viscosidad del líquido. La forma del menisco y la aceleración del líquido también reflejan este comportamiento. Nuestros hallazgos destacan la complejidad del flujo en el menisco, donde un aumento en la viscosidad del gas no siempre lo estabiliza.

Artículo V Nuestro estudio proporciona un análisis completo del enfoque de flujo transónico en SFX, demostrando la efectividad de nuestro análisis de estabilidad numérica y la precisión de las leyes de escalado derivadas. Los resultados ofrecen ideas prácticas para optimizar las condiciones de chorro, con aplicaciones potenciales más allá de SFX en otros campos que requieren control preciso de chorros líquidos. Esta investigación contribuye a una comprensión más profunda de la dinámica involucrada en el enfoque de flujo transónico, allanando el camino para futuras investigaciones en configuraciones más complejas y líquidos de mayor viscosidad.

Artículo VI Estudiamos la transición viscoelástica en el enfoque de flujo transónico con polímeros de bajo peso molecular en agua. La transición de enrollado a estiramiento en el menisco estabiliza el flujo y reduce el caudal mínimo para el chorro. Este efecto, robusto en diversas condiciones, reduce el caudal y el diámetro del chorro en un orden de magnitud. La transición ocurre en números de Weissenberg alrededor de 0.5, alterando significativamente el comportamiento del fluido en concentraciones críticas de polímeros. Estos hallazgos son valiosos para aplicaciones en microfluídica, farmacia, biotecnología y cristalografía.

Artículo VII Producimos chorros casi newtonianos que fluyen sin romperse a largas distancias, estabilizados añadiendo 1% en peso de PEO100K. Esto retrasa la inestabilidad BOAS, permitiendo que chorros de aproximadamente 2 μm de diámetro fluyan más de 1 cm. La estabilidad se atribuye al estrés axial de un perfil de velocidad no uniforme y a efectos de memoria de larga duración debido al entrelazamiento de polímeros. A pesar del bajo peso molecular y concentración, estos efectos previenen la transición de chorro a goteo y la inestabilidad de hinchazón, destacando la complejidad de los fenómenos involucrados.

12
Papers not included

Besides the papers included in the present dissertation, the author has contributed to the following publications previously and during this thesis:

1. A. Rubio, V. Faustino, M. G. Cabezas, R. Lima and E. J. Vega. Fire-shaped cylindrical glass micronozzles to measure cell deformability. *Journal of Micromechanics and Microengineering*, vol. 29, p. 105001, 2019.

2. A. Ponce-Torres, E. Ortega, M. Rubio, A. Rubio, E. J. Vega and J. M. Montanero. Gaseous flow focusing for spinning micro and nanofibers. *Polymer*, vol. 178, p. 121623, 2019.

3. S. Blanco-Trejo; M. A. Herrada; A.M.Gañán-Calvo; A. Rubio; M.G. Cabezas; J. M. Montanero. Whipping in gaseous flow focusing. International Journal of Multiphase Flow. 130, pp. 103367. 2020.

4. M. G. Cabezas; J. M. Montanero; A. Rubio; A. M. Gañán-Calvo; F.J. Galindo-Rosales. Método y dispositivo para la focalización gaseosa de fluidos transonicos de chorro débilmente viscoelásticos. Nº of patent P202230313. 06/04/2022. Spain.

5. A. Rubio;F. J. Martínez-Vázquez; M. G. Cabezas; J. M. Montanero; E. J. Vega. Effect of the air coflow temperature and spinneret position on the solution blow spinning technique. Fibers and Polymers. 23, 2299-2305. 2022.

6. P. Rodríguez-Díaz; A. Rubio; J. M. Montanero; A. M. Gañán-Calvo; M. G. Cabezas. Bubble bursting in a weakly viscoelastic liquid. Physics of Fluids. 35, 102107, 2023.

7. A. Rubio; E. J. Vega; M. G. Cabezas; J. M. Montanero; J. M. López-Herrera; M. A. Herrada. Bubble rising in the presence of a surfactant at very low concentrations. Physics of Fluids. 36, 062112, 2024.

8   A. Rubio; D.Fernández-Martínez; Y. Yokoyama; K. Hashimoto; S. Miyatake; Y. Tagawa; E.J.Vega. Droplet impact of a rheologically-relevant blood simulant at body temperature. Book chapter Elsevier (under review). 2024.

References

[1] E. K. Sackmann, A. L. Fulton, and D. J. Beebe. The present and future role of microfluidics in biomedical research. *Nature*, 507:181–189, 2014.

[2] L. Vilas-Boas, V. Faustino, R. Lima, J. M. Miranda, G. Minas, C. S. Veiga-Fernandes, and S. Oliveira-Catarino. Assessment of the deformability and velocity of healthy and artificially impaired red blood cells in narrow polydimethylsiloxane (pdms) microchannels. *Micromachines*, 9:384, 2018.

[3] L. Shang, Y. Cheng, and Y. Zhao. Emerging droplet microfluidics. *Chem. Rev.*, 117:7964–8040, 2017.

[4] O. Otto, P. Rosendahl, A. Mietke, S. Golfier, C. Herold, D. Klaue, S. Girardo, S. Pagliara, A. Ekpenyong, and A. Jacobi et al. Real-time deformability cytometry: On-the-fly cell mechanical phenotyping. *Nat. Methods*, 12:199–202, 2015.

[5] A. Rubio, V. Faustino, M. G. Cabezas, R. Lima, and E. J. Vega. Fire-shaped cylindrical glass micronozzles to measure cell deformability. *J. Micromech. Microeng.*, 29:105001, 2019.

[6] A. S. Utada, E. Lorenceau, D. R. Link, P. D. Kaplan, H. A. Stone, and D. A. Weitz. Monodisperse double emulsions generated from a microcapillary device. *Science*, 308:537–541, 2005.

[7] D. P. DePonte, U. Weierstall, K. Schmidt, J. Warner, D. Starodub, J. C. H. Spence, and R. B. Doak. Gas dynamic virtual nozzle for generation of microscopic droplet streams. *J. Phys. D: Appl. Phys.*, 41:195505, 2008.

[8] J. Guerrero, Y. Chang, A. A. Fragkopoulos, and A. Fernández-Nieves. Capillary-based microfluidics-coflow and flow-focusing and electro-coflow and drops and jets and and instabilities. *Small*, 16:1904344, 2020.

[9] J. M. Montanero and A. M. Gañán-Calvo. Dripping and jetting and tip streaming. *Rep. Prog. Phys.*, 83:097001, 2020.

[10] B. N. Muñoz-Sánchez and M. G. Cabezas. Borosilicate nozzles manufactured by reproducible fire shaping. *J. Mater. Proces. Tech.*, 261:173–183, 2018.

[11] B. N. Muñoz-Sánchez, A. M. Gañán-Calvo, and M. G. Cabezas. A new fire shaping approach to produce highly axisymmetric and reproducible nozzles. *J. Mater. Process. Tech.*, 270:241–253, 2019.

[12] A. V. Nielsen, M. J. Beauchamp, G. P. Nordin, and A. T. Woolley. 3D printed microfluidics. *Annu. Rev. Anal. Chem.*, 13:45–65, 2020.

[13] J. Knoška, L. Adriano, S. Awel, K. R. Beyerlein, O. Yefanov, E. Peña Murillo, N. Roth, I. Sarrou, P. Villanueva-Perez, and et al. Ultracompact 3d microfluidics for time-resolved structural biology. *Nat. Commun*, 11:657, 2020.

[14] M. V. Bandulasena, G. T. Vladisavljevic, O. G. Odunmbaku, and B. Benyahia. Continuous synthesis of PVP stabilized biocompatible gold nanoparticles with a controlled size using a 3D glass capillary microfluidic device. *Chem. Eng. Sci.*, 171:233 – 243, 2017.

[15] M. V. Bandulasena, G. T. Vladisavljevič, and B. Benyahia. Versatile reconfigurable glass capillary microfluidic devices with Lego® inspired blocks for drop generation and micromixing. *J. Colloid Interface Sci.*, 542:23–32, 2019.

[16] C. Y. Wei, C. Z. Yu, J. J. Wu, J. W. Li, S. S. Li, S. J. Dai, and T. J. Li. Easy-to-operate fabrication of tapered glass capillaries for microdroplet generation. *J. Micromech. Microeng.*, 29:037001, 2019.

[17] M. Levenstein, L. Bawazer, C. M. Nally, w. Marchant, X. Gong, F. Meldrum, and N. Kapur. A reproducible approach to the assembly of microcapillaries for double emulsion production. *Microfluid. Nanofluid*, 20:143, 2016.

[18] B. R. Benson, H. A. Stone, and R. K. Prud?homme. An "off-the-shelf" capillary microfluidic device that enables tuning of the droplet breakup regime at constant flow rates. *Lab Chip*, 13:4507, 2013.

[19] Gary L. Switzer. A versatile system for stable generation of uniform droplets. *Rev. Sci. Instrum.*, 62:2765–2771, 1991.

[20] T. A. Comunian, R. Ravanfar, S. D. Alcaine, and A. Abbaspourrad. Water-in-oil-in-water emulsion obtained by glass microfluidic device for protection and heat-triggered release of natural pigments. *Food Res. Int.*, 106:945–951, 2018.

[21] A. M. Gañán-Calvo. Generation of steady liquid microthreads and micron-sized monodisperse sprays in gas streams. *Phys. Rev. Lett.*, 80:285–288, 1998.

[22] S. Blanco-Trejo, M. A. Herrada, A. M. Gañán-Calvo, A. Rubio, M. G. Cabezas, and J. M. Montanero. Whipping in gaseous flow focusing. *Int. J. Multiphase Flow*, 130:103367, 2020.

[23] A. Ponce-Torres, E. Ortega, M. Rubio, A. Rubio, E. J. Vega, and J. M. Montanero. Gaseous flow focusing for spinning micro and nanofibers. *Polymer*, 178:121623, 2019.

[24] T. Si, F. Li, X.-Y. Yin, and X.-Z. Yin. Modes in flow focusing and instability of coaxial liquid-gas jets. *J. Fluid Mech.*, 629:1–23, 2009.

[25] A. M. Gañán-Calvo and J. M. Montanero. Revision of capillary cone-jet physics: Electrospray and flow focusing. *Phys. Rev. E*, 79:066305, 2009.

[26] E. J. Vega, J. M. Montanero, M. A. Herrada, and A. M. Gañán-Calvo. Global and local instability of flow focusing: The influence of the geometry. *Phys. Fluids*, 22:064105, 2010.

[27] J. M. Montanero, N. Rebollo-Muñoz, M. A. Herrada, and A. M. Gañán-Calvo. Global stability of the focusing effect of fluid jet flows. *Phys. Rev. E*, 83:036309, 2011.

[28] A. Bayram, M. Serhatlioglu, B. Ortac, S. Demic, C. Elbuken, M. Sen, and M. E. Solmaz. Integration of glass micropipettes with a 3D printed aligner for microfluidic flow cytometer. *Sens. Actuator A-Phys.*, 269:382–387, 2018.

[29] K. R. Beyerlein, L. Adriano, M. Heymann, R. Kirian, J. Knoska, F. Wilde, H. N. Chapman, and S. Bajt. Ceramic micro-injection molded nozzles for serial femtosecond crystallography sample delivery. *Rev. Sci. Instrum.*, 86:125104, 2015.

[30] V. Piotter, A. Klein, K. Plewa, K. R. Beyerlein, H. N. Chapman, and S. Bajt. Development of a ceramic injection molding process for liquid jet nozzles to be applied for X-ray free-electron lasers. *Microsyst. Technol.*, 24:1247–1252, 2018.

[31] A. J. Acero, C. Ferrera, J. M. Montanero, and A. M. Gañán-Calvo. Focusing liquid microjets with nozzles. *J. Micromech. Microeng.*, 22:065011, 2012.

[32] H. N. Chapman, P. Fromme, A. Barty, T. A. White, R. A.Kirian, A. Aquila, M. S. Hunter, J. Schulz, D. P. DePonte, U. Weierstall, and et al. Femtosecond x-ray protein nanocrystallography. *Nature*, 470:73–79, 2011.

[33] H. N. Chapman *et al.* Femtosecond X-ray protein nanocrystallography. *Nature*, 470:73–79, 2011.

[34] M. López, M. Rubio, S.H. Sadek, and E . J. Vega. A simple emulsification technique for the production of micro-sized flexible powder of polydimethylsiloxane (PDMS). *Powder Technology*, 366:610–616, 2020.

[35] M. Brust, C. Schaefer, R. Doerr, L. Pan, M. Garcia, P. E. Arratia, and C. Wagner. Rheology of Human Blood Plasma: Viscoelastic Versus Newtonian Behavior. *Phys. Rev. Lett.*, 110:078305, 2013.

[36] P. C. Sousa, R. Vaz, A. Cerejo, M. S. N. Oliveira, M. A. Alves, and F. T. Pinho. Rheological behavior of human blood in uniaxial extensional flow. *J. Rheol.*, 62:447–456, 2018.

[37] F. Cruz-Mazo, M. A. Herrada, A. M. Gañán-Calvo, and J. M. Montanero. Global stability of axisymmetric flow focusing. *J. Fluid Mech.*, 832:329–344, 2017.

[38] M. A. Herrada, A. M. Gañán-Calvo, A. Ojeda-Monge, B. Bluth, and P. Riesco-Chueca. Liquid flow focused by a gas: Jetting and dripping and and recirculation. *Phys. Rev. E*, 78:036323, 2008.